



**HAL**  
open science

# Small spatial scales in wetting on non-structured and structured surfaces: thin films of liquid crystals & small-scales wetting properties of ionic liquids

Céline J. E. Richard

► **To cite this version:**

Céline J. E. Richard. Small spatial scales in wetting on non-structured and structured surfaces: thin films of liquid crystals & small-scales wetting properties of ionic liquids. *Soft Condensed Matter* [cond-mat.soft]. Université Pierre et Marie Curie - Paris VI, 2011. English. NNT: . tel-00662524

**HAL Id: tel-00662524**

**<https://theses.hal.science/tel-00662524>**

Submitted on 24 Jan 2012

**HAL** is a multi-disciplinary open access archive for the deposit and dissemination of scientific research documents, whether they are published or not. The documents may come from teaching and research institutions in France or abroad, or from public or private research centers.

L'archive ouverte pluridisciplinaire **HAL**, est destinée au dépôt et à la diffusion de documents scientifiques de niveau recherche, publiés ou non, émanant des établissements d'enseignement et de recherche français ou étrangers, des laboratoires publics ou privés.

DEPARTEMENT DE PHYSIQUE DE L'ÉCOLE NORMALE SUPÉRIEURE  
LABORATOIRE DE PHYSIQUE STATISTIQUE



THÈSE DE DOCTORAT DE L'UNIVERSITÉ PARIS 6  
PIERRE ET MARIE CURIE  
UFR DE PHYSIQUE  
SPECIALITÉ : PHYSIQUE DES LIQUIDES

SMALL SPATIAL SCALES IN WETTING ON  
NON-STRUCTURED AND STRUCTURED  
SURFACES  
THIN FILMS OF LIQUID CRYSTALS &  
SMALL-SCALE WETTING PROPERTIES OF IONIC LIQUIDS

par Céline J. E. RICHARD

Soutenue le 28 novembre 2011 :

Mme Martine BENAMAR	Présidente du Jury
Mme Anne-Marie CAZABAT	Directrice de thèse
Mme Elise LORENCEAU	Rapporteur
M. Hamid KELLAY	Rapporteur
M. John RALSTON	Examineur, co-directeur de thèse
M. Michel VOUE	Examineur

# Acknowledgments

Une thèse, un sujet en deux parties étudiées dans deux laboratoires différents situés aux antipodes géographiques l'un de l'autre. C'est une double richesse scientifique, culturelle et humaine qu'il m'a été donné de découvrir pendant ces trois ans.

C'est grâce à Anne-Marie Cazabat, ma directrice, que cette thèse a pu s'organiser ainsi. Je tiens à la remercier chaleureusement de m'avoir permis de travailler dans son équipe et pour avoir partagé son sens de la rigueur de la physique et ce dans une ambiance toujours détendue. Cela a été une expérience extrêmement enrichissante de pouvoir travailler à son contact. Merci également d'accorder une grande importance à l'encadrement des doctorants et ce quelles que soient les circonstances. Enfin, merci de m'avoir ouvert les portes de la collaboration avec l'Australie.

Je remercie également Martine Ben Amar d'avoir accepté de présider mon jury ainsi que pour la collaboration fructueuse sur le volet théorique du sujet "cristaux liquides". Avant une thèse, il y a un master 2, celui de physique des liquides, et j'en profite aussi pour la remercier d'y organiser un cursus de qualité.

Je remercie Elise Lorenceau et Hamid Kellay d'avoir accepté d'être mes rapporteurs ainsi que Sylvie Cohen-Addad d'avoir accepté de co-signer le rapport d'Elise Lorenceau pour raison administrative. Je remercie également Michel Voué d'avoir accepté de faire partie de mon jury.

Du côté français, je remercie le LPS de m'avoir accueilli pendant ces 3 ans.

Je remercie Jacques Meunier pour son savoir technique et ses conseils ainsi que pour le prêt de son matériel sans quoi certaines expériences n'auraient pas été possibles.

Je remercie également les personnes avec qui j'ai pu travailler sur le sujet "cristaux liquides". Merci à Ulysse Delabre pour le passage de relais. Cela a été très agréable de travailler avec quelqu'un d'aussi organisé et rigoureux. Je me rappellerai également des nombreuses discussions sur la physique et sur la transmission aux plus jeunes autour d'un bon café (parfois un peu décalé !). Merci à Yann Yip Cheung Sang pour la collaboration et les discussions sur les expériences ainsi que pour avoir partagé son sens de l'astuce pour l'amélioration des dispositifs expérimentaux ! Merci à Oksana Manyuhina d'avoir partagé son savoir sur la partie théorique du sujet (au laboratoire et sous le soleil de Cargèse) et sa passion pour la physique.

Je remercie Sébastien Moulinet pour sa disponibilité, pour être toujours prêt à aider par ses très bons conseils techniques et pour avoir aidé quelques générations de doctorants à décrypter le labyrinthe qu'est la S11 ! Je remercie également les anciens membres du groupe pour m'avoir accueilli très chaleureusement: Geoffroy Guéna, Peder Moller, Christophe Chevallier et Didi Derks (especially for the nice chocolate-coffee breaks in the garden).

Je remercie également tous ceux qui ont contribué à rendre la vie au laboratoire sympathique: Kristina Davitt (j'espère que l'on continuera à partager notre passion des gâteaux, même à distance !), Satoshi Sasaki, Claudia Pantalei (merci pour l'idée des séances de roller !), Elsa Bayart (merci pour la co-organisation du séminaire thésards... et à quand la prochaine randonnée

?!), Xavier Rojas et Arnaud Arvengas (merci à tous les deux pour les pauses / discussions / café).

Je remercie également ceux sans qui les thèses du laboratoire n'iraient pas bien loin : merci à José da Silva Quintas et à tout l'atelier mécanique ; merci à Christophe Hermann et à tout l'atelier électronique ; merci au secrétariat: Nora Sadaoui (merci pour le temps passé à m'aider pour les nombreuses commandes et pour les nombreux papiers pour l'Australie), Marie Gefflot et Annie Ribeau ; merci à Zaïre Dissi et à tout le service informatique ; merci à Michael Rosticher et à toute l'équipe d'entretien de la salle blanche ; merci à Didier Courtiade et à tout le service entretien général et magasins (en particulier pour les cas d'urgences avec les fuites d'eau récurrentes au deuxième sous-sol) ; merci au service électrique.

This thesis carried on in Australia, so I would like to thank the team, I was able to work with in the Ian Wark Research Institute.

I thank John Ralston for welcoming me in his laboratory and for giving me the great opportunity to work in his team. I thank him also for making me discover the enigmatic and always entertaining ionic liquids. I also thank him for being a member of my jury and for writing a report on my manuscript as it was impossible for him to attend to the defense.

I thank Marta Krasowska for her constant support, for her passion for physics, especially AFM (!!!) and for her enthusiasm. I also had to say, that "I give you my pen" !

I thank Mihail Popescu for his help and for numerous discussions on the project.

I thank the scientific services for their help, especially Scott Abbott (for carbon vapor deposition) and Chris Bassell (for XPS).

I would also like to thank the members of the group and of other groups who were welcoming and of great help to me, especially at the beginning: Mélanie Ramiasa (merci pour tout et un gros bisous au petit Luca !), Muireann O'Loughlin (thanks for the discussions !), Lorena Dieguez (thank to you and Sam, especially for welcoming me at your place in July and August), Audrey Beaussart and Jairo Garnica (merci pour tout !), Régis Méjard (merci pour beaucoup... le téflon, les discussions en direct et sur skype, la chasse aux fautes d'anglais dans le "manuscript" et pour la suite, lis le dernier paragraphe...), Gabor Rozipal, Valentin Vancea (thanks for explaining everything about the purification of ionic liquids), Bogale Tadesse, Li Jiang, Hua Li, Zhantao Wang.

I would also like to thank the non-physicist friends who also helped me feel like home at the other end of the world: Nathalie and Isabelle ; Leesa ; Karen ; Xavier et Perrine ; Sam ; Jared ; Tom.

Enfin, je tiens à remercier ma famille et mes amis pour leur soutien constant et pour leur présence tout simplement ! Merci tout spécialement à mes parents ; à mes "vieux" amis Elsa C. (bon surf à toi et Romain à Los Angeles... ou plutôt bon séjour à LA sans surf !), Keyan (Bonne chance pour le Canada !) et Mathilde (bientôt des vacances en Australie ?!) ; et puis à Régis (promis, j'apporte des marrons glacés en février !... merci d'avoir été là !)





# Introduction

Drizzle falls. But what is the shape of the falling drops ? A thin tube of glass is dipped into water and water is sucked inside the tube. Why ? The answer to these questions was given in the studies of Pierre Simon de Laplace about capillary phenomena. Already in the 18th century, the behaviour of “small” quantities of liquids at an interface (liquid / gas for the drop ; liquid / solid and liquid / gas for the tube) was questioned. Since this pioneering work, small-scale wetting behaviour stayed a vivid area of physics and this partly because the definition of “small” changed along with advances in technologies. New methods allowing one to scan the properties of interfaces on smaller and smaller scales were indeed developed. One could cite for example Brewster Angle Microscope (BAM), Atomic Force Microscopy, ... What is then meant by the expression “small-scale wetting behaviour” ? In this work, the so-called “small-scales” will refer to sub-micron phenomena. Sub-micron interfacial phenomena are of key importance in industrial processes (e.g. cleaning) and also in the growing field of nanotechnologies and microfluidics which final aim is to develop “labs on a chip”.

At a time where miniaturization is one of the main challenges in science, the physics of wetting at small-scales is far from being completely understood. Going towards microscopic scales, systems’ behaviour changes. The structuring role of the interface(s), the heterogeneities of the substrate or the growing importance of line effects over surface effects begin to play a major role. The aim of the present thesis is then to bring new clues to help the development of theoretical tools and models. Two examples of complex small-scale systems will be presented: thin films of nematic liquid crystals on liquid substrates as well as droplets and precursors of ionic liquids on solid substrates.

Liquid crystals are well-known for their everyday life applications. The most common one is the Liquid Crystal Display (LCD) flat screen which can be found nowadays on almost every computer, cell-phone or television. Liquid crystals are a very specific kind of materials. They indeed are able to flow like liquids but they also possess a long range order like solids. Compared to an usual liquid, two additional ingredients must be added to describe the wetting properties of nematic liquid crystals: elasticity which is the source of long range interactions and anchoring which describes the specific role played by the boundary conditions for a nematic liquid crystal. Because of the specific nature of liquid crystals, for thicknesses less than one micrometer, films

of nematic liquid crystal deposited on a substrate in hybrid configuration (antagonist anchoring conditions at the boundaries) have an unusual wetting behaviour:

- There is a forbidden thickness zone: films thicker than 20 – 30 nm or thinner than 3.5 nm far from the phase transition, are observed and may eventually coexist.
- The structure of films thicker than 20–30 nm is quite specific, at least on liquid substrates: they show striped instability patterns understood as a way to relax nematic elasticity.

In an ideal situation, it would be possible to build up a unique model of the nematic free energy to describe these behaviours. Unfortunately, such a model, taking into account phenomena at different scales, has not been developed yet. As a first approach, an attempt of description of the behaviour of striped films is based on the continuum theory of nematic elasticity. However, a large part of experimental observations escapes to the analysis and the model does not account for the forbidden range of thicknesses. Hence, the experimental work in progress is aimed at producing precise data to bring new clues for future theoretical analysis. The structure of these thin nematic films as well as the one of their rim were then studied both in the nematic range of temperature as well as coming close and crossing the nematic / isotropic phase transition.

Ionic liquids are molten salts at ambient temperature. They are now ubiquitous in industry: gas handling, nuclear fuel reprocessing, solar cells, batteries, chemical industry... Considering chemical industry, ionic liquids have an important role to play in the field of green chemistry. Because of their very low saturating vapor pressure, using ionic liquids does indeed not contaminate the atmosphere. One of the possible ways of contamination for the environment is then eliminated, that is why they are considered as an alternative to organic solvents. However, if these so-called “green solvents” do not evaporate in the atmosphere, it does not mean that they are not toxic ! Pollution caused by ionic liquids is just more controllable than for usual organic solvents. In order to be able to completely control the pollution created by ionic liquids, their interfacial properties are a key problem. This is one of the reasons that makes their wetting behaviour on small-scales a hot topic. Small quantities of ionic liquid were deposited on several substrates, smooth or rough. The microscopic landscape obtained, droplets and thin films, was then imaged using Atomic Force Microscopy (AFM). The AFM images allowed for a first characterization leading to the emergence of general trends on the modification of the contact angle when going towards small-scales or on the presence and evolution of thin films.

# Chapter 1

## An introduction to wetting phenomena

### 1.1 Phenomenological description

#### 1.1.1 Common observations, some questions and comments

Dew on leaves or water on clean glass, is there a difference ? Dew on leaves looks like small drops whereas water on clean glass spreads and a water film covers the whole surface. For the same liquid, changing the substrate thus allows for the creation of two different wetting situations: drop or film. What would happen then if drops of two different liquids were deposited on the same substrate ? Using the example of water, would there be a difference in between water deposited on clean glass and mercury deposited on clean glass ? There would: mercury unlike water would not spread on the clean glass surface, it would form a drop<sup>1</sup>. Those observations show that it is the couple liquid/substrate which matters in wetting phenomena.

But is that all ? What if, instead of changing the liquid or the substrate, the ambient environment is changed ? Let us first consider dodecane deposited on a teflon substrate in

---

<sup>1</sup>Mercury on glass is actually one rare example of drying: at the equilibrium, the liquid drop is separated from the substrate by a macroscopic vapor layer.

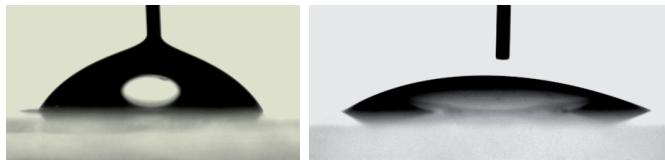


Figure 1.1: Dodecane on teflon substrate. On the left side in air. On the right side in water.

air. It forms a drop as shown in figure 1.1. The same experiment is now repeated, but in a cell filled with water. The dodecane also forms a drop on the teflon substrate, only it is much flatter (see figure 1.1). Changing the environment modified the way the liquid spreads on the substrate. The ambient environment interacts indeed individually with the substrate and with the liquid. Wetting phenomena is then a problem with three components interacting with each other individually: the liquid phase and the substrate, the liquid phase and the ambient environment and the substrate and the ambient environment. Those interactions will determine which situation is the most favorable from an energetic point of view.

However, some care must be taken when going from mere observation to theoretical description as three phases are present. When mentioning dew, i.e., condensation, one implicitly assumes that air is humid, that is, there are water molecules in the gas phase. And the water drop? If the atmosphere is not saturated with water, it will evaporate after some time. Two problems are hidden here: the mutual solubility of the phases, e.g. liquid evaporation in the gas phase, and the time scale. The condensation of water on leaves also implies that they are slightly colder than air. Therefore, our simple observations are not so simple to analyze. Moreover, having a drop sitting on the substrate does not mean that the substrate is dry around. There is always a microscopic film, more or less dense, which is adsorbed. There is then a third problem: the analysis must take into account all spatial scales, from macroscopic to microscopic ones.

This introduction to wetting phenomena will not be exhaustive. We shall focus on well-defined situations, where equations can be conveniently written. Let us give further comments.

Thermodynamic equilibrium requires all phases to be mutually saturated. However, as mechanical and thermal equilibrium are usually much faster than chemical equilibrium, it is often possible to neglect the mutual solubility of the phases all over the experiment: this is referred to as "initial" conditions. The spatial scales are defined in reference to the range of interactions. In interface science, a relevant scale is the range  $l$  of the interaction between infinite half-spaces<sup>2</sup> separated by a third phase, that is, interaction across a flat film<sup>3</sup>. The macroscopic scale is much larger than  $l$ . At the mesoscopic scale  $\approx l$ , the medium is continuous. The molecular scale does not require specific definition.

### 1.1.2 Total wetting, partial wetting, Contact angle

As described before, when liquid is deposited on a substrate it can either spread or form a drop. When the liquid spreads, the situation is called total wetting. When the liquid forms a drop, the situation is called partial wetting.

In the latter case, looking at a macroscopic drop from the side enables one to observe that the liquid makes an angle with the substrate. It is called the contact angle (see figure 1.2). This angle stays the same for each three-component system, liquid / substrate / ambient environment,

---

<sup>2</sup> $l$  is of the order of hundred of nanometers for Van der Waals interaction.

<sup>3</sup>It is worth noting that droplets, nanometric both in radius and thickness, cannot be treated as the juxtaposition of slices of flat films. The characteristic length of the range of interaction is much shorter than  $l$ .

no matter what the volume of deposited liquid is and provided the drop is macroscopic<sup>4</sup>. The contact angle can take any value in the range  $0^\circ$  to  $180^\circ$  and therefore allows to describe any possible partial-wetting situation.

As water is the most common liquid, there is a specific terminology for water droplets deposited on a substrate in air. If the contact angle is less than  $90^\circ$ , the substrate is called hydrophilic and if the contact angle is more than  $90^\circ$ , it is called hydrophobic. When the contact angle comes close to  $180^\circ$ , the substrate is called superhydrophobic. Some superhydrophobic substrates are quite specific as they are covered with pillars. The pillar's shape and the fraction of the surface of the substrate covered by the pillars controls the superhydrophobic behavior.

Returning to the comments in 1.1.1, it comes that:

- Contact angles can be defined unambiguously only at thermodynamic equilibrium, or in the "initial" situation if it is properly controlled,
- They are defined at the macroscopic scale.

### 1.1.3 Interfacial tension

Interfacial tension is a macroscopic excess free energy per unit area defined between two infinite phases at thermodynamic equilibrium. Keeping in mind the previous comments, we shall present the basic equations in an ideal situation where phases are strictly immiscible, avoiding the ambiguity between initial and equilibrium quantities. The point will be discussed later when required.

Let us consider two immiscible phases at equilibrium. Having an interface means that the contact in between the molecules of the two different phases is not favorable. Bringing molecules

---

<sup>4</sup>The macroscopic drop is a spherical shape if gravity is negligible. This means that the length scale of the drop, i.e. its radius, has to be smaller than the capillary length,  $\kappa^{-1}$ . It corresponds to the length scale where the hydrostatic pressure compensates exactly the capillary pressure:  $\frac{\gamma}{\kappa^{-1}} = \rho g \kappa^{-1}$  where  $\gamma$  is the surface tension;  $\rho$  is the density of the liquid and  $g$  the acceleration of gravity. The capillary length can therefore be written as  $\kappa^{-1} = \sqrt{\frac{\gamma}{\rho g}}$ ;  $\kappa^{-1} \approx 3$  mm for water.

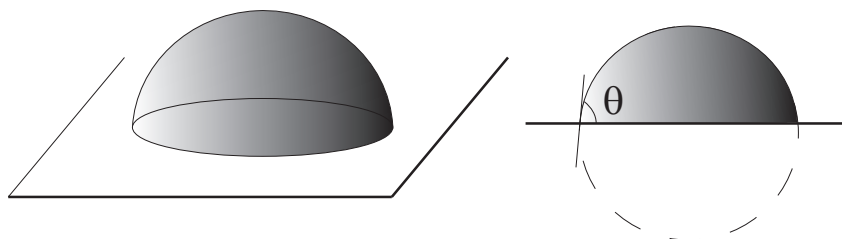


Figure 1.2: The ideal case of the spherical shaped droplet (partial wetting, the droplet is small enough to avoid gravity effects and the substrate is smooth). On the left, 3D. On the right: the droplet is seen from the side, the tangent to the spherical shape at the junction with the substrate defines the contact angle,  $\theta$

at the interface thus costs a certain amount of energy. This cost is represented by the interfacial tension,  $\gamma$ . It is indeed the energy needed to increase in a reversible way the area of an interface by one unit at given temperature and phase volumes. To describe this process, the free surface energy,  $F$ , is introduced:

$$F = \gamma A \quad (1.1)$$

where  $A$  the area of the flat interface and  $\gamma$  is the surface tension (in  $J.m^{-2}$  or  $N.m^{-1}$ ). The interfacial tension is the excess free energy per unit area associated to the interfacial zone, which properties differ from the ones of the bulk phases ([19], [32]). It can be calculated explicitly if the interaction potentials between molecules are known.

For liquid deposited on a substrate, as mentioned before, there are three phases to take into account: the liquid, the substrate and the ambient environment. One must then consider three interfacial tensions:

- $\gamma_{sg}$ , the surface tension associated to the interface substrate / ambient environment. The ambient environment will be symbolized by a “g”, as in the present case it is a gas phase.
- $\gamma_{lg}$ , the interfacial tension associated to the interface liquid phase / ambient environment<sup>5</sup>.
- $\gamma_{ls}$ , the interfacial tension associated to the interface liquid phase / substrate.

Each interfacial tension is defined for a couple of two phases in the absence of the third one (which causes no ambiguity in the ideal case considered here of strictly immiscible phases). The interfacial tension between a dense phase, liquid or solid, and a gas phase is commonly called surface tension. As mentioned above, surface tension comes from the balance of interactions in between the molecules in the phases. Among these interactions, one may mention Van der Waals forces, hydrogen bonds (in the case of water for example), ionic bonds or metallic bonds (in the case of liquid metals like mercury for example).

#### 1.1.4 Young’s law

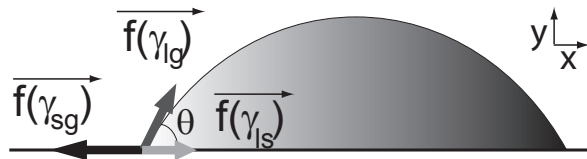


Figure 1.3: Side view of a macroscopic drop. The forces induced by interfacial tensions on the three-phase contact line are drawn as arrows.  $\gamma_{sg}$ ,  $\gamma_{lg}$  and  $\gamma_{ls}$  stand respectively for the interfacial tension of the gas phase v.s. the substrate, of the liquid phase v.s. the gas phase and of the liquid phase v.s. the substrate

<sup>5</sup>At the ambient temperature, an order of magnitude of  $\gamma_{lg}$  is:  $\approx 20$  mN/m for most oils,  $\approx 72$  mN/m for water because of hydrogen bonds,  $\approx 500$  mN/m for mercury because the cohesion within this liquid metal is very strong.

In the ideal case of strictly non miscible phases, the relationship between the interfacial tensions and the contact angle can be written unambiguously. On solid, non deformable substrates, this relationship is called Young's law. Two different approaches can be used to introduce it. The first one is based on forces and the second one on energy. They will be presented in the 2D case of a liquid wedge on the solid substrate.

In the first approach, the forces acting per length unit on the contact line are counted (see figure 1.3). On a flat, non deformable substrate, as the drop is at the equilibrium, the cancellation of the three forces components per length unit along the substrate leads to:

$$-f_{sg} + f_{lg} * \cos\theta + f_{ls} = 0 \quad (1.2)$$

Young's law is obtained:

$$-\gamma_{sg} + \gamma_{lg} * \cos\theta + \gamma_{ls} = 0 \quad \text{or} \quad \cos\theta = \frac{\gamma_{sg} - \gamma_{ls}}{\gamma_{lg}} \quad (1.3)$$

The second approach relies on the calculation of the reversible virtual work,  $dW$  done by a moving liquid wedge ahead of the contact line by a small distance,  $dx$ , corresponding to a small change  $dA$  of the area covered on the substrate. The reversible work done is the change in free energy and can be expressed as:

$$dW = -\gamma_{sg} * dA + \gamma_{lg} * \cos\theta * dA + \gamma_{ls} * dA \quad (1.4)$$

At the equilibrium,  $\frac{dW}{dA} = 0$

$$0 = -\gamma_{sg} + \gamma_{lg} * \cos\theta + \gamma_{ls} \quad (1.5)$$

Which is again the expression of Young's law.

Young's law is a powerful tool as it links the equilibrium contact angle of a drop to the three interfacial tensions involved. However, one must keep in mind that reversibility is assumed in the derivation (even if it is implicit in the force approach). Moreover, the unrealistic assumption of complete immiscibility must now be reconsidered: two physically well-defined situations are, (i) "initial conditions" implying the achievement of mechanical and thermal equilibrium, but a negligible transfer of molecules between phases, and (ii) the thermodynamic equilibrium.

### 1.1.5 Initial spreading parameter, thermodynamic equilibrium

**“Initial conditions” implying the achievement of mechanical and thermal equilibrium, but a negligible transfer of molecules between phases**

The initial spreading parameter,  $S_0$ , compares the free energy per area unit of a substrate covered by a macroscopic liquid film to the one of the dry substrate in contact with the same (here gas)



phase. This is a macroscopic quantity.

$$S_0 = \frac{\Delta F}{A} = \gamma_{sg} - (\gamma_{lg} + \gamma_{ls}) \quad (1.6)$$

The sign of the initial spreading parameter allows one to predict if a macroscopic liquid drop just deposited on the substrate will spread completely or not. If  $S_0$  is positive,  $\gamma_{sg} > \gamma_{lg} + \gamma_{ls}$ , liquid covering the substrate is more favorable than having the substrate in direct contact with the ambient environment. The drop spreads: it is the case of total wetting. On the contrary, if  $S_0$  is negative,  $\gamma_{sg} < \gamma_{lg} + \gamma_{ls}$ , liquid covering the substrate is less favorable than having the substrate in direct contact with the ambient environment. The drop does not spread. This is the case of partial wetting.

It is usual to define two categories of substrates: high-energy substrates and low-energy substrates. For clean high-energy substrates (e.g. clean glass), the surface tension is very high  $\gamma_{sg} \approx 500$  to  $5000$  mN/m. This kind of substrates contains ionic, covalent or metallic bonds. Most liquids spread on them (see equation 1.6). For low-energy substrates (e.g. teflon),  $\gamma_{sg} \approx 10$  to  $20$  mN/m, they have a poor wettability. This kind of substrates are mostly molecular crystals or plastics.

### Thermodynamic equilibrium

At the thermodynamic equilibrium, the phases are mutually saturated, which means that the gas phase is saturated with evaporated liquid molecules (and that the liquid is saturated with gas ; the solid is not considered). In partial wetting, a microscopic film of liquid is adsorbed on the solid and is a part of the solid-gas interface, which surface tension may significantly differ from the one of the "dry" solid. Therefore, the initial spreading parameter  $S_0$  differs from the equilibrium one  $S$ . In complete wetting, a macroscopic film of liquid is present on the solid and is a part of the solid-gas interface. The equilibrium spreading parameter is zero ( $S_0 > 0$ ,  $S = 0$ ). Striking examples of an initial spreading ( $S_0 > 0$ ) followed by a retraction ( $S < 0$ ), as benzene on water, are warnings against uncontrolled use of formulae at interfaces.

#### 1.1.6 Contact angle hysteresis

So far, the substrates have been considered to be ideally smooth and homogeneous, as for the derivation of Young's law, for which reversibility is assumed. However, most solid substrates are not. Roughness or chemical heterogeneities can induce irregularities and even pinning of the three-phase contact line (see figure 1.4). In the presence of wettable defects, when the mutual affinity between the liquid and the defects is stronger than the average value on the substrate, a receding contact line tends to stay longer on the defects. On the contrary, when the affinity between the liquid and the defects is weaker, an advancing contact line has difficulties to cover them. Defects can play at the microscopic scale, in which case the macroscopic contact line looks

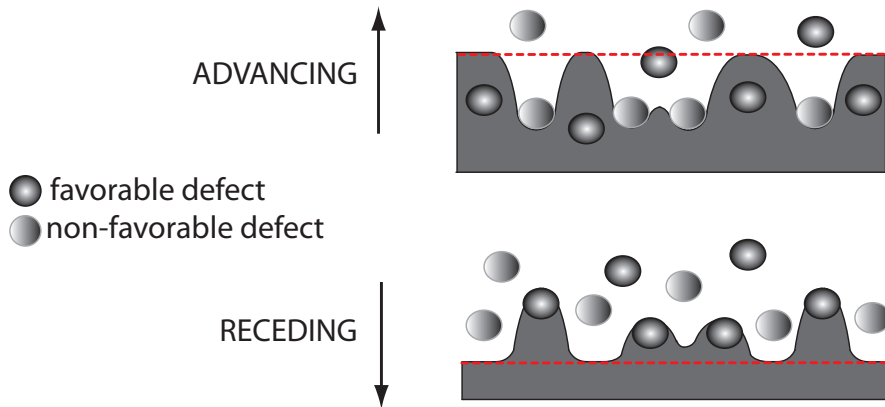


Figure 1.4: Schematic top view of the microscopic pinning of the contact line on a heterogeneous substrate in presence of favorable and non-favorable defects. White: substrate; grey: liquid. The dotted lines represent the position of the contact line in the absence of defects. Top: The advancing contact line is temporarily pinned on the non-favorable zones and merely covers the favorable ones. Bottom: The receding contact line stays temporarily pinned in the favorable zones and merely escapes from the non-favorable ones. There is elasticity of the contact line and as quoted in the text, this schematic figure refers to weak pinning [24].

smooth. This is the case considered here ([24]). The general problem of hysteresis is much more complex ([1]).

These microscopic processes have a macroscopic consequence on the contact angle of drops: poorly wettable defects increase the contact angle at an advancing contact line, while highly wettable defects decrease the contact angle at a receding contact line. Let us take the example of a drop sitting on a substrate. If the substrate is slightly tilted, the drop does not roll, it deforms. This is because the three-phase contact line is pinned. As long as this pinning is strong enough to counteract the gravity force induced by tilting the substrate, the drop stays still. If the tilting angle of the substrate is then increased until the drop begins to move, it is possible to observe

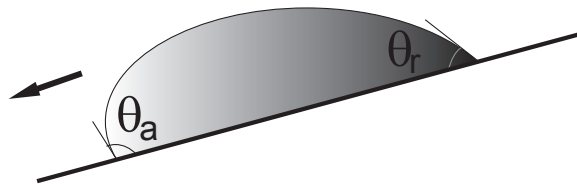


Figure 1.5: Hysteresis of the contact angle: The profile of a drop rolling with negligible velocity on a tilted substrate shows two different contact angles, the advancing contact angle  $\theta_a$  at the front and the receding contact angle  $\theta_r$  at the rear ;  $\theta_a > \theta > \theta_r$ . With increasing drop velocity the angle at the front increases and the angle at the rear decreases.

that the angles at the front and at the rear are different (see figure 3.3). In the limit of zero contact line velocity, the angle at the front of the rolling drop is called the advancing contact angle and the angle at the rear, the receding contact angle.

This contact angle hysteresis can also be observed for growing or shrinking drops<sup>6</sup>. If more liquid is injected to a pre-existing drop, it grows. The drop first inflates without moving until the contact angle reaches the advancing value. Once the advancing contact angle is reached, the three-phase contact line begins to move and the drop increases its lateral extension. The exact reverse phenomenon can be observed for drops where liquid is sucked instead of injected.

### 1.1.7 Wetting on an heterogeneous substrate, Wenzel and Cassie-Baxter models

Let us now consider two models dealing with larger scale heterogeneities, although still much smaller than the drop size. No hysteresis is present. In the Wenzel model, the substrate is rough, but chemically-homogeneous. In the Cassie-Baxter model, the substrate is chemically-heterogeneous, but smooth.

#### Wenzel model

Roughness reinforces the natural tendency of a chemically-homogeneous substrate. Let us consider a drop of liquid on a chemically-homogeneous smooth substrate with a contact angle in the range  $0^\circ$  to  $90^\circ$ . In that case, the liquid wets the substrate pretty well. If the same drop is deposited on the same substrate, but rough instead of smooth, the contact angle decreases: wetting is better than on the smooth substrate. In the same way, let us consider a drop of liquid with a contact angle in the range  $90^\circ$  to  $180^\circ$ . For a drop of the same liquid on the same substrate, but rough instead of smooth, the contact angle increases. Poor wetting becomes even poorer if the substrate is rough<sup>7</sup>.

The model of Wenzel allows to understand this phenomenon. The roughness is supposed to be small in comparison to the size of the drop. The contact angle on such a rough surface,  $\theta^*$  can be obtained by considering the elementary virtual work,  $dW$ , when the liquid wedge is moved reversibly of a small distance  $dx$  corresponding to a small change  $dA$  of the apparent area covered on the substrate (cf figure 1.6):

$$dW = r(\gamma_{ls} - \gamma_{sg})dA + \gamma_{lg}\cos\theta^*dA \quad (1.7)$$

where  $r$  is the roughness ratio of the solid<sup>8</sup>.  $r = 1$  if the solid is smooth ;  $r > 1$  if the solid is

<sup>6</sup>Growing or shrinking drops are used in Chapter 3 to measure the contact angle hysteresis of ionic liquids on several substrates. The technique used is the one of the sessile drop, where a drop is linked to a syringe which either dispenses or sucks liquid.

<sup>7</sup>This is used to obtain superhydrophobic substrates: a smooth hydrophobic substrate can become superhydrophobic in presence of roughness.

<sup>8</sup>The roughness ratio is defined as the ratio of true area of the solid surface to the apparent (projected) area.

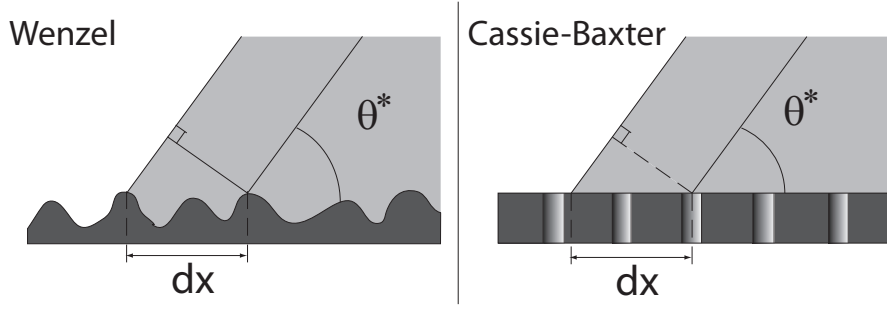


Figure 1.6: Moving the contact line of a liquid wedge of a small distance on a heterogeneous substrate. On the left, a physically-heterogeneous, i.e. rough, substrate: Wenzel model. On the right, a smooth, chemically-heterogeneous substrate: Cassie-Baxter model

rough. At the equilibrium,  $\frac{dW}{dA} = 0$ . Therefore, using Young's law:

$$\cos\theta^* = r\cos\theta \quad (1.8)$$

This is the Wenzel relation. As  $r > 1$ , it is the sign of the  $\cos\theta$  which matters. If  $\theta$  is in the range  $0^\circ$  to  $90^\circ$ ,  $\cos\theta > 0$  and  $\theta^* < \theta$ , the wetting of the liquid on the rough substrate is better than on the smooth one. On the contrary, if  $\theta$  is in the range  $90^\circ$  to  $180^\circ$ ,  $\cos\theta < 0$  and  $\theta^* > \theta$ , the wetting of the liquid on the rough substrate is poorer than on the smooth one.

Wetting transitions can occur due to roughness. Increasing roughness can lead good wetting to become total wetting or poor wetting to become non-wetting. For a given substrate / liquid / ambient environment situation, this transition is given by a critical roughness  $r^*$ . Considering Wenzel relation (cf equation 1.8),  $r^*$  corresponds to the value of  $r$  which makes  $\cos\theta^*$  equal to either 1 for total wetting transition or  $-1$  for non-wetting transition.

### Cassie-Baxter model

If the substrate is now a smooth chemically-heterogeneous plane surface, the Cassie-Baxter model can be used. The two different chemical patches lead to two different contact angles  $\theta_1$  and  $\theta_2$ . They occupy a fraction of the surface respectively equal to  $f_1$  and  $f_2$  ( $f_1 + f_2 = 1$ ). As in Wenzel model, the characteristic spatial scale of the chemical heterogeneity needs to be small in comparison to the size of the drop. The contact angle,  $\theta^*$  is again obtained by considering the reversible virtual work,  $dW$ , when the liquid wedge is moved of a small distance  $dx$  (cf figure1.6):

$$dW = f_1(\gamma_{ls} - \gamma_{sg})_1 dA + f_2(\gamma_{ls} - \gamma_{sg})_2 dA + \gamma_{lg}\cos\theta^* dA \quad (1.9)$$

At the equilibrium,  $\frac{dW}{dA} = 0$ . Using Young's equation, this leads to:

$$\cos\theta^* = f_1\cos\theta_1 + f_2\cos\theta_2 \quad (1.10)$$

This last relation is the Cassie-Baxter relation. The observed contact angle therefore belongs to the range  $[\theta_1; \theta_2]$ .

An example of drops and droplets deposited on a rough substrate will be presented in chapter 3.

## 1.2 Towards thin films and microscopic scales

### 1.2.1 Macroscopic, mesoscopic and microscopic scale

The first section of this chapter was focused on drops deposited on a substrate. Macroscopic physical concepts, such as interfacial tension and contact angle, were used to describe them. The macroscopic scale corresponds to lengths or film thicknesses much larger than the characteristic length  $l$  introduced above (cf 1.1.1), which characterizes the range of interaction across a flat film. This means that the free energy per area unit of a film of macroscopic thickness does not depend on the thickness. As previously mentioned, the mesoscopic scale corresponds to lengths or film thicknesses of order  $l$ . A continuous description is still valid, but now the free energy of a film depends on its thickness. Such films are frequently referred to as "thin" films. Finally, at the molecular scale, the media are not continuous anymore. Wetting has now gradually changed from a three-dimensional macroscopic problem to a two-dimensional problem. Films of molecular thickness are frequently referred to as "ultra-thin".

### 1.2.2 Thin flat films

Let us write explicitly the free interfacial energy of the three-phase system: substrate, flat film of thickness  $z$ , ambient environment. It depends now on  $z$ . For the sake of simplicity, we shall restrict the presentation to the "initial situation", where there is no exchange of molecules between phases. Limiting cases are already known. If  $z$  is macroscopic, the free energy per surface unit,  $\frac{F}{A}$ , is merely the sum of the interfacial tensions of the two interfaces: liquid / substrate,  $\gamma_{ls}$ , and liquid / ambient environment,  $\gamma_{lg}$ . In the opposite limit, i.e. the limit where  $z$  is 0, the energy per surface unit is the one of the interface substrate / ambient environment,  $\gamma_{sg}$ . In the general case, it is possible to define an expression of the energy per surface area as follows:

$$\frac{F}{A} = \gamma_{ls} + \gamma_{lg} + \mathcal{P}(z) \quad (1.11)$$

with  $\mathcal{P}(\infty) = 0$  and  $\mathcal{P}(0) = \gamma_{sg} - (\gamma_{lg} + \gamma_{ls}) = S_0$ . The interfacial energy,  $\mathcal{P}(z)$ , accounts for the interaction across the film. A force per area unit, i.e. a pressure, can therefore be defined as:

$$\Pi(z) = -\frac{d\mathcal{P}}{dz} \quad (1.12)$$

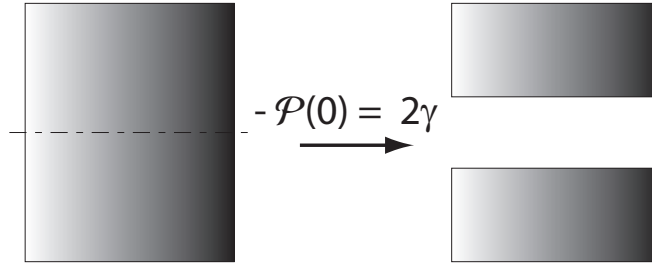


Figure 1.7: One phase is separated in two parts in vacuum. The two parts are taken apart until all interactions are not significant anymore. Two interfaces were then created and the amount of corresponding interfacial energy is  $-\mathcal{P}(0) = 2\gamma$ .

$\Pi(z)$  is called the disjoining pressure, it has been introduced by Derjaguin ([14]). The disjoining pressure is a powerful tool to describe thin films. Moreover, one must keep in mind that a thin film is not an isotropic medium, just like the interfacial zone between two coexisting phases.

### 1.2.3 Surface tension: long range and short range interactions

Both long range, i.e. mesoscopic scale, and short range, i.e. molecular scale, interactions contribute to interfacial tension. Actually, the interfacial tension can be calculated if formulae for these interactions are known. In many cases, the long range contribution is Van der Waals interaction, that is, dipole-dipole induced interaction, and screened coulombic interaction in polar media. It is then possible to use general formulae. On the contrary, short range interactions are much more specific. They for example include structural effects. Interfacial tensions, or more precisely the initial spreading parameter  $S_0$ , can be reconsidered in terms of the interfacial energy  $\mathcal{P}(z)$  defined above. Let us now consider a simple situation: the surface tension between a non-volatile condensed medium and vacuum.

The surface tension,  $\gamma$ , is the necessary amount of energy to create an unit of interface reversibly and isothermally. In the situation, where one phase is cut in two parts and the two parts are taken apart until all interactions are not significant anymore, the gain in energy per surface unit corresponds to the creation of the two new interfaces (see figure 1.7). It is then equal to  $2\gamma$ . This is also the opposite of the interaction energy,  $\mathcal{P}(0)$ , which is precisely  $S_0$  for the system (phase 1 / vacuum / phase 1):  $\mathcal{P}(0) - \mathcal{P}(\infty) = \mathcal{P}(0) = -2\gamma$

In the frequent case where Van der Waals interaction is the most important, the long range part of the interaction between molecules scales as  $\frac{1}{r^6}$ :

$$u(r) = -\frac{K}{r^6} \quad (1.13)$$

where  $K$  is a constant. In that case, the direct calculation of  $\mathcal{P}(z)$  for the two separated parts

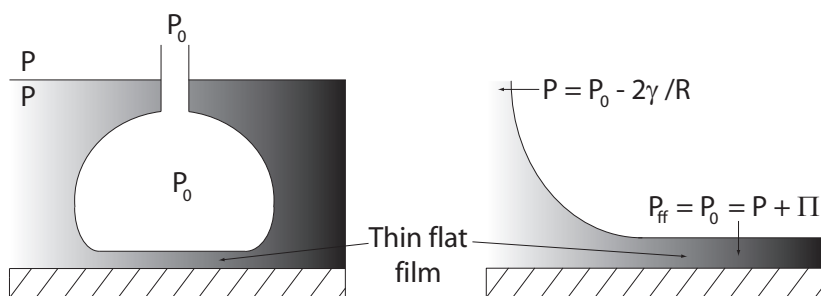


Figure 1.8: The captive bubble experiment, schematic view. The bubble is macroscopic. It flattens close to the substrate and creates a zone where the liquid forms a thin flat film.

of the same initial phase leads to:

$$\mathcal{P}(z) = -\frac{\pi\rho^2 K}{12z^2} = -\frac{A_H}{12\pi z^2} \quad (1.14)$$

where  $\rho$  is the density of molecules and  $A_H$ , the Hamaker constant. If the short range interactions do not play significantly, it is then possible to define a cutoff length  $D_0$  using equation 1.14:

$$\mathcal{P}(D_0) = -2\gamma \approx -\frac{A_H}{12\pi D_0^2} \quad (1.15)$$

$$\gamma \approx \frac{A_H}{24\pi D_0^2} \quad (1.16)$$

The length  $D_0$  is almost the same (0.165 nm) for many liquids where Van der Waals interaction is dominant.  $D_0$  allows to avoid difficulties linked to the divergence of equation 1.14 at vanishing  $z$ , where the formula is no longer valid. For an exact calculation of  $\mathcal{P}(z)$  at any scale, one should first use the proper complete expression of the potential. Second, taking an uniform density  $\rho$  is not possible anymore at the molecular scale where the pair correlation function must be introduced in the calculations.

#### 1.2.4 Static non-flat films, transition zone

So far, films have been considered to be flat. However, in the transition zone where the film connects itself to a macroscopic wedge, the curvature of the interface must be taken into account. This problem has been extensively treated by Derjaguin, Ivanov and collaborators [14] for mesoscopic films and slowly varying curvatures. Well-known experimental setups, as the captive bubble or the porous ring, have been developed, allowing to measure both the disjoining pressure and the thickness profile of films ([23]).

The captive bubble setup is a convenient introduction to non-flat films, see figure 1.8. The liquid is non-volatile and wets totally the substrate. Neglecting gravity, the pressure in the

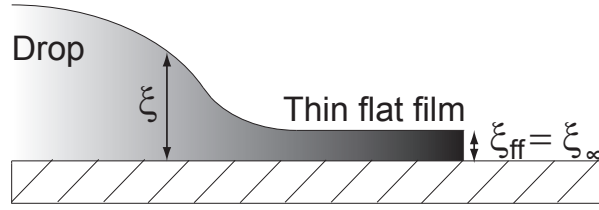


Figure 1.9: Geometry in partial wetting: the drop is in equilibrium with the thin film (the figure does not respect the real scale !).

macroscopic liquid is the external pressure  $P$ . The pressure in the bubble is  $P_0 > P$ . In its macroscopic part the bubble is spherical, with a radius  $R$ , so  $P = P_0 - \frac{2\gamma}{R}$ <sup>9</sup> (Laplace law). At its bottom, the bubble flattens out and a thin flat film is formed of thickness  $\xi_{ff}$ . The normal pressure in the thin film is then  $P_{flat\ film} = P_0$ . This film is connected to the macroscopic liquid reservoir, then  $P_{flat\ film} = P + \Pi(\xi_{ff})$ . The difference  $P - P_0$  is  $-\frac{2\gamma}{R}$  in the macroscopic part and  $-\Pi(\xi_{ff})$  in the flat film. For the local thickness  $\xi$ , the (constant) difference  $P - P_0$  is shown to be  $-\gamma C(\xi) - \Pi(\xi)$ , where  $C(\xi)$  is the local curvature of the interface (anticipating on the forthcoming discussion of films, the curvature here is defined as the mathematical one of the interface profile). One then has:

$$\gamma C(\xi) + \Pi(\xi) = Constant = \Pi(\xi_{ff}) = \gamma C_{bulk} \quad (1.17)$$

where  $C_{bulk}$  is the curvature of the bubble,  $C_{bulk} = \frac{2\gamma}{R}$ . This relation corresponds to the sum of both Laplace and disjoining pressure contributions, provided the film is mesoscopic and the curvature varies slowly.

This constant quantity is a characteristic of the interface<sup>10</sup>, this is a general expression, also valid in the partial-wetting case. In the partial-wetting case, it is a relevant parameter for the analysis of drops coexisting with thin films as long as the drop in question has a macroscopic part (in order to define the curvature,  $C_{bulk}$ ), see the corresponding geometry in figure 1.9.

In partial wetting, the limiting case of a very large drop, therefore a reservoir, defines the flat film of thickness  $\xi_{ff} = \xi_\infty$  where  $\Pi(\xi_\infty) = 0$ . It is worth noting that the only well-defined experimental equilibrium situation is a control by the vapor phase at saturation. The disjoining pressure is then strictly zero and the proper structure of the film with  $\xi_\infty$  is achieved through exchanges with the vapor phase.

More generally, the interface invariant gives the equilibrium condition between flat film and drop, but nothing on the actual size of the drop. For volatile liquids, equilibration times are not too long, therefore the problem may in principle be well-posed if the experimental system

<sup>9</sup> $\gamma_{lg}$  will now be noted as  $\gamma$  to simplify the notations.

<sup>10</sup>The curvature was initially defined as positive if the center of curvature is in the liquid: Russian convention, see [14].



is properly controlled. For non-volatile ones, equilibration times through films might well be extremely long. For simple systems, the film is sub-molecular as soon as the contact angle exceeds a few degrees. However, with complex molecules and substrates, the film may become a compact structure, mono- or multilayer. In the presence of layering, the disjoining pressure will oscillate.

It is worth noting at that the present discussion holds only for very flat films, that is situations where the spatial scale along the substrate is much larger than the local film thickness<sup>11</sup>.

### 1.2.5 Dynamic case: Adiabatic precursor films, diffusive films

This paragraph completes the analysis with a brief description of the dynamics in the simple case of total wetting, when a non-volatile liquid spreads on a smooth substrate ( $S_0 > 0$ ). The specific case of diffusive films will be useful for a further understanding of experiments with liquid crystals. A macroscopic drop of liquid is first deposited on the substrate. The macroscopic dynamic contact angle of the drop,  $\theta_D$  decreases as the drop spreads more and more. Tanner's law ([42], [38], [15], [9], [10])<sup>12</sup> describes satisfactorily the evolution of small contact angles:

$$\theta_D^3 = K_{Tanner} \frac{\eta U}{\gamma} \quad (1.18)$$

where  $K_{Tanner}$  is approximately constant ;  $U$  is the contact line velocity ;  $\eta$  the viscosity of the spreading fluid.

As  $K_{Tanner}$  is approximately constant, the macroscopic dynamic contact angle is practically independent of the initial spreading parameter,  $S_0$ , although the force which pulls the liquid is essentially equal to  $S_0$ . The reason is that a precursor film develops ahead of the spreading drop. On most of their extent, the precursor films are of molecular thickness and layering is frequent. In the immediate vicinity of the drop, their thickness is in the mesoscopic range.

Mesoscopic precursors can be described by solving hydrodynamic equations taking into account disjoining pressure in thin zones. Equations are written below in the simple 1D case of a liquid wedge.

**Adiabatic films** Let us consider the corner of a macroscopic spreading drop and its mesoscopic precursor (see figure 1.10). Navier-Stokes equation is written with the following conditions: the situation is stationary (the macroscopic edge velocity  $U$  is constant), in the context of the lubrication approximation and with a no-slip condition at the boundary between the liquid and the substrate. These films are called "adiabatic films", their length and profile depend only on

---

<sup>11</sup>In contrast, forthcoming discussions on nanometric droplets with non-vanishing contact angles will require a specific analysis. As previously mentioned, the characteristic length, defining the range of interactions will be much shorter.

<sup>12</sup>The demonstration of Tanner's law will be described in the next paragraph concerning adiabatic films.

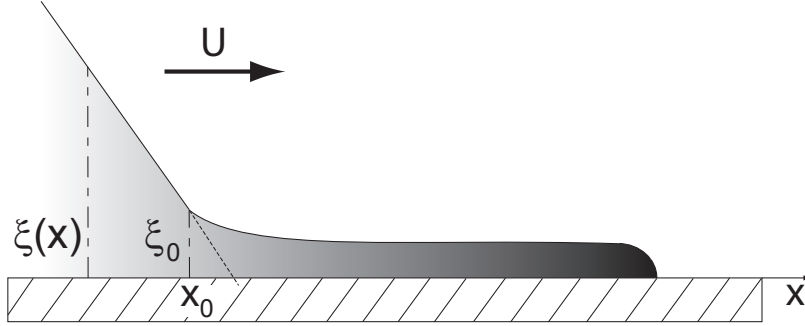


Figure 1.10: Total wetting, schematic side view. The corner of a spreading drop and its precursor film.

the macroscopic edge velocity. It comes then:

$$\eta U = -\frac{1}{3}\xi^2 \frac{\partial P}{\partial x} \quad (1.19)$$

where  $\eta$  is the viscosity of the spreading fluid ;  $U$ , its velocity ;  $\xi$ , the thickness of the film ;  $x$ , the horizontal coordinate and  $P(\xi)$ , the pressure in the film.  $P(\xi)$  is given by:

$$P(\xi) = P_0 - \gamma C(\xi) - \Pi(\xi) \quad (1.20)$$

The Navier-Stokes equation is then:

$$\eta U = \frac{1}{3}\xi^2 \frac{\partial}{\partial x} \left[ \gamma \frac{\partial^2 \xi}{\partial x^2} + \Pi(\xi) \right] \quad (1.21)$$

In the zone corresponding to the precursor, the term linked to curvature is negligible.

In the macroscopic range, it is the disjoining pressure which is negligible (relatively thick zone). The equation 1.21 is then:  $\eta U = \frac{1}{3}\xi^2 \gamma \frac{\partial^3 \xi}{\partial x^3}$ , whose approximate solution is Tanner's law [42], [38], [15], [9], [10].

In the microscopic range, coming back to equation 1.21, one can reduce it to:

$$\eta U = \frac{1}{3}\xi^2 \frac{\partial \Pi(\xi)}{\partial x} \quad (1.22)$$

Knowing the disjoining pressure, it is then possible to calculate the profile of the precursor film.

**Diffusive films** In practice, studying a film ahead a moving wedge is not easy. Most of the time, films are observed without macroscopic velocity (climbing film connected to a static meniscus) or without macroscopic reservoir. Such films are not stationary. They obey a diffusion-like equation, as first described by Derjaguin for mesoscopic films. The calculation starts just like

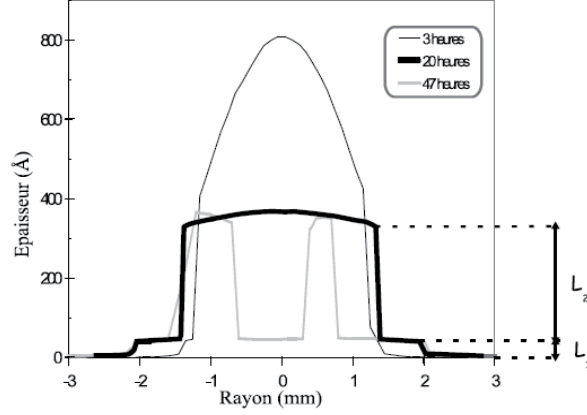


Figure 1.11: Extract of S. Bardon PhD thesis: Ellipsometric measurement of the profile of a microdroplet of *5CB* in nematic phase spreading slowly on a silicon wafer. Steep zones are observed. They suggest the existence of levels in the disjoining pressure. The film with a thickness noted as  $L_1$  is a trilayer of molecules. Note the huge difference in thickness and lateral scales.

the previous one, but now the dynamics is described by the conservation equation:

$$\frac{\partial \xi}{\partial t} + \frac{\partial(\xi U)}{\partial x} = 0 \quad (1.23)$$

As the time of equilibration for the velocity profile is much shorter than the characteristic spreading time, equation 1.22 can be used for  $U$  in the conservation equation:

$$\frac{\partial \xi}{\partial t} + \frac{\partial}{\partial x} \left[ \frac{\xi^3}{3\eta} \frac{\partial \Pi(\xi)}{\partial x} \right] = 0 \quad (1.24)$$

$$\frac{\partial \xi}{\partial t} + \frac{\partial}{\partial x} \left[ \frac{\xi^3}{3\eta} \frac{\partial \Pi(\xi)}{\partial \xi} \frac{\partial \xi}{\partial x} \right] = 0 \quad (1.25)$$

Defining then  $D(\xi) = -\frac{\xi^3}{3\eta} \frac{\partial \Pi(\xi)}{\partial \xi}$ , the equation 1.25 takes the shape of a diffusion equation (which justifies the name of diffusive films):

$$\frac{\partial \xi}{\partial t} - \frac{\partial}{\partial x} \left[ D(\xi) \frac{\partial \xi}{\partial x} \right] = 0 \quad (1.26)$$

The profile of the precursor is changing slowly. It is therefore possible to have local information about it considering:

$$D(\xi) \frac{\partial \xi}{\partial x} \approx \text{Constant} \quad (1.27)$$

If there are levels in the disjoining pressure (cf Maxwell's equal construction rule), steep zones are observed in the profile of the film (see figure 1.11).

To summarize, in total wetting conditions and with non-volatile liquids, a deposited drop does not spread on a completely dry substrate, there is a precursor film which develops ahead of the macroscopic front. Most of the precursor film is of a molecular thickness and may undergo a structuration due to the substrate. A mesoscopic description still allows one to determine that steps are caused by “Maxwell’s levels” in the disjoining pressure.

### 1.2.6 Line tension and modified Young equation

Let us go back to partial wetting, and more specifically to the description of small droplets. Actually, small scales do not only mean thin films: small-scale effects are supposed to affect drops which diameter is below the micrometer range.

As previously discussed, the contact angle of a macroscopic drop is described by Young’s law:  $\cos\theta = \frac{\gamma_{sg} - \gamma_{ls}}{\gamma_{lg}}$ . Surface terms in the free energy per surface unit, i.e. surface tension terms, are responsible for the value of the macroscopic contact angle. For smaller-sized drops, the contribution of terms depending linearly on the perimeter of the drop are no longer negligible. “Line-effects” begin to matter and must be included in the free energy of the system. Without discussing details for the moment, the minimization of the free energy at equilibrium leads to:

$$-\gamma_{sg} + \gamma_{lg} * \cos\theta_{micro} + \gamma_{ls} + \frac{\tau}{r} = 0 \quad (1.28)$$

Where  $\theta_{micro}$  is the contact angle of the droplet,  $\tau$  is the energy per unit length associated to the three phase contact line, called the line tension and  $r$ , the radius of the perimeter of the droplet’s base. The contact angle is deduced as:

$$\cos\theta_{micro} = \frac{\gamma_{sv} - \gamma_{ls}}{\gamma_{lv}} - \frac{\tau}{r * \gamma_{lv}} \quad (1.29)$$

$$\cos\theta_{micro} = \cos\theta - \frac{\tau}{r * \gamma_{lv}} \quad (1.30)$$

This is the modified Young equation. For droplets, there is a size dependence of the contact angle.

An exemple of a such a dependence for non-volatile liquids was studied by Berg et al. [3] (see figure 1.12). For drops with radii above 30 nm, the droplets show the macroscopic contact angle. Below the value of 30 nm, line effects begin to matter and there is a decrease of the contact angle of the drops in function of their radius. This corresponds to a negative line tension term  $\approx 10^{-11}$  J/m. It is worth noting that line tension can be either positive or negative [32], [2].

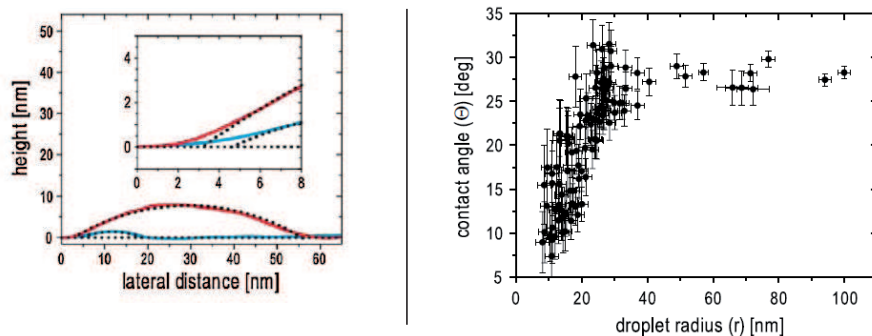


Figure 1.12: Figures taken from [3]. On the left side, AFM profiles of sessile fullerene droplets deposited on silicon wafers. On the right side, evolution of the contact angle of sessile fullerene droplets in function of the radius.

### 1.2.7 Preliminary comment: Line tension versus boundary tension

Before going any further, let us recall the difference in between line tension and boundary tension. In both cases, the description in terms of free energy is the same. That is why their names are often mixed up in the literature. Line tension and boundary tension represent though two different concepts.

We have introduced the line tension through its influence on the contact angle of small droplets. More fundamentally, it corresponds to the excess energy per unit length associated to the contact between three bulk phases along a three-phase contact line [32]. On the other hand, the boundary tension describes the energy associated to the perimeter between two phases in surface. Phases in surface are usually molecular layers or thin films. In this latter case, the boundary tension is the two-dimensional equivalent of the surface tension or thin films. It is always positive unlike line tension. Situations where boundary tension plays a role are found in Chapter 2 for liquid crystal films. Situations where line tension plays a role are found in Chapter 3 for ionic liquid droplets. In the following, some methods of measurement of boundary or line tension are presented and discussed.

### 1.2.8 Measurement of boundary tension

As energy is associated to the perimeter between two phases in surface, a non-perturbed phase has a circular perimeter. The most common method for measuring the boundary tension consists in increasing this perimeter by deforming it and observing the relaxation towards the equilibrium. The relaxation can then be modeled and the boundary tension calculated. The deformation of the domain can be due to an external constraint (small or large deformations applied directly by the user ([48], [25]) or hydrodynamically (elongation due to flows created by rotating cylinders) or by a coalescence of several domains (reorganization within the system). This dynamic method

gives access to the boundary tension between the two phases in surface. Another method, a static one, which is based on the concept of the 2D equivalent of Laplace pressure allows to measure ratios of boundary tensions [12].

These methods will be presented in the case of thin films of nematic liquid crystals on a water substrate studied below in Chapter 2. Here, the liquid crystal is 6CB far from the nematic-isotropic transition. We have already reported the stepped profiles of 5CB microdroplets on silica (see figure 1.11). With 6CB on water, one observes a coexistence between flat films of various thicknesses. Going from the thinnest to the thickest, one finds: monolayer ( $\approx 1.2$  nm), trilayer ( $\approx 3.5$  nm) and flat striped domains ( $20 - 30$  nm to  $600 - 800$  nm)<sup>13</sup>. The shape of one domain depends on the phases that are in direct contact. The measurement of the boundary tension between the striped domains and the trilayer will be the one presented in this part. It will be noted as  $\tau(h)$  as it depends on the thickness  $h$  of the striped domain<sup>14</sup>.

### The dynamic method

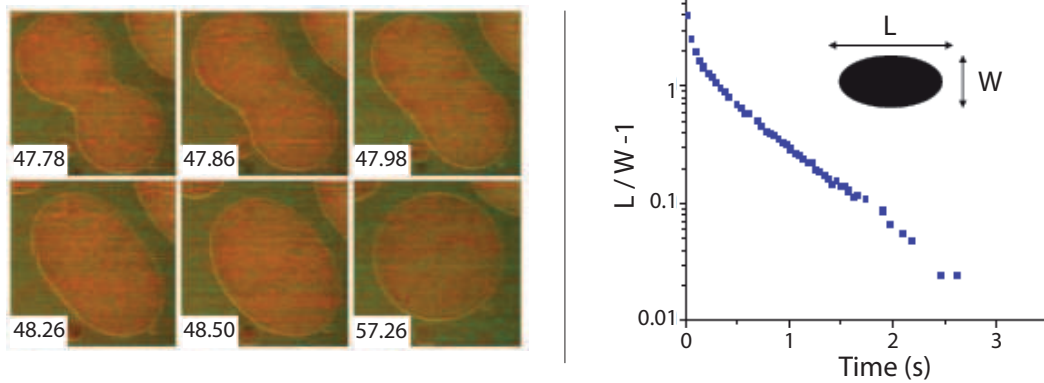


Figure 1.13: Extract of [12]. On the left side, a coalescence of two striped domains completely surrounded by the trilayer (no monolayer present) is followed under optical microscope (the time is indicated in seconds on each image). On the right side, a typical semi-logarithmic plot showing the anisotropy of a new domain vs time.

As mentioned above, the dynamic method is based on deformations of domains. Small deformations are easier to follow from an experimental point of view in the case of liquid crystals. Actually, small deformations in thin films of liquid crystals deposited on water can be observed during the coalescence of two striped domains surrounded by a trilayer. Let us point out that as the boundary tension  $\tau(h)$  depends on the thickness  $h$  of the domain of striped film, measure-

<sup>13</sup>The striped structure of the thickest films will be analysed in Chapter 2.

<sup>14</sup>The thickness of the striped domain can be easily measured. The method used is going to be described later, see Chapter 2.

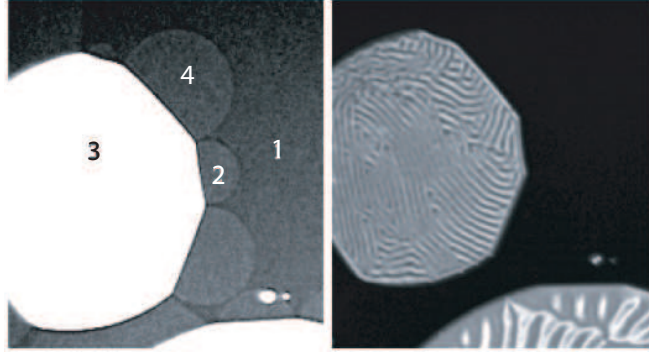


Figure 1.14: Extract of [12]: microscope images of 6CB films on water at ambient temperature. On the left side, the contrast of the image is modified in order to see the limits between the different layers. On the right side, the unmodified image is presented. It allows one to see that the domains which appeared as saturated in the picture on the left side possess in fact a striped structure. 1: monolayer, 2 and 4, trilayer, 3 striped domain. Here, the striped domain contacts simultaneously the monolayer and trilayer domains. This explains the angular shape.

ments of  $\tau(h)$  can only be performed for coalescing domains sharing the same thickness. Once this condition is fulfilled, the coalescence process can be described in two steps: on short time scales, the two domains meet each other and merge ; on long time scales, the new domain relaxes its (now) elliptical shape towards a circular shape (see figure 1.13). As the dissipation in the sub-phase dominates the dissipation in surface [25], the relaxation dynamics towards a circular shape of radius  $R_0$  becomes exponential with a characteristic time  $T_{relax}$  [37]. This characteristic time is given by the formula of Stone and Mc Connell<sup>15</sup>:

$$T_{relax} \approx \frac{5\pi}{16} \frac{\eta_B R_0^2}{\tau(h)} \quad (1.31)$$

where  $\eta_B$  is the viscosity of the sub-phase (water in our case). The measurement of the anisotropy of the new domain versus time then allows one to calculate the value of the boundary tension (see figure 1.13).

### The static method.

The static method is based on the concept of 2D equivalent of Laplace pressure<sup>16</sup> (see figure 1.14). For a system at the equilibrium or metastable (which is the case here), the 2D pressures on both sides of a boundary between two coexisting films (i and j) are linked by a relation similar

<sup>15</sup>The method of Stone and Mc Connell is based on a decomposition of the shape of the domain in Fourier modes.

<sup>16</sup>The surface pressure  $\pi$  is presented in the Appendix about Langmuir isotherms.

to the 3D Laplace law<sup>17</sup>:

$$\Delta\pi = \pi_i - \pi_j = \frac{\tau}{R_{ij}} \quad (1.32)$$

where  $\pi_i$  and  $\pi_j$  are the film pressures, respectively for film  $i$  and film  $j$ ;  $\tau$  the boundary tension and  $R_{ij}$ , the curvature radius of the 2D boundary between the films. For example, considering the monolayer 1 and the trilayer 2 of figure 1.14, equation 1.32 writes:

$$\pi_2 - \pi_1 = \frac{\tau_0}{R_{21}} \quad (1.33)$$

where  $\tau_0$  is the boundary tension between the monolayer and the trilayer. A systematic combination of the various possible equations allows one to obtain the ratio  $\frac{\tau(h)}{\tau_0}$ :

$$\frac{\tau(h)}{\tau_0} = \frac{\left(\frac{1}{R_{41}} - \frac{1}{R_{21}}\right)}{\left(\frac{1}{R_{32}} - \frac{1}{R_{34}}\right)} \quad (1.34)$$

Using the static method, the ratio of the striped domains / trilayer over the trilayer / monolayer boundary tensions can then be calculated by repeated measurements of curvature radii.

## 1.2.9 Measurement of line tension

### Introductory comment

Motivated by the development of miniaturization (e.g. microfluidics), attempts to measure line tension effects have been numerous in the last few years. However, up to date, line tension measurements are highly controversial and the orders of magnitude obtained show a large scatter (from  $10^{-12}$  to  $10^{-5}$  N).

There are good reasons for such a scatter. Like surface tension, line tension is an excess energy. It is well defined in the ideal case where three bulk phases with flat macroscopic ideal interfaces meet along a straight contact line [32]: the line tension is merely the excess energy associated to the vicinity of the contact line, where the properties differ from the ones of the isolated interfaces. Experimental situations with solid substrates, therefore unavoidable heterogeneities, and also curved interfaces, therefore Laplace pressure, are not easily interpreted in reference to this ideal model case.

Let us however add some comments:

On a ideal, smooth solid substrate, the effect of line tension on a macroscopic liquid wedge is to deform the liquid-gas interface in the vicinity of the solid. From the deformation, the line tension can be calculated, this is the interface potential method ([29], [2], [18]). A precise knowledge of the interface profile in the nanometer range is required.

It seems easier to measure the contact angle of small droplets and use modified Young's equation. The modified contact angle results from the minimization of the free energy. It is

---

<sup>17</sup>The 2D surface pressure has the dimensions of a surface tension, that is of a force over a length



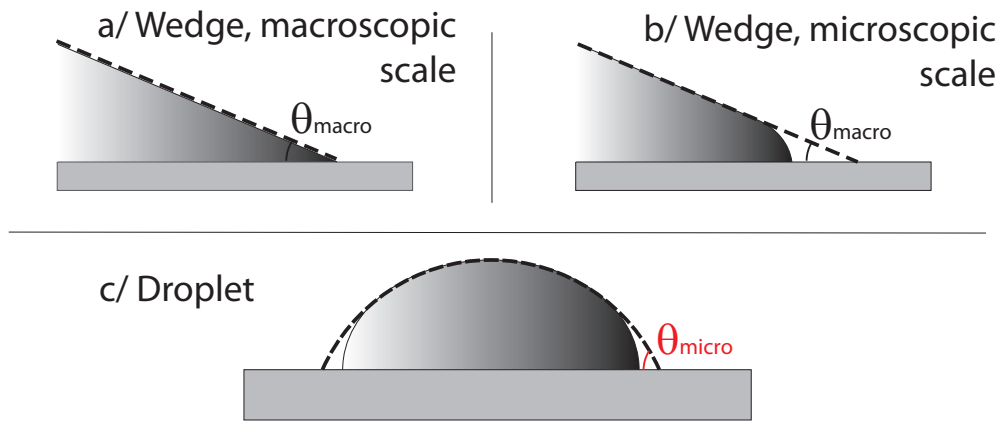


Figure 1.15: a/ and b/: Case of a wedge. The wedge is undeformed when it is macroscopic (a/), but shows a local deformation at the contact line due to line tension when going towards small scales (b/). c/: Case of a droplet. There is a local deformation at the contact line from the spherical shape (dotted line). The contact angle measurement is made from the spherical shape fitting the bulk part of the droplet.

deduced from the extrapolation of the spherical cap which fits the non-deformed top of the droplet (see figure 1.15). Reversibility is assumed.

In both cases, every linear contribution to the free energy is counted as "line tension", e.g. the heterogeneities for real surfaces [7], [8].

### Method of the interface potential

On a liquid wedge, i.e. a zone of the three-phase contact line showing no or negligible macroscopic curvatures, it is possible to measure the effective interface potential without artifacts else than the defects of the solid substrate. From the AFM image of the wedge, the deviation at the level of the contact line from the actual extension of the three-dimensional profile of the drop is measured. It allows for the calculation of the free energy contribution of the three-phase interaction in the contact region. The effective interfacial potential is then obtained from the Euler-Lagrange equation for the profile. Line tension is finally deduced [29].

### Modified Young equation

The modified Young equation ( $\cos\theta_{micro} = \cos\theta - \frac{\tau}{r*\gamma_{lg}}$ , 1.30) expresses the cosine of the microscopic contact angle as the cosine of the macroscopic contact angle linearly corrected by a line tension term. The value of the line tension is deduced from the slope of the (linear) plot formed by the measurements of  $\cos\theta_{micro}$  in function of  $1/r$ , where  $r$  is the base radius of the droplet. Droplets whose radius is of the order of a few tens of nanometers are spherical caps except for the last nanometers close to the substrate. Deducing line tension from the modified Young equation

means measuring microscopic contact angles. For drops' diameters in the micrometer range, much smaller than the capillary length,  $\kappa^{-1} = \sqrt{\frac{\gamma l_g}{\rho g}}$ ; their shape is spherical except very close to the substrate. As already quoted, the spherical shape part is required as modified Young equation is deduced from the minimization of free energy with volume, surface and line terms.

Shortly after first attempts using interferometry (e.g. Stöckelhuber et al. [36]), the Atomic Force Microscope (AFM) in the non-contact mode became a privileged imaging tool. AFM imaging provides the shape of the droplets and of the surrounding substrate. From the AFM images, the method of measurement for the contact angle of a droplet is not different than the one used for a macroscopic drop (for further details, see the Appendix about AFM and STM imaging). A general rule for the fit of the spherical shape is to exclude the region linking the droplet to the substrate where deviations take place. However, it is clear that the exact location of the substrate is crucial, both for the contact angle value, and for any analysis in terms of interface potential. Specific discussion of nanometric droplets will be found in Chapter 3.

As mentioned in the introductory comment, the data analysis is complex.

- The incidence of substrate's heterogeneity has been thoroughly discussed by Checco et al [7], [8]. It contributes whether the system is a wedge or a nanoscopic drop.
- Considering wedges and drops, more fundamental difficulties show up in the thermodynamic analysis. In the case of the wedge, the pressure is the same in the three phases. Without entering into details [35], [34], there is no ambiguity generated by the choice of the dividing surface in Gibbs analysis. In contrast, the choice of the dividing surface is a real concern when considering droplets: the surface of tension, that is, the one used in the Laplace law, is not the equimolar dividing surface, that is, the one where there is no excess adsorption. Another way to express this is to say that the interfacial tensions depend on the Laplace pressure. The case of isolated droplets has been extensively studied since Tolman's work [39], where the Tolman length actually corresponds to the distance between the surface of tension and the equimolar surface.

While the thermodynamic analysis is now well-understood ([35], equation 6.30), the exact way to separate pressure-induced contributions and true line tension in the modified Young equation is still an open question for the experimentalist.

## 1.3 Conclusion

In this first chapter, we presented the physical tools which were developed to understand macroscopic wetting phenomena as well as the emergence of new problems when going towards small-scales: disjoining pressure, precursor films, boundary and line tension, ... These problems play a central role for the two systems investigated in this thesis and will be further discussed in the following.

In Chapter 2, nematic liquid crystals are deposited on liquid substrates in a total wetting situation. Here, the substrate is free from roughness or heterogeneities. The wetting problem is though complex because of the nature of the nematic phase, where long-range elastic interactions are present. The competition between these long-range interactions and the short-range structural interactions at both interfaces (liquid substrate / liquid crystal and liquid crystal / air) result in a complex organization of the nematic liquid crystal into molecular films in coexistence with mesoscopic flat pancakes. The present chapter provides keys for the description of thin films and boundary tension.

In Chapter 3, ionic liquids, i.e. molten salts, are deposited on solid substrates in a partial wetting situation. The ionic liquid, forming films and droplets is clearly affected by roughness and heterogeneities of the substrates. Fluctuations of the contact line, pinning, development of thin films and line tension are in the center of the questions raised by this system.

# Bibliography

- [1] Arthur W. Adamson and Alice P. Gast. *Physical Chemistry of Surfaces, 6th Edition*. Wiley-Interscience publication, 1997.
- [2] C. Bauer and S. Dietrich. Quantitative study of laterally inhomogeneous wetting films. *The European Physical Journal B*, 10:767–779, 1999.
- [3] J.K. Berg, C.M. Weber, and H. Riegler. Impact of negative line tension on the shape of nanometer-size sessile droplets. *Phys. Rev. Lett.*, 105:076103, 2010.
- [4] TD Blake. The physics of moving wetting lines. *Journal of colloid and interface science*, 299:1–13, 2006.
- [5] D. Bonn, J. Eggers, J. Indekeu, J. Meunier, and E. Rolley. Wetting and spreading. *Rev. Mod. Phys.*, 81:739–805, 2009.
- [6] Anne-Marie Cazabat. M2 lessons about interfaces and wetting. 2007-2008.
- [7] A. Checco, P. Guenoun, and J. Dailant. Nonlinear dependence of the contact angle of nanodroplets on contact line curvature. *Phys. Rev. Lett.*, 91:186101–1–4, 2003.
- [8] A. Checco, H. Schollmeyer, J. Dailant, P. Guenoun, and R. Boukherroub. Nanoscale wettability of self-assembled monolayers investigated by noncontact atomic force microscopy. *Langmuir*, 22:116, 2006.
- [9] R.G. Cox. The dynamics of the spreading of liquids on a solid surface. part 1. viscous flow. *Journal of Fluid Mechanics*, 168:169–194, 1986.
- [10] P.G. de Gennes. Wetting: statics and dynamics. *Rev. Mod. Phys.*, 57:827–863, 1985.
- [11] P.G. de Gennes, F. Brochart-Wyart, and D. Quéré. *Gouttes, bulles, perles et ondes*. Belin, 2005.
- [12] U. Delabre, C. Richard, J. Meunier, and Cazabat A.-M. Line tension of nematic pancakes at the air-water interface: Static and dynamic measurements. *Europhysics Letters*, 83:66004, 2008.

- [13] Ulysse Delabre. *Films nématiques minces sur substrats liquides*. PhD thesis, Université Paris VI, 2009.
- [14] B.V. Derjaguin, N.V. Churaev, and V.M. Muller. *Surface forces*. Consultants Bureau, New York and London, 1987.
- [15] E.B. Dussan. On the spreading of liquids on solid surfaces: Static and dynamic contact lines. *Annu. Rev. Fluid Mech.*, 11:371, 1979.
- [16] R. Fetzer and J. Ralston. Influence of nanoroughness on contact line motion. *J. Phys. Chem. C*, 114 (29):12675–12680, 2010.
- [17] F.M. Fowkes. Attractive forces at interfaces. *Ind. Eng. Chem.*, 56:40–52, 1964.
- [18] Dietrich S Getta T. Line tension between fluid phases and a substrate. *Phys. Rev. E*, 57:655–671, 1998.
- [19] Josiah Willard Gibbs. *The collected works of J. Willard Gibbs*. Longmans, Green and Co, 1928.
- [20] H. Gouin. Liquid nanofilms. a mechanical model for the disjoining pressure. *International Journal of Engineering Science*, 47:691–699, 2009.
- [21] Geoffroy Guéna. *Discussions sur l'évaporation d'une gouttelette mouillante*. PhD thesis, Université Paris VI, 2007.
- [22] E. Guyon, J.P. Hulin, and L. Petit. *Hydrodynamique Physique*. CNRS Editions, EDP Sciences, 2001.
- [23] RG Horn, M Asadullah, and JN Connor. Thin film drainage: Hydrodynamic and disjoining pressures determined from experimental measurements of the shape of a fluid drop approaching a solid wall. *Langmuir*, 22:2610–2619, 2006.
- [24] J. F. Joanny and P. G. de Gennes. A model for contact angle hysteresis. *J. Chem. Phys.*, 81:552–562, 1984.
- [25] E. K. Mann, S. Hénon, D. Langevin, J. Meunier, and L. Léger. Hydrodynamics of domain relaxation in a polymer monolayer. *Phys. Rev. E*, 51:5708, 1995.
- [26] Sébastien Moulinet. *Rugosité et dynamique d'une ligne de contact sur un substrat désordonné*. PhD thesis, Université Paris 7, 2003.
- [27] Xavier Noblin. *Mouillage et dé mouillage inertiels: triplons, flaques vibrées, ondes de chocs*. PhD thesis, Université Paris VI, 2004.
- [28] T. Pompe. Line tension behavior of a first-order wetting system. *Phys. Rev. Lett.*, 89:076102–1–4, 2002.

- [29] T. Pompe and S. Herminghaus. Three-phase contact line energetics from nanoscale liquid surface topographies. *Phys. Rev. Lett.*, 85:1930–1933, 2000.
- [30] Christophe Poulard. *Dynamique de gouttelettes mouillantes*. PhD thesis, Université Paris VI, 2005.
- [31] J. Ralston, M. Popescu, and R. Sedev. Dynamics of wetting from an experimental point of view. *Annual Review of Materials Research*, 38:23–43, 2008.
- [32] J.S. Rowlinson and B. Widom. *Molecular Theory of Capillarity*. Dover publications, 2003.
- [33] A.I. Rusanov. Thermodynamic line tension of a molecular solid. *Journal of Chemical Physics*, 131:244713–1/2, 2009.
- [34] L. Schimmele and S. Dietrich. Line tension and the shape of nanodroplets. *Eur. Phys. J. E*, 30:427–430, 2009.
- [35] L. Schimmele, M. Napiórkowski, and S. Dietrich. Conceptual aspects of line tensions. *Journal of Chemical Physics*, 127:164715–1/28, 2007.
- [36] K.W. Stöckelhuber, B. Radoev, and H.J. Schulze. Some new observations on line tension of microscopic droplets. *Colloids and Surfaces A: Physicochemical and Engineering Aspects*, 156:323–333, 1999.
- [37] H.A Stone and H. M. McConnell. Hydrodynamics of quantized shape transitions of lipid domains. *Proc. R. Soc. Lond. A*, 448:97–111, 1995.
- [38] L.H. Tanner. The spreading of silicone oil drops on horizontal surfaces. *J. Phys. D: Appl. Phys.*, 12:1473–1979, 1979.
- [39] R.C. Tolman. The effect of droplet size on surface tension. *J. Chem. Phys.*, 17:333, 1949.
- [40] Damien van Effenterre. *Instabilité d'un film mince de nématique*. PhD thesis, Université Paris VI, 2002.
- [41] François Vandenbrouck. *Films minces de cristaux liquides*. PhD thesis, Université Paris VI, 2001.
- [42] O.V. Voinov. *Fluid Dynamics*, 11:714, 1977.
- [43] JY Wang, S Betelu, and BM Law. Line tension effects near first-order wetting transitions. *Phys. Rev. Lett.*, 83:3677–3680, 1999.
- [44] CA Ward and JY Wu. Effect of contact line curvature on solid-fluid surface tensions without line tension. *Phys. Rev. Lett.*, 100:256103– 1/4, 2008.
- [45] J.H. Weijs, A. Marchand, B. Andreotti, D. Lohse, and J.H. Snoeijer. Origin of line tension for a Lennard-Jones nanodroplet. *Phys. Fluids*, 23:022001– 1/11, 2011.

- [46] Widom. Line tension and the shape of a sessile drop. *J. Phys. Chem.*, 99:2803, 1995.
- [47] Widom. Structure and tension of interfaces. *Molecular Physics*, 96(7):1019, 1999.
- [48] LU Zou, JI Wang, Prem Basnet, and Elizabeth K. Mann. Line tension and structure of smectic liquid-crystal multilayers at the air-water interface. *Phys. Rev. E*, 76:031602, 2007.

## Chapter 2

# Thin films of liquid crystals

### 2.1 Introduction to hybrid nematic films

#### 2.1.1 Liquid crystals, general introduction

##### 2.1.1.1 Definition, Mesophases

Simple chemical compounds have three phases: solid crystalline phase, isotropic liquid phase and gaseous phase. The difference between the solid crystalline and isotropic liquid phase can be described in terms of broken symmetry. In the liquid phase, the molecules are completely free to move so that no symmetry is broken. On the contrary, in the solid crystalline phase, the molecules have a position defined by the unit of a lattice. The  $3D$  translational symmetry is then broken. Phases which are intermediary between these two situations exist, they are called mesophases. Liquid crystals are mesophases. It is in fact as a consequence of the first observations of liquid crystals by biologists in the middle of the 19th century, that the notion of mesophase was defined in 1922 by G. Friedel [30].

Liquid crystal phases can exhibit nematic phases, columnar phases, cholesteric phases, ... The reason why liquid crystals tend to form one or several mesophases when simple chemical compounds present only solid, liquid and gas phase lies in the chemical and geometrical properties of their molecules. On the chemical point of view, the molecules are often amphiphilic ones (the association in a single molecule of two immiscible compounds via a covalent bond). On the geometrical point of view, they often have a particular shape: rods, discs,...

However, the notion of broken symmetry in itself is not sufficient to differentiate condensed matter phases. For example, the liquid and the gas phases are obviously different though they share the same symmetry. It is the same for liquid crystals. For example, distinct smectic phases exists though they all present the same symmetry. In those two examples, it is the local level of order which is different: the correlation function of the order parameter must be taken into account.



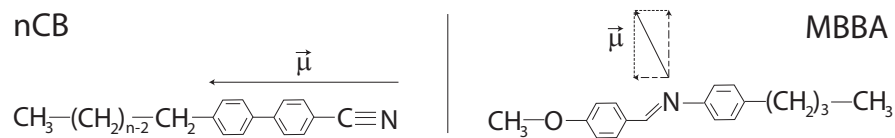


Figure 2.1:  $\vec{\mu}$  represents the respective dipole moment for each molecule. On the left side: nCB molecule. The dipole moment, is along the benzene rings. On the right side: MBBA molecule.

In conclusion, liquid crystal molecules tend to form mesophases because of their anisotropic nature. They have an intermediate degree of symmetry compared to the solid crystalline and the liquid isotropic phase and sometimes, for a same degree of symmetry, a different local order.

### 2.1.1.2 Thermotropic liquid crystals

For thermotropic liquid crystals, the transition between the solid crystalline phase, the liquid crystal phases and the isotropic liquid phase is triggered by temperature. They are the only ones considered here<sup>1</sup>. Thermotropic liquid crystals are pure compounds, usually amphiphilic molecules of low molecular weight. Considering individually the two parts of the molecule, one notices that the respective melting points for each compound are very different. However, as they are linked by a covalent bound in the liquid crystal molecule, phase separation is impossible. The formation of a mesophase is then the answer to the molecular frustration [55].

### 2.1.1.3 nCB's family and MBBA

Two different sorts of thermotropic liquid crystal molecules were used for the present experiments: n-cyanobiphenyl (nCBs) family and MethoxyBenzylidene-n-ButylAniline (MBBA) (cf figure 2.1).

The nCB family is composed of one alkyl chain with  $n$  carbon atoms, two benzene rings and a cyano group. The alkyl chain is slightly tilted compared to the benzene rings, the tilt angle depending on the even or odd number of carbons present in the alkyl chain (the first carbon is on the axis). The cyano group has a strong dipole moment which stretches out on the benzene cycles ( $\mu = 4.9 - 6$  Debye).

The consequence of this property is that the cyanobiphenyls in bulk tend to form dimers. Two molecules are then associated head-to-tail. The number of carbons in the alkyl chain also plays a role. Shorter nCB molecules only have a nematic phase, whereas longer molecules ( $n \geq 8$ ) also have a smectic A phase<sup>2</sup>. Furthermore, depending on whether the number of carbon atoms in the alkyl chain is odd or even, the interaction [cyano with cyano group] or the interaction

<sup>1</sup>Other kind of liquid crystals exist. For example, for lyotropic liquid crystals, which are solutions of amphiphilic molecules in a solvent, it is the concentration of amphiphilic molecules or the nature of solvent that controls the transition to a liquid crystal phase.

<sup>2</sup>The smectic A phase is observed in the temperature range between the solid crystalline phase and the nematic phase. In the smectic A phase, there is a long range orientational order, as in the nematic phase, plus a positional order: the molecules form layers.

5CB	nematic 22.5 - 35 °C
6CB	nematic 15 - 29 °C
7CB	nematic 30 - 42.8 °C
8CB	smectic 21.5 - 34 °C nematic 34 - 40.5 °C
MBBA	nematic 21 - 42 °C

Figure 2.2: Temperature of phase transitions of the liquid crystals used for the present experiment.

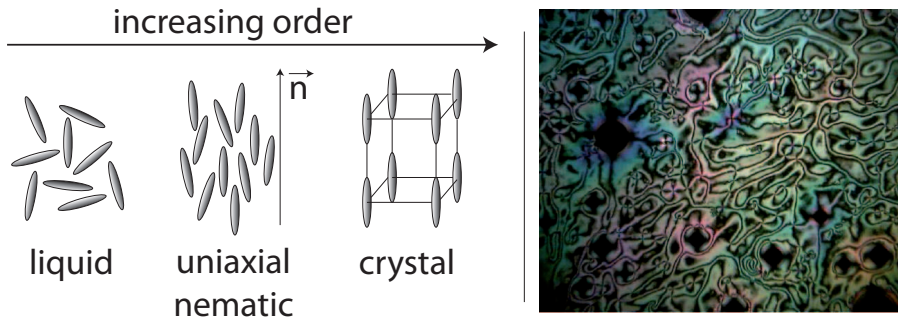


Figure 2.3: On the left side: schematic view of the liquid, uniaxial nematic and crystalline phases. On the right side: picture from U.Delabre PhD thesis [19], a thick film of nematic liquid crystal between crossed polarizers.

[cyano with benzene group] is more favorable. The temperatures of the phase transitions clearly show this odd-even effect: the temperatures of transition from the crystal to nematic and from nematic to isotropic liquid are lower for the even members of the nCB family than for the odd ones (cf figure 2.2).

The MBBA, on the contrary, has a transverse dipole moment and does not form dimers. It provides then a good comparison with the nCB family.

#### 2.1.1.4 Uniaxial nematic phase

The nematic phase is a mesophase of broken rotational symmetry. There is a resulting long range orientational order. It implies that all the molecules follow the same mean orientation. The direction of a vector, the nematic director,  $\vec{n}(\vec{r})$ , is used to represent the mean orientation of the liquid crystal molecules at a given position,  $\vec{r}$  (cf figure 2.3). As  $+\vec{n}$  and  $-\vec{n}$  are equivalent, the nematic order is quadrupolar. We restrict here to uniaxial nematic phases<sup>3</sup>, which possess rotational invariance around the director. To describe ordering, one defines the second rank ordering traceless tensor, which is diagonal in uniaxial phases for a reference frame where the

<sup>3</sup>For some polymers and lyotropic systems, the nematic phase can be biaxial.

axis is along  $\vec{n}$  [71]:

$$\vec{Q}(\vec{r}) = S(\vec{r}) \begin{pmatrix} -\frac{1}{2} & 0 & 0 \\ 0 & -\frac{1}{2} & 0 \\ 0 & 0 & 1 \end{pmatrix} \quad (2.1)$$

where  $S(\vec{r})$  is equal to:

$$S(\vec{r}) = \frac{1}{2} \langle 3\cos^2\phi - 1 \rangle \quad (2.2)$$

with  $\phi$ , the angle of a molecule with the director and  $\langle . \rangle$  represents the mean value taken on the molecules for a given temperature.  $S(\vec{r})$  represents the way that the molecules orient themselves along the director's axis. It is thus the order parameter<sup>4</sup>. If the molecules are strictly parallel,  $S(\vec{r})$  is equal to one. The order parameter is equal to zero in an isotropic phase.

Because of boundaries or other constraints, bulk nematic liquid crystals show topological defects called disclinations. For a macroscopic film of nematic liquid crystal, the disclinations look like threads (cf figure 2.3. The name "nematics" comes from the Greek word for thread.). Moreover, a characteristic glimmering is observed because of thermal fluctuations of the local director that make the nematic liquid crystals strongly scatter light. In the absence of defects, bulk nematic samples are uniaxial birefringent media. They have two refractive indices, the ordinary one,  $n_0$ , and the extraordinary one  $n_e$ . One defines the mean refractive index,  $n_m$  as:

$$n_m = \frac{2n_0 + n_e}{3} \quad (2.3)$$

The evolution in temperature of the optical indices of the liquid crystals used for our experiments is shown on figure 2.4

### 2.1.2 Nematic elasticity

Nematic liquid crystals have elastic properties close to those of solids. Elastic solids come back to their shape and structure after a strain, producing a deformation, has been released. For nematics, let us first consider a bulk sample at the equilibrium and undergoing no strain (including the one that could be produced by the boundaries). In that case, the director is the same everywhere. On the contrary, if the nematic structure is deformed, for example by the action of an electric field, the direction of the nematic director varies slowly in the bulk. Slowly means that the variation of the director has a characteristic length which is much larger than the size of the molecules. When the strain on the nematic is released, the nematic director comes back to its original configuration.

It is clear that such a continuous approach focuses on the variations of the director, and ignores any spatial change in the order parameter which is supposed to be constant everywhere. While it is a plausible assumption in bulk, it will require some discussion when considering thin films.

---

<sup>4</sup> $S(\vec{r})$  has no relation with  $S$ , the spreading parameter defined in Chapter 1.

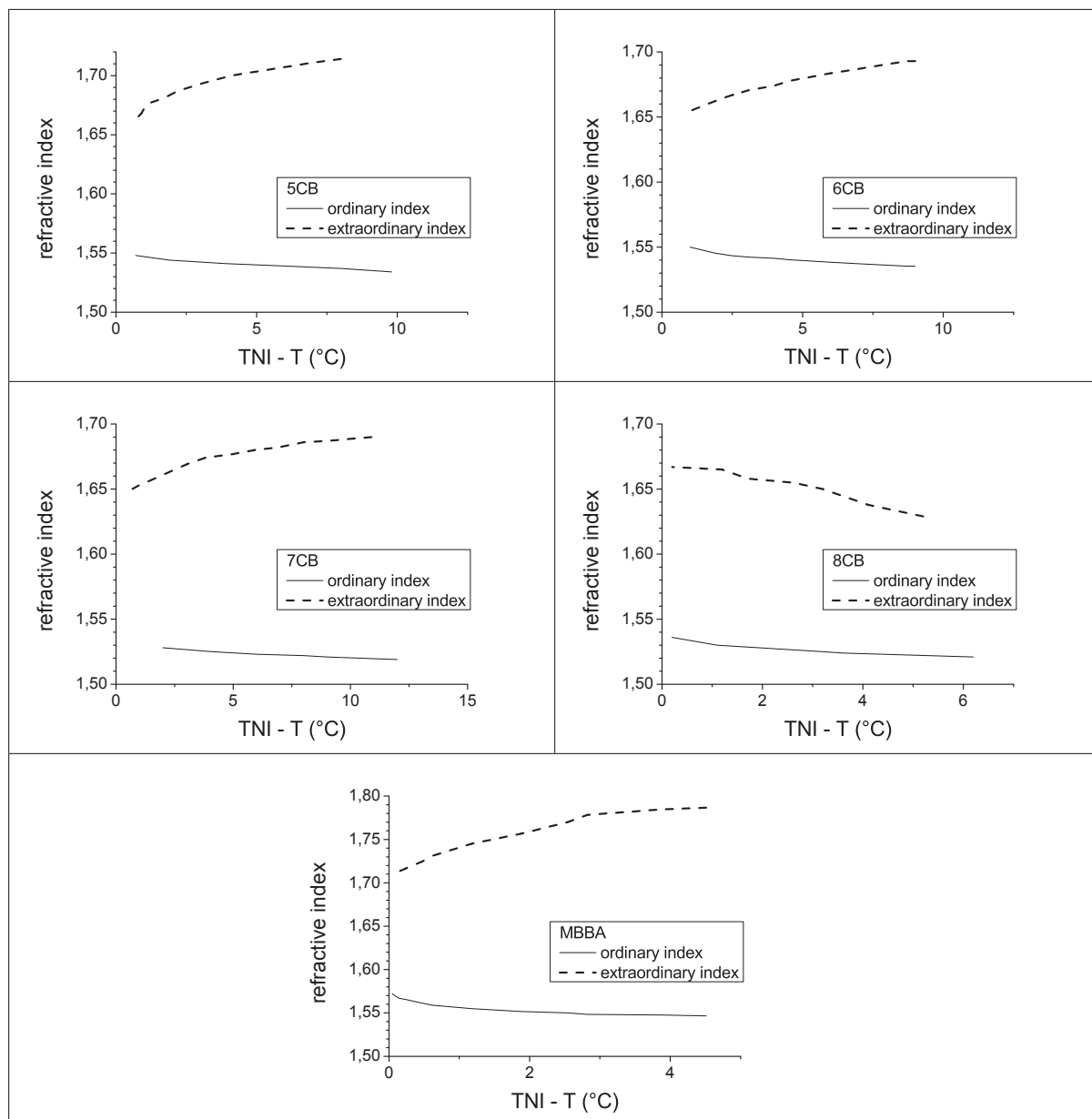


Figure 2.4: Ordinary and extraordinary refractive indices versus the temperature shift  $T_{NI} - T$ , where  $T_{NI}$  represents the temperature of the nematic / isotropic phase transition and  $T$  the temperature of the sample. The values for 5CB, 6CB, 7CB and 8CB are taken from [21] and the values for MBBA from [34]. Other experiments measuring the refractive index can be found in [35].

Nematic elasticity is described using a free energy density, which is a quadratic function of the curvature-strains<sup>56</sup>:

$$F = \int dV(f_{ext} + f_{Frank} + K_{13}div(\vec{n} div \vec{n}) - (K_{22} + K_{24})div(\vec{n} div \vec{n} + \vec{n} \wedge rot \vec{n})) + \int dS f_S \quad (2.4)$$

This expression describes nematic elasticity at the first order. Its different terms are now going to be detailed:

- Within the volume integral, the  $f_{ext}$  term accounts for the energy density induced by an external field (electric or magnetic for example).
- The surface integral  $\int dS f_S$  represents the energy due to anchoring at both interfaces (in a continuous approach).
- The term  $f_{Frank}$  stands for the free energy density first introduced by Frank [29]:

$$f_{Frank} = \frac{1}{2}K_{11}(div \vec{n})^2 + \frac{1}{2}K_{22}(\vec{n} rot \vec{n})^2 + \frac{1}{2}K_{33}(\vec{n} \wedge rot \vec{n})^2 \quad (2.5)$$

In this expression, each term describes an elementary elastic deformation, the coefficients appear as analogs to the elastic moduli of solids. The pure deformations associated to the constants  $K_{11}$ ,  $K_{22}$  and  $K_{33}$  are respectively splay, twist and bend (see figure 2.5). Measurements of the elastic constants for the liquid crystals used in the experiments presented in this work are reported on figure 2.6.

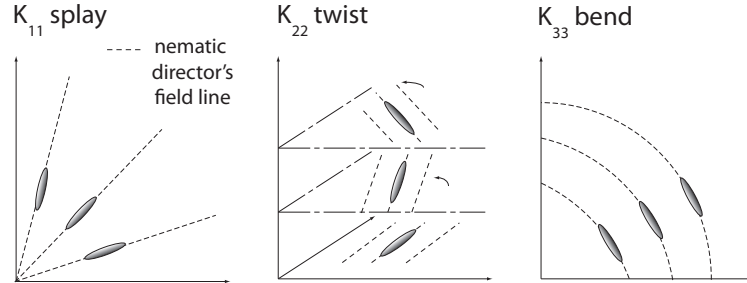


Figure 2.5: Schematic view of the elementary deformations of Frank's free energy density. For  $K_{11}$ ,  $K_{22}$  and  $K_{33}$ , field lines of the nematic director encounter respectively splay, twist and bend deformation.

<sup>5</sup>A theory for nematic elasticity was first developed by Oseen [54]. He used an approach analog to the one of Cauchy for solids: the energy of liquid crystals was written as a sum of pair interactions of molecules. However, the formalism used nowadays is due to Frank [29]. His phenomenological approach is based on the symmetry properties of the medium. Frank's expression of the free energy density was thus incomplete and missing terms were reintroduced afterwards by Nehring and Saupe [50], [51]

<sup>6</sup>Depending on the authors, there are variations in the notations used in the equation of the free energy density. In particular, the  $K_{24}$  constant sometimes stands for  $(K_{22} + K_{24})$ .

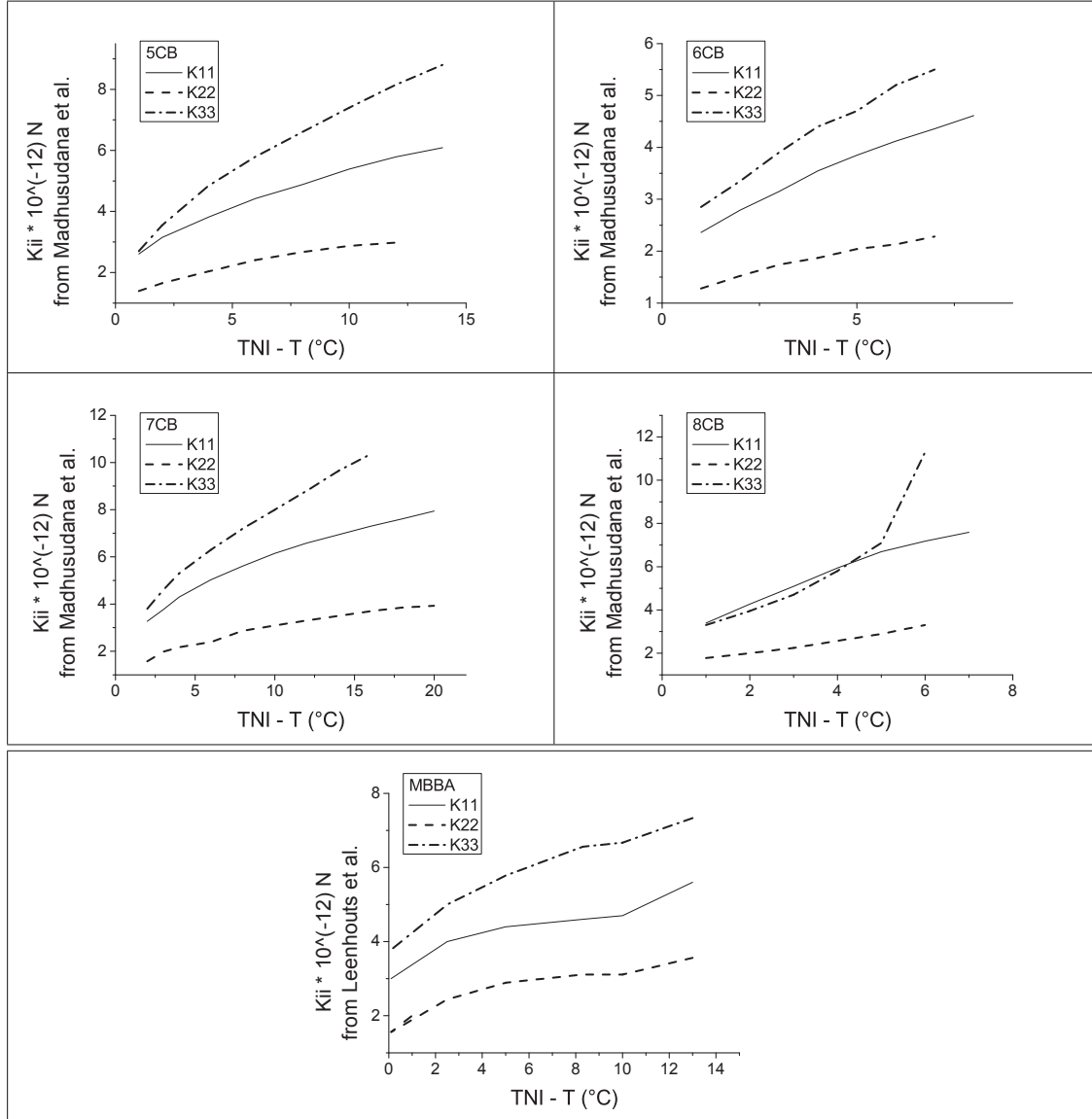


Figure 2.6: Elastic constants in function of the distance to the Nematic / Isotropic transition:  $T_{NI} - T$ . For the  $nCB$  family, the values are taken from [46], other measurements can be found in [10] and [23]. For MBBA, the values are taken from [43]

- Finally, the  $(K_{22} + K_{24})$  and  $K_{13}$  terms are the so-called surface-like terms (still in a continuous approach). As divergence terms, they can indeed be transformed in surface integrals using Gauss-Ostrogradsky's theorem. This allows to obtain for equation 2.4:

$$\int dV(f_{ext} + f_{Frank}) + \int dS(f_S + K_{13} \vec{k} \cdot (\vec{n} \operatorname{div} \vec{n}) - (K_{22} + K_{24}) \vec{k} \cdot (\vec{n} \operatorname{div} \vec{n} + \vec{n} \wedge \operatorname{rot} \vec{n})) \quad (2.6)$$

where  $\vec{k}$  stands for the vector normal to the surface and directed outwards. Expression 2.6 allows to separate surface and volume terms. The surface-like terms do not enter the Euler-Lagrange equation related to equation 2.4. They can only affect the nematic director through boundary conditions and can be neglected as long as the sample is thick enough. This will not be the case in our experiments. That is why the meaning of the two surface-like terms is further detailed in the following paragraphs.

### 2.1.2.1 About the saddle-splay surface-like term $(K_{22} + K_{24})$

The  $(K_{22} + K_{24})$  term finds its geometrical interpretation in Gauss curvature:

$$\vec{k} \cdot (\vec{n} \operatorname{div} \vec{n} + \vec{n} \wedge \operatorname{rot} \vec{n}) = \frac{1}{R_1 R_2} \quad (2.7)$$

where  $R_1$  and  $R_2$  are the two curvature radii of a geometric surface normal to the nematic director's field. The  $(K_{22} + K_{24})$  term is associated to a saddle-splay deformation of this geometric surface. The configurations obtained for a positive and a negative sign of the  $(K_{22} + K_{24})$  term, corresponding to a positive or negative Gauss curvature, are represented on figure 2.7. Systems where the saddle-splay term plays a role are for example systems where weak anchoring occurs at the interfaces of thin nematic films.

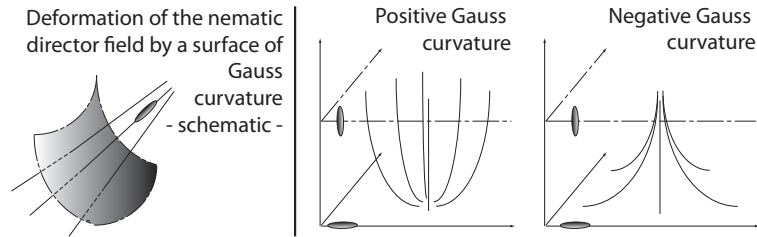


Figure 2.7: Illustration of the deformations of the nematic field by the  $(K_{22} + K_{24})$  term. On the left side, a schematic view of the interpretation of Gauss curvature. On the right side, schematic illustration of the dependence of the deformation of the nematic director for a sample in hybrid configuration in function of the sign of the  $(K_{22} + K_{24})$  term.

### 2.1.2.2 About the $K_{13}$ term

$K_{13}$  term is a combination of splay and bend deformation. Its influence is not obvious compared to other elastic terms as it does not have any direct geometrical interpretation. In fact, its presence in equation 2.4 has been controversial since its reintroduction by Nehring and Saupe [50].

Unlike the saddle-splay surface-like term, which was proven to be equivalent to a quadratic term of first order derivatives of the nematic director, the  $K_{13}$  term explicitly contains second order derivatives of the nematic director. Furthermore, its order of magnitude is supposed to be in the same range than the one of Frank's bulk elastic constants<sup>7</sup>. The  $K_{13}$  term could then, in principle, lead to infinite deformations of the nematic liquid crystals close to the interfaces and to a free energy that does not allow any lower bound [53]. This is known as the Oldano-Barbero paradox. Several approaches were developed to remove this singularity as the second order theory developed by the same authors. On the other hand, Yokoyama et al. [91] consider the  $K_{13}$  term as an artifact of the construction of the free energy density and thus take a  $K_{13}$  term equal to zero.

Some models also showed that the splay-bend surface-like term changes linearly with the nematic order parameter,  $K_{13} \approx S(\vec{r})$ , unlike other elastic constants that vary proportionately to  $S^2(\vec{r})$ . It could explain anchoring transitions observed for varying temperature [5].

### 2.1.3 Liquid crystals at an interface: about anchoring

For nematic liquid crystal, contact with an interface induces structuring of the first layers. Structuration occurs on a molecular scale as long as the system is far from a phase transition. The structured layers can show a very different order than the nematic one: for example smectic or even crystalline [36]. Beyond the first layers, the nematic director field is modified by the presence of the interface. This phenomenon is called anchoring. In a continuous description, anchoring will then account for the boundary condition at an interface.

Practically, the presence of an interface can lead to one or several possible azimuthal orientations of the nematic director: the anchoring is then said to be monostable (one preferred orientation) multistable (a finite number of preferred orientations) or degenerate (no preferred orientations). The preferred azimuthal anchoring angle(s) will be defined as  $\phi_0$  (see figure 2.8). In terms of polar orientation, there are three main kind of anchorings depending on the angle,  $\theta_0$ , between the normal at the interface and the nematic director close to the interface. They are the planar, homeotropic and tilted anchorings. Planar anchoring means that the preferred orientation of the nematic director is parallel to the interface, homeotropic anchoring that it is perpendicular to the interface and tilted anchoring that it makes an angle with the interface belonging to  $0 ; \frac{\pi}{2}$ . The two angles  $\phi_0$  and  $\theta_0$  define the equilibrium direction of the nematic

---

<sup>7</sup>It has been shown by Nehring and Saupe, [50], that the order of magnitude of the induced-dipole / induced-dipole part of the molecular interaction is the same for  $K_{13}$  and Frank's elastic constants



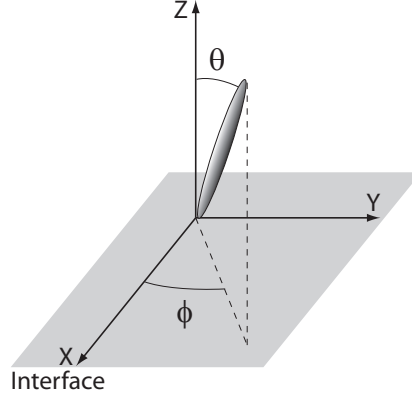


Figure 2.8: Continuous description of anchoring: at an interface, one can define two angles,  $\theta$  and  $\phi$  that represent respectively polar and azimuthal anchoring.

director near an interface, the easy axis. Once the number of possible orientations and their possible geometries has been defined, the question of the strength of the anchoring can be asked.

The anchoring energy is the anisotropic part of surface tension and has the same dimension. To estimate the strength of an anchoring, taking into account the response of the bulk nematic, one can then define the extrapolation length: it compares the elastic effects to the anchoring effects:

$$L = \frac{K}{W} \quad (2.8)$$

where  $K$  is the elastic constant in  $J.m^{-1}$  and  $W$  the anchoring energy in  $J.m^{-2}$ . The ratio  $\frac{K}{W}$  has the dimension of a length, hence the name of extrapolation length. In terms of strength, the smaller is the extrapolation length, the stronger is the anchoring.  $L$  indeed corresponds to the position of an imaginary interface, beyond the real one, where the anchoring would be infinitely strong (see figure 2.9). Considering this definition, an analogy with the hydrodynamic slip length can be drawn. The larger is  $L$ , the further is the imaginary interface from the real interface and thus the weaker is the anchoring. For example, if  $L$  was equal to zero, the imaginary and the real interface would coincide: the anchoring would then be infinitely strong. In practice, depending on the order of magnitude of the extrapolation length, it is still possible to define “strong” and “weak” anchorings.  $L$  is then written in function of the energies of interaction between molecules [55]:  $K \approx \frac{U_e}{a}$  where  $U_e$  is the elastic energy of interaction and  $a$  the molecular length ;  $W \approx \frac{U_s^a}{a^2}$  where  $U_s^a$  is the anisotropic part of the energy of interaction between the surface and the nematic. One then obtains:

$$L \approx a \frac{U_e}{U_s^a} \quad (2.9)$$

If  $U_e \approx U_s^a$ , the extrapolation length corresponds to the molecular dimension, the anchoring is said to be strong. On the contrary if  $U_e \gg U_s^a$ , the extrapolation length is greater than the

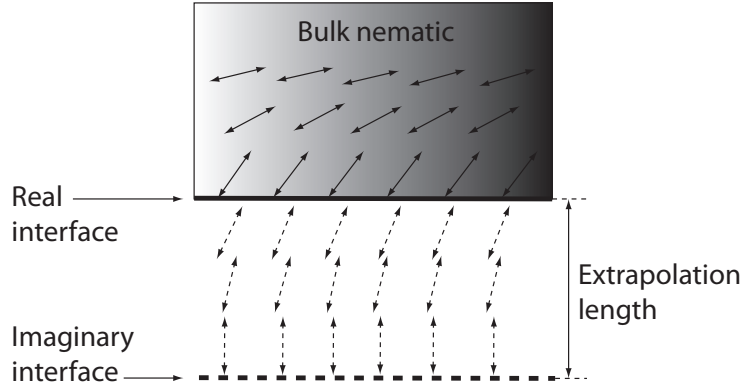


Figure 2.9: Schematic illustration of the meaning of the extrapolation length that corresponds to the position of an imaginary interface, beyond the real one, where the anchoring would be infinitely strong (the director is along the preferred direction: here, homeotropic).

molecular dimension, the anchoring is said to be weak.

Anchoring describes the preferred orientation of the nematic director close to an interface. If the actual orientation differs from the preferred one, for example by the action of an external field, a price in energy is paid. Several phenomenological models were developed to estimate this cost (The microscopic mechanisms at the origin of the anchoring phenomena are still poorly understood). The Rapini and Papoular model [63] is the most used in the literature<sup>8</sup>. It was first developed to calculate the value of the critical magnetic field which triggers the Fredericks instability. The Rapini and Papoular model is a first order development of the anchoring term of the surface free energy per area unit around the easy axis. In the case of an azimuthal degenerate anchoring, one obtains:

$$W_{RP} = \frac{W_{Polar}}{2} \sin^2(\theta - \theta_0) \quad (2.10)$$

where  $W_{Polar}$  is the polar anchoring energy and  $\theta_0$  the preferred polar anchoring angle. Although the equation 2.10 is simple, the Rapini and Papoular model is a good qualitative description of the distortions observed at the macroscopic and mesoscopic scale (e.g. when ignoring any change in the order parameter). The reason lies in the fact that the notion of anchoring strongly depends on the distance at which the anchoring properties are investigated. For example, anchoring measurements performed on the same system but with different methods lead to scattered results [90]. On the theoretical point of view, the scale dependence of the anchoring energy was demonstrated by Fournier and Galatola using a renormalization approach [27]. At a macroscopic scale, the angular dependence of the renormalized potential is dramatically smoothed. As the Rapini and Papoular model is a continuous macroscopic model, it explains why a simple equation such as 2.10 provides such a good description.

<sup>8</sup>Description of other models can be found in [20] or [45] for example

### 2.1.4 Uniaxial nematic / Isotropic phase transition in bulk: phenomenological model of Landau - de Gennes

The phenomenological model of Landau - de Gennes allows for the description of liquid crystals in the vicinity of the bulk uniaxial nematic / isotropic phase transition (NI phase transition). This model is a generalization by de Gennes of the Landau model for phase transitions of the second order to weak first order transitions, which is the case of the NI transition. The free energy per volume unit,  $f_{vol}$  is developed as a series of powers of the order parameter  $S$  defined above. The nematic is supposed to undergo neither distortions nor gradients of the order parameter: the nematic is then in bulk, far from any perturbation. As the free energy shall not depend on the choice of the referential, only the terms invariants by rotation are present in the development. At a given temperature, the minimization of  $f_{vol}$  gives the equilibrium value of the order parameter  $S$  with  $S = 0$  for high temperatures (isotropic phase) and  $S > 0$  for low temperatures (nematic phase). The consequences of the fixed extreme values of the order parameter are that there cannot be any first-order term in the development and that the sign of the second-order term changes below a well-defined temperature, the spinodal temperature  $T^*$ . A simple model for the constant of the second order term can then be written as  $A(T) = A_0(T - T^*)$ . The spinodal temperature, below which the isotropic phase is unstable, is slightly less than the transition temperature  $T_{NI}$ . To ensure stability, the development needs to go to the fourth order. The coefficients of the third and fourth terms are usually considered to be constant and positive close to the NI phase transition. The free energy per unit of volume is then written as:

$$f_{vol} = f_0(T) + \frac{1}{2}A_0(T - T^*)S^2 - \frac{1}{3}BS^3 + \frac{1}{4}CS^4 \quad (2.11)$$

This expression assumes that  $S$  is uniform which is true for nematic in bulk.

Let us comment further on this point. Actually, a change of the order parameter occurs in the vicinity of the interfaces. More precisely,  $S(\vec{r})$  increases at interfaces with either homeotropic anchoring, or planar non-degenerate anchoring [68], [48], [26], [94], [62], [89]. These interfaces are “ordering” ones. In contrast,  $S(\vec{r})$  decreases at interfaces with planar-degenerate anchoring, which are “disordering” ones. This can be understood as a “preferential wetting” of the interface by either the nematic (if the local order increases) or the isotropic phase (if the local order decreases), or as a “surface phase transition” [71], [65], [66], [67], [68].

For thin films, the two interfaces interplay. Without entering into details, for films of thickness  $\xi$  sandwiched between solid walls with identical anchorings, the transition temperature  $T_C(\xi)$  is shifted upwards for “ordering” walls, and downwards for “disordering” ones [71], [65], [66], [67], [68], [48]. In both cases, the shift  $\Delta T = T_{tr} - T_{NI} \approx \frac{1}{\xi}$  is small, 0.1 to 0.2°C for  $\xi \approx 100 \text{ nm}$  [89]. For solid walls with antagonist anchorings, the net result is always a significant shift downwards  $\Delta T \approx \frac{1}{\xi^2}$  [71]. An experimental confirmation is given in [87] in a planar-non-degenerate / homeotropic configuration, with a shift  $\Delta T \approx -2.5^\circ\text{C}$  for  $\xi \approx 100\text{nm}$ .

Practically, considering changes in  $S(\vec{r})$  close to film interfaces, that is, going farther the

continuous description, would make the calculations intractable. However, we must keep in mind that it is a weak point of the analysis.

### 2.1.5 Hybrid Aligned Nematic (HAN) films

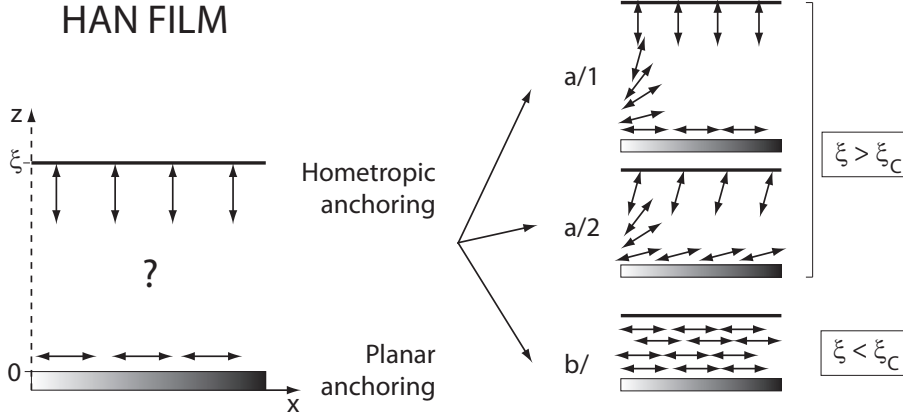


Figure 2.10: HAN films,  $xz$  plane. On the left side, conditions at the boundaries: at the bottom, the anchoring is planar along  $x$ , the preferred anchoring angle is then  $\theta_P^0 = 90^\circ$ ; at the top, the anchoring is homeotropic,  $\theta_H^0 = 0^\circ$ . On the right side, depending on the thickness, the configuration of the nematic director is different: for  $\xi > \xi_C$  the nematic director is distorted, the anchoring angles in  $a/1$  and  $a/2$  correspond respectively to the preferred anchoring angles ( $\xi \gg \xi_C$ ) or slightly differ; for  $\xi < \xi_C$ , the nematic director is uniform, its direction is imposed by the strongest anchoring, here the planar one ( $b/$ ).

An hybrid aligned nematic (HAN) [74] is made of a layer of nematic liquid crystal in between two surfaces inducing antagonist anchorings. One of the anchorings is planar non-degenerate and the other is homeotropic (see figure 2.10). The preferred anchoring angles at the two interfaces are then  $\theta_P^0 = 90^\circ$  for the planar anchoring and  $\theta_H^0 = 0^\circ$  for the homeotropic anchoring<sup>9</sup>. In such a configuration, the thickness of the film will determine the final configuration of the nematic director. Three different behaviours are observed corresponding to three ranges of thicknesses (see figure 2.10):

- If the film is thick, the two interfaces do not feel each other's presence. The nematic director field adapts itself to the two antagonist boundary conditions: its direction changes continuously across the film. Such a structure with translational invariance along  $x$  and the director rotating inside a  $xz$  plane is referred to as a "distorted nematic".
- If the film is thin enough so that the two interfaces begin to feel each other's presence, the

<sup>9</sup>Let us remind that an anchoring angle is the angle made between the normal to the interface and the nematic director.

nematic director is still distorted, but the observed anchoring angles at the interfaces shift from their preferred values  $\theta_P^0$  and  $\theta_H^0$

- If the film is very thin, the cost of the elastic distortion is too large. The nematic director cannot distort itself and the strongest anchoring imposes its direction across the film. In a situation corresponding to liquids crystals deposited on silica, the strongest anchoring is the homeotropic one whereas for liquid crystals deposited on liquid substrates (e.g. water or glycerol), it is the planar anchoring that is the strongest.

Considering the configuration of the field of the nematic director, an anchoring transition controlled by the thickness occurs from a distorted to a uniform configuration. A critical thickness,  $\xi_C$ , is then defined. For films whose thickness is more than the critical thickness,  $\xi > \xi_C$ , the nematic director is distorted. For films which thickness is less than the critical thickness,  $\xi < \xi_C$ , the film is uniform. This transition is a second order one, so that nothing specific is expected when the film thickness crosses the value  $\xi_C$ .

The critical thickness can be obtained by minimization of the free energy per surface unit of a nematic film with a thickness  $\xi$ . This calculation was done first by Barbero and Barberi [3] in a continuous approach (constant  $S$ ). In the HAN configuration that they considered, only the splay and bend elastic terms come into play. In the ‘‘one constant approximation’’ ( $K_{11} = K_{33} = K$ ), Frank’s expression of the nematic free energy can then be complemented with two terms representing the anchoring free energy per surface unit for each interface (Rapini and Papoular model):

$$F = \int_0^\xi \frac{1}{2} K \left( \frac{d\theta(z)}{dz} \right)^2 dz + \frac{1}{2} W_P \sin^2(\theta_P - \theta_P^0) + \frac{1}{2} W_H \sin^2(\theta_H - \theta_H^0) \quad (2.12)$$

where  $W_P$  and  $W_H$  are the polar anchoring energies respectively in the planar and homeotropic case ;  $\theta_P$  and  $\theta_H$  the anchoring angles at the planar and homeotropic interface ;  $\theta_P^0$  and  $\theta_H^0$  the preferred anchoring angles at the planar and homeotropic interface:  $\theta_P^0 = 90^\circ$  and  $\theta_H^0 = 0^\circ$ . The minimization leads to an Euler-Lagrange equation:  $\frac{d^2\theta(z)}{dz^2} = 0$ . The angle of the director changes linearly with the  $z$  coordinate in the film:

$$\theta(z) = \theta_P(\xi) + \frac{\theta_H(\xi) - \theta_P(\xi)}{h} z \quad (2.13)$$

The free energy per surface unit is then:

$$F = \frac{K(\theta_P(\xi) - \theta_H(\xi))^2}{2\xi} + \frac{1}{2} W_P \sin^2(\theta_P - \theta_P^0) + \frac{1}{2} W_H \sin^2(\theta_H - \theta_H^0) \quad (2.14)$$

The angles at the boundaries,  $\theta_P$  and  $\theta_H$  are found to depend on the thickness  $h$  of the film. However, it is not possible to find an analytic solution to the equations describing their variation. A graphic resolution was used for example in the reference [19]. The critical thickness  $\xi_C$

corresponds to the difference of the extrapolation lengths:

$$\xi_C = |L_P - L_H| = \left| \frac{K}{W_P} - \frac{K}{W_H} \right| \quad (2.15)$$

This critical thickness is also called Barbero and Barberi's critical thickness. The order of magnitude of the critical thickness for nematic liquid crystals deposited on silica is the micrometer. The analysis described above hence deals with relatively thick films.

The critical thickness can be observed experimentally using a nematic liquid crystal cell shaped as a wedge [32]. The two walls of the cell are treated so that the configuration corresponds to antagonist anchoring conditions, the homeotropic anchoring being stronger than the planar one. Close to the angle of the wedge, the orientation of the nematic director is found to be uniform and homeotropic. Further from the angle of the wedge, the local thickness increases and a change in the orientation of the nematic director is observed: the nematic director becomes distorted. More recently, studies at small scales have been performed with SFA (Surface Force Apparatus) [93]. One of the mica surfaces is coated using CTAB ensuring homeotropic anchoring. No anchoring transition was observed even for nanometric thicknesses. The results in this case are complex due to the presence of a disclination in the nematic film resulting from the curvature of the upper wall. Moreover the incidence of compression on the CTAB layer is not fully clear.

One must stress that all the experiments presented in this paragraph concern samples between solid walls. However, in our experimental configuration there will be a free interface and it will then be necessary to come back on these results.

## 2.2 Review of wetting properties and questions to be answered

### 2.2.1 From classical HAN films towards hybrid nematic thin films

In the classical description of HAN films (see above), the thickness of the film is imposed by the interfaces: the typical case is a cell filled with nematic liquid crystal with solid walls inducing a well-defined anchoring in a parallel or a wedge geometry. But what would happen if thickness is not fixed ? Let us deposit liquid crystal on a substrate which is known to create a planar anchoring. At the bottom, the preferred anchoring of the liquid crystal is fixed by the substrate, it is planar. At the top, the anchoring of the liquid crystal is homeotropic. In such a configuration, only the average thickness is fixed. Experiments were performed previously on solid substrates (for further details, see [9], [85], [82]). A brief summary of the former studies both on solid and on liquid substrates will first be presented to introduce the motivations of the present work. It will be followed by the presentation of experiments performed on liquid substrates in the nematic range of temperature and coming close to the nematic / isotropic transition.

## 2.2.2 Solid substrates: Forbidden thickness range

### 2.2.2.1 Far from the nematic / isotropic transition

The deposition of a microdroplet of nematic liquid crystal (5CB) on an oxidized silicon wafer in total wetting conditions leads to a peculiar situation: at long times, a film which thickness is  $\xi_{LB} = 3.5$  nm coexists with a flat drop which thickness,  $\xi_{UB}$ , is around 17 nm (see figure 2.11).

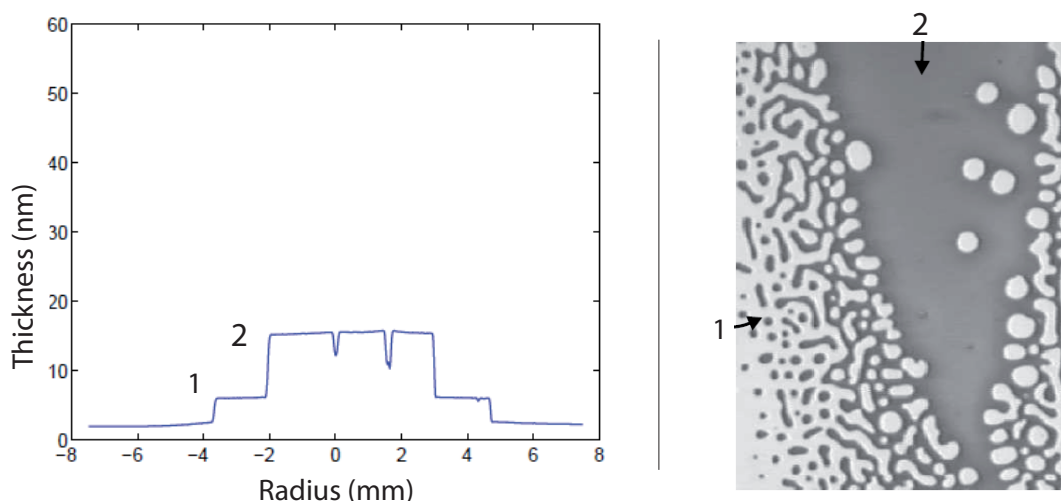


Figure 2.11: Figures taken from [85]. On the left side, a drop of 5CB deposited on a silicon wafer at a temperature of 24°C (nematic range). On the right side, a film of 5CB spin-coated on the same substrate. The picture is taken close to the edge of the wafer, where a gradient of average thickness is observed. The average thickness is less than  $\xi_{UB}$  and the film is separating itself in two parts which thicknesses are respectively  $\xi_{LB}$  (white zones) and  $\xi_{UB}$  (dark zones).

The deposition method can be changed in order to obtain a film instead of a drop: 5CB is spin-coated on the wafer through the use of a volatile solvent. Once the solvent is evaporated, the film of liquid is found to be stable only if its thickness is below  $\xi_{LB}$  or above  $\xi_{UB}$ . If the thickness of the spin-coated film is in between  $\xi_{LB}$  and  $\xi_{UB}$ , the film is unstable and separates itself into a succession of zones which thicknesses correspond to either  $\xi_{LB}$  or  $\xi_{UB}$  (see figure 2.11). As a conclusion, the previous studies led to the observation that for nematic liquid crystals deposited on silicon wafers, there is a forbidden thickness range:  $\xi_{LB}$  is the lower boundary of the forbidden range and  $\xi_{UB}$ , the upper boundary (more details about the corresponding experiments can be found in [9], [85], [82]). The films corresponding to  $\xi_{LB}$  have a structure which is controlled by the presence of the substrate. This structure was shown to be a trilayer for all nCB investigated nCB: 5CB, 6CB, 7CB, 8CB ([9]).

The structure of the films corresponding to the thickness  $\xi_{UB}$  is not known. Considering the structure of classical HAN films, there are two possibilities. If  $\xi_{UB}$  is below the critical thickness,  $\xi_C$ , the structure of the films is expected to be homogeneous and imposed by the strongest of

the two anchorings. If it is above, a distorted structure is expected.

Moreover, it is then necessary to compare the anchoring energies with air and with silicon wafers. The value of the anchoring energy have been measured in the case of air by Lavrentovich et al. [42] by optical methods. They obtain  $W_H = 1 \pm 0.5 \times 10^{-5} J/m^2$ . On the other hand, the anchoring energy with silicon wafers was never measured. However, measurements on glass plates covered by evaporated SiOx are available. In that case, values are scattered due to the fact that the different methods used scan different scales and, as already mentioned, anchoring depends on the scale. One could separate the results in two groups: first, Van Sprang et al. [83] and Faetti et al. [25] found values similar to the anchoring energy with air ( $W_{P1} = 1 - 2 \pm 0.5 \times 10^{-5} J/m^2$ ); second, Yokoyama et al. [90] found values one order of magnitude higher ( $W_{P2} = 13 \times 10^{-5} J/m^2$ ). The values found for evaporated SiOx would suggest that the anchoring energy for with silicon wafer would be of the same order of magnitude or above the one with air. However, there is a paradoxical consensus in the literature agreeing that the anchoring energy with air is higher than the one on silicon wafers [23]. One would then expect that if  $\xi_{UB}$  is below the critical thickness,  $\xi_C$ , the nematic is in an homeotropic configuration. On the other hand, if  $\xi_{UB}$  is above the critical thickness,  $\xi_C$ , the configuration is distorted.

Finally, one must know the value of  $\xi_C$ . As  $\xi_C$  is equal to the difference of the two extrapolation lengths, its value is a function of the elastic constant,  $K$ , and of the coefficients of the anchoring energies for the system. The values of the elastic constants are known (see figure 2.6), as well as the one of the anchoring energy with air. The extrapolation length with air is then:

$$L_H = \frac{K}{W_H} \approx \frac{6 \times 10^{-12}}{1 \times 10^{-5}} \approx 0.8 \pm 0.4 \mu m \quad (2.16)$$

The anchoring with air is then strong for thicknesses well above the micrometer range. Concerning, the interface with the silicon wafer, the problem of the unknown anchoring energy remains. However, considering the value of  $L_H$  and the order of magnitude usually found for  $\xi_C$  (see Barbero, [32]), one can still assume that the value of  $\xi_C$  is most probably of the order of the micrometer. The case where  $L_H$  and  $L_P$  are very close, corresponding to  $\xi_C \ll \mu m$ , should be exceptional. Between solid walls, a film with a thickness corresponding to  $\xi_{UB} \approx 17$  nm should therefore show an homeotropic structure.

Several models were developed to explain this coexistence of thicknesses  $\xi_{LB}$  and  $\xi_{UB}$  and the structure of UB films: pseudo-Casimir effect arising because of fluctuations of the nematic director at the interfaces in the hypothesis where the UB film is in homeotropic configuration<sup>10</sup> (Ziherl et al. [95]) or competition of elasticity and spontaneous spreading in the hypothesis of a nematic in distorted configuration (Valignat et al. [79]). However, both models<sup>11</sup> imply that nematics could be distorted for thicknesses as low as 20 – 40 nm, which is in contradiction with

---

<sup>10</sup>In principle, a fine study of the birefringence could have helped to determine the structure of the UB film. In fact, the question was raised much later and the experiments were not performed on solid substrates [85], [82]. In [82], birefringence was only studied on glycerol.

<sup>11</sup> $\xi_C$  is calculated in the Ziherl model. It is slightly larger than  $\xi_{UB}$  but of the same order of magnitude.



the characteristic thicknesses of Barbero unless the anchoring values are very close (4 – 5%) or if both anchorings are much stronger than accepted values. These implausible requirements suggest that the analysis should be reconsidered and specifically the role of the free interface. In this situation, a change of the experimental conditions can bring new clues to understand the organization of thin nematic films in general.

## 2.2.3 Liquid substrates: One system, two problems

### 2.2.3.1 About liquid substrates for liquid crystals

In wetting experiments, liquid substrates provide perfectly smooth substrates. They are free from physical heterogeneities, which implies that no pinning phenomena have to be taken into account. This is particularly important in the case of liquid crystals, where defects on the substrate can be the source of topological defects in the structure of the nematic. It is also important because it ensures that the molecules of liquid crystal will not be pinned on the surface. For example, let us consider two substrates possessing a planar degenerate anchoring, one being solid (e.g. silicon wafer) and the other one liquid (e.g. water or glycerol). On the solid substrate, the planar degenerate anchoring means that the anchoring is azimuthally degenerate, but it does not ensure that the molecules are free to move: they can be pinned randomly on defects. It is in fact well-known that once liquid crystal molecules are deposited on a silicon wafer, the molecules of the first layers cannot change their orientation even if annealing is performed. On the contrary, on liquid substrates, the planar degenerate anchoring means that the molecules are free to rotate. There is then no memory effect for liquid substrates.

### 2.2.3.2 Description of the experiments

Glycerol and pure water (MiliQ water, 18.2  $M\Omega$ ) were the chosen liquids, they were poured in a Petri dish<sup>12</sup>. Water and glycerol are polar liquids with a relatively high surface tension (respectively 72.8 mN/m and 64 mN/m at 20°C) and with a refractive index smaller than the mean refractive index of the liquid crystals used (respectively 1.33 and 1.47 at 20°C). The anchoring of liquid crystals on these liquids is planar degenerate, as in the case of silicon wafers. However, in the case of liquid substrates, the anchoring with the liquid substrate is larger than the one with air. For thicknesses less than the critical thickness,  $\xi_C$ , the nematic film will then adopt a planar configuration instead of an homeotropic configuration in the case of silicon wafers.

A specific property of glycerol is that it is a hygroscopic liquid. All the experiments with glycerol were then performed with 99.9 % pure glycerol (Sigma Aldrich) and the samples were kept in a confined environment (box) with dessicant.

Not all the liquid crystals that were used are nematic at ambient temperature (see figure 2.2). When heating was required, Petri dishes were cut to reduce their depth, so that the liquid substrate did not experience convection when the temperature was increased, especially for water

---

<sup>12</sup>We filled completely the Petri dishes in order to reduce meniscus effects.

which has a lower viscosity than glycerol. The convection threshold,  $t$ , indeed scales as  $t \approx \frac{1}{d^3}$ , where  $d$  is the liquid depth. The cut Petri dishes were then placed on a custom made heating plate<sup>13</sup>, small enough to allow for observation under optical microscopes (PolyvarMET, Reichert Young). Liquid crystals were deposited on the liquid substrates by the mean of a volatile solvent: more or less diluted solutions of liquid crystal in pure hexane (Sigma Aldrich) were prepared. Droplets of the solution are then gently deposited on the Petri dish. The solvent helps the liquid crystal to spread and then evaporates. The sample is observed after complete evaporation of the solvent. During observation, the sample was protected by a custom made box<sup>14</sup> from dust, air flows,...

Images were then taken using cameras. Three different cameras were used: two color cameras, one being extra-sensitive (ExiAqua, Qimaging), and a sensitive black and white camera (Coolsnap, Roper scientific). It explains the differences in color and in quality of the images presented hereafter.

### 2.2.3.3 Wetting on glycerol and first observations

All the liquid crystals used are in a total wetting configuration on glycerol<sup>15</sup>. For large liquid crystal thickness, one observes the classical morphology and defects of an hybrid aligned nematic. For submicron thicknesses, the landscape is completely different: the surface of the liquid substrate is covered by a thin nematic film showing striped patterns and colors (see figure 2.13). The colors correspond to Newton's colors, colors characteristic from interferences obtained with thin materials. More precisely, one color and one index correspond to one thickness. Stripes represent in fact changes in the orientation of the nematic director of the liquid crystal as the incident light is polarized, but not a change in the thickness. Newton's scale of colors was then used to measure the thickness of striped films. A stripe of one color shows dark and bright zones, we chose for the measurements the brightest one (see figure 2.12). The optical index used to calculate the thickness from the color is the mean optical index<sup>16</sup>.

---

<sup>13</sup>The heating plate was made by C. Poulard during his PhD thesis and was modified by C. Hermann, LPS electronic workshop.

<sup>14</sup>The box, including the sample, the heating plate and a part of the microscope, was made by J. da Quintas (LPS mechanical workshop).

<sup>15</sup>Let us remind that 5CB on silicon wafers was also in a total wetting configuration.

<sup>16</sup>The measurements of thicknesses were always made on unmodified images. However, to ensure clarity, the images presented in the manuscript sometimes have modified contrast, the colors are just indicative.

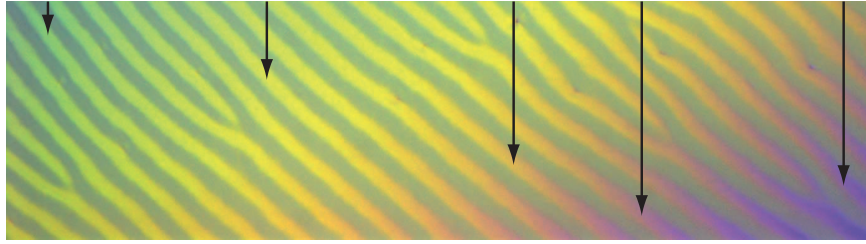


Figure 2.12: Arrows showing the brightest tone for stripes of different color (6CB on glycerol). The thickness of the nematic films is deduced from this brightest tone via Newton's colors and using the mean optical index of the nematic. Thickness increasing from green to purple ; thickness range :  $0.24 - 0.35 \mu\text{m}$

As the pictures presented on figure 2.13 show, gradients of thicknesses for the nematic film, are allowed on glycerol. The wavelength of the stripes varies with the thickness of the film and does not differ significantly if it is measured in a zone presenting gradients or in a flat zone of the thin nematic film.

The formation of striped patterns is triggered by the thickness. To understand this phenomenon, let us first remind that for thick hybrid aligned nematics, the nematic director is distorted in the vertical plane in order to satisfy the antagonist boundary conditions: planar anchoring with the substrate and homeotropic anchoring with the air. When the thickness of the nematic film decreases, the interfaces begin to feel each others presence: the distortion of the nematic director in the vertical plane is not sufficient anymore, so that the nematic director begins to undulate azimuthally. Breaking the in-plane symmetry has for consequence the formation of the striped periodic patterns (see figure 2.14).

The morphology of the stripes can remind of the classical Fredericks instability which occurs for nematic films put under the constraint of an electric or a magnetic field. However the order of magnitude and mechanism are different in our case. There is indeed the presence of a free interface and the fact that striped patterns are long wavelength patterns, their wavelength is typically two orders of magnitude higher than the corresponding thickness. To help comprehension, it is possible to see the role of the thickness in our case as similar to the one of the field in Fredericks instability as it is the parameter which controls the formation of striped patterns.

Theoretical analyses of stripe patterns (dependence of wavelength with film thickness) are mainly due to Sparavigna and Strigazzi [75] and also Lavrentovich and Pergamenschik [42], [40], even if the latter approach relies on the value of the parameter  $K_{13}$  (see the end of this chapter). These models, that are critically sensitive to the values of elastic constants, including  $K_{24}$ , have to be improved. The question is not fully solved, despite the development of new approaches [47]. The aim here is to constrain the theories to be robust with respect to the precise values of elastic constants, by investigating a large range of similar compounds. What can be mentioned as a general guide line is that the Barbero critical thickness (that is, the

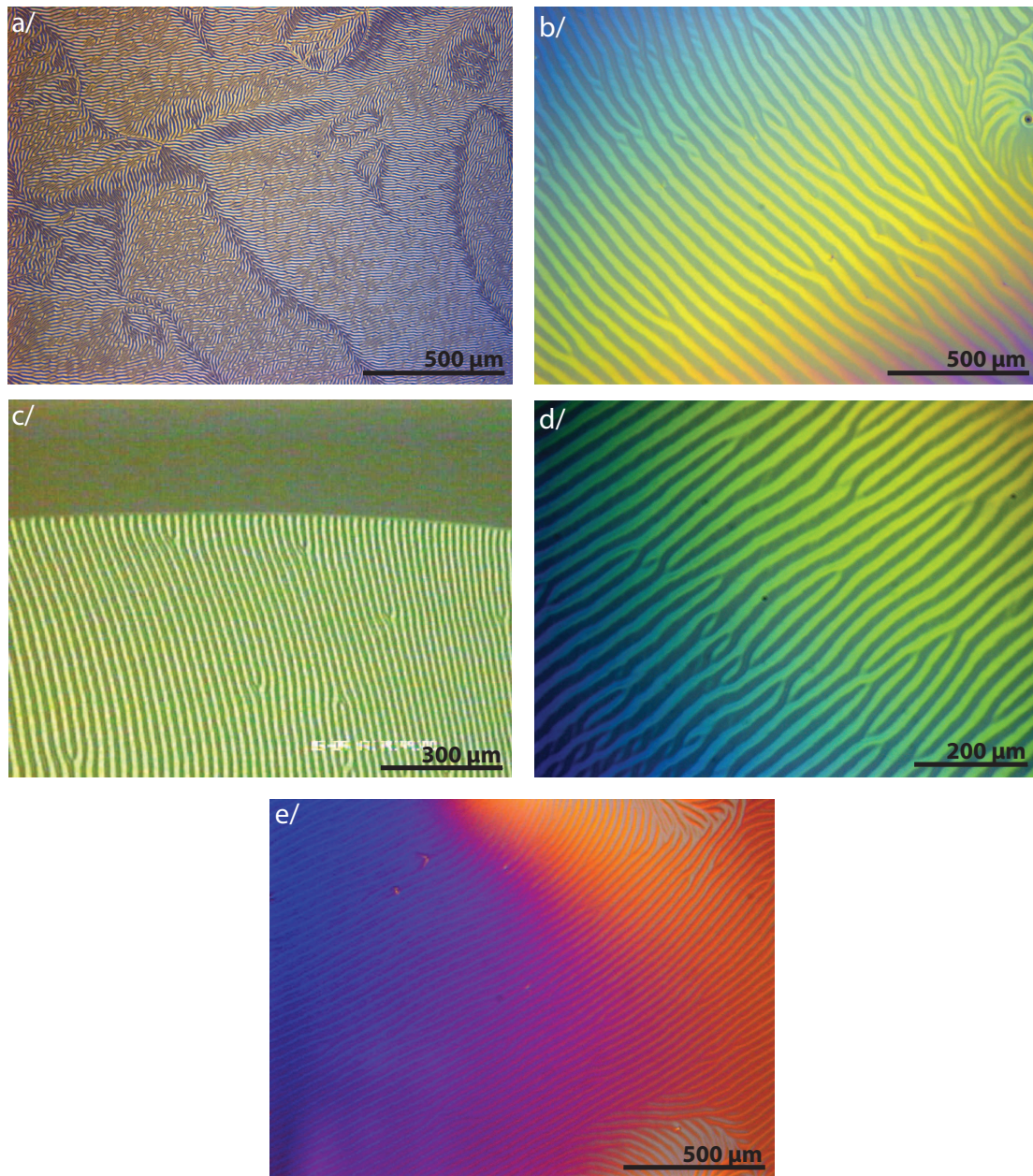


Figure 2.13: Examples of striped films of nCB and MBBA on glycerol far from the nematic / isotropic phase transition. a/5CB - Thickness  $0.14 \mu\text{m}$  ; b/ 6CB - Thickness range  $0.19\text{--}0.35 \mu\text{m}$  ; c/ 7CB - Thickness  $0.07 \mu\text{m}$  ; d/ 8CB - Thickness range  $0.22\text{--}0.29 \mu\text{m}$  ; e/ MBBA - Thickness  $0.29\text{--}0.35 \mu\text{m}$ . The image shown for 7CB, image c/, illustrates the shape of the border of the film close to the fringe of the Petri dish. On the pictures, each color corresponds to one thickness (Newton's colors, see main text). This will be the case for all colored pictures of liquid crystals taken with the optical microscope (except in the case of crossed polarizers).

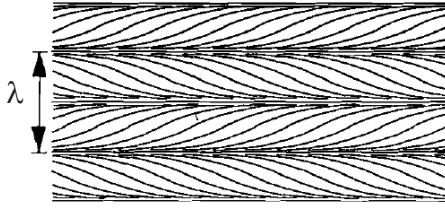


Figure 2.14: Figure taken from [40]. Schematic top view of the azimuthal undulation of the nematic director in striped patterns,  $\lambda$  corresponds to one wavelength.

difference of the extrapolation lengths) is a plausible characteristic length for the analysis but is no longer the thickness threshold towards planar configuration.

Further description of the striped patterns will be presented in the following.

On glycerol, striped films cover almost the whole surface of the Petri dish. However, on its frontiers, it is possible to see a succession of several molecular films. Their nature still needs to be determined.

One last phenomenon must be mentioned: glycerol molecules slowly diffuse in liquid crystal films. A further description of the process and of its consequences is presented in the following. Let us just mention that the diffusion of glycerol in the liquid crystal films constraints the experiments in two ways. First, a sample must not be kept more than half an hour after deposition. In such a configuration, the diffusion of glycerol does not disturb the striped patterns. Second, one must be very careful for heated samples as increasing the temperature increases the diffusion of the glycerol. It is critical especially for liquid crystal molecules with short alkyl chain (the longer is the chain the less quickly the glycerol diffuses) and for samples which have to be heated up to high temperatures. In practice, far below the nematic / isotropic phase transition, glycerol diffusion is negligible for all the nCB investigated.

#### 2.2.3.4 Wetting on water and first observations

On water, not all the liquid crystals used are in a total wetting configuration. MBBA does indeed not wet water substrates. The situation of 5CB and 7CB is more complex. Compounds of two different purities were indeed used in our experiments: 99% pure liquid crystals (Sigma Aldrich) and > 99% liquid crystals (Frinton). Only the high purity ones (> 99%) wet water. The presence of impurities is then critical for our systems, which is not surprising as interfaces are concerned. For 5CB, the measurement of surface tension found in the literature are scattered (e.g. [61], [33], [37], [73], [78]): from 28 mN/m to 40 mN/m at room temperature. The scattering is due to the purity of the compounds. The 28 mN/m value is found for “standard” liquid crystal and the 40 mN/m is found for purified liquid crystal. At least part of these impurities are surface active, they alter the wetting behaviour of the liquid crystals.

For nCBs, deposited on water, the landscape of the system is different than on glycerol.

Images obtained under optical microscope show flat striped domains. On the same sample, striped domains of different thicknesses (different colors) coexist (see figure 2.15).

This configuration is obtained shortly after deposition<sup>17</sup> and lasts on long time scales (week). The system is then metastable. Focusing on the zone in between domains, it is possible to observe that it is covered by two different molecular films. Experimentally, this can be achieved by using a sensitive camera and by modifying the contrast of the images (see figure 2.16). Determination of the nature of the molecular films was done previously [88], [16], [31], [19] using Langmuir isotherms (see Appendices) and structural measurements performed with the Brewster angle microscope. For 6CB and 8CB, the thinnest of the molecular films is a monolayer and the thickest is a trilayer. For 5CB and 7CB, Langmuir isotherms experiments were performed. The same behaviour than the one observed for even nCBs was found (see figure B.1). For all nCB investigated, the molecular films are then a monolayer and a trilayer far from the nematic / isotropic phase transition.

The flat striped domains observed on water are not always circular. The exact shape of the domain is determined by the coexistence with domains of mono- or trilayer. Domains do not always show stripes. Smallest domains, less than twice the wavelength, adopt indeed a planar configuration [19]. Moreover, even for striped domains, it is always a planar rim which is in contact with the molecular films [19]. The planar structure can be evidenced by observing samples between crossed polarisers (see figure 2.18). The planar configuration is due to the thickness gradient at the edge. Gradients introduce a preferred orientation which destroys the orientational freedom and therefore prevents the formation of stripes. The width of the rim is approximately half the stripe wavelength. The boundary tension  $\tau(\xi)$  between striped domains and surrounding trilayer is acceptably accounted for as being the contribution of the anchoring energy in the edge. Per unit area, as  $\theta_H = \theta_P = \pi/2$ ,  $f_S = W_H/2$  and therefore  $\tau(\xi) \approx \lambda W_H/4$  [19].

## 2.2.4 Characterization of the striped phase

### 2.2.4.1 Experimental characterization

**Stripes** Characterizing the striped phase is done from the images obtained with the polarized optical microscope. The wavelength of the stripes ( $\lambda$ ) is measured in function of the thickness ( $\xi$ ) of the corresponding nematic film or domain. The thickness is obtained via Newton's color scale:

$$\xi = \frac{\delta}{2n_m} \quad (2.17)$$

where  $n_m$  is the mean optical index of the liquid crystal, i.e. the effective index for distorted films (see figure 2.4 for the corresponding values) and  $\delta$  is the optical path corresponding to

---

<sup>17</sup>Just after deposition a transient state is observed where there are reorganizations in the system. The main phenomenon observable with the microscope is the coalescence of striped domains. Coalescence between domains of the same thickness was studied in details by U. Delabre, see [19], [17]



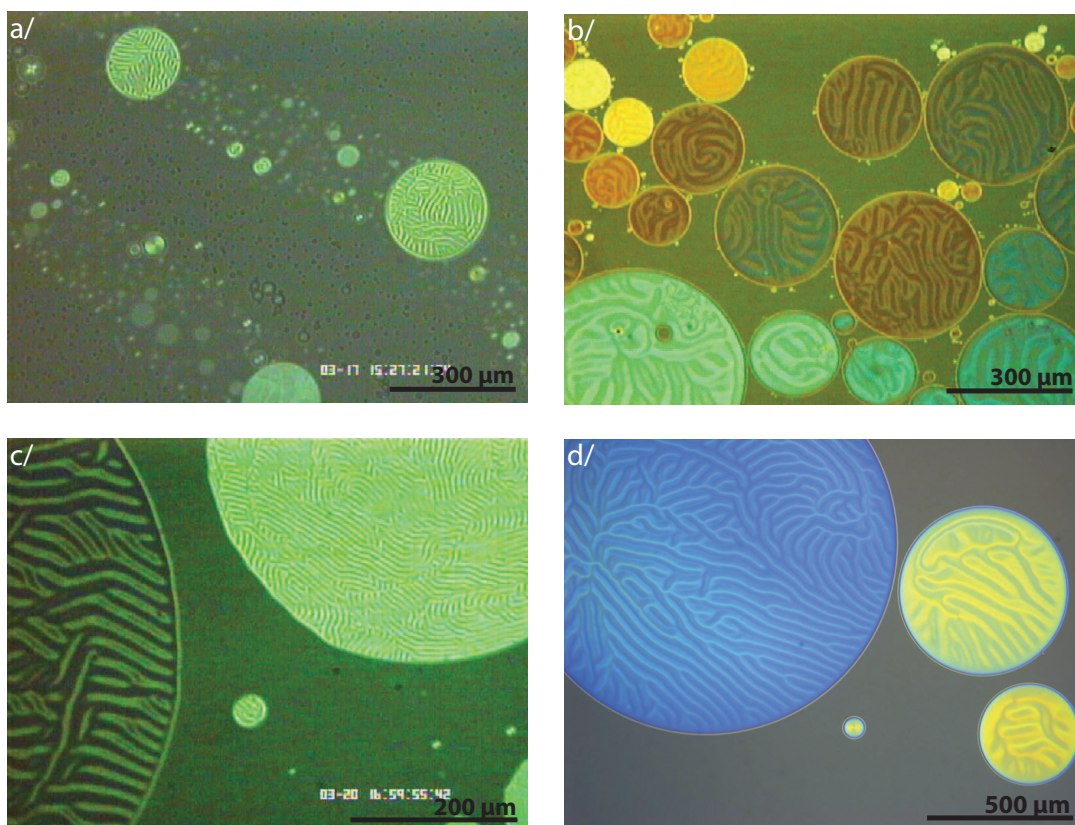


Figure 2.15: Examples of striped domains of nCB on water far from the nematic / isotropic phase transition. a/ 5CB ; Thickness of striped domains  $0.05 - 0.09 \mu\text{m}$  ; b/ 6CB ; Thickness of striped domains  $0.08 - 0.21 \mu\text{m}$  ; c/ 7CB ; Thickness of striped domains  $0.09 - 0.19 \mu\text{m}$  ; d/ 8CB ; Thickness of striped domains  $0.21 - 0.29 \mu\text{m}$ . Note that 5CB and 7CB wet water only when high purity liquid crystals are used and that there is no picture of MBBA, as MBBA only wets partially water.

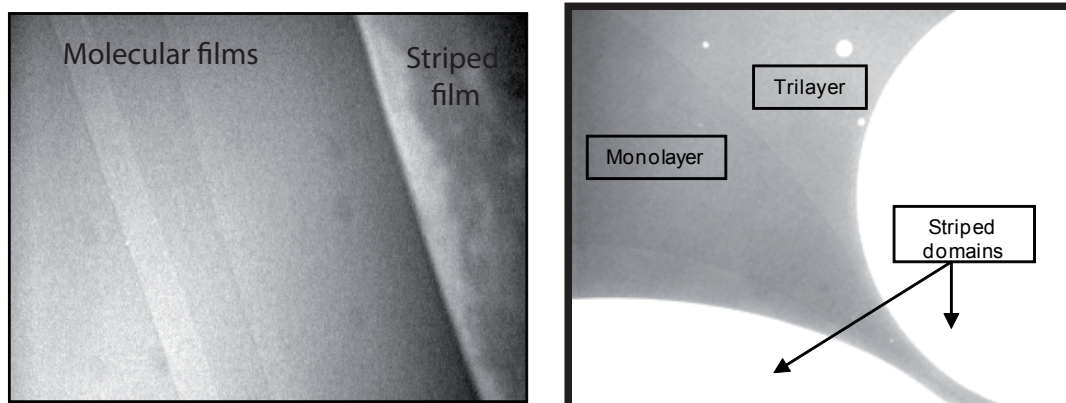


Figure 2.16: Molecular films in coexistence with striped films: The images have a modified contrast in order to see the molecular films. On the left side, 8CB on glycerol. On the right, 6CB on water. The saturated zone corresponds to domains of striped phase. They coexist with no intermediary with a trilayer and a monolayer.

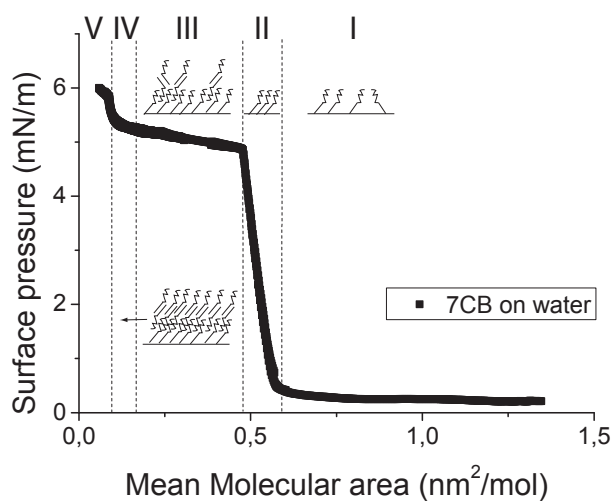


Figure 2.17: Example of a surface pressure versus mean area per molecule isotherm for 7CB on water at room temperature. This isotherm allows one to distinguish several zones. Zone I: diluted monolayer ; zone II: compressed monolayer ; zone III: coexistence of dense monolayer and trilayer ; zone IV: compressed trilayer ; zone V: crystallization in a 3D phase.



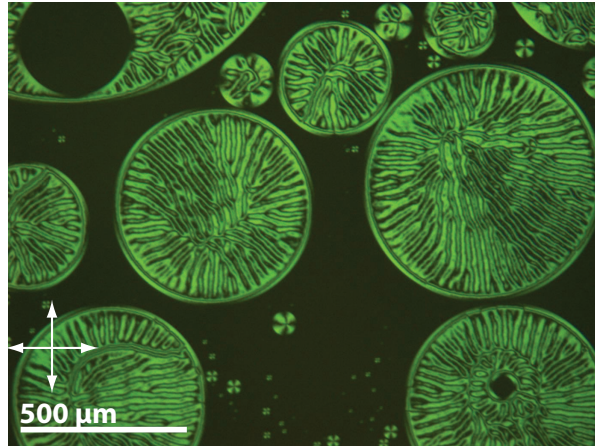


Figure 2.18: Image of 6CB on water between crossed polarizers, the two double arrows showing the directions of the polarizers. Smallest domains, which are not striped, show a cross-like extinction characteristic of a planar structure (radial symmetry, with a radial planar structure, and a defect in the center). With increasing the domain size, the radial symmetry is lost, the black cross shifts to one edge: the rim of the striped domains and of their holes show extinctions along the directions of the polarizers.

the color of the nematic. The optical path is given by Newton's color scale (black center). For the thinnest films or domains, corresponding to grey tones in Newton's color scale, a sensitive black and white camera (CoolSnap, Roper scientific) was used: the reflected intensities were then compared. To ensure that the evaluation of the colors does not depend on the appreciation of the experimentalist, several cross-checks were performed. First, a calibration of Newton's colors as seen under our microscope was done with a lens showing a thin spherical shape by measuring the thicknesses and comparing the results with the ones obtained with a green filter (2.19). It allowed for showing that small steps systematically obtained in the thickness curves corresponded to characteristic zones of Newton's color scales. The small steps are then artifacts produced certainly by the spectrum of the lamp of our microscope (halogen lamp) and of the response of the cameras. Second, independent measurements were performed by three different people and did not show differences. Furthermore, the first measurements, performed by U. Delabre [19] for 5CB and 6CB on glycerol, 6CB on water and MBBA on glycerol give exactly the same trends than the ones presented. The data previously obtained in our group by U. Delabre [19] were as well compared to the preceding study performed by Lavrentovich, Pergamenschick and Sparavigna ([42],[75]) for 5CB on glycerol (see figure 2.19).

As previously explained, the wavelength increases with the thickness of the nematic and corresponds to around one hundred times the thickness. There is an upper boundary for the striped phase,  $D$ , specifically investigated for 5CB and 6CB: when reaching thicknesses around

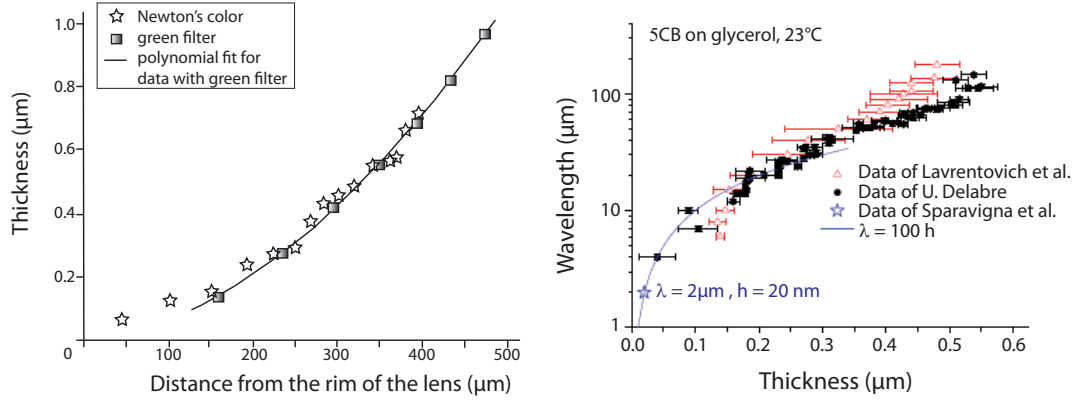


Figure 2.19: Cross-checks performed on the characterization of striped patterns. On the left, calibration of Newton's color scale. The measured thickness of a spherically-shaped thin lens is compared when Newton's color scale and a green filter are used. On the right, figure taken from [19]. The figure compares data obtained in our group by U. Delabre compared to the ones of Lavrentovich et al. [42] and Sparavigna et al. [75] in the case of 5CB on glycerol. Note that the wavelength is plotted here in logarithmic scale.

$0.6 \mu\text{m}$ , the wavelength shows a steep increase<sup>18</sup>. Above this thickness, nematic films or domains exist, only they show the characteristic morphology and defects of hybrid nematics. For the lower bound of the striped phase, measurements were also made on MBBA: in each case, for the nCB family as well as for MBBA, it is possible to observe striped films until thicknesses corresponding to 20 – 40 nm. Not only this minimum value is similar to the one of the upper boundary,  $\xi_{UB}$ , observed for 5CB on silicon wafers, but on water, the striped domains coexist directly with trilayers. The situation then seems close to the one on solid substrates, although with two differences. First, on liquids,  $\xi_{UB}$  is the thickness of the thinnest striped film, but thicker films may coexist, which suggests metastability. Second, the film with thickness  $\xi_{UB}$  observed on the silicon wafers is not striped.

These first results were completed by complementary measurements on the previous systems as well as new measurements on 7CB and 8CB on glycerol and 5CB, 7CB and 8CB on water. The wavelength v.s. thickness ( $\lambda(\xi)$ ) relationship was then compared for the different substrates and different compounds at a given interval in temperature from the nematic / isotropic (NI) phase transition (see figure 2.20<sup>19</sup>).

On water, only measurements for the nCB series are available as MBBA is not in a total wetting configuration. The behaviour observed for 5CB, 6CB, and 7CB is similar: The lower

<sup>18</sup>It is not clear yet if a divergence is expected nor if it is observable considering the emergence of structural defects.

<sup>19</sup>Close to the nematic / isotropic phase transition, a first order phase transition, the  $\lambda(\xi)$  relationship is modified significantly due to the divergence of the extrapolations lengths (see 2.2.5). To be relevant, comparisons of the  $\lambda(\xi)$  relationship for the different compounds must then be drawn at a given temperature interval from the phase transition.

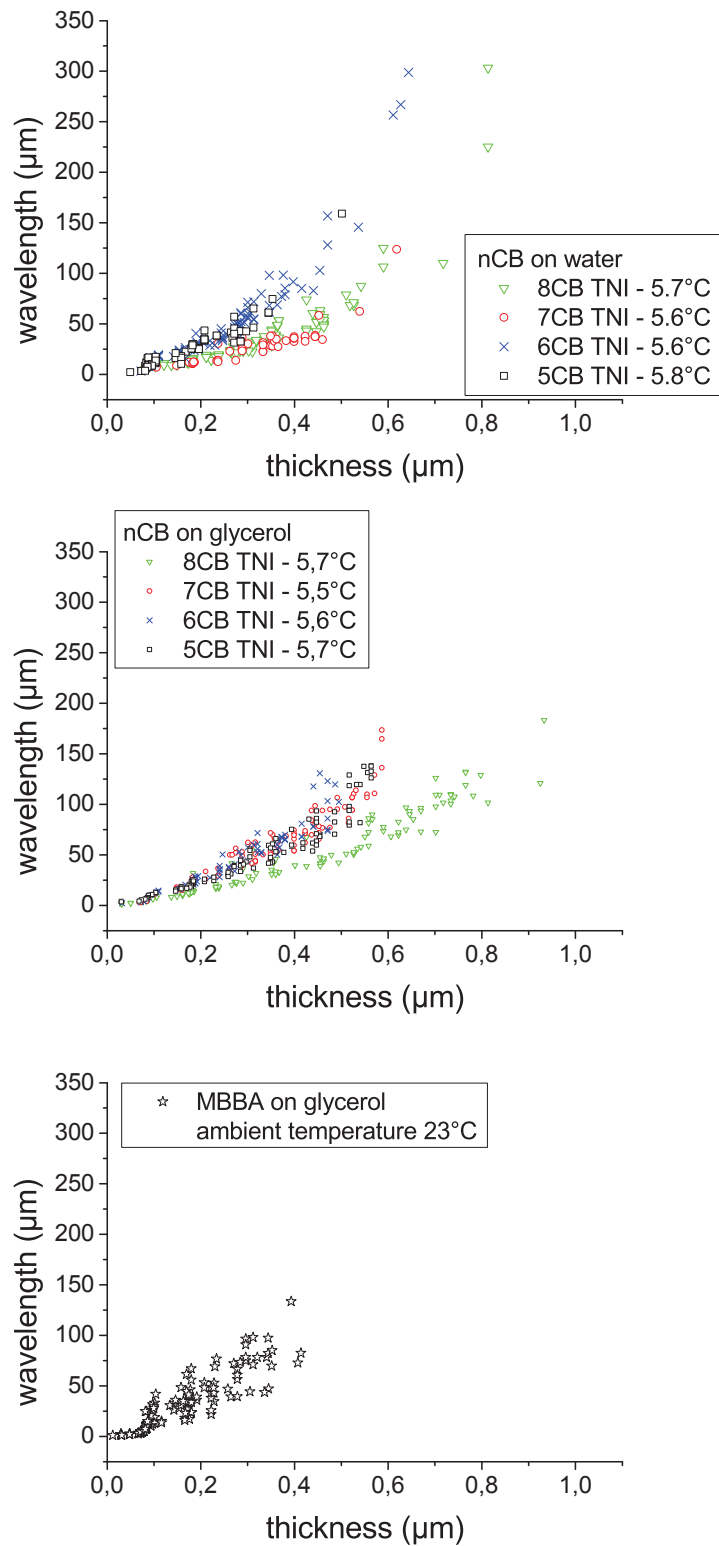


Figure 2.20: Characterization of the wavelength v.s. thickness relation far from the nematic /isotropic phase transition for striped patterns on water (top) and on glycerol (middle and bottom). For the nCB, to allow for comparison, the measurements are done at a given temperature interval from the nematic / isotropic phase transition. For MBBA, the measurements are done at ambient temperature and were not pushed towards thickest striped films.

boundary of the striped phase occurs for thicknesses corresponding to 20 – 40 nm and the upper boundary is marked out by a steep increase occurring for a thickness close to 0.6  $\mu\text{m}$ . The case of 8CB shows however a difference as the steep increase, characteristic of the upper boundary of the striped phase, occurs for larger thicknesses close to 0.8  $\mu\text{m}$ . 8CB is indeed the only of the four nCBs which presents a smectic phase. Its nematic range of temperature is as well relatively narrow. Being far from the NI transition ( $T_{NI} = 40.5^\circ\text{C}$ ) means for 8CB to be close to the smectic / nematic transition ( $T_{SmN} = 33.5^\circ\text{C}$ ). In the smectic range, 8CB films on water or glycerol do not show stripes, because the smectic elasticity differs from the nematic one: twist is not allowed. Far from the NI transition, post-transitional effects of the smectic / nematic transition still matter.

On glycerol, for the nCB family the behaviour is similar for 5CB, 6CB and 7CB as well as for MBBA (lower boundary of the striped phase only). The case of 8CB has again to be considered apart. The difference in this case with the other nCB is more important, as no steep increase could be observed at this temperature. The  $\lambda(\xi)$  relationship however recovers the steep increase for higher temperatures, far enough from the SmN transition. Once again, these temperatures are unfortunately too close to the NI transition to allow for comparison with the other nCBs. Furthermore, one must stress that although the diffusion of glycerol in the nematic films does not seem to affect the striped patterns as long as special precautions are taken (see the following of this Chapter and the Appendix about glycerol's tricks), the results obtained on glycerol must be considered as less robust than the ones obtained on water especially when glycerol is heated up.

**More complex patterns** Thin nematic films or domains show in fact other structures than parallel stripes. The other kind of patterns are observed usually on extended films (glycerol). One can define two categories: patterns made of a linear superposition of stripes (squares) and patterns due to non-linear terms in the development of the free energy (“chevrons”, ...).

Square patterns occur on flat zones. Their appearance indeed requires a degenerescence of the planar anchoring, which is not the case in zones showing gradients of thicknesses. Squares are an orthogonal superposition of stripes which wavelength is the same than the one of the stripes for a given thickness (see figure 2.21).

Examples of more complex patterns are presented on figure 2.22. Let us just mention that they mainly occur on thin zones of the films and that their structure reminds of the ones observed in Williams instability although the scale is once again different: the wavelength of the “entangled” stripes is of the same order of magnitude than the one of usual stripes, around one hundred times the thickness.

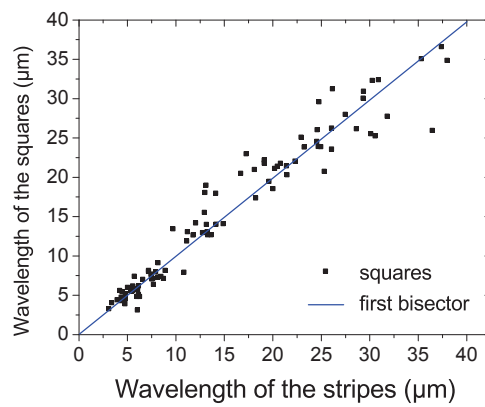
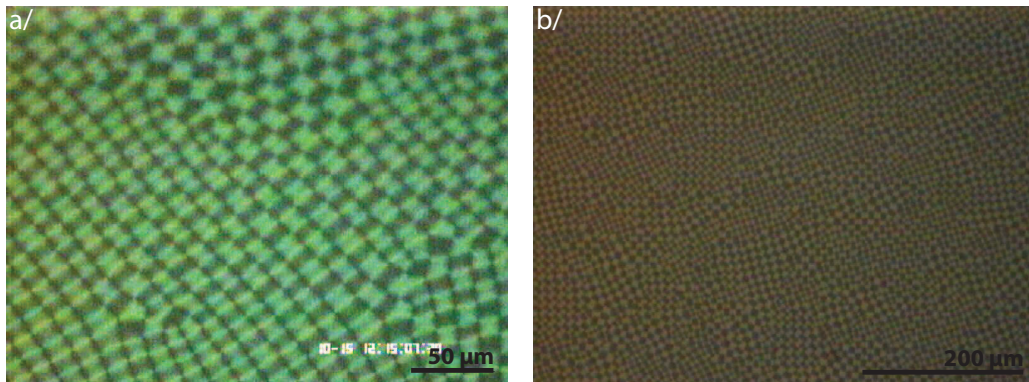


Figure 2.21: Top part: pictures of square patterns taken with an optical microscope. On the left, a/, 8CB on glycerol and on the right, thickness  $0.23 \mu\text{m}$  ; b/, 6CB on glycerol, thickness  $0.19 \mu\text{m}$ . Bottom part, comparison between the wavelength of stripes and squares for the same thickness of the nematic film. The comparison with the first bisector shows that there is a correspondence.

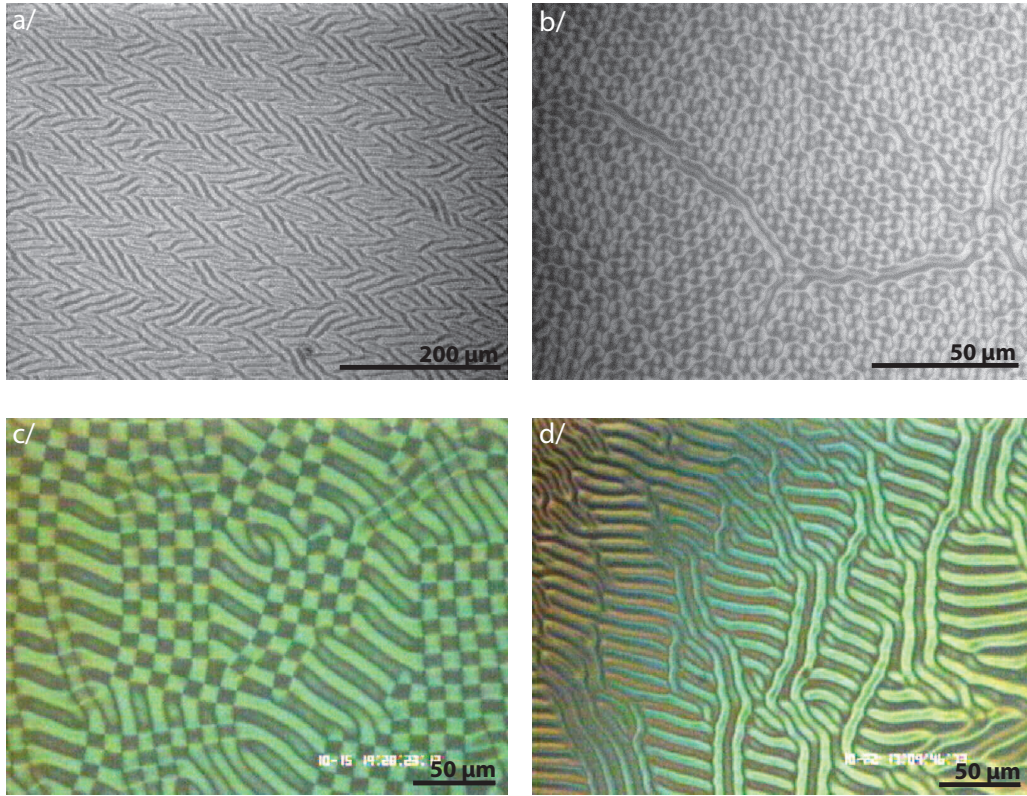


Figure 2.22: Examples of more complex patterns on glycerol. a/ 6CB ; b/, c/, d/ 8CB.

### 2.2.5 From nematic phase to liquid phase, a phase transition and a wetting transition - 6CB on water substrate -

The nematic / isotropic transition in bulk is a weak first order transition. Changing the scale, this transition has been studied in the case of thin films and droplets of liquid crystals deposited on a solid substrate [85], [82]. On the nematic side, a phase diagram representing the forbidden thickness zone in function of the temperature was built. The corresponding experiments are described in details in the two aforementioned references. Regarding thin films, 5CB in solution with a volatile solvent is deposited and spin-coated on a silicon wafer. The resulting thin nematic film presents two thicknesses as described above:  $\xi_{LB}$  and  $\xi_{UB}$ . These characteristic thicknesses increase when the temperature of the sample is set closer to the nematic / isotropic phase transition and finally merge at the temperature corresponding to the transition.

The measurements of the characteristic thicknesses,  $\xi_{LB}$  and  $\xi_{UB}$ , were done using two methods: Newton's colors and X-ray reflectivity. The resulting phase diagram is presented on figure 2.23. Along with the nematic isotropic transition occurs a wetting transition: while nematic

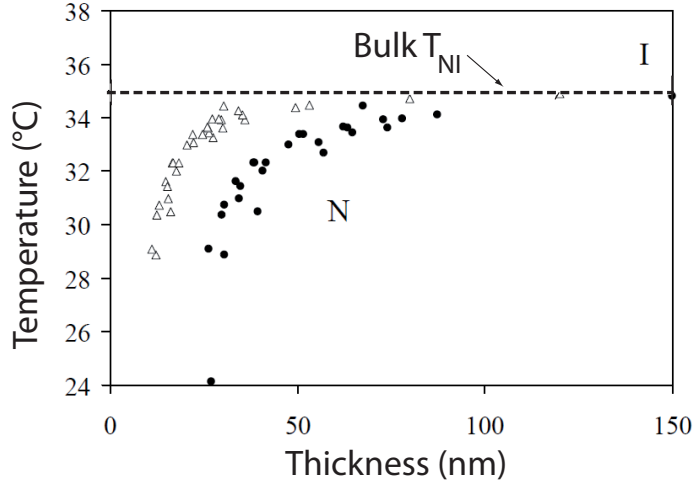


Figure 2.23: Figure taken from D. Van Effenterre’s PhD thesis [82]: Phase diagram for 5CB on silicon wafer. The thickness  $\xi_{LB}$  is represented by triangles and the thickness  $\xi_{UB}$  by squares. N stands for nematic phase and I for liquid isotropic phase.

5CB is in a total wetting configuration, isotropic 5CB is in partial wetting configuration. In isotropic phase, the evolution of the contact angle with the temperature was then measured. From these measurements, the spreading parameter<sup>20</sup>,  $S_{spreading} = \gamma(\cos\theta_C - 1)$ , was found to be proportional to the square root of the rescaled temperature,  $S_{spreading} \propto (T - T_{NI})^{\frac{1}{2}}$  (see figure 2.24). This suggests that an explanation can be found in the framework of the Landau - de Gennes theory [84].

In this section, the nematic / isotropic transition is studied for thin films deposited on a liquid substrate, i.e. water. The case of glycerol, showing qualitatively the same results is presented in a different section (2.2.5.3) because the relevance of the experiments is not ensured (glycerol molecules can diffuse in nematic liquid crystal layers and this diffusion is enhanced when the temperature is increased). The experiments were conducted with 6CB and 8CB which wet easily water even if they are not extra-pure and are known for their stability in temperature (see [24]). 6CB has the advantage of possessing no smectic phase: unlike 8CB, there are no post-transitional effects due to the smectic / nematic phase transition while the samples are in the nematic range of temperature. On the nematic side of the phase transition, modifications in the shape and stripe patterns of nematic pancakes are investigated as well as the thickening of molecular layers. The nematic / isotropic transition is once again accompanied by a wetting transition: isotropic liquid crystals dewet and contact angles of the isotropic droplets are measured. These results are compared to the ones previously obtained on silicon wafers.

<sup>20</sup>To avoid ambiguity with the order parameter of the phase transition, the spreading parameter is referred to as  $S_{spreading}$

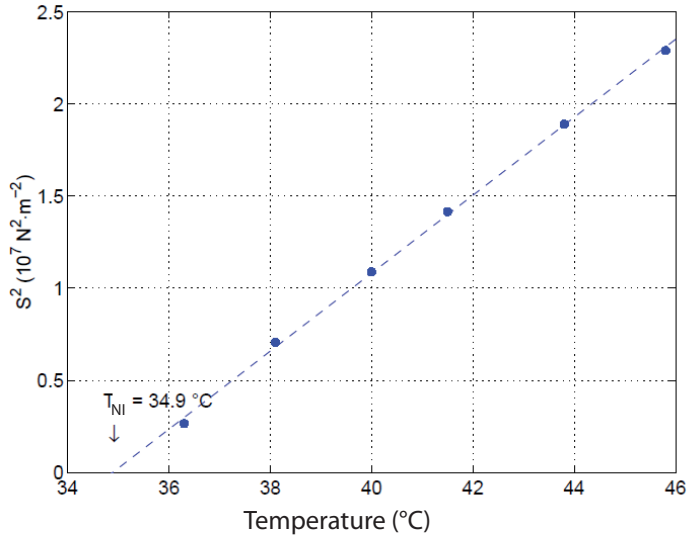


Figure 2.24: Figure taken from F. Vandenbrouck's PhD thesis [85]: From the measurements of contact angles of isotropic *5CB* droplets on silicon wafer, the dependence of the spreading parameter was found to be proportional to the square root of the rescaled temperature, i.e.  $S \propto (T - T_{NI})^{\frac{1}{2}}$ .

### 2.2.5.1 On the nematic side: pre-transitional effects

On the nematic side, close to the nematic / isotropic (NI) phase transition, the characteristics of the thin nematic films are modified by pre-transitional effects. Modifications occur on:

- The striped domains (thickness above  $\xi_{UB}$ ). The relationship between the thickness of the domains and the wavelength of the stripes is modified. It is also more difficult to obtain thick striped domains when the volume of deposited liquid crystal is increased.
- The molecular films. The nature of the films showing no stripe patterns (thickness below  $\xi_{LB}$ ) is modified: far from the NI transition, they were molecular films, i.e. monolayer and trilayer; close to the NI transition their thickness increases.

For striped domains, both their internal structure (stripes) and rim have been studied. The stripe patterns indeed show an evolution close to the NI phase transition. The relationship between the wavelength and the thickness is modified as follows: For a given thickness, the wavelength of the corresponding stripes is greater close to the NI transition than it was in the nematic range (see figure 2.25)<sup>21</sup>. This modification can be related to a known phenomenon: close to the NI transition, the extrapolation length of an interface,  $L_i = \frac{K}{W_i}$ , diverges. In the case of our liquid crystal films, two interfaces are to be considered and then, close to the NI transition,

<sup>21</sup>The evolution of the relationship between the wavelength of the stripes and the thickness of the films on glycerol substrates shows the same tendency. For further details, see the following of this Chapter



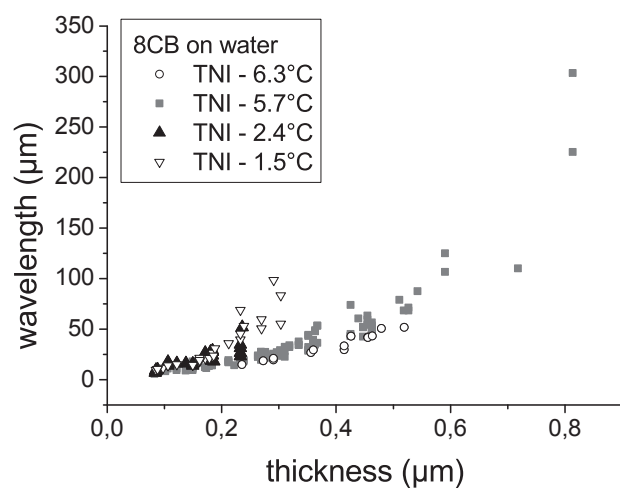
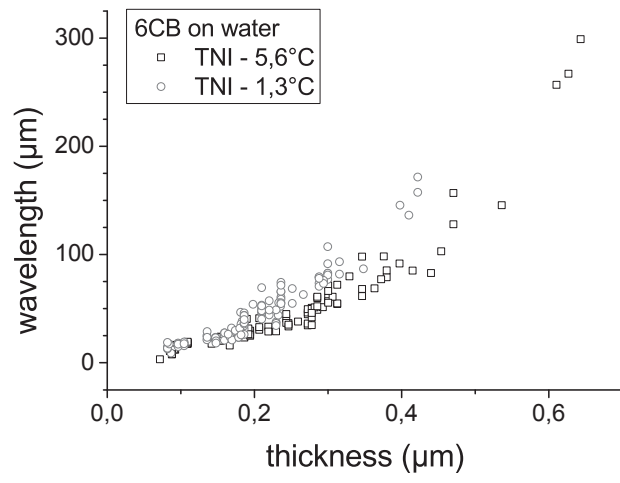


Figure 2.25: Evolution in temperature of the relation wavelength/thickness when getting closer to the nematic-isotropic transition.

two diverging extrapolation lengths. The relevant combination of these two extrapolation lengths in our case is not easy to determine. Moreover, no measurements of the anchoring energies for the interface nCB / water and nCB / air versus temperature are available in the literature although it is likely that the anchoring energies should decrease when getting close to the NI transition temperature. Theories indeed predict the decrease of the anchoring energies versus temperature and it was verified in the case of solid substrates [25]. Furthermore, the variation in temperature of surface-like elastic constants is also poorly known. Attempts of comparison of our data with the sole variation of the bulk elastic constants in temperature were performed but led to no convincing results (see figure 2.6 for details of the variation of the elastic constants of the liquid crystals that we used).

Another question about striped domains arises when the temperature is increased close to the NI transition as it becomes more difficult to obtain samples that wet the substrate. When a sample is prepared, a known quantity of liquid crystal in solution with hexane is deposited on the liquid substrate. Controlling the quantity deposited allows for the control of the thickness of the liquid crystal film. Using this method to create nematic films at a temperature close to the NI transition often leads to dewetting of the film for large quantities of deposited liquid crystals. It is then easy to obtain thin striped domains close to the NI transition whereas it is very difficult to obtain striped domains thicker than  $0.25 \mu m$ . The same phenomenon is observed when samples are deposited well-below the NI transition temperature and then heated up close to the NI transition temperature. The increasing lack of stability of thick striped domains still needs to be understood. Once again, the pertinence of any theoretical description of striped domains is limited by the large number of poorly known parameters. To obtain robust data, accumulating experiments was then even more crucial.

As the stripe patterns are strongly affected when approaching the NI transition, the question of an evolution of their planar rim with temperature can be asked. Observations under polarized optical microscope first allow one to check that coming close to the NI transition, the rims of the domains still are in a planar configuration. The width of the rim was also measured and compared to the wavelength of the corresponding stripes. The results are presented on figure 2.26. Although the data are scattered, the ratio between the rim's width and the wavelength is independent of the temperature.

To complete this observation, the molecular films coexisting with striped domains have been considered. Approaching the NI phase transition, the thickness  $\xi_{LB}$  increases like on silicon wafers (see figure 2.23). Thickness' measurements were performed together with Y.Y. Cheung Sang (for further details, see [11]). For example, for a temperature  $0.5^\circ C$  below the NI transition temperature, the thickness  $\xi_{LB}$  is found to be  $61 \pm 15 nm$  whereas in nematic range,  $\xi_{LB}$  corresponds to the thickness of the trilayer of 6CB, which is around  $3.5 nm$ . It is worth noting that the increase of  $\xi_{LB}$  close to the NI transition should have direct consequences on the boundary tension of the striped domains. The boundary tension is not anymore the one of a striped domain surrounded by a trilayer ; it is now the boundary tension of a striped domain surrounded by

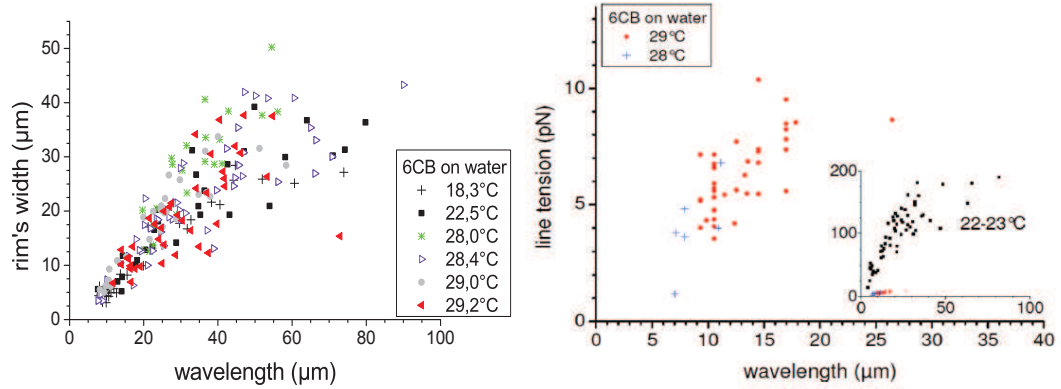


Figure 2.26: On the left side, the rim's width of striped domains of 6CB on water versus the wavelength of the corresponding stripes. Although the data are scattered, one may exclude a strong influence of the temperature. On the right side, boundary tension measurements by Y.Y. Cheung Sang for 6CB on water close to the NI transition and comparison with results far from the NI transition (inset) (measurements by U. Delabre).

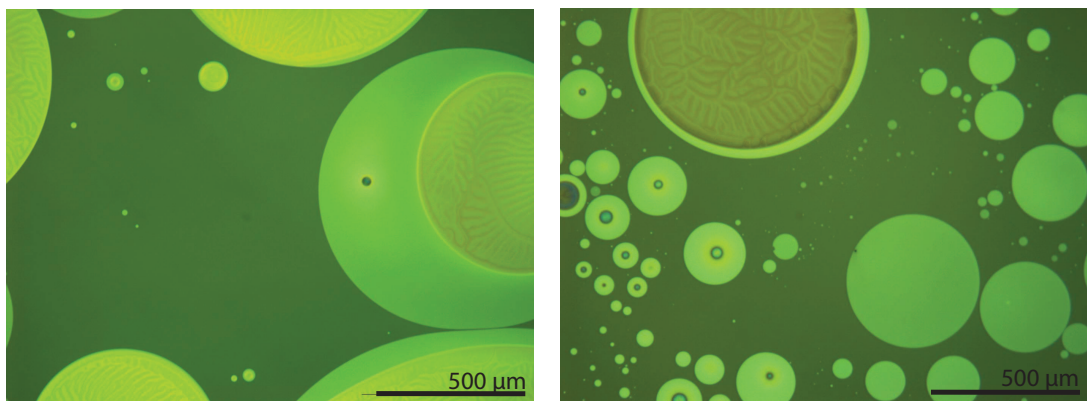


Figure 2.27: 6CB close to the nematic / isotropic transition, 29°C. Thickness of the striped domains: left side 0.09 μm ; right side 0.16 μm

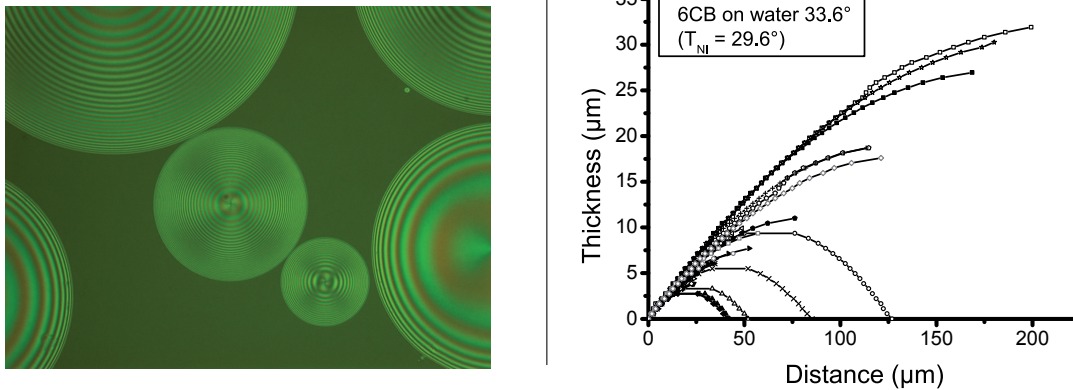


Figure 2.28: 6CB droplets on water in isotropic phase. On the left, picture of the droplets,  $31.3^{\circ}\text{C}$  optical microscope  $\times 20$ . On the right, example of the profiles obtained  $4^{\circ}\text{C}$  after the transition.

a much thicker film. To quantify this effect, boundary tension measurements close to the NI transition were performed by Y. Y. Cheung Sang (see figure 2.26). The boundary tension clearly drops down when the NI transition is close. Considering the boundary tension model used for a planar rim of width  $\frac{\lambda}{2}$ , one finds  $\tau(\xi) \approx \lambda \frac{W_H}{4}$  (see [19] for further details). The difference between data far and close to the NI transition can be explained by a decreasing value of the anchoring energy of the air interface,  $W_H$ . The decrease of  $W_H$  was already mentioned in the case of a solid substrate (see above and [25]).

### 2.2.5.2 On the isotropic side: dewetting

On the isotropic side, 6CB dewets and forms spherically-shaped droplets. A wetting transition occurs. To characterize it, the evolution of the contact angle of the droplets was measured in order to find the dependence in temperature of the spreading parameter  $S_{spreading}$  which plays, for a wetting transition, a role analogous to the one of the order parameter for a phase transition. To perform the measurements, interferometry was used (see the appendix about contact angle measurements). The droplets were imaged by monochromatic green light,  $550\text{ nm}$ , under microscope and the contact angle was measured from the profiles. To calculate the profiles of the droplets from interferometry data, it was necessary to know the value of the optical index of the liquid crystal in isotropic phase at given temperatures. The optical index was thus measured using a refractometer<sup>22</sup>. The results of the measurements for 6CB ( $T_{NI} = 29.6^{\circ}\text{C}$ ) in isotropic phase are:

<sup>22</sup>In a refractometer, some liquid is placed onto a prism of known optical index. After the liquid / prism interface, there is a lighted zone and a dark zone. The frontier between the two zones corresponds to the critical angle, i.e. the angle of incidence above which total internal reflection occurs. Localizing the frontier then allows for the calculation of the optical index using Snell-Descartes law.

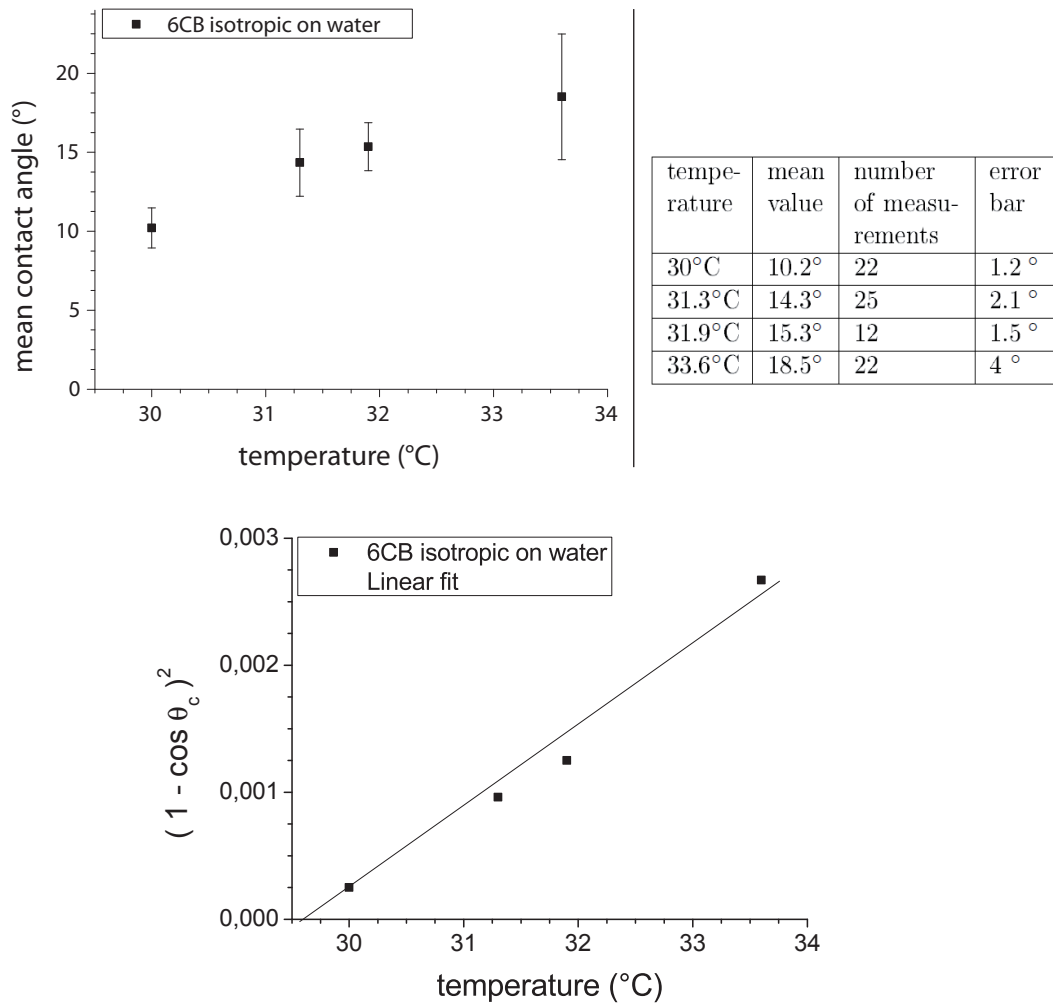


Figure 2.29: 6CB, liquid isotropic phase on water. On the left side, mean contact angles in function of the temperature. On the right side, details corresponding to the measurements. The errors bars reflect the scattering of the data. On the bottom,  $(1 - \cos \theta_C)^2$  in function of the temperature.

temperature (°C)	optical index
30	1.5820
31	1.5815
32	1.5810
33	1.5805
34	1.5800
35	1.5795
36	1.5793
37	1.5790

Once the optical index of the liquid crystal in isotropic phase was determined, the contact angle measurements were repeated on several droplets in order to calculate the mean value of the contact angle for a given temperature. Examples of the profiles obtained are presented in figure 2.28. The error bars represented on figure 2.28 reflect the scattering of the measurements. Because of the scattering of the measured contact angle values, accumulating data is required to obtain reliable contact angle values and spreading parameter dependence. For example, if the square of the spreading parameter is concerned,  $S_{spreading}^2$ , a small variation of the contact angle provides a large relative change as  $\frac{\delta S_{spreading}^2}{S_p^2} = \frac{2\delta\theta_C}{tg(\frac{\theta_C}{2})}$  and the measured contact angles are small. We repeated the measurements until the average values provide a smooth  $\theta_C(T)$  dependence, (see figure 2.29). From these mean values, the spreading parameter is calculated. As in the experiments done on solid substrates ([85], [82]), the spreading parameter dependence in temperature is compatible with (see figure 2.29):

$$S_{spreading} = \gamma(\cos\theta_C - 1) \propto (T - T_W)^{\frac{1}{2}} \quad (2.18)$$

where  $T_W$ , the wetting transition temperature, is compatible with the measured phase transition temperature for the film,  $T_{NI} = 29,6^\circ$ .

Critical parameters of the experiments were the temperature, as mentioned in the last paragraph, and the purity of the liquid crystals. The influence of the purity of the liquids crystals was tested with the following process: First, measurements were performed on a sample made with pure water and liquid crystal from a brand new bottle (purity, 99%, purchased from Frinton Laboratories), *a/* ; Second, measurements were performed on a sample made with pure water and liquid crystal from a bottle already opened and kept refrigerated in a closed container with desiccant to minimize contaminations, *b/*. The results are presented on figure 2.30. Although the wetting transition temperature does not change much:  $29,6^\circ C$  for *a/* and  $29,4^\circ C$  for *b/*, the contact angle for sample *a/* increases much less with temperature than for sample *b/*. For  $T - T^* \approx 4^\circ C$ ,  $\theta_C$  is around  $19^\circ$  for sample *a/*, but may reach  $33^\circ$  for sample *b/*. Such a change due to impurities was not observed in the case of the experiments done on a solid substrate. The reason is that the drops formed from nematic films on a heated liquid substrate are more

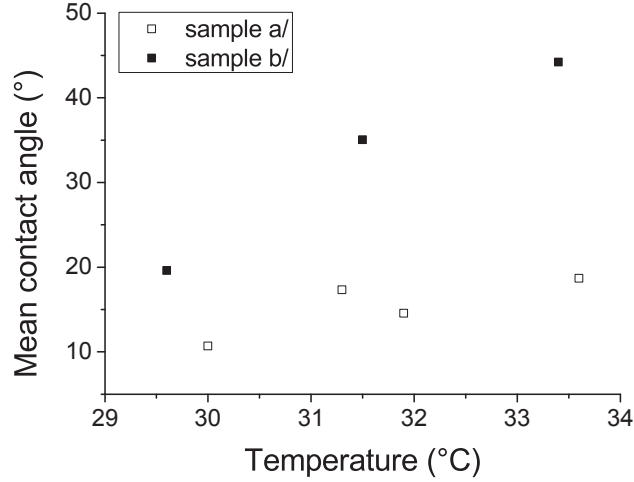


Figure 2.30: Illustration of the effect of impurities on the contact angle in isotropic phase. Two samples of 6CB are compared: sample *a/*, made with pure water and liquid crystal from a brand new bottle (purity, 99%, purchased from Frinton Laboratories) ; sample *b/*, made with pure water and liquid crystal from a bottle already opened and kept refrigerated in a closed container with desiccant to minimize contaminations. Measured contact angles for sample *b/* are much larger than for sample *a/*

sensitive to impurities than the microdrops deposited on silicon wafer. The total amount of impurities, which is proportional to the drop volume, is indeed small for the microdrops but is much larger with deposited films. These impurities are surface-active, that is why surface tensions of nCBs in the literature are scattered. For example, the values found for 5CB go from  $\gamma_{5CB} = 40 \times 10^{-3} Nm^{-1}$  [61] to  $\gamma_{5CB} = 28 \times 10^{-3} Nm^{-1}$  [33], [38], [37]. The consequence on contact angles is dramatic, especially on a water substrate<sup>23</sup>. The results presented in figure 2.29 come only from samples of the *a/* type. The fact that the measured temperature of the phase transition is  $29.6^\circ C$ , which is larger than the value of  $29^\circ C$  commonly found in literature reflects the high purity of the samples.

### 2.2.5.3 Diffusion of glycerol molecules and characterization of striped patterns on glycerol coming close to the NI transition

Glycerol was used as an alternative liquid substrate for liquid crystal films. As water, glycerol is a polar liquid, with relatively high surface tension but lower than the one of water. Considering the experiment:

- the liquid crystal's anchoring on a glycerol surface is planar, as for water ;

<sup>23</sup>In the present case, the angle increases for pure compounds which means that impurities preferentially go to the water / air interface after the liquid crystal is put on the water surface.

- glycerol's refractive index is smaller than the refractive indices of the liquid crystals (1.47 at 20°C) whereas the ordinary (smaller) index is around 1.52 for the liquid crystals which were used.

Therefore, the experimental conditions are *a priori* close to the ones on water substrates. Glycerol's viscosity (see [14]) is greater than that of water which is an advantage as it reduces hydrodynamic motions at the interface in the subphase, noticeably convection when the samples were heated<sup>24</sup>. Although glycerol substrates seem to be of simple use, one has to be aware of some difficulties.

First it is well known that glycerol is very hygroscopic, therefore a free surface adsorbs atmospheric water. As glycerol is a strongly associated liquid, the structural changes induced by water adsorption are expected to be significant. Second, while the problem of adsorption of water in glycerol is well-recognized, another question arose during experiments.

### Diffusion of glycerol molecules in liquid crystal layers

**Introduction** It was first shown by Nazarenkov et al. [49] and further studied by Smalyukh et al. [72] and Nych et al. [52] that it is possible to trap colloidal particles of glycerol in HAN layers (30 – 100  $\mu m$ ). The trapped glycerol particles are stabilized at the nematic liquid crystal / air interface by elastic-capillary interactions. Their presence induces distortions of the nematic director of the dipole type. Depending on the orientation of the elastic dipole created, the glycerol particles organize themselves with different degrees of order. They can form 2D crystalline lattices or order themselves as 2D hard spheres. In these studies, the glycerol particles were trapped in the nematic layers, which illustrates the ability of glycerol's molecules to penetrate into our liquid crystals and diffuse inside the films. Nematic layers of 5CB were deposited on a glycerol surface. The samples were then heated up to 50°C to enhance the diffusion of the glycerol molecules in the HAN layer and then cooled down to trigger the condensation of glycerol droplets. Some of these droplets stayed trapped in the HAN layer. The size and number of the droplets could be tuned by temperature conditions. Knowing about this experiment, the possible, and in our case unwanted, diffusion of glycerol molecules in our liquid crystal films comes as a natural concern. The case of HAN, striped and molecular films is somewhat different.

**Diffusion in thin layers: importance of the thickness of the film and of the length of the liquid crystal molecule** Before going any further, one should remember that striped films are thinner than the HAN films studied in the experiments presented in [49], [72] and [52]. The maximum thickness for a striped film was measured around 0.8 $\mu m$  (for 8CB) whereas the HAN layers in the experiments involving colloids of glycerol are in the range 30 – 100  $\mu m$ .

---

<sup>24</sup>However, viscosity is not the most critical parameter concerning the appearance of convection motion. The convection threshold depends indeed linearly on viscosity whereas it depends on the thickness of the liquid layer at the power 3. That is why, to avoid any convection, the thickness of the subphase layer, water or glycerol, was simply decreased when the samples were heated.



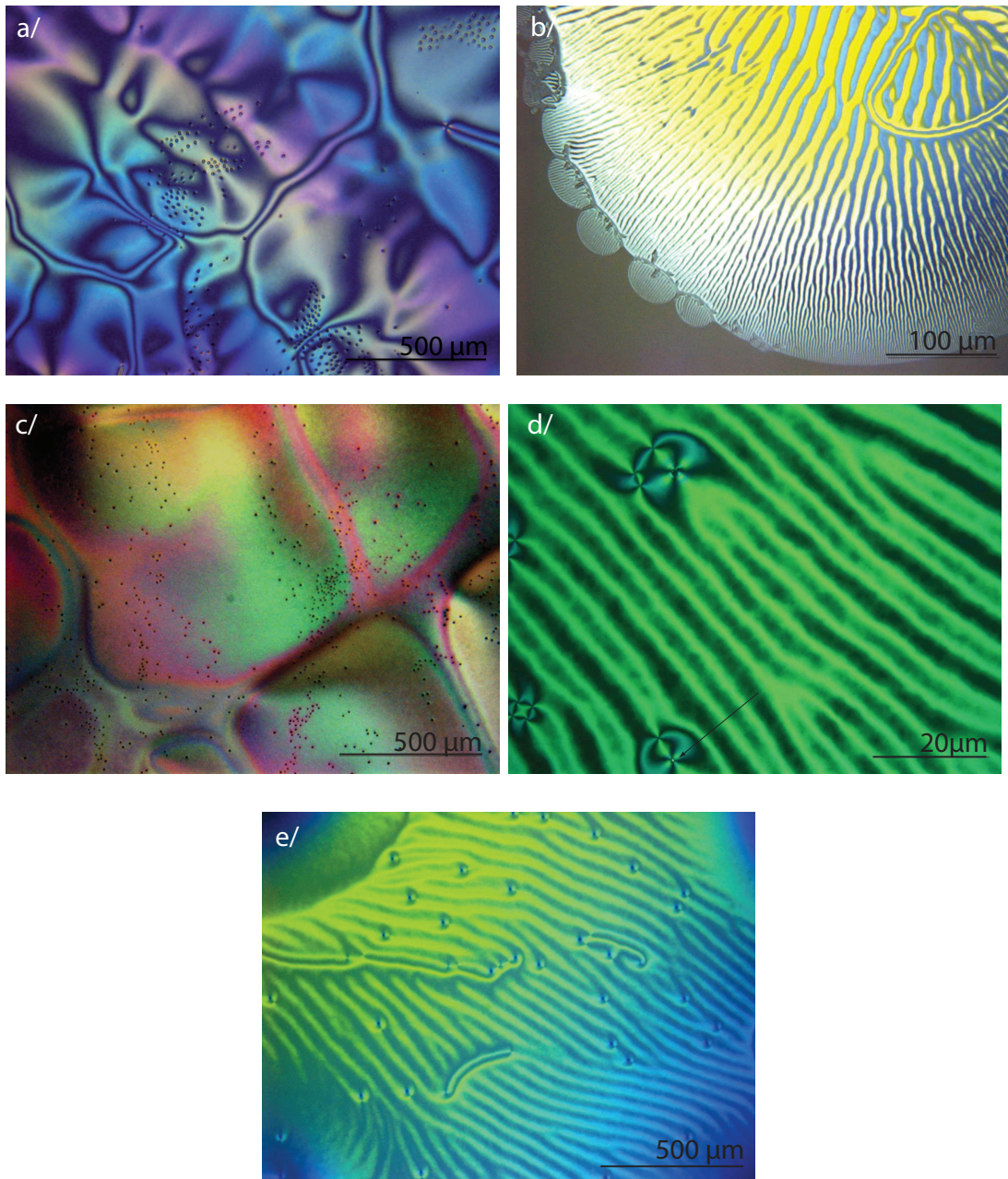


Figure 2.31: Microscope images of films of liquid crystals which were heated. a/ HAN layer of 5CB ; b/ striped layers of 6CB ; c/ and d/ HAN and striped layers of 8CB (striped layers are thinner than HAN layers) and e/ striped layer of MBBA. For *nCB*s, glycerol droplets appear clearly in macroscopic layers (see a/and c/). On the other hand, no glycerol droplets are seen in the thinnest zones of the striped films (see b/) and some droplets in the thickest zones of the striped films (see d/). The longer is the *nCB* molecule, the less glycerol droplets are observed in striped films. In the case of MBBA, glycerol droplets are present in substantial number even in striped films (see e/).

Between these two kind of films, there is a difference in thickness, but also in structure (see Chapter 2). These two parameters could change the ability of the nematic to trap glycerol droplets.

Experiments were performed by heating nematic layers of *5CB*, *6CB*, *8CB* and MBBA until the whole samples were isotropic and then letting them cool down to the initial nematic temperature. This process was repeated for both HAN layers and striped layers. Pictures showing the final stage of some experiments are presented in figure 2.31. Concerning HAN layers, glycerol droplets appeared for all the tested liquid crystals. For striped layers, one has to distinguish the case of MBBA from the case of *nCB*s. First, for the *nCB* series, no glycerol droplets are observed in the thinnest parts of the striped films. For increasing thicknesses of the striped layer, an increasing number of droplets appear. The number and the size of these droplets depend on the length of the *nCB* molecule. The longer is the *nCB* molecule, the less glycerol droplets are observed. For example, very few droplets of glycerol are observed in *8CB*. The few droplets which are inserted in the film are also very small (see figure 2.31, image d/ for an example). Let us now change the experiment and heat the samples only in the nematic range (below the nematic-isotropic transition). In that case, no glycerol droplets are observed in *8CB* samples. There is then an important difference in the diffusion of glycerol depending on the heating temperature. On the other hand, for MBBA, glycerol droplets were always observed in striped layers whether the samples were heated until they reached the isotropic phase or only heated in the nematic range. The diffusion and stabilization of glycerol droplets in MBBA layers is then stronger than for the *nCB* family. Plausible explanations for the common trends are that:

- droplets can be formed only if the film is thick enough;
- the affinity of glycerol for the *nCB*s decreases if the length of the aliphatic tail is increased;
- glycerol has probably a larger affinity for MBBA than for the *nCB* series. We were not able to find solubility data to support these assumptions.

These observations lead to several conclusions. The first one is that glycerol molecules diffuse easily inside our *nCB*. Even if glycerol droplets are not observed, this diffusion may play a role in the behavior of liquid crystal films. In practice, as diffusion is a slow process, any experiment on a glycerol substrate must be done in a limited time, i.e. less than half of an hour at room temperature. When samples are heated up, the allowed time decreases. However, it is clear that the presence of glycerol droplets in the striped films does not destabilize the striped patterns on a long range: glycerol droplets create punctual defects that do not change the stripes. That is why the characterization of the striped patterns on glycerol was possible and the results reproducible.

**Characterization of striped patterns on glycerol substrates in function of the temperature** As well as for water substrates, the characterization of striped patterns when approaching the nematic / isotropic (NI) transition was done. Because of the possible diffusion of

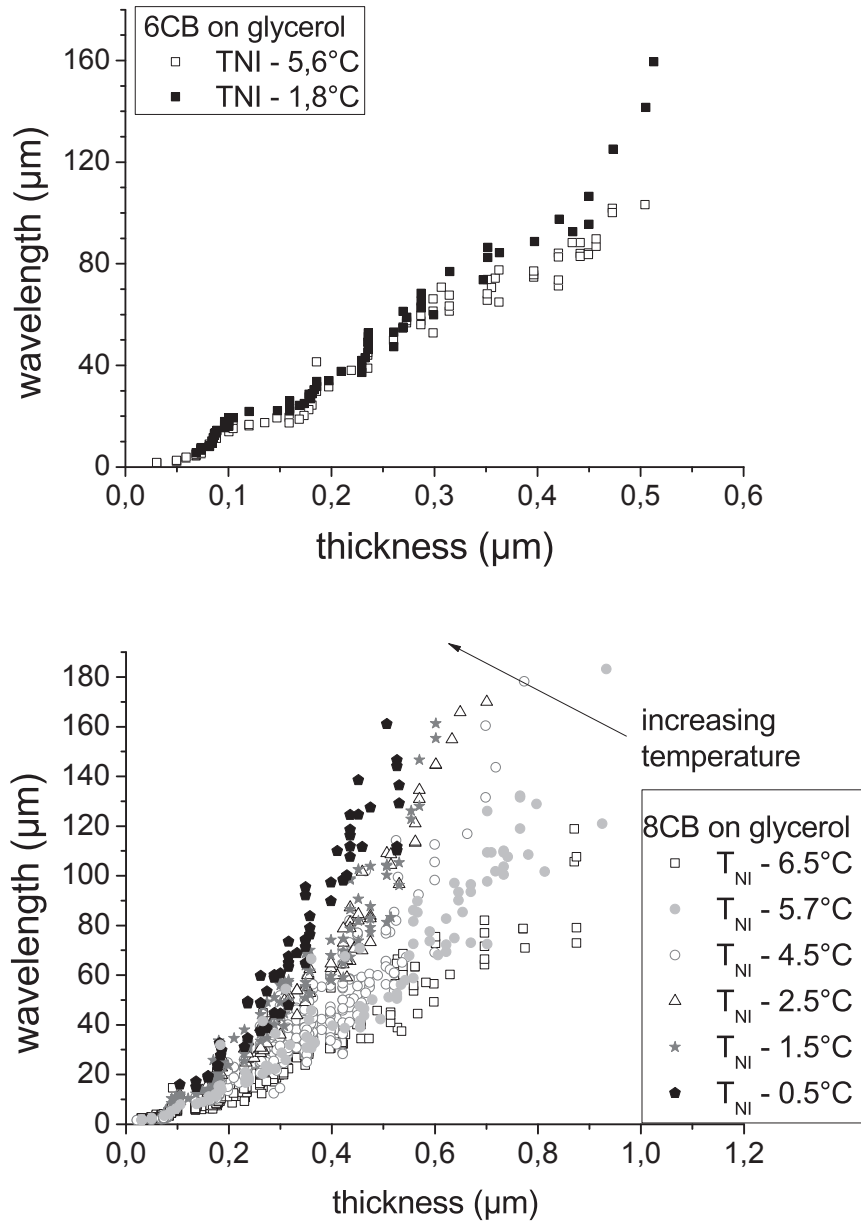


Figure 2.32: Wavelength of the stripes versus thickness of the nematic film for 6CB and 8CB on glycerol coming close to the NI phase transition.

glycerol molecules inside the nematic films, these results are presented apart although they show the same trend than the results on water substrates (see figure 2.32). For a given thickness, at a temperature close to the NI transition the wavelength of the stripes is indeed larger than the one obtained for a temperature in the nematic range. The maximum thickness of the film showing stripes is also shifted towards small values when the temperature increases (see data of 8CB on glycerol). However, from a purely experimental point of view, it was much easier to obtain data on heated glycerol than on heated water substrates: no dewetting problems occurred on glycerol substrates for thick striped films close to the temperature of the NI transition. The fact that the data for glycerol substrates show the same trends than the data for water substrates although no wetting problem occurred close to the NI transition is then a clear confirmation that the trends observed are quite robust. It is also possible once again to conclude that striped nematic films of nCBs heated not above the nematic range do not show perturbations due to the diffusion of glycerol molecules.

In contrast, what happens with the thinnest films, monolayer and trilayer, where glycerol molecules may penetrate, therefore significantly changing the film structure, is a real concern, and not yet understood. The appendix about glycerol and Langmuir isotherms experiments is an illustration of this problem.

#### 2.2.5.4 Conclusion

The specificity of the problem is the presence of (1) a free interface but also (2) the possibility of stripe's formation.

In simple cases, coexistence is studied by writing the free enthalpy of a system as a function of a relevant variable. A common-tangent construction defines the coexisting phases. Here, the free energy must be written as a function of the film thickness. Even if the role of metastability on liquid substrates is ignored, two types of difficulties are met:

- A continuous analysis is relevant close to the NI transition, but not for the thinnest films far from the transition. Writing an analytical expression of the free energy valid in the whole range of thickness, and therefore allowing a common-tangent construction, is merely impossible.
- For the thicker films, where a continuous analysis is valid, the free energy is considerably reduced if stripes are present. The coexistence condition is strongly modified.

Let us first comment about the continuous description of a homogeneous film without stripes. In the framework of the Landau / de Gennes analysis [69], the free energy density is an expansion in powers of the order parameter and its spatial derivatives. In the simple case where  $S(\vec{r})$  is uniform, the spatial derivatives reduce to the usual nematic elasticity, Eqs. (5.6). The Frank elastic constants scale as  $S^2$ . If surface elasticity is ignored, and considering that the anchoring energy can be expressed as a function of  $S$  ([12], [92]), then the free energy depends only on  $S$  and  $\xi$ . A first minimization with respect to  $S$  at given  $\xi$  gives a function of  $\xi$  alone, then a

common tangent construction provides the equilibrium thicknesses  $\xi_{LB}$  and  $\xi_{UB}$ . This is the procedure used in [81] to account for the forbidden range of thickness observed with 5CB films on oxidized silicon wafers [80]. Instead of an explicit dependence of anchoring energies with  $S$ , the hypothesis of strong anchorings, that is  $\theta_H = 0$ ,  $\theta_P = \frac{\pi}{2}$ , independent of  $\xi$ , is used.

The procedure [81] is interesting, as it accounts qualitatively for the trend  $\xi_{LB}$ ,  $\xi_{UB} \approx (|\Delta T|)^{-1/2}$  [80], where  $\Delta T = T - T_{NI}$  is the negative distance to the transition temperature. It should be improved by considering more plausible values for the anchorings, which in actual fact are not strong. However, the main question deals with the possible presence of short-wavelength stripes<sup>25</sup> in the  $\xi_{UB}$  film ([57], [42], [40]), which would radically change the value of the free energy. As these stripes have never been observed on wafers, the question was merely not raised till more recently the similarity of global behaviors on wafers and liquid substrates became obvious.

We shall now present in a simple way, that is, easily related to experimental observations, the procedures used to describe stripe patterns. Only films with thickness  $\xi \geq \xi_{UB}$  are considered, therefore a continuous description is acceptable, except possibly for the thinnest films far from the NI transition ( $\xi \cong \xi_{UB} \approx 20 - 30$  nm). We include the possibility of adding azimuthal anchoring in the free energy, that is, preferred values for the azimuthal angles  $\phi_H$  and  $\phi_P$ , associated to azimuthal anchoring energies.

## 2.2.6 Existing models of striped patterns far from the NI transition

Pioneering works are due to Lavrentovich and Pergamenschchik (LP) ([41], [57], [42], [40]) and Sparavigna and coworkers ([74], [75]) twenty years ago. At that time their theoretical predictions were compared with an experimental study of 5CB films on a glycerol substrate, far from the NI transition. Later on, theoretical studies of the stability of liquid crystals films developed more sophisticated mathematical and numerical tools ([6], [86], [39], [13]). Evolved discussions on anchoring conditions, nematic elasticity and surface viscosity are still a very active field of research ([27], [28], [22], [60], [70], [1], [59], [7], [44], [64], [8], [4]). For the experimentalist, the difficulty comes from the large number of poorly-known parameters, as anchoring energies and surface elastic constants. Moreover, experiments are easier far from the transition, while the continuous approach is better close to it. This requires being very careful when checking experiments against theoretical predictions. Accumulating experimental data helps to define robust results.

It is therefore useful to discuss data in reference to the simplest “reference” models.

**The model by Lavrentovich and Pergamenschchik** The LP model ([41], [57], [42], [40]) is a linear perturbation of the HAN state for a given thickness  $\xi$ . As previously discussed, the

---

<sup>25</sup>On silicon wafers, the planar anchoring is weaker than the homeotropic one at the free interface. In that case, stripes are predicted, but with a short wavelength, of the order of the film thickness, therefore hardly observable (see later)

HAN state corresponds to a planar-non-degenerate anchoring parallel to  $x$  on the substrate and homeotropic at the free interface, the only variable is  $z$  (see figures 2.8 and 2.10). The azimuthal angle  $\phi(z)$  is zero for any  $z$ . The polar angle  $\theta(z)$  obeys:

$$\theta(z) = \theta(0) + z \cdot \frac{\theta(z) - \theta(0)}{\xi} \quad (2.19)$$

The values  $\theta(0)$  and  $\theta(\xi)$  are obtained by minimization of the free energy of the HAN state at given  $\xi$ . Linear perturbations  $\delta\theta(z, y)$  and  $\delta\phi(z, y)$  are considered. Stripes are periodic solutions with respect to  $y$ . Long wavelengths correspond to  $\chi = \frac{2\pi\xi}{\lambda} \ll 1$ , which allows specific approximations. This is achieved for intermediate thicknesses, where  $\chi$  is almost constant and much smaller than 1. Typical values are around 0.05, both on water and glycerol, which validates the approximation  $\chi \ll 1$  (see figure 2.33).

As the HAN structure is the base state for the linear perturbation, the threshold thickness  $\xi_C$  [3] is the lower threshold (HAN-Planar) for the stripes. A more evolved base state is obtained by considering the surface term  $K_{13}$  ([42]) ( $K_{24}$  does not play due to the translational invariance along  $x$ ), in which case the lower threshold thickness is larger than  $\xi_C$ .

The LP model is quite efficient for thicknesses between 0.15 and 0.5  $\mu\text{m}$  typically. Experimental  $\lambda(\xi)$  values are well accounted for, and the model is not too sensitive to the precise values of the elastic constants and anchoring energies. This is a requirement considering that the present experiments are not restricted to the initial 5CB / glycerol system, as similar results are obtained for the other nCB, and both on glycerol and on water.

An apparent weakness of the LP model is that experimental values of  $\delta\theta(z, y)$  and  $\delta\phi(z, y)$  are not small. Noticeably,  $\delta\phi(z, y)$  amounts  $\pm\frac{\pi}{4}$ . It is not surprising that more complex patterns, requiring a non-linear analysis, are frequently observed. This behavior is reminiscent of the “chevron-like” and “zig-zag” structures in convective Williams instabilities [15]. However, like in the case of Williams domains, the linear analysis provides correct values for the wavelength of the fundamental pattern.

The actual difficulty of the model deals with the threshold values  $\xi_{UB}$  and  $D$  (upper threshold of the striped phase or Periodically Hybrid Aligned Nematics (PHAN)). As stripes are experimentally observed for  $\xi \geq \xi_{UB}$ , then  $\xi_{UB} \geq \xi_C$ . However, typical  $\xi_C$  values far from  $T_{NI}$  are around 0.2 – 0.3  $\mu\text{m}$  for all our systems, while  $\xi_{UB}$  is ten times less (20.30 nm). Considering  $D$ , the LP model is critically sensitive to the value of  $K_{13}/K_{11}$ , which is not plausible.

**The model by Sparavigna and coworkers** Another approach has been proposed by Sparavigna et al. [75] in the simple case  $K_{11} = K_{22} = K_{33}$ ,  $K_{13} = 0$ , and later on refined numerically by Krzyzanski [39] with the proper elastic constants values for 5CB, that is,  $K_{33} \approx 1.3K_{11}$ ,  $K_{22} \approx 0.5K_{11}$ ,  $K_{13} = 0$ . We shall briefly comment about the analysis of the lower threshold  $\xi_{UB}$ . In contrast with the LP model, where the lower threshold is a transition between a planar state and the HAN state [3], here the threshold is supposed to be a transition between a planar

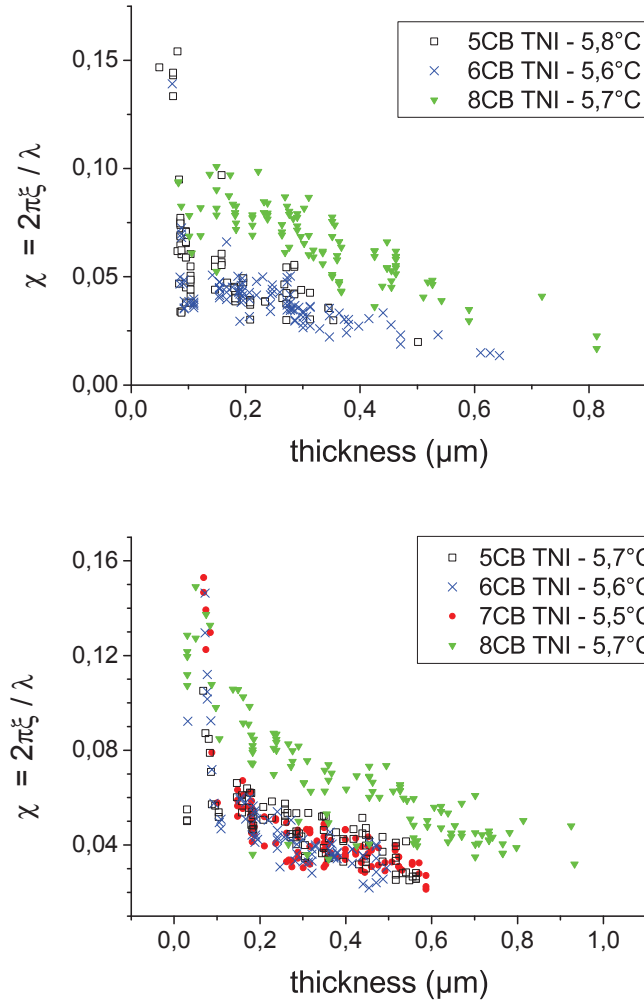


Figure 2.33: Figure representing the parameter  $\chi = \frac{2\pi\xi}{\lambda}$  calculated from the experimental data in function of the thickness  $\xi$ . The parameter  $\chi$  was calculated both on water and on glycerol at a given temperature from the nematic / isotropic phase transition. Small values of  $\chi$  correspond to long (observable) wavelengths which is achieved for intermediate thicknesses. On the top, results for water and on the bottom, results for glycerol.

state and a periodically modulated state (PHAN). Depending on the value of the saddle splay constant  $K_{24}$ , the threshold value varies between  $\xi_C$  and 0 ([75], [39]). In the case of 5CB, with  $K_{33} \approx 1.3K_{11}$ ,  $K_{22} \approx 0.5K_{11}$ ,  $K_{13} = 0$ , the experimental value of  $\xi_{UB}$  coincides with the calculated one for  $|K_{24}| \leq 0.6K_{11}$ , compatible with NMR measurements of the saddle splay constant [2]. Similar results would be obtained with the other nCB.

**More recent analysis** A difficulty with the Sparavigna model is that the wavelength is not known. Noticeably, it is not guaranteed that stripes are observable, which means that the calculated lower threshold is not necessarily the experimental one  $\xi_{UB}$ . In actual fact, the question makes sense. A recent calculation [47] using the evolved techniques ([1], [7], [44]) has provided threshold and wavelength values at the planar-PHAN transition. It allows recovering threshold values in the proper range  $\xi_{UB} \approx 20 - 30$  nm, with  $\chi = \frac{2\pi\xi}{\lambda} \ll 1$ . However, a non-zero, although very small azimuthal anchoring is required to get a finite value of the wavelength: without azimuthal anchoring, the wavenumber  $\chi$  vanishes at the threshold. Experimentally,  $\chi$  increases slightly when  $\xi$  decreases towards the threshold  $\xi_{UB}$ .

Therefore, the present situation is as follows: In the intermediate range of thickness, the LP model, which uses a first order perturbation of the HAN base state, accounts satisfactorily for the stripe wavelength. For the thinnest striped films, the HAN structure is no longer the proper base state, and the lower threshold is not recovered. The Sparavigna model, and more evolved versions of it, allow one to recover the lower stripe threshold  $\xi_{UB}$  for plausible values of the anchoring energies and elastic constants, noticeably the saddle splay surface elastic constant  $K_{24}$ . However, the requirement of a small azimuthal anchoring to obtain finite wavelengths at the threshold raises the question of the validity of a continuous analysis and a “first order elastic theory” for the thinnest striped films far from the NI transition.

**Stripes on solid substrates ?** Let us mention that the theory predicts the existence of stripes on silicon wafers, but with short wavelengths (of the order of magnitude of the film thickness). The short wavelength of these stripes would not allow for observation under optical microscope. An attempt of AFM imaging of thin 6CB films deposited on silicon wafers was then performed. Although non-contact mode was used (see Appendix about AFM for details), the interaction of the liquid crystal with the AFM tip was strong and triggered a fast spreading process. No stripes were seen on the images. However, the system seems to be significantly disturbed by the tip of the AFM: Unlike examples presented in Chapter 3 where the tip caused depinning of ionic liquid and very slow relaxation of the thin ionic liquid films, in the case of liquid crystals, a stable sample deposited several days before experiences fast spreading as soon as the scanning process begins. Fast spreading implies the existence of gradients in the thickness of the film. It could be that, as in the case of the planar rim of striped domains on water, gradients introduce a preferred orientation and destroys the orientational freedom and therefore prevent the formation of stripes.



### 2.2.7 General conclusion

The present study showed that the forbidden thickness range is a general behaviour for thin films of hybrid liquid crystals, observed on different substrates and with different compounds. Close to the nematic isotropic transition, the values of the thickness thresholds,  $\xi_{LB}$  and  $\xi_{UB}$  increase. They diverge at the phase transition that is also a wetting transition. On liquid substrates, long wavelength striped patterns are observed for films which thickness is larger than  $\xi_{UB}$ . In contrast with spin-coated solid substrates, where only two films are observed at coexistence, here films thicker than  $\xi_{UB}$  may coexist with the film of thickness  $\xi_{LB}$ , making the measurement of  $\xi_{UB}$  inaccurate. A summary of the experimental characterization of striped patterns is presented on figures 2.34, 2.35 and 2.36.

Figure 2.37 summarizes the estimated values of  $\xi_{LB}$ ,  $\xi_{UB}$  and of the upper threshold for the stripes far from the NI transition. The trends when approaching the transition are also shown.

The present contribution illustrates a specific case of thin films, where long-range orientational order and boundary conditions at interfaces play an important role. In contrast with more common situations, where the long range interaction in non-ionic systems is basically a van der Waals one scaling as  $\xi^{-2}$  in the free energy, here the contribution of the nematic elastic energy in the case of antagonist anchorings scales as  $\xi^{-1}$  at large thickness. In the same way, the well-known layering at interfaces due to short-range structural interaction gives rise in the present case to smectic-like structures. There is no longer a well-cut separation between molecular, mesoscopic and macroscopic scales, which makes any theoretical analysis quite complex. However, the robustness of the results for the nCB series and the MBBA requires to be accounted for by future theoretical analyses.

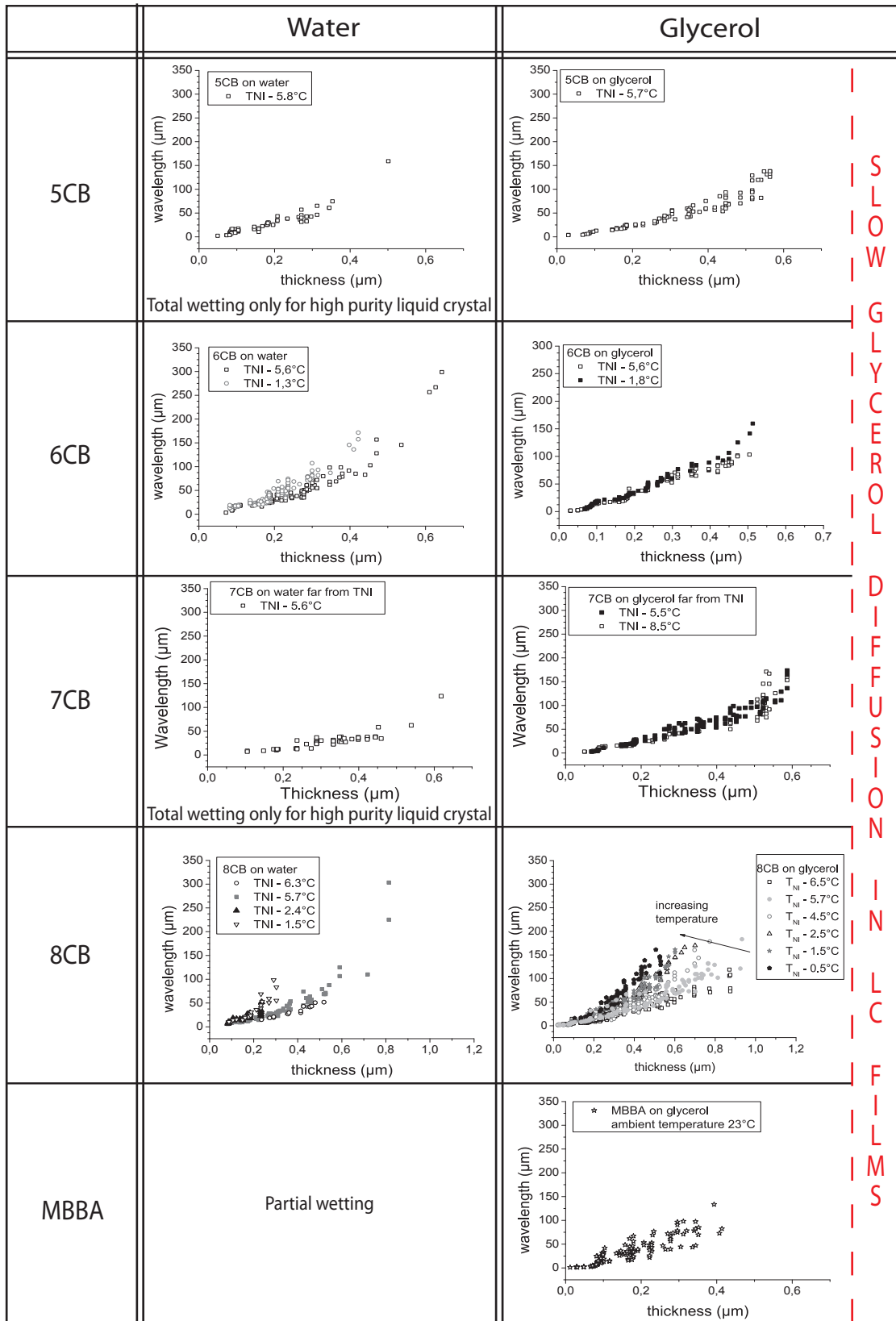


Figure 2.34: Summary of the characterization of striped patterns for each liquid crystal studied. Note that scales are similar except for thickness in the case of 8CB. Zooms of the graphs of nCBs are presented in the following figures 2.35 and 2.36. One reminds that  $T_{NI}$  is equal to 35°C for 5CB, 29°C for 6CB, 42.8°C for 7CB, 40.5°C for 8CB and 42°C for MBBA.

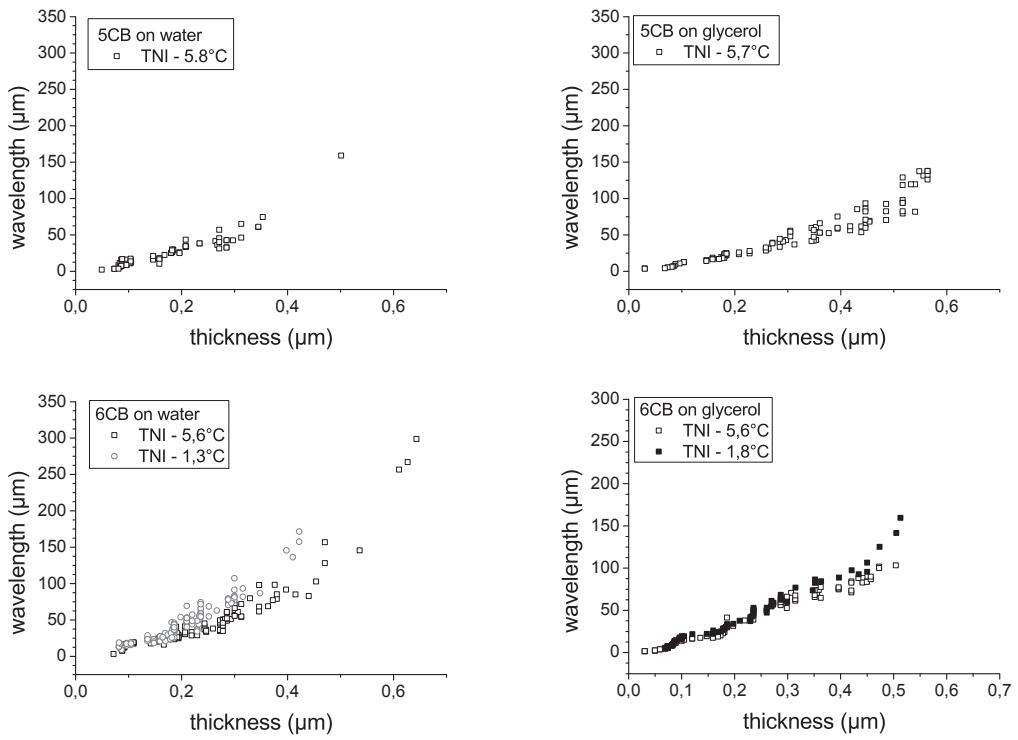


Figure 2.35: Zoom of the plots showing the characterization of striped patterns for 5CB and 6CB. The essential of quantitative data were obtained for 6CB on water and on glycerol. 6CB has the lowest  $T_{NI}$  value, which reduces the probability of glycerol diffusion into nematic layers. Moreover, its wettability on water is not critical.

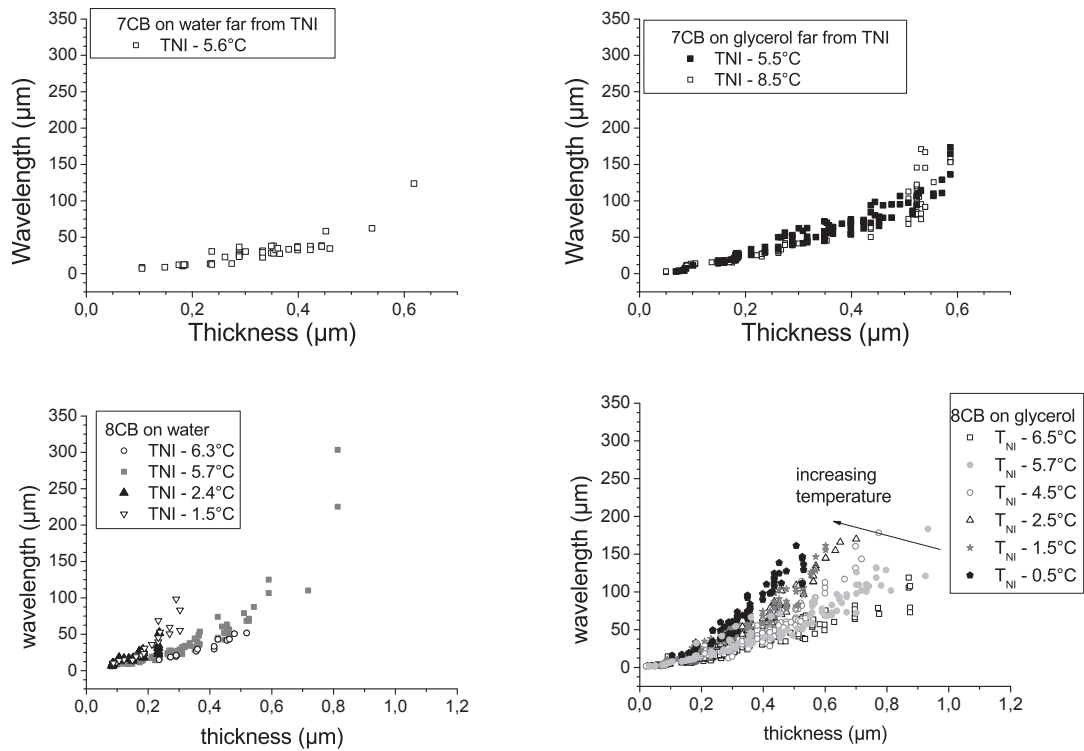


Figure 2.36: Zoom of the plots showing the characterization of striped patterns for 7CB and 8CB. It would be tempting to analyze the differences in the behaviour of 8CB on water and on glycerol. However, the occurrence of post-transitional effects from the Sm-N transition and the action of heating the samples on glycerol (even if 8CB has the longest alkyl chain and is then less subject to glycerol diffusion) make the situation complex.

On water - far from $T_{NI}$					
	5CB	6CB	7CB	8CB	MBBA
estimated $\xi_{LB}$ (nm)	trilayer 3.5	trilayer 3.8	trilayer 4.0	trilayer 4.3	non
estimated $\xi_{UB}$ (nm)	$\leq 50$	$\leq 70$	$\leq 100$	$\leq 80$	wetting
estimated upper stripes' threshold (nm)	500	650	600	800	on water
On glycerol - far from $T_{NI}$					
estimated $\xi_{LB}$ (nm)	Succession of molecular films observed under optical microscope. Exact nature of the molecular films not established (see Appendix about glycerol).				
estimated $\xi_{UB}$ (nm)	30	30	$\leq 70$	20	10
estimated upper stripes' threshold (nm)	550	500	600	unmeasurable, post-transitional effects due to Sm-N phase transition	

On water - close to $T_{NI}$		
	$T_{NI} - T$ ( $^{\circ}\text{C}$ )	6CB
estimated $\xi_{LB}$ (nm)	5.5	3.8
	1.5	50
	0.5	80
estimated $\xi_{UB}$ (nm)	5.5	$\leq 70$
	1.5	80
	0.5	150
estimated upper stripes' threshold (nm)	5.5	650
	1.5	400

Figure 2.37: Table summarizing the estimated values of  $\xi_{LB}$ ,  $\xi_{UB}$  and of the upper threshold for the stripes while approaching the NI transition. On the top, the cells filled in gray indicate the compound either wetting only when extra-pure (5CB and 7CB on water) or non wetting (MBBA). On the bottom, no results on glycerol are indicated as they can not be totally reliable when coming close to the NI transition. On water close to the NI transition, results are only presented for 6CB. Even though 8CB was the only other compound with proper wetting conditions when it was not extra-pure, the competition between post-transitional effects from the Sm-N transition and pre-transitional effects from the NI transition made the interpretation of the data not straightforward.

# Bibliography

- [1] A. L. Alexe-Ionescu, G. Barbero, and I. Lelidis. Periodic deformations in nematic liquid crystals. *Phys. Rev. E*, 66:061705, 2002.
- [2] D. W. Allender, G. P. Crawford, and J. W. Doane. Determination of the liquid-crystal surface elastic constant  $k_{24}$ . *Phys. Rev. Lett.*, 67:1442–1445, 1991.
- [3] G. Barbero and R. Barberi. Critical thickness of a hybrid aligned nematic liquid crystal cell. *Journal de Physique*, 44:609–616, 1983.
- [4] G. Barbero, I. Dahl, and L. Komitov. Continuum description of the interfacial layer of nematic liquid crystals in contact with solid surfaces. *The journal of chemical physics*, 130:174902, 2009.
- [5] G. Barbero and G. Durand. Splay-bend curvature and temperature-induced surface transitions in nematic liquid crystals. *Phys. Rev. E*, 48:1942–1947, 1993.
- [6] G. Barbero, LR. Evangelista, and P. Pieranski. *An elementary course on the continuum theory for nematic liquid crystals*. Singapore: World scientific, 2001.
- [7] G Barbero and I Lelidis. Modulated structures of flexoelectric origin in nematic liquid crystals. *Phys. Rev. E*, 67:061708, 2003.
- [8] G. Barbero and L. Pandolfi. Surface viscosity in nematic liquid crystals. *Phys. Rev. E*, 79:51701, 2009.
- [9] Sébastien Bardon. *Organisation au voisinage d'une surface solide*. PhD thesis, Université Paris VI, 1999.
- [10] M.J. Bradshaw, E.P. Raynes, J.D. Bunning, and T. E. Faber. The frank constants of some nematic liquid crystals. *J. Physique*, 46:1513–1520, 1985.
- [11] A.M. Cazabat, U. Delabre, C.J.E. Richard, and Y.Y. Cheung Sang. Experimental study of hybrid nematic wetting films. *Advances in Colloid and Interface Science*, 2011.
- [12] P. Chiarelli, S. Faetti, and L. Fronzoni. Structural transition at the free surface of the nematic liquid crystals MBBA and EBBA. *Journal de Physique*, 44:1061, 1983.

- [13] C Chiccoli, P Pasini, A Sarlah, C Zannoni, and S Zumer. Structures and transitions in thin hybrid nematic films: A monte carlo study. *Phys. Rev. E*, 67:050703, 2003.
- [14] R.L. Cook, H.E. King, Jr. Chris, A. Herbst, and D.R. Herschbach. Pressure and temperature dependent viscosity of two glass forming liquids: Glycerol and dibutyl phthalate. *J. Chem. Phys.*, 100:5178, 1994.
- [15] P.G. de Gennes and J. Prost. *The Physics of liquid crystals*. Oxford University Press, second edition edition, 1993.
- [16] M.N.G. de Mul and J. Adin Mann. Multilayer formation in thin films of thermotropic liquid crystals at the air-water interface. *Langmuir*, 10:2311, 1994.
- [17] U. Delabre and A.M. Cazabat. Coalescence driven by line tension in thin nematic films. *Phys. Rev. Lett.*, 104:227801, 2010.
- [18] U. Delabre, C. Richard, and A-M Cazabat. Some specificities of wetting by cyanobiphenyl liquid crystals. *J. Phys : Condensed matter*, 21:464129, 2009.
- [19] Ulysse Delabre. *Films nématiques minces sur substrats liquides*. PhD thesis, Université Paris VI, 2009.
- [20] E. Dubois-Violette and de Gennes P.G. Effects of long range van der waals forces on the anchoring of a nematic fluid at an interface. *Journal of Colloid and Interface Science*, 57:403, 1976.
- [21] D.A. Dunmur, M. R. Manterfield, W.H. Miller, and J. K. Dunleavy. The dielectric and optical properties of the homologous series of cyano-alkyl-biphenyl liquid crystals. *Molecular Crystals and Liquid Crystals*, 45:127, 1978.
- [22] S. Faetti. Theory of surfacelike elastic contributions in nematic liquid crystals. *Phys. Rev. E*, 49:4192–4205, 1994.
- [23] S. Faetti, M. Gatti, and V. Palleschi. Measurements of surface elastic torques in liquid crystals : a method to measure elastic constants and anchoring energies. *Rev. Phys. Appl.*, 21:451–461, 1986.
- [24] S. Faetti and V. Palleschi. Nematic-isotropic interface of some members of the homologous series of 4-cyano-4'-(n-alkyl)biphenyl liquid crystals. *Phys. Rev. A*, 30:3241, 1984.
- [25] Sandro Faetti, Marta Gatti, Vincenzo Palleschi, and Timothy J. Sluckin. Almost critical behavior of the anchoring energy at the interface between a nematic liquid crystal and a sio substrate. *Phys. Rev. Lett.*, 55(16):1681, 1985.
- [26] M.B. Feller, W. Chen, and Y.R. Shen. Investigation of surface-induced alignment of liquid-crystal molecules by optical second-harmonic generation. *Phys. Rev. A*, 43:6778–6792, 1991.

- [27] J.-B. Fournier and P. Galatola. Coarse-grained surface energies and temperature-induced anchoring transitions in nematic liquid crystals. *Phys. Rev. Lett.*, 82:4859–4862, 1999.
- [28] J.-B. Fournier and P. Galatola. Effective anchoring and scaling in nematic liquid crystals. *The European Physical Journal E: Soft Matter and Biological Physics*, 2:59–65, 2000.
- [29] F. C. Frank. I. Liquid crystals. On the theory of liquid crystals. *Discuss. Faraday Soc.*, 25:19 – 28, 1958.
- [30] G. Friedel. Les états mésomorphes de la matière. *Annales de physique*, 18:273, 1922.
- [31] M.C. Friedenbergh, G.G. Fuller, C.W. Frank, and C.R. Robertson. Formation of bilayer disks and two-dimensional foams on a collapsing/expanding liquid-crystal monolayer. *Langmuir*, 10:1258, 1994.
- [32] Barbero G. and G. Durand. On the validity of the rapini-papoular surface anchoring energy form in nematic liquid crystals. *J. Phys. France*, 47:2129–2134, 1986.
- [33] M. G. J. Gannon and T. E. Faber. The surface tension of nematic liquid crystals. *Philosophical Magazine A*, 37:117–135, 1978.
- [34] I. Haller, H.A. Huggins, and M.J. Freisera. On the measurement of indices of refraction of nematic liquids. *Molecular Crystals and Liquid Crystals*, 16:53–59, 1972.
- [35] R. G. Horn. Refractive indices and order parameters of two liquid crystals. *Journal de Physique*, 39:105, 1978.
- [36] B. Jérôme. Surface effects and anchoring in liquid crystals. *Rep. Prog. Phys.*, 54:391–451, 1991.
- [37] V. A. Korjenskaya and M. G. Tomilin. Experimental investigation of the surface energy of a nematic liquid crystal. *Liquid Crystals*, 15:643–649, 1993.
- [38] S. Krishnaswamy. Experimental determination of the surface tension of two liquid crystals. *Proceedings of the international liquid crystal conference, Bangalore*, page 487, 1980.
- [39] D. Krzyzanski and G. Derfel. Structure of spontaneous periodic deformations in hybrid aligned nematic layers. *Phys. Rev. E*, 63:021702, 2001.
- [40] Lavrentovich and Pergamenschick. Patterns in thin liquid crystal films and the divergence (“surfacelike”) elasticity. *International Journal of Modern Physics B*, 9:2389–2437, 1995.
- [41] O. D. Lavrentovich and V. M. Pergamenschchik. Periodic domain-structures in thin hybrid nematic layers. *Mol. Cryst. Liq. Cryst.*, 179:125, 1990.
- [42] O. D. Lavrentovich and V. M. Pergamenschchik. Stripe domain phase of a thin nematic film and the K13 divergence term. *Phys. Rev. Lett.*, 73:979 – 983, 1994.



- [43] F. Leenhouts and A.J. Dekker. Elastic constants of nematic liquid crystalline Schiff's bases. *J. Chem. Phys.*, 74:1956–1965, 1981.
- [44] I Lelidis and G Barbero. Novel surface-induced modulated texture in thick nematic samples. *Europhysics letters*, 61:646–652, 2003.
- [45] H. Mada. Study on the surface alignment of nematic liquid crystals: temperature dependence of pre-tilt angles. *Molecular Crystals and Liquid Crystals*, 51:43, 1979.
- [46] N.V. Madhusudana and R. Pratibha. Elasticity and orientational order in some cyanobiphenyls: Part iv. reanalysis of the data. *Molecular Crystals and Liquid Crystals*, 89:249, 1982.
- [47] O.V. Manyuhina, A.-M. Cazabat, and M. Ben Amar. Instability patterns in ultrathin nematic films: Comparison between theory and experiment. *Europhysics letters*, 92:16005, 2010.
- [48] T. Moses and R. Shen. Pretransitional surface ordering and disordering of a liquid crystal. *Phys. Rev. Lett.*, 67:2033, 1991.
- [49] V.G. Nazarenkov, A.B. Nych, and B.I. Lev. Crystal structure in nematic emulsion. *Phys. Rev. Lett.*, 87:075504, 2001.
- [50] J. Nehring and A. Saupe. On the elastic theory of uniaxial liquid crystals. *The Journal of Chemical Physics*, 54:337–343, 1971.
- [51] J. Nehring and A. Saupe. Calculation of the elastic constants of nematic liquid crystals. *The Journal of Chemical Physics*, 56:5527–5528, 1972.
- [52] A.B. Nych, U.M. Ognysta, V.M. Pergamenschik, B.I. Lev, V.G. Nazarenko, I. Musevic, M.S. Karabot, and O.D. Lavrentovich. Coexistence of two colloidal crystals at the nematic-liquid-crystal-air interface. *Phys. Rev. Lett.*, 98:057801, 2007.
- [53] C. Oldano and G. Barbero. An ab initio analysis of the second-order elasticity effect on nematic configurations. *Physics Letters A*, 110:213–216, 1985.
- [54] C.W. Oseen. The theory of liquid crystals. *Discuss. Faraday Soc.*, page 883, 1932.
- [55] P. Oswald and P. Pieranski. *Les cristaux liquides, tome 1*. GB Science Publishers, 2000.
- [56] P. Oswald and P. Pieranski. *Les cristaux liquides, tome 2*. GB Science Publishers, 2002.
- [57] V. M. Pergamenschik. Surfcelike-elasticity-induced spontaneous twist deformations and long-wavelength stripe domains in a hybrid nematic layer. *Phys. Rev. E*, 47:1881, 1993.
- [58] V. M. Pergamenschik. K13 term and effective boundary condition for the nematic director. *Phys. Rev. E*, 58:R16, 1998.

- [59] V. M. Pergamenschchik. Spontaneous deformations of the uniform director ground state induced by the surfacelike elastic terms in a thin planar nematic layer. *Phys. Rev. E*, 61:3936 – 3941, 2000.
- [60] VM. Pergamenschchik, D. Subacius, and OD. Lavrentovich. K-13-induced deformations in a nematic liquid crystal: Experimental test of the first-order theory. *Molecular crystals and liquid crystals*, 292:25–27, 1997.
- [61] J.E. Proust, E. Perez, and L. Ter-Minassian-Saraga. Films minces de cristal liquide nématique sur support liquide: Structure, tensions superficielles et tension de ligne. *Colloid & Polymer Science*, 256:666–681, 1978.
- [62] Tiezheng Qian, Xiaowei Zhaung, and Y.R. Shen. Surface-monolayer-induced bulk alignment of liquid crystals: From nematic to smectic-a phase. *Phys. Rev. E*, 59:1873–1879, 1999.
- [63] A. Rapini and M. Papoular. Distorsion d’une lamelle nématique sous champ magnétique. conditions d’ancrage aux parois. *J. Phys. Colloques*, 1969.
- [64] R Rosso and EG Virga. Local stability for a general wetting functional. *Journal of physics A*, 37:8751–8751, 2004.
- [65] A. K. Sen and D. E. Sullivan. Landau - de gennes theory of wetting and orientational transition at a nematic / liquide substrate interface. *Phys. Rev. A*, 35:1391–1403, 1987.
- [66] P. Sheng. Phase transition in surface-aligned nematic films. *Phys.Rev. Lett*, 37:1059, 1976.
- [67] P. Sheng. Boundary-layer phase transition in nematic liquid crystals. *Phys.Rev. A*, 26:1610, 1982.
- [68] P. Sheng, Bo-Zang Li, M. Zhou, T. Moses, and Y.R. Shen. Disordered-surface-layer transition in nematic liquid crystals. *Phys. Rev. A*, 46:946–950, 1992.
- [69] P. Sheng and EB. Priestley. *Introduction to liquid crystals*. N.Y. and London: Plenum Press, 1974.
- [70] G Skacej, AL Alexe-Ionescu, G Barbero, and S Zumer. Surface-induced nematic order variation: Intrinsic anchoring and subsurface director deformations. *Phys. Rev. E*, 57:1780–1788, 98.
- [71] T.J. Sluckin and A. Poniewierski. Novel phase transition in nematic liquid crystals : wetting and the kosterlitz-thouless transition. *Phys. Rev. Lett.*, 55:2907, 1985.
- [72] I.I Smalyukh, S. Chernyshuk, B.I. Lev, A.B. Nych, U. Ognysta, V.G. Nazarenko, and O.D. Lavrentovich. Ordered droplet structures at the liquid crystal surface and elastic-capillary colloidal interactions. *Phys. Rev. Lett*, 93:117801, 2004.

- [73] B. Song and J. Springer. Surface phenomena of liquid crystalline substances: Temperature-dependence of surface tension. *Molecular Crystals and Liquid Crystals*, 307:69, 1997.
- [74] A Sparavigna, L Komitov, and A Strigazzi. Hybrid aligned nematics and 2nd-order elasticity. *Molecular Crystals and Liquid Crystals*, 43:210–215, 1991.
- [75] A. Sparavigna, O. D. Lavrentovich, and A. Strigazzi. Periodic stripe domains and hybrid-alignment regime in nematic liquid crystals: Threshold analysis. *Phys. Rev. E*, 49:1344–1352, 1994.
- [76] A. Sparavigna, O.D. Lavrentovich, and A. Strigazzi. Magnetic field effect on periodic stripe domains in nematic liquid crystals. *Phys. Rev. E*, 51:792–796, 1995.
- [77] A. Sparavigna and A. Strigazzi. Splay stripes in hybrid aligned nematics with bulk elastic isotropy: The role of  $k_{24}$ . *Molecular Crystals and Liquid Crystals*, 221:109, 1992.
- [78] M. Tintaru, R. Moldovan, T. Beica, and S. Frunza. Surface tension of some liquid crystals in the cyanobiphenyl series. *Liquid crystals*, 28:793, 2001.
- [79] M. P. Valignat, S. Villette, J. Li, R. Barberi, R. Bartolino, E. Dubois-Violette, and Cazabat. Wetting and anchoring of a nematic liquid crystal on a rough surface. *Phys. Rev. Lett.*, 77:1994–1997, 1996.
- [80] D. van Effenterre, R. Ober, M. P. Valignat, and A. M. Cazabat. Binary separation in very thin nematic films: Thickness and phase coexistence. *Phys. Rev. Lett.*, 87:125701, 2001.
- [81] D. van Effenterre, M.P. Valignat, and D. Roux. Coupling between the nematic/isotropic transition and a thickness transition: A theoretical approach. *Europhys. Lett.*, 62:526–532, 2003.
- [82] Damien van Effenterre. *Instabilité d'un film mince de nématique*. PhD thesis, Université Paris VI, 2002.
- [83] H. A. Van Sprang and R. G. Aartsen. Torsional anchoring of 5cb and 5pch on various substrates. *Molecular Crystals and Liquid Crystals*, 123:355–368, 1985.
- [84] F. Vandenbrouck, S. Bardon, M. P. Valignat, and A. M. Cazabat. Wetting transition and divergence of the extrapolation length near the nematic-isotropic transition. *Phys. Rev. Lett.*, 81:610–613, 1998.
- [85] François Vandenbrouck. *Films minces de cristaux liquides*. PhD thesis, Université Paris VI, 2001.
- [86] EG. Virga. *Variational theories for liquid crystals*. London: Chapman and Hall, 1994.
- [87] M.M. Wittebrood, D.H. Luijendijk, Th. Stallinga, S. and Rasing, and I. Musevic. Thickness-dependent phase transition in thin nematic films. *Phys. Rev. E*, 54:5232–5234, 1996.

- [88] J. Xue, C.S. Jung, and Kim M. W. Phase transitions of liquid-crystal films on an air-water interface. *Phys. Rev. Lett.*, 69:474–477, 1992.
- [89] H. Yokoyama. Nematic-isotropic transition in bounded thin films. *J. Chem. Soc, Faraday trans. 2*, 84:1023, 1988.
- [90] H. Yokoyama. Surface anchoring of nematic liquid-crystals. *Molecular crystals and liquid crystals*, 165:265–316, 1988.
- [91] H. Yokoyama. Density-functional theory of surfacelike elasticity of nematic liquid crystals. *Phys. Rev. E*, 55:2938, 1997.
- [92] H. Yokoyama, S. Kobayashi, and H. Kamei. Temperature dependence of the anchoring strength at a nematic liquid crystal-evaporated SiO interface. *Journal of Applied Physics*, 61:4501–4518, 1987.
- [93] B. Zappone, Ph. Richetti, R. Barberi, R. Bartolino, and H. T. Nguyen. Forces in nematic liquid crystals constrained to the nanometer scale under hybrid anchoring conditions. *Physical Review E (Statistical, Nonlinear, and Soft Matter Physics)*, 71:041703, 2005.
- [94] Xiaowei Zhuang, Lorenzo Marucci, and Y.R. Shen. Surface-monolayer-induced bulk alignment of liquid crystals. *Phys. Rev. Lett.*, 73:1513–1516, 1994.
- [95] P. Ziherl, R. Podgornik, and S. Zumer. Pseudo-casimir effect in nematic liquid crystals in frustrating geometries. *Physical Review Letters*, 84:1228, 2000.



## Chapter 3

# Small volume of ionic liquid in contact with selected substrates

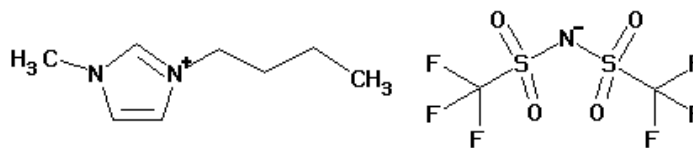
## - wetting behaviour and morphology -

### 3.1 Going towards nano-scales

When it comes to microscopic scales, wetting properties can be modified and the way they are is still subject to controversies (see Chapter 1). In such a situation, finding a “liquid / substrate” system to perform experiments is a question. In this study, the liquid phase was chosen to be ionic liquids. First, their wetting properties are not yet completely understood and they have a wide range of possible applications in the electro-chemistry field. They also have a very low saturating vapor pressure which implies that in standard conditions of temperature and pressure, evaporation is negligible. In the first part of this chapter, the properties of ionic liquids will be further detailed as well as the specific methods of deposition and imaging that are adapted to small scales. Finally, experiments where ionic liquids are deposited on different substrates will be presented.

#### 3.1.1 About ionic liquids

“Ionic liquids” are strictly speaking molten salts. They have a low melting temperature explained by the structure of their ions. The sterical mismatch between anions and cations implies that coulombic attractions are dampened and that lattice packing arrangements are frustrated. The liquid structure is then favoured at a lower temperature compared to a common salt. Besides



chemical formula	$C_{10}H_{15}F_6N_3O_4S_2$
molecular weight	419.36 $g.mol^{-1}$
density	1.4431 $g.cm^{-3}$ at 293.40K
viscosity	59.8 $mPa.s$ at 293.40K
flash point	> 473K(200°C)
optical index	1.428
surface tension	33.9 $mN.m^{-1}$ at 297K
miscibility with water	no
Molecular volume of ion pair / $nm^3$	0.50
Diameter of ion pair / nm	0.79

Figure 3.1: Characteristics of [BMIM][TFSI]. On the top, images representing the two ions. On the bottom, table summarizing some properties of [BMIM][TFSI]. Density and viscosity data were taken from [6] ; surface tension from [10]

their low vapor pressure, characteristics of ionic liquids are their high thermal stability and high viscosity as well as the fact that they are electric conductors.

Ionic liquids are quite recent materials. The first synthesis of an ionic liquid was performed in 1914 by P. Walden, but it is only in the 70s – 80s that ionic liquids based on the ions used in the present work were developed. The ionic liquid that we used is butyl - methyl - imidazolium bis (trifluoromethylsulfonyl) - imide: [BMIM][TFSI] (or [BMIM][NTf2]). The figure 3.1 presents a picture of both ions along with a few characteristics of the compound. [BMIM][TFSI] is not miscible with water, but as other ionic liquids, [BMIM][TFSI] might be contaminated by water from the atmosphere [5]. Studies of the evolution of different properties of [BMIM][TFSI] in function of water contamination can be found in [6]. In the conditions corresponding to our experiments (see thereafter), this absorption is negligible.

### 3.1.2 Methods for the deposition of small droplets of ionic liquids

Generating droplets which diameter is less than 50  $\mu m$  is not an easy process. Several methods of deposition can be used:

- Direct deposition of the studied liquid. This can be done using an aerosol [9] or by direct deposition using small tools such as etched wires, or very sharp needles (condensation is also used for volatile liquids [17], [13], [4]).
- Deposition via a dispersion or a solution of the studied liquid with a volatile solvent. The first possible deposition method is then spin-coating: solution is deposited on a substrate

which will undergo spinning. During the spinning step, the volatile solvent evaporates leaving tiny droplets on the substrate [2]. Another possible method is based on the fact that the two liquids, volatile “solvent” and liquid of interest, are immiscible. The prepared dispersion is shaken (sonication) and a tiny amount of it is deposited on the substrate<sup>1</sup>. After evaporation of the volatile compound, droplets are left on the substrate.

In the experiments described in this work, both methods were used: the paintbrush-syringe method for the direct deposition and the dispersion method for the deposition via a volatile solvent.

In the paintbrush-syringe method, a micro-syringe is filled up with ionic liquid. A small needle, 33 gauge, is then fixed to the syringe. Ionic liquid is then dispensed to create a droplet at the end of the needle. The droplet should be as small as possible. By gently tapping on the syringe, the “mother” droplet is thrown towards the substrate which results in several “child” droplets. The advantage of this method is to produce small droplets without the presence of a solvent: it ensures that the droplets are free from remaining solvent molecules. However, the fact that the droplets are splashed onto the substrate has an influence on their final shape and they often do not recover a spherical shape even on a smooth substrate (which suggests that pinning plays a role)<sup>2</sup>. The droplets obtained are still smaller size than for the other direct deposition methods that we tested (aerosol and etched tungsten wires).

On the other hand, the dispersion method produces spherical shaped droplets on smooth substrates but with the intermediary of a dispersion with a volatile compound. Controlling the concentration of ionic liquid in the dispersion allows one to control the amount of ionic liquid left after a drop of dispersion is deposited on a substrate and the volatile compound is evaporated. The concentration plays also a role on the deposition mechanism: the less concentrate is the dispersion, the more is the proportion of the ethanol and then the evaporation process of the ethanol ensures a smooth deposition. To make sure that the droplets left after evaporation are indeed free from ethanol, cross-checks were performed. First, for each substrate, the evaporation process was followed under optical microscope with a high speed camera. The biggest ionic liquid droplets left on the substrate were resolved by the optical microscope and did not show any sign of ethanol contamination<sup>3</sup>. Second, the sample, which evaporation process was followed, was placed in a plasma cleaner for around 2 minutes. The color of the plasma was not modified (it would have been in the presence of a significant amount of ethanol). The sample was then observed again under optical microscope and showed no modifications. Both the color of the plasma and the fact that no change was observed on the sample after the plasma treatment allow one to believe that there is no significant presence of ethanol molecules in our samples after the ethanol evaporation. Third, the refractive index of ionic liquid previously mixed with

---

<sup>1</sup>The polydispersity of the emulsion was not characterized.

<sup>2</sup>As the ionic liquid is in a non-wetting configuration, it is not possible to deposit the droplet by creating a direct contact with the substrate: the droplet would stay on the syringe.

<sup>3</sup>Ethanol appears under microscope with a different contrast than ionic liquid: before evaporation, the dispersion then is a mix of small dark gray and light gray zones. After evaporation of the ethanol, only dark gray subsists, i.e. ionic liquid.



ethanol was measured after the ethanol had been evaporated. This refractive index was found to be the same than the one of pure ionic liquid<sup>4</sup>. The corresponding results are presented in the table below:

	refractive index measured with green filter (546 nm)	refractive index measured with orange filter (589 nm)
high purity [BMIM][TFSI]	1.4286	1.4274
high purity [BMIM][TFSI] previously mixed with ethanol	1.4290	1.4273

With each filter, the difference in the refractive indices does not exceed  $10^{-4}$  which correspond to the error bar of the refractometer that we used: it is hence negligible. To conclude, as the dispersion method produces spherical shaped droplets on smooth substrates and does not seem to induce contamination of the ionic liquid, it is the method which was used most of the time for our experiments.

### 3.1.3 How to visualize wetting processes on nano-scales ?

Visualizing droplets and precursor films of ionic liquids was performed using two Scanning Probe Microscopy (SPM) techniques: Atomic Force Microscopy (AFM) and Scanning Tunneling Microscopy (STM). AFM and STM are complementary techniques when it comes to image ionic liquids. While AFM images are not free of distortions due to the tip geometry, STM images are. However, STM only allows for imaging conductive samples, i.e. conductive liquids as ionic liquids, on a conductive substrate. AFM can then potentially image a greater variety of systems than STM, but STM provides more precise images.

The description of these two imaging techniques as well as specific questions related to the process of imaging ionic liquids, such as specific problem of capture and precision, will be discussed in the Appendix about AFM and STM. One can still mention that the question of the perturbation of the system by the scanning tip in the AFM method is delicate to answer.

## 3.2 Wetting on a model of smooth hydrophilic substrate

### - Ionic liquids on mica substrate -

#### 3.2.1 About mica substrate

Mica is the name of a group of silicate minerals, which means that silica groups are part of their chemical composition. The molecules present in mica combine themselves to form distinct layers

<sup>4</sup>The refractive index of ethanol is different than the one of the studied ionic liquid:  $n_{eth} = 1.36$ .

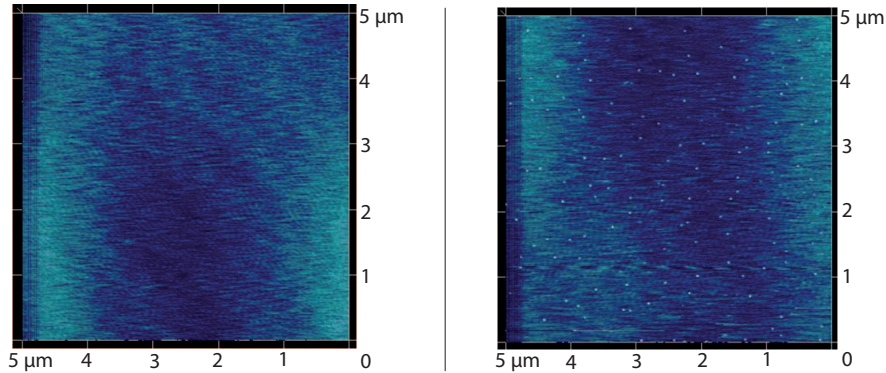


Figure 3.2: Freshly cleaved bare mica imaged in contact mode. 3D mixed height and phase images of: on the left, mica sheet and on the right, mica disk.

which can be cleaved. The substrates that were used were freshly cleaved mica (green muscovite, V-1 grade). Two kind of mica were used, first, large sheet, cut into samples of the appropriate size (purchased from S&J Trading Co) and second, small disks of mica with controlled size (12 mm diameter). In an ideal situation, cleavage would produce an atomically smooth substrate. However, as the cleavage process is never perfect, one obtains a substrate which consists in a succession of smooth terraces. In such a situation droplets show a tendency to be pinned on the frontiers separating the different atomic planes. However, as the characteristic area of the terraces is quite large (typically more than  $90 \mu\text{m}$  in the center of the mica sample), droplets are observed everywhere on the mica samples, not only pinned on the frontiers of the atomic planes. The mica substrates were imaged just after cleavage with contact mode AFM. The images show no terraces except for rare exceptions, but always show small features due to non-perfect cleavage. From these images, roughness measurements were performed (see figure 3.2 for examples of AFM scans.). The summary of the results obtained from several  $5 \mu\text{m}$  scans is presented below:

	RMS roughness	Roughness average	max peak to peak value
Mica sheets	$0.1 \text{ nm}$	$0.1 \text{ nm}$	$2.5 \text{ nm}$
Mica disks	$0.1 \text{ nm}$	$0.1 \text{ nm}$	$4.5 \text{ nm}$

The results are quite similar for the two different kinds of mica except for the maximum peak to peak value which is a bit higher for the mica disks than for the mica sheets. The roughness measurements show that the freshly cleaved micas used for our experiments are smooth, but not atomically smooth. There will then be a possibility of pinning for the ionic liquid on the features of the substrates. Considering that the characteristic area of the observed mica terraces is quite large, the small features resulting from non-perfect cleavage will constitute the most important influence on the morphology of the samples.

From the roughness results, it is clear that despite the fact that the two micas share the same quality, they show differences. Mica is indeed a mineral and for different mica samples made from

different ores, a difference in the exact chemical composition can be observed. This difference in the chemical composition results in a difference in the chemical heterogeneities present at the surface of the mica. The two surfaces, of mica sheets and mica disks although they share the same roughness are indeed slightly different as experiments will show in the following paragraphs. Before focusing on the microscopic wetting behaviour of ionic liquid on mica, its macroscopic wetting behaviour must be investigated.

## 3.2.2 Macroscopic wetting behaviour

### 3.2.2.1 Overview

First, the contact angle of macroscopic drops of the ionic liquid used in our experiments, [BMIM][TFSI], was measured with the sessile drop method (see the appendix on macroscopic contact angle measurement methods). The advancing, receding and so called "equilibrium" (advancing contact angle measured after long time, see below) mean values for high purity [BMIM][TFSI] are reported on the table:

	mica sheets	mica disks
advancing contact angle	$46 \pm 5^\circ$	$42 \pm 5^\circ$
receding contact angle	$16 \pm 5^\circ$	$23 \pm 4^\circ$
equilibrium contact angle	$26 \pm 5^\circ$	$24 \pm 4^\circ$

There is a large hysteresis between the advancing and the receding contact angle. This hysteresis seems to find its origin in the pinning of the contact line on the features observed with the AFM on freshly cleaved mica. The drops indeed showed a stick / slip behaviour during the advancing step, when liquid was dispensed. The hysteresis is larger on mica sheets than on mica disks. Mica sheets and mica disks possess similar roughness (see above). However, the difference in the chemical heterogeneities characteristic of each mica might be the origin of the difference observed in the hysteresis values.

A confirmation that the drops experience pinning on bare mica was given by a simple experiment: first, the advancing and receding contact angle of a drop were measured ; second, ionic liquid was dispensed on the same spot. The advancing and receding contact angles of the new drop were then measured. Several successive advancing and receding cycles performed on the same spot show the same tendency:

- For the first advancing / receding cycle, performed on bare, freshly cleaved mica, there is a very large hysteresis (around  $19^\circ$  on mica disks).
- From the second advancing / receding cycle and on, the advancing contact angle shows an important decrease and the hysteresis falls down to a few degrees (around  $3^\circ$  on mica disks)

- If enough liquid is dispensed so that the drop advances past the zone covered by the previous one, the advancing contact angle increases again and recovers the value measured during the first advancing / receding cycle.

An example of such a succession of cycles is presented on figure 3.3. The advancing contact line is then pinned for advancing drops on bare, freshly cleaved mica. After the first deposition and aspiration of an ionic liquid drop, the surface of the mica was modified which is a sign that some ionic liquid was left behind the receding drop. The exact morphology of the ionic liquid left after a receding drop was studied with the AFM. The corresponding experiments will be described thereafter (see 3.2.4.1).

Moreover another specific behaviour is observed for macroscopic drops of [BMIM][TFSI] deposited on mica substrates: if a drop is left free, its contact angle decreases with time. The contact angle's decrease is quite important on short time scales and then becomes less steep until a stabilization, on long time scales (more than 3 hours). It has to be noted that the relaxation is the same whatever the volume of the drop and that the relaxation leads to different final contact angle values for the two kinds of mica. Two examples of such a relaxation are shown on figure 3.4. Complementary experiments performed only on mica sheets, seem to indicate that along with this evolution of the contact angle, a precursor film could develop ahead of the drop<sup>5</sup>.

### 3.2.2.2 Precursor film, complementary experiments performed on mica sheets

A first evidence of the existence of the precursor was indirectly obtained with an optical microscope. Drops of [BMIM][TFSI] were deposited on mica and observed at regular intervals. After half a day, a few dust particles were found on the mica, not touching the drops (The samples were not protected during the observations. They were only covered during the waiting periods.). Although the dust particles did not touch the drop, they were surrounded by a rim of ionic liquid (see figure 3.5). This observation strongly suggested the presence of a precursor film<sup>6</sup>. This was confirmed by X-Ray Photoelectron spectroscopy (XPS) measurements (XPS measurements were performed with the help of Christopher Bassell)<sup>7</sup>. A drop of [BMIM][TFSI] was deposited on freshly cleaved mica and analyzed by XPS after one night. The XPS analysis showed clear evidence of the presence of the [TFSI] ion far from the drop (see figure 3.6). A precursor film then spreads from the drop. Its exact nature remains an open question after the XPS experiment, which can only provide clear evidence of the presence of the [TFSI] ion<sup>8</sup>. The precursor film could then either be composed of ionic liquid, i.e. [BMIM] and [TFSI] ions, or only of [TFSI] ion. However, the eventuality of a precursor only formed of [TFSI] ion is unlikely to happen because of a simple electrostatic argument: the mica surface is known to be negatively charged as well

<sup>5</sup>We call "precursor" the thin film growing ahead of the main drop, although the liquid wets only partially the substrate.

<sup>6</sup>The dust particle is wetted by the liquid it is then not likely that it could have touched the drop without being trapped.

<sup>7</sup>With the XPS device used, the detector is at 90° of the surface and the analysis area is of 300 by 700 μm.

<sup>8</sup>The chemical composition of the [BMIM] ion does not allow one to distinguish the XPS peaks due to the [BMIM] from the peaks due to the mica substrate.

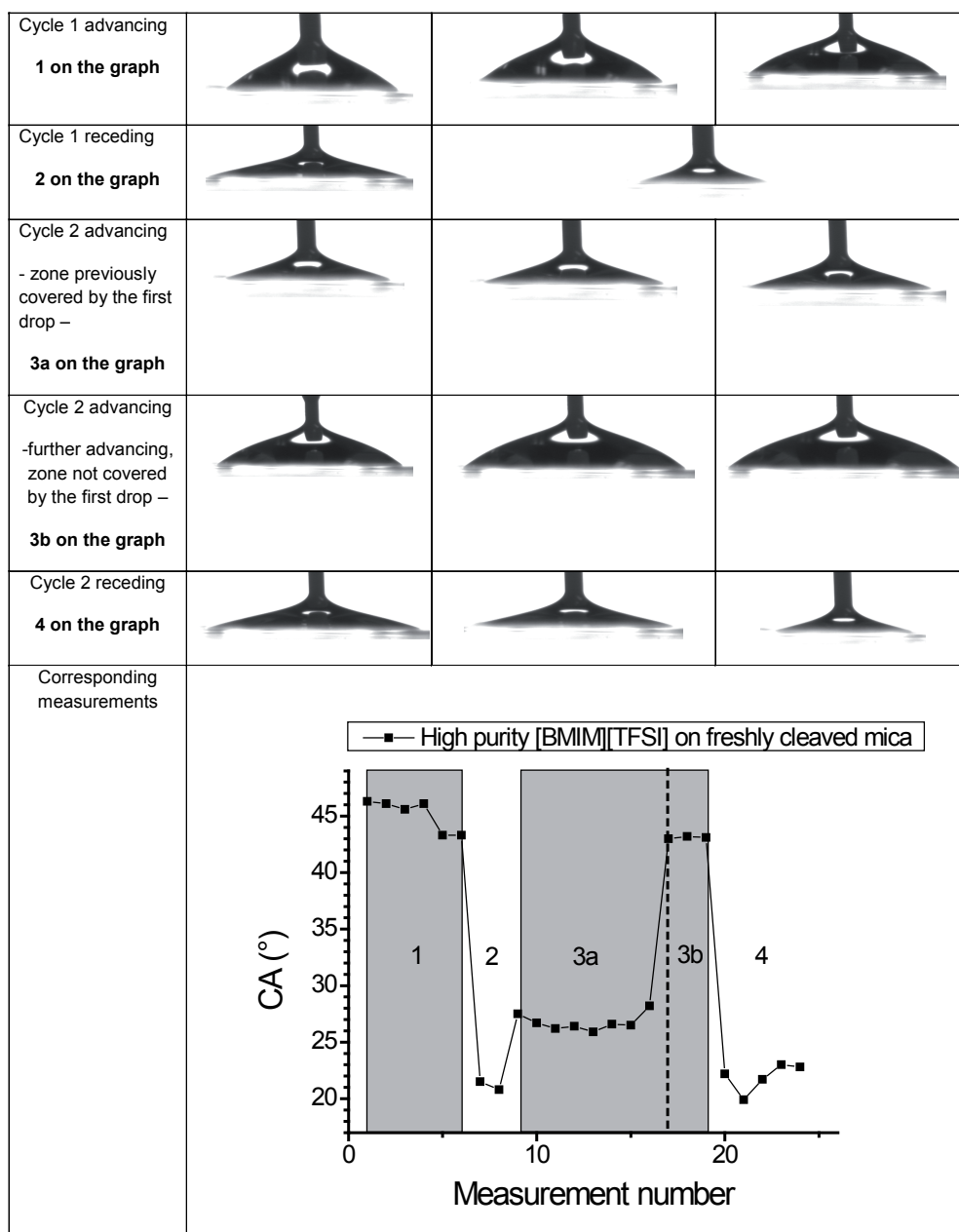


Figure 3.3: Succession of advancing and receding cycles performed at the same spot for [BMIM][TFSI] on freshly cleaved mica.

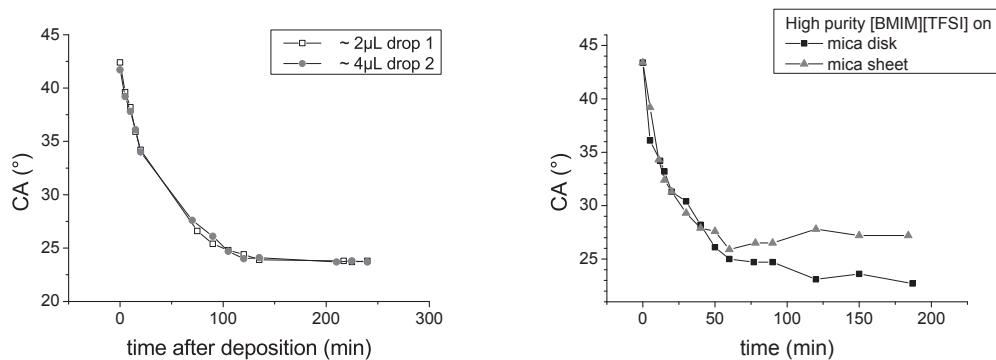


Figure 3.4: Examples of relaxation of the contact angle of drops of [BMIM][TFSI] deposited on freshly cleaved mica disk. On the left, two drops of different volumes deposited at the same time, i.e. in similar atmospheric conditions, relax to the same value, showing that the relaxation does not depend on the volume of the drop. On the right side, two drops deposited at the same time on the two different kind of micas relax towards a different value, showing once more that the difference in the mica substrates plays a role.

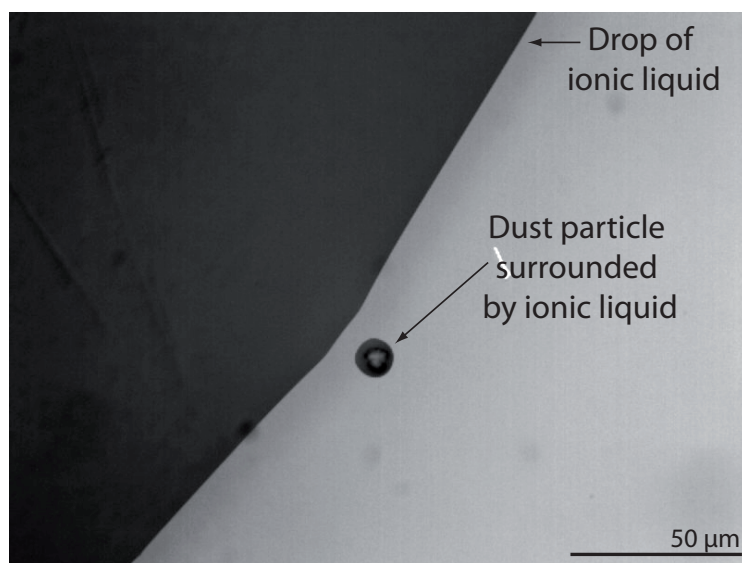


Figure 3.5: Drop of [BMIM][TFSI] on mica substrate. Around a dust particle which does not touch the drop, a rim of ionic liquid is present. This suggests the presence of a precursor film.

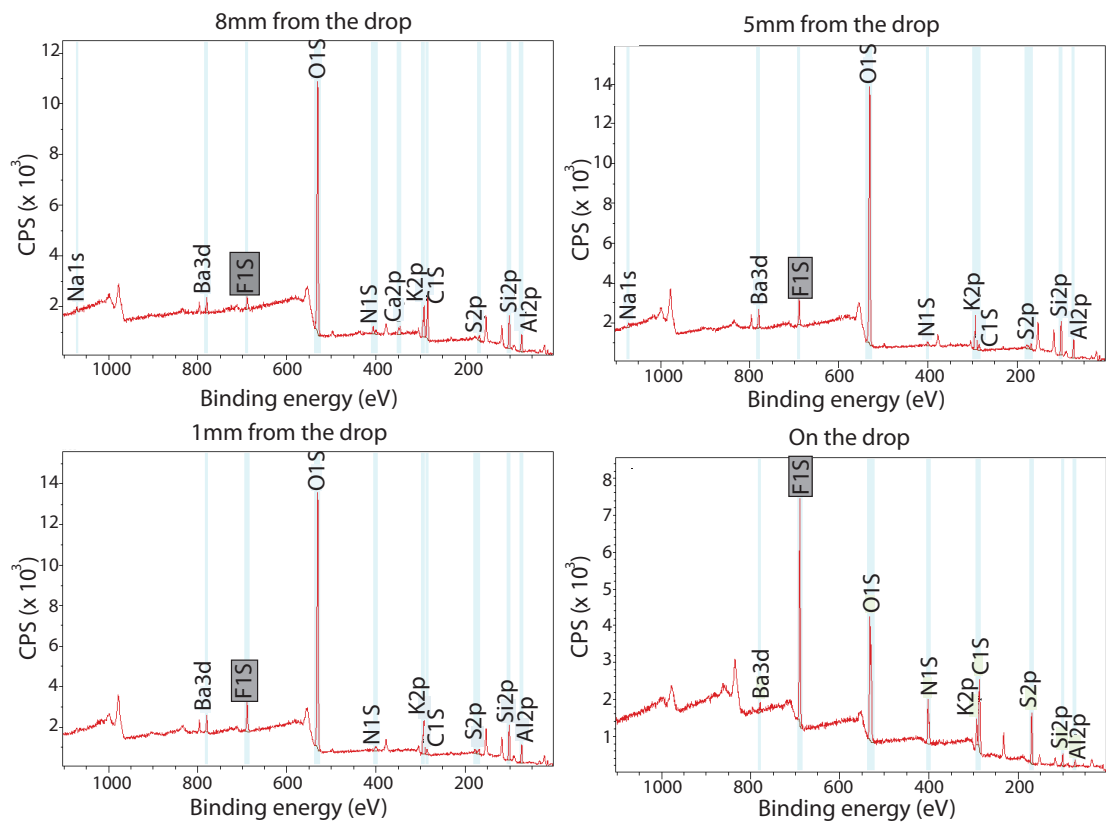


Figure 3.6: XPS results for a drop of [BMIM][TFSA] deposited on a freshly cleaved mica substrate and analyzed after one night. At a distance of 8 mm from the drop, the presence of fluorine is characteristic of the presence of the [TFSA] ion.

as the [TFSI] ion. The presence of the [BMIM] counterion is necessary to ensure the stability of the precursor. The precursor film must then be constituted of both ions.

For macroscopic quantities of [BMIM][TFSI] deposited on mica substrates, it is then possible to observe a drop, which contact angle diminishes as a precursor film develops ahead of the drop. The contact angle is always below  $60^\circ$ , which is the ideal case for AFM imaging (see the appendix on AFM and STM images).

Note that the same behavior was observed with non-ionic surfactants (the so-called super-spreaders) [14] and isotropic (non wetting) 5CB macroscopic droplets deposited on oxidized silicon wafers [16] (see figure 3.7). The progressive development of a trilayer ahead of the main drop was recorded using spatially resolved ellipsometry. The associated decrease of contact angle was followed by interferometry, as the angles were significantly smaller (less than  $10^\circ$ ) (see figure 3.7).

### 3.2.3 Discussion about reproducibility of the experiments

As already mentioned, slight differences in mica substrates can play a role on the measured contact angles. Other parameters which could be critical while performing the experiments were also tested as cross-checks: the importance of a fresh cleavage of the mica substrates, the purity of the ionic liquid and the humidity.

#### 3.2.3.1 Freshly cleaved vs aged mica

Mica is a high energy surface and after cleaving, it then gets contaminated immediately (by water from the atmosphere for example). Deposition of ionic liquid just after cleaving then takes place on slightly contaminated mica. On the contrary, if the ionic liquid is deposited on aged mica (mica cleaved for example several days before), the deposition occurs on a completely contaminated mica surface. Cleavage is known to be a critical parameter for experiments on high energy surfaces, the question was then evaluate how critical it was in our case for the reproducibility of the results. To address this question, the relaxation of the contact angle of a drop of [BMIM][TFSI] deposited on aged mica was followed in parallel with the contact angle of a drop deposited on freshly cleaved mica at the same time (same atmospheric conditions). To obtain aged mica, the mica disks were simply used as received from the supplier, without cleaving them again. The contact angle on such aged mica stabilizes itself much more quickly than for freshly cleaved mica, typically 15 minutes instead of more than 180 minutes. Another difference with freshly cleaved mica is that the stable value of the contact angle is not reproducible. On figure 3.8, three examples of relaxation on aged mica are presented. The final values exhibit much more scattering than for drops deposited on freshly cleaved mica in similar atmospheric conditions. The final value is also always larger than the one obtained on freshly cleaved mica (for example, more than  $5^\circ$  for sample 1). The lack of reproducibility results from the difference in the actual composition of the molecules adsorbed on the mica which constitute the contamination of the



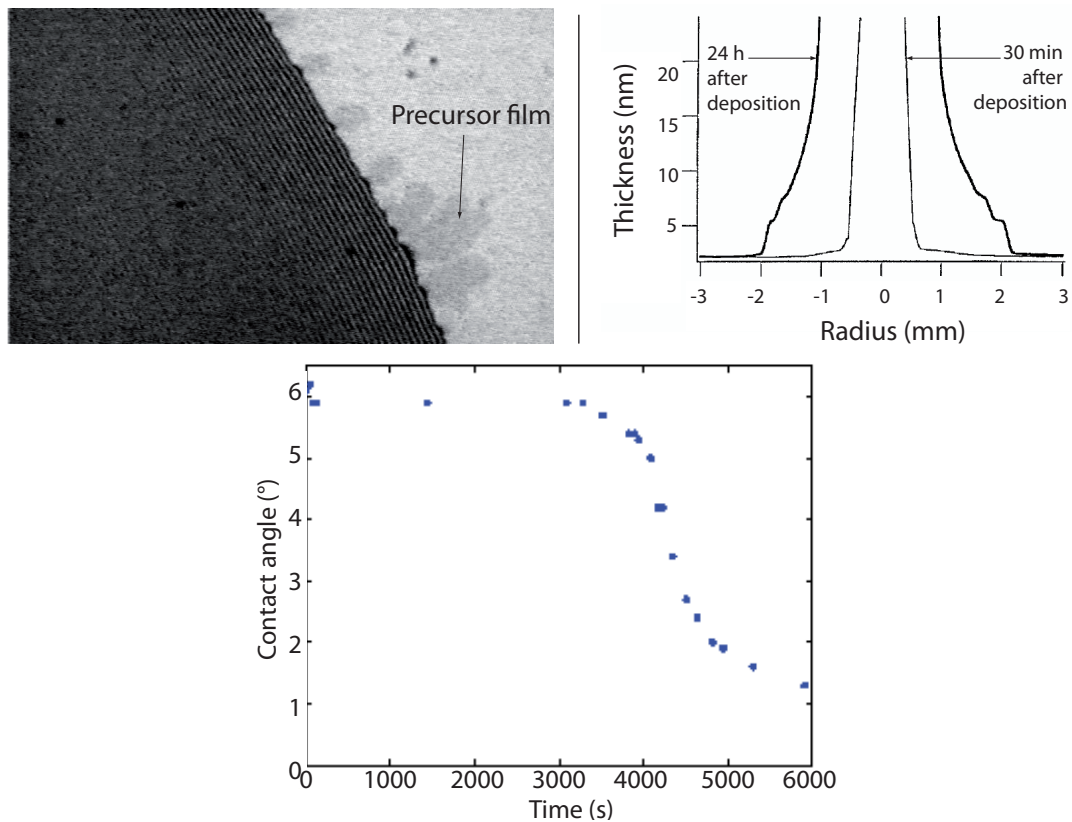


Figure 3.7: Images taken from [16]. 1/ On the top : On the left side, under microscope, a drop of isotropic 5CB (non wetting) on a silicon wafer, close to the nematic / isotropic phase transition. The image is taken 44 min after deposition. A precursor film is developing ahead of the drop. On the right side, ellipsometric profiles of a micro-drop of isotropic 5CB (non wetting) on a silicon wafer, close to the nematic / isotropic phase transition. 30 min after deposition, the drop does not show any structuration. 24 h after deposition, the drop's foot is structured. Meanwhile, the precursor film spread ahead of the drop and the contact angle of the drop decreased. 2/ On the bottom, the evolution in time of the contact angle for the same system.

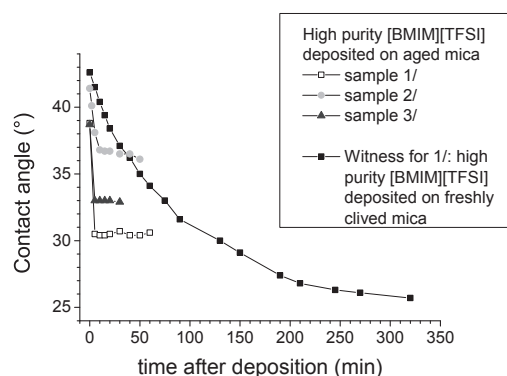


Figure 3.8: Contact angle relaxation of [BMIM][TFSI] deposited on aged mica substrate disks. Comparison with the relaxation obtained on freshly cleaved mica is provided by the curve showing black squares and corresponding to a drop of [BMIM][TFSI] deposited on freshly cleaved mica at the same time than sample number 1.

surface. As expected, the use of freshly cleaved mica is then fundamental for the reproducibility of the experiments.

### 3.2.3.2 Purity of the ionic liquid

Two different kinds of ionic liquids were used: for synthesis ionic liquid and high purity ionic liquid (purchased from Mercks), the “for synthesis” quality being poorer than the “high purity” one. The surface tension and the macroscopic contact angle on mica substrates of [BMIM][TFSI] of both quality were measured.

The surface tensions of the two different ionic liquids in air were measured via the pendant drop technique with the sessile drop device. A drop of ionic liquid is then dispensed from a syringe possessing a specific, large needle. The dispense process is stopped when the drop is on the verge of falling from the needle. A picture of the system is then taken and image analysis allows one to deduce the corresponding value of the surface tension ionic liquid / air,  $\gamma_{BT-Air}$ <sup>9</sup>. The measured surface tensions are presented in the table below<sup>10</sup>:

Quality of the ionic liquid	Surface tension
for synthesis	$32.0 \pm 0.6$ mN/m
high purity	$32.6 \pm 0.2$ mN/m

<sup>9</sup>Image analysis was performed via the OCA software of the sessile drop device.

<sup>10</sup>For comparison, the surface tension obtained from the literature for [BMIM][TFSI] is of 33.9 mN/m from reference [10]. There is then a small difference with our measurements. A cross-check was then performed with our device and milliQ water. The value obtained is of 73.0 mN/m at 24° to be compared to the characteristic values obtained for water: 72.9 mN/m at 20° and 72.0 mN/m at 25°. The small difference obtained for water ensures that the value of the surface tension of the ionic liquid is reliable. The slight difference with the value of the literature is still not explained but could be due to the purity of the ionic liquid.

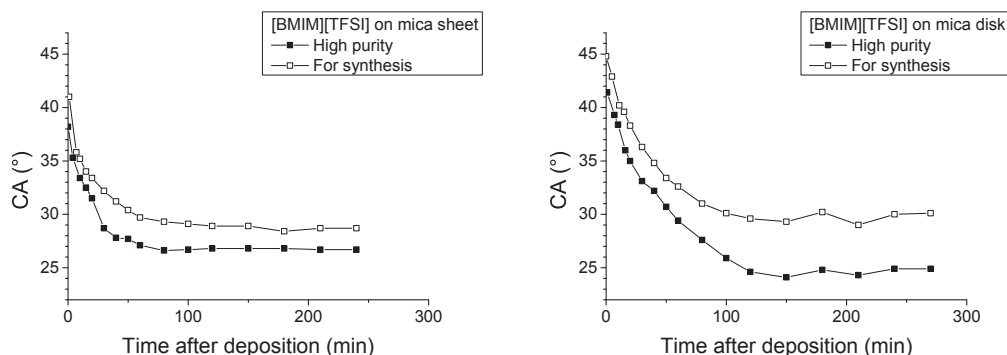


Figure 3.9: Example of relaxation of the macroscopic contact angle of ionic liquid of different qualities, respectively “for synthesis” and “high purity”, on mica. On the left side, the ionic liquid drops were deposited on a mica sheet. On the right side, the ionic liquid drops were deposited on a mica disk. The relaxation of the high purity ionic [BMIM][TFSI] always leads to a smaller contact angle than for the for synthesis [BMIM][TFSI].

As for other liquids, the presence of a certain amount of impurities affects the ionic / liquid air surface tension and could also affect the other two surface tensions. One then expects to observe a difference in the macroscopic contact angle of the ionic liquid.

The macroscopic equilibrium contact angle was then measured in function of time to observe the relaxation phenomenon. An example of the results of such a test is presented on figure 3.9. The “equilibrium” contact angle of “for synthesis” ionic liquid is always higher than the one of the “high purity” ionic liquid (the difference in the two values is comparable to the error bars of the system). The same tendency is observed on both mica substrates: mica sheets and mica disks. As expected, the difference in purity of the ionic liquid plays then a role on the macroscopic wetting behaviour but reproducibility of the results can still be obtained with a slightly contaminated ionic liquid.

### 3.2.3.3 Humidity

The humidity of the ambient atmosphere can show variations in the laboratory where the experiments were performed. Its influence on the wetting behaviour of ionic liquids was then an important cross-check to perform to ensure the reproducibility of the results. For that purpose, a drop of [BMIM][TFSI] was deposited on freshly cleaved mica. The contact angle was then followed during the relaxation and until it adopted a stable value. At this stage, the humidity of the room was increased of 6%. The contact angle of the drop then showed a decrease of one degree. The results are presented in figure 3.10 which is negligible compared to the error bars obtained for contact angle measurements with the sessile drop device. For a variation of the humidity of this order of magnitude, the consequence on the macroscopic contact angle is then negligible and humidity does not appear in that case as a critical parameter for the reproducibility of the

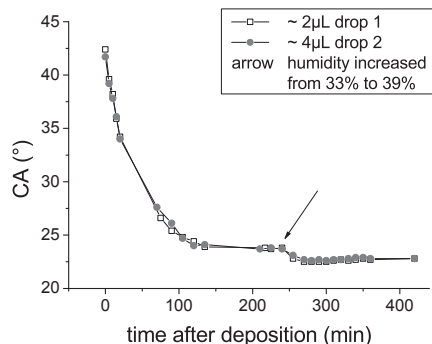


Figure 3.10: Influence of increasing humidity on the final contact angle of [BMIM][TFSI] drops deposited on freshly cleaved mica.

experiments.

### 3.2.4 Microscopic wetting behaviour: precursor and droplets

One of the properties of mica is to be an electric insulator. Droplets created on such a substrate could then not be imaged with STM. That is why the results presented in this part are only AFM images.

The ionic liquid, [BMIM][TFSI], was deposited on the mica substrate using the ethanol dispersion method. Depending on the concentration of the initial dispersion, the general trend revealed by AFM images was different. Three different dispersions of different concentrations were prepared. The same quantity of each dispersion was deposited on several samples of freshly cleaved mica disks. For dispersions with a low concentration, the ethanol evaporation occurs smoothly. Droplets, surrounded by a liquid film and isolated liquid film patches are observed. For dispersions of higher concentration, the observed landscape is different: droplets are still present, with a larger diameter in average, but they are not surrounded by a film. Except from the droplets, ionic liquid is present in that case as patches on the mica which do not seem to be liquid (this is going to be detailed in the following paragraphs). No matter what is the concentration of the dispersion, the shape of the patches of ionic liquid is irregular and thus reveals the presence of pinning.

In both case, the droplets observed show no foot (no deformation in the vicinity of the substrate)<sup>11</sup>. The contact angle of these droplets was measured from the AFM images and compared to the macroscopic value. It was also possible to focus on the structure of the film and patches far and close to droplets.

<sup>11</sup>As mentioned in the Appendix about AFM images, the droplets of pure IL showed only slight deformations at their base that can not be interpreted as a foot because of their narrow lateral extension compared to the lateral resolution of the AFM tip. It is worth noting that a foot with a significant lateral extension was only observed in the case of a contaminated sample.

### 3.2.4.1 Films and patches

From the general trend revealed by the AFM images, the concentration of the dispersions and then the evaporation of the ethanol seems to play a pregnant role on the morphology of the samples. Being able to compare the situation with a configuration where only pure ionic liquid is used was then important. Before further describing the structure of films and patches obtained with ethanol dispersions, let us first explore the morphology of samples where no ethanol was used.

**Pure ionic liquid** The experiment is the deposition of a large macroscopic drop using the sessile drop device, which consists in a syringe, fixed in a vertical position and with tunable dispense rate. Once the drop was deposited, the dispense was reversed and the drop was then slowly sucked by the syringe. The zones where the drop was sitting on the mica disks, zone 1, and where the drop was not sitting on the mica disk, zone 2, were imaged with the AFM (see figure 3.11). Imaging zone 1 reveals patches of ionic liquid (different phase than the mica, characteristic height around 2nm) and imaging zone 2, bare mica. The irregular rim of the patches indicates that there is pinning of the ionic liquid on the mica. In zone 1, scanning several times in a row the same zone allows one to observe that the interaction with the AFM tip (non contact mode) triggers the un-pinning of the rim of the patches, a slight spreading and coalescence phenomena. As a consequence, there is a slight variation of the surface covered by the patches. There is also a very slight decrease of the mean height of the patches which is negligible compared to the dominant effect which is the unpinning of the rim of the patches<sup>12</sup>. It is worth noting that in non-contact tapping mode, the choice of the AFM parameters is limited. If the parameters are set too “loose”, the tip does not sense the sample and images nothing. On the contrary, if the parameters are set too “tight”, the tip touches alternately the sample and the mode changes from non-contact to intermittent contact. In our case a result from this is a contamination of the tip seen on the phase image. There is then not much amplitude in the choice of the AFM parameters (see the Appendice about AFM and STM for more details).

Finally, this experiment provides the answer to the question raised when performing several advancing and receding cycles at the exact same spot of the mica. The hysteresis was then decreasing after the first cycle due to the strong decrease of the advancing macroscopic contact angle. This strong decrease found in fact its cause in the patches of ionic liquid left on the mica by the former drop: after the first cycle, the ionic liquid did not spread on bare mica anymore, but on mica covered by ionic liquid patches.

---

<sup>12</sup>The mean area covered by the patches as well as the mean height were measured using particle analysis performed respectively with the imageJ software for the mean area and with the Nanoscope Analysis software. (The imageJ particle analysis plugin can not compute the mean height and the particle analysis software of Nanoscope Analysis does not give the area fraction covered by the patches. An example of such measurement for two successive scans is presented on figure 3.12.)

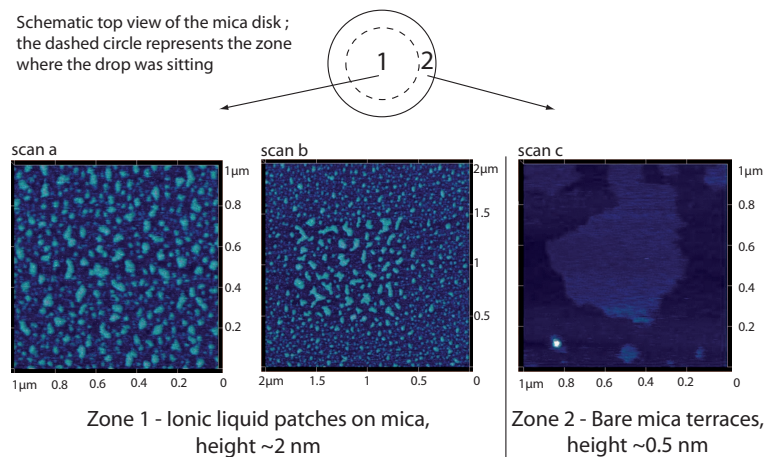


Figure 3.11: Imaging zones 1 and 2 (3D AFM images) for high purity [BMIM][TFSI] on freshly cleaved mica disk. On the left, zone 1 represents the zone where the drop was. This zone shows liquid patches of ionic liquid increasing their lateral extension when the AFM tip is scanning. Scan *a* was taken just before scan *b*. Scan *b* was taken zooming out. It presents a central square zone, corresponding to scan *a*, where the patches of ionic liquid have a greater lateral extension as this central square zone was scanned previously. The respective mean thickness of the patches for scan *a* and the central square zone of scan *b* are both of 2 nm. On the right side, scan *c* represents the bare mica in zone 2. As the image was taken close to the edge of the sample, the cleavage of the mica is less good and small terraces are visible.

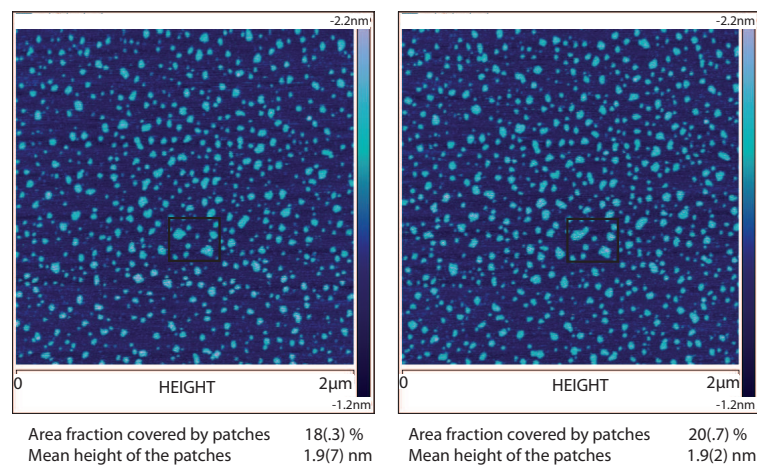


Figure 3.12: High purity [BMIM][TFSI] on freshly cleaved mica disk, zone 1. From left to right, two successive  $2 \mu\text{m}$  AFM scans showing that the patches are increasing their lateral extension due to the AFM tip that un-pins the contact line. The square focuses on the same zone for the two scans.

**Dispersions of low concentration** The dispersion deposition method leaves droplets surrounded by a film and also isolated patches on the mica<sup>13</sup>. As for the liquid patches which are formed after the retraction of a pure ionic liquid drop, the patches and the film surrounding the droplets when a low concentration dispersion is used are liquid: they show an irregular rim and spread when the AFM tip is scanning. If the film is spreading, the question of the evolution of its thickness arises. From the AFM images, the dependence in time of the thickness was measured: the position of both the film and of the mica substrate were fitted in a linear way (with the software Origin pro 8.1). The thickness was then deduced by measuring the distance between the two fitted lines (see figure 3.13). The same procedure was used for isolated patches (see figure 3.13). The general trend is that the thickness of the isolated patches is quite constant: its value is always around 2 nm as the one of the patches of pure ionic liquid. Within one patch, the surface shows small variations, but the thickness is overall constant. However, the film surrounding droplets takes different morphologies. For small droplets, base radius less than around  $1 \mu\text{m}$ <sup>14</sup>, the film is uniform in thickness, but this initial thickness is not the same for each observed droplet. There is however a common point to all the films surrounding small droplets: No matter what is the thickness of the film at the beginning of the scanning process, higher or lower than 2nm, the more the AFM tip is scanning, the more the film tends to approach this thickness of 2nm. The observation of this process was made by measuring both the average thickness of the film and the area fraction covered by the film on several successive scans.

---

<sup>13</sup>This experiment was performed with mica sheets and for synthesis [BMIM][TFSI] as well as mica disks and for synthesis and high purity [BMIM][TFSI]

<sup>14</sup>The more complex case of larger droplets is described in the last Appendix.

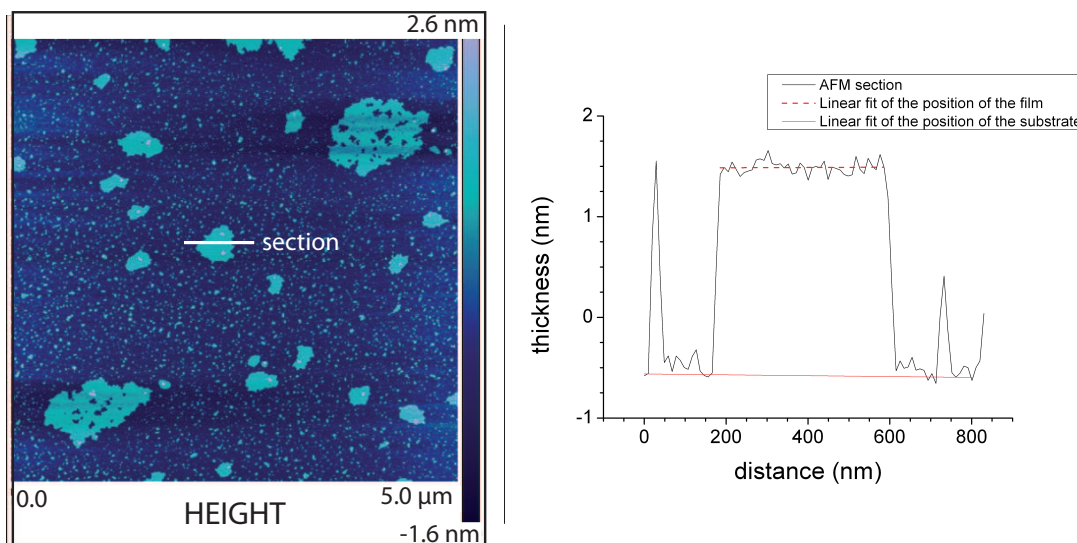


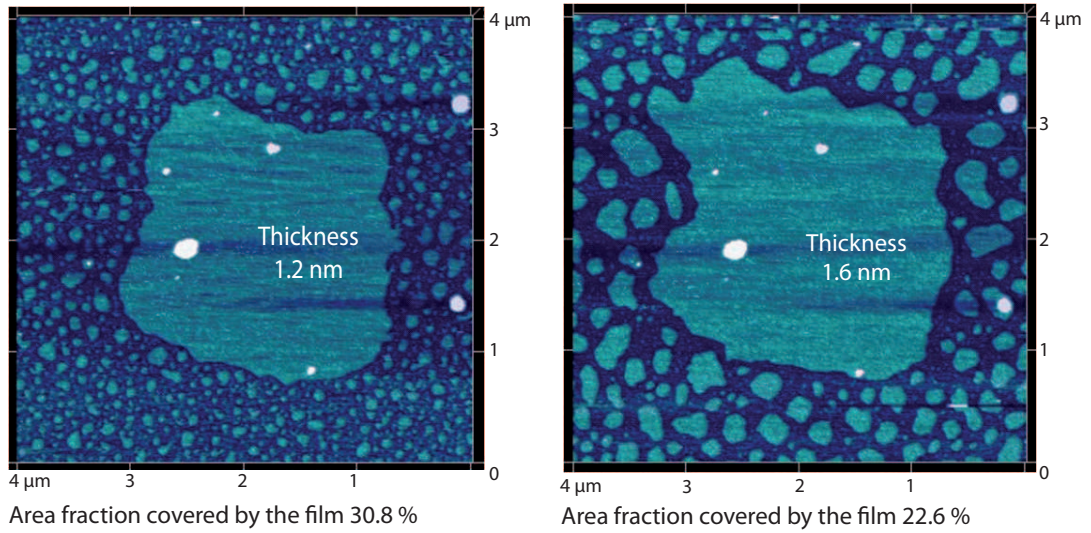
Figure 3.13: Steps for the measurement of the thickness of a film. On the left side, AFM height image of isolated patches of film of [BMIM][TFSI] on mica substrate. The white line localizes the section represented on the right side. On this section, the position of the film and the position of the substrate are fitted in a linear way. The thickness is then deduced from the distance between these two lines.

Two examples are presented on figure 3.14. In this case, there is then liquid films surrounding droplets. These films show pinning that is overcome by the scanning process, the films are then free to evolve. Their evolution always tends to go towards 2 nm which is apparently the preferential thickness for a film of [BMIM][TFSI] on mica. This is confirmed by the fact that the 2 nm value also corresponds to the thickness observed for patches of pure ionic liquid on mica.

**Dispersions of high concentration** For dispersions of high concentration, droplets are not surrounded by a film. Only small patches of ionic liquid are present all over the mica and their density decreases with the increasing concentration of the dispersion. These patches are ionic liquid as they show a different phase than the mica on the AFM phase image and are higher than the features observed on bare mica. However unlike the patches observed for pure ionic liquid and the film and patches observed when using low concentration dispersions, they do not spread when the AFM tip is scanning. It suggests that their structure might not be liquid and they might be solidified. The structure of the patches is then completely different when high concentration dispersions are used. In the vicinity of droplets, the organization of the patches sometimes happen to show a previous position of the contact line. The contact line then underwent a retraction after deposition leaving patches behind. This is another confirmation that the patches, although they do not flow are made of ionic liquid. An example of such a structure is shown on figure 3.15. The features observed when high concentration dispersions



a/ Thickness of the film below 2nm, increasing when scanning



b/ Thickness of the film above 2nm, decreasing when scanning

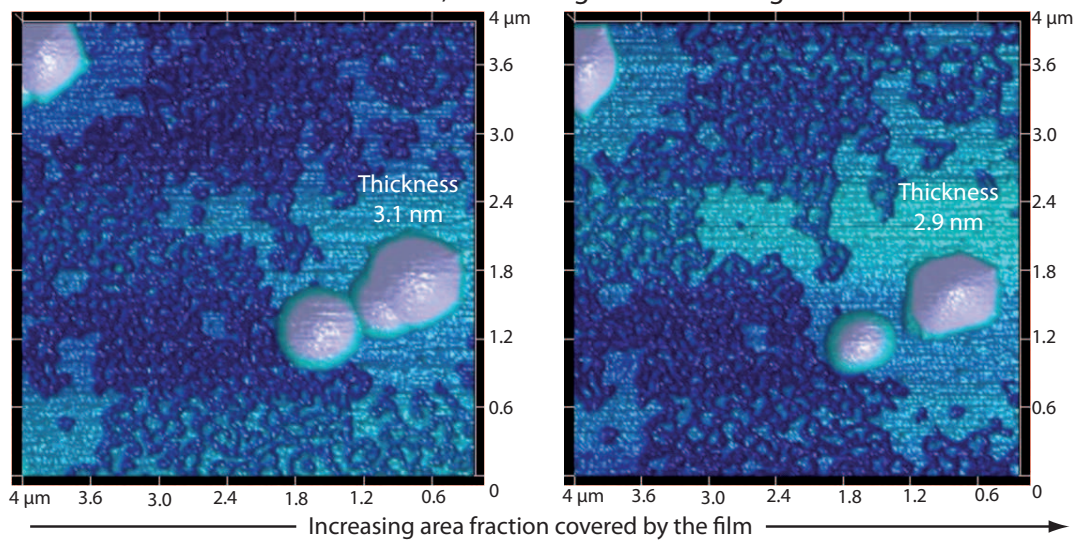


Figure 3.14: Examples of evolution of the thickness of films linked to small droplets (3D AFM images): the thickness tends to approach 2 nm. On the top, the thickness at the beginning is below 2 nm and then increases towards 2 nm when the tip is scanning. On the bottom, the thickness at the beginning is above 2 nm and then increases towards 2 nm when the tip is scanning.

are used tend to show that when the concentration is increased, the deposition process is not efficient.

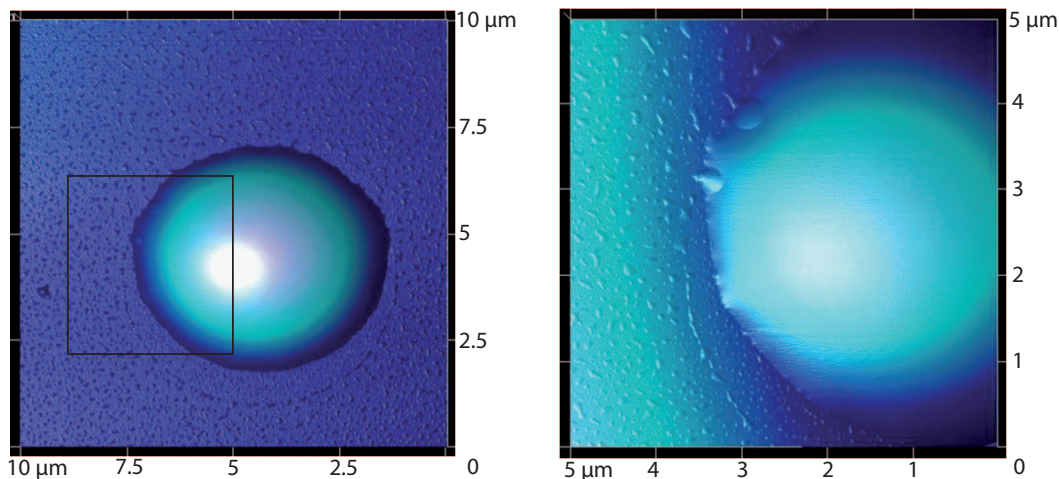


Figure 3.15: 3D AFM scans showing an organization of patches implying that the droplet retracted after deposition for high concentration dispersions. On the left side, 10  $\mu\text{m}$  scan. On the right side, zoom on the zone defined by the rectangle, 5  $\mu\text{m}$  scan.

### 3.2.4.2 “Microscopic” contact angle of ionic liquid droplets

The contact angle of the [BMIM][TFSI] droplets was measured from the unflattened height scans of the AFM<sup>15</sup>. First, sections were extracted from the AFM data (see figure 3.16). If the substrate does not appear as horizontal on the section (as the images are not flattened), the AFM section was straightened up by rotating the frame of reference. The shape of the droplet and the position of the precursor film were then fitted on the section respectively with a spherical shape and in a linear way. The tangent to the spherical shape at the intersection with the position of the precursor is then computed (see figure 3.17). The contact angle is finally deduced from the equation of this tangent<sup>16</sup>. The measurements of the contact angle of the droplets were done on samples deposited imaged at least three hours after their deposition to be sure that the contact angle is stable. The macroscopic contact angle (“equilibrium” one) of a drop deposited at the same time and in the same atmospheric conditions than the sample was also measured to ensure that there was no significant deviation from the measured mean value of the macroscopic contact angle. The results are presented in figure 3.18. Once again an effect of the concentration is observed: the lower is the concentration of the dispersion, the lower is the measured microscopic contact angle. For the range of tested concentrations, the microscopic

<sup>15</sup>AFM scans are unflattened to avoid any risk of modifying the nature of the data with flattening artefacts.

<sup>16</sup>In this method, the fits were performed with the Origin pro 8.1 software and the calculations were performed by a Java plugin designed for ImageJ. Another version of this data analysis process, easier to use, was developed in Mathematica.

contact angle is always below the macroscopic “equilibrium” contact angle even for radii that are more than  $1\ \mu\text{m}$ . At a scale corresponding to  $1\ \mu\text{m}$ , line effects should in principle not be so important and the contact angle should be close to the macroscopic value. For a comparison with a system with a non-volatile liquid showing an evolution of the microscopic contact angle with the radius of the droplets, see the discussion presented in Chapter 1 about the work of Berg et al. The results are interpreted in terms of line-tension effects. The non-evolving contact angle of the droplets with the radius of the droplets is then puzzling.

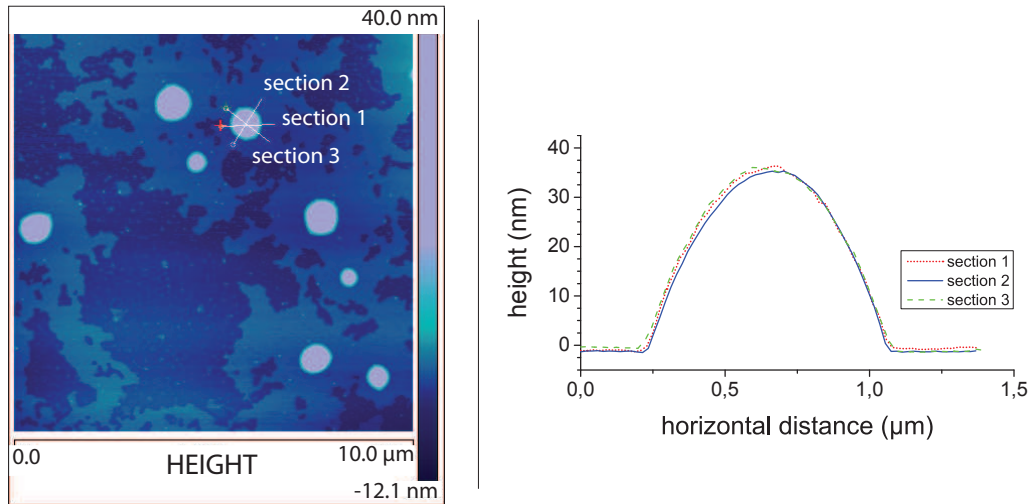


Figure 3.16: On the left side, AFM height image. The white lines represent the position of the three sections plotted on the right side of the image. The fact that the three sections of the same drop overlay each other prove that the shape of the drop is axisymmetric. Moreover, the fit with a spherical cap is excellent.

### 3.2.4.3 Films, patches and droplets: Summary and discussion

The results of the present experiments are summarized in the figure 3.19.

At this stage, a few comments can be made about the preceding results<sup>17</sup>:

- The difference between the results obtained with low and high concentration dispersions should result from the deposition step as there is no ethanol left at the moment of the imaging. The spreading process of the dispersion and the evaporation process of the ethanol obviously differ when the concentration is changed. No quantitative analysis of this dependence is available yet.

<sup>17</sup>The complex case of droplets with larger base radius, deposited with a low-concentration dispersion is discussed in the last Appendix.

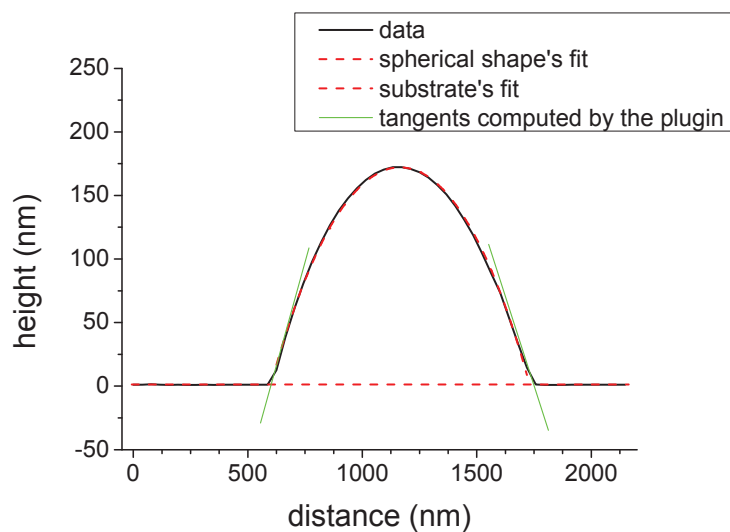


Figure 3.17: Analysis of a profile extracted from an AFM image. The red dotted lines represent the fit of the droplet (by a spherical shape) and the linear fit of the position of the precursor. The calculated tangents to the spherical shape at the intersection with the position of the precursor are presented in bright green.

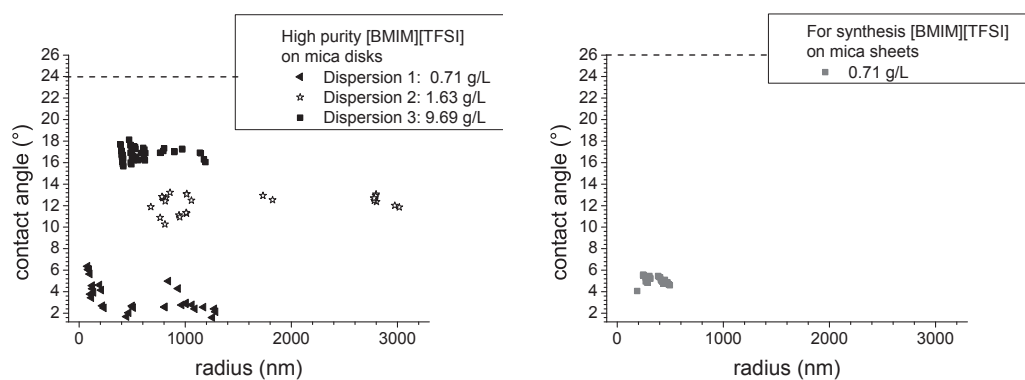


Figure 3.18: Contact angle of droplets of [BMIM][TFSI] on mica substrates. A deviation to the macroscopic “equilibrium” contact angle (dashed line on the graphs), depending on the concentration of the dispersion, is observed. On the left side, high purity [BMIM][TFSI] on mica disks; On the right side, for synthesis [BMIM][TFSI] on mica sheets. The results do not depend significantly on the quality of the mica or of the ionic liquid.

		High purity [BMIM][TFSI]	For synthesis [BMIM][TFSI]
	Surface tension	$32.6 \pm 0.2$ mN/m	$32.0 \pm 0.6$ mN/m
	Macroscopic «equilibrium» CA	$24 \pm 4^\circ$	$26 \pm 5^\circ$
	Film		indications of the presence of a film (dust experiment, XPS)
Pure IL, no dispersion in ethanol	Film / patches	Patches, spreading when the tip is scanning	
Low concentration 0.71 g/L	Microscopic «equilibrium» CA	$4 \pm 2^\circ$	$5 \pm 1^\circ$
	Film / patches	Film around droplets and patches, spreading when the tip is scanning	Film around droplets and patches, spreading
High concentration	Microscopic «equilibrium» CA	for 1.63 g/L : $12 \pm 2^\circ$	
		for 9.69 g/L: $17 \pm 2^\circ$	
	Film / patches	Patches, NOT spreading when the tip is scanning	

Figure 3.19: Summary of the results concerning film, patches and droplets of ionic liquid on mica.

- The influence of the scanning process, which allows for unpinning the ionic liquid is fundamental for any of the observations made on microscopic scales.
- Then, we have to make clear what "equilibrium" means in the present case, and to what extent a thermodynamic analysis in terms of free energy can be used.

These are two fundamental questions.

As mentioned in Chapter 1, equilibrium is very slow if transport occurs only through thin films and is probably never reached if pinning is present. Here, the scanning process of the AFM helps depinning and liquid transport. Results converge towards a 2 nm thick film, which is probably the "equilibrium" one. "Equilibrium" film means that it is the films with a thickness  $h_0$  such that  $\Pi(h_0) = 0$ <sup>18</sup>. This film would be the one in equilibrium with a macroscopic drop.

Considering the thermodynamic analysis, the droplet in figure 3.16 has a maximum thickness around 35 nm, that is much smaller than the range,  $l$ , of molecular interactions across a flat film (see Chapter 1). The important point when dealing with nanometric droplets is that thickness and lateral dimensions are similar. The typical characteristic length above which thermodynamic quantities as surface tension can be defined is now the Tolman length [15], [12] which is of the order of nanometers. The good fit of nanometric droplets with spherical shapes is therefore not surprising [2].

However, the microscopic contact angle of our nanometric droplets of ionic liquids does not change clearly with droplets' radius (figure 3.18), although it is significantly smaller than the macroscopic contact angle. One may argue that the scanning process of the AFM does not allow to reach full equilibrium for droplets, which prevents any quantitative analysis in terms of line tension.

#### 3.2.4.4 Solidification

Solid patches were observed both on droplets and on precursor films. For droplets, the solid patches are seen on the AFM height image as zones where the spherical-shaped profile is modified. This corresponds to the observation of a different phase on the phase image which is the sign of a different nature than the ionic liquid<sup>19</sup>. Considering that the substrate is smooth, the patches can not be constituted of mica ; and considering the phase image, they can neither be constituted of ionic liquid. As no other material should be left on the sample after the evaporation of the ethanol, this leads to the conclusion that the patches must be made of solidified ionic liquid. This seems coherent with the shape of the patches observed on the height images (see figure 3.21). Smaller solid patches were also observed in precursor films. For precursors, unlike the case of droplets, solidification does not constitute an important perturbation: the thickness of

<sup>18</sup>Being totally rigorous, the disjunction pressure is defined for a continuous film, a film with a large lateral extension and uniform in thickness. Although it is not the case for our system, the general behaviour of the system as well as the stable 2 nm thick patches let us think that it could be a relevant hypothesis.

<sup>19</sup>On AFM scans, a different phase on one zone of the sample which is imaged indicates that the physical nature of the material is different. For further details, see the appendix about AFM imaging.

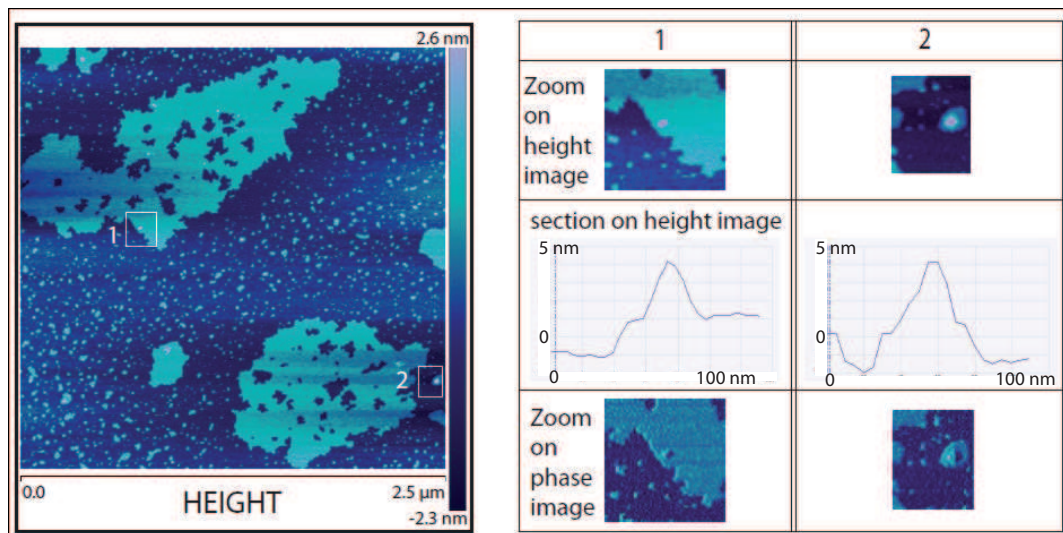


Figure 3.20: Solidification patches on a precursor film. On the left side, AFM height image. The two white rectangles show the zones corresponding to the ones presented on the tabular on the right side. In the tabular zooms on height and phase images are presented. The solid patches correspond to the bright zones in height, i.e. thick zones, and to the dark zones in phase, i. e. different nature than the ionic liquid. The two sections of height images presented in the tabular allow one to see that the shape of the patches looks like solid material.



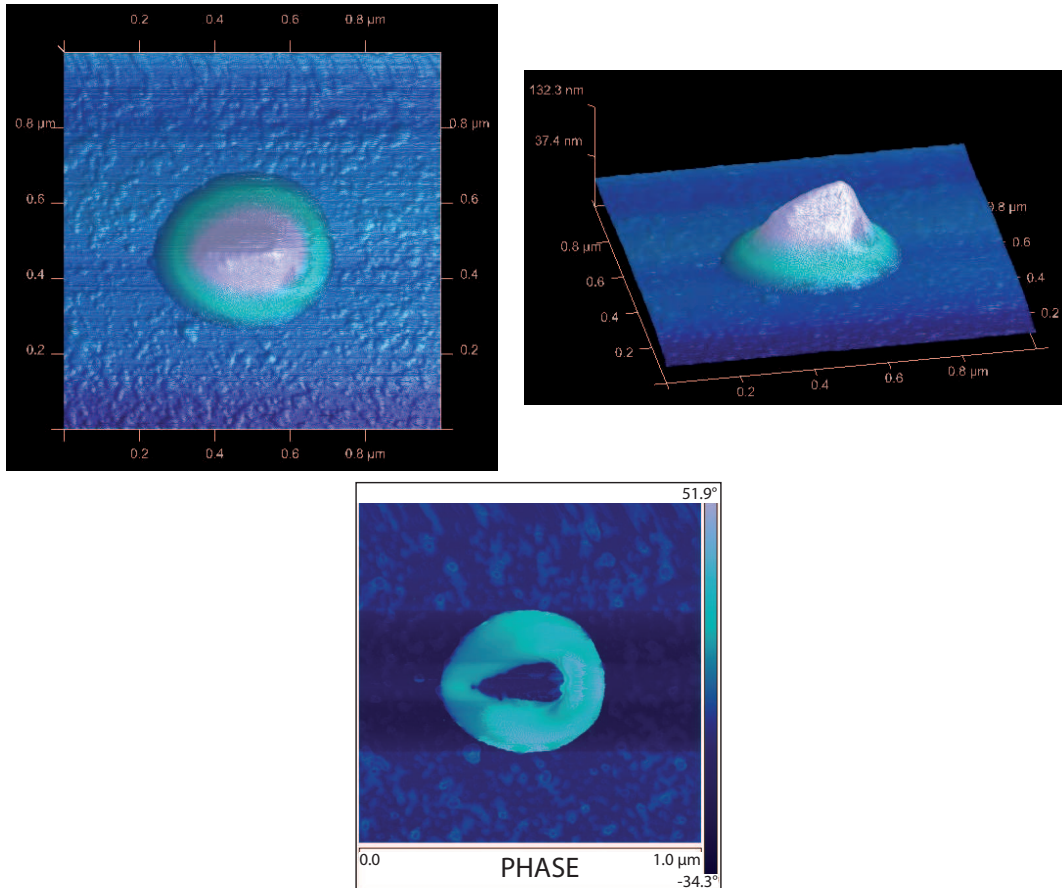


Figure 3.21: Solidification in a droplet. The first two images on the bottom are 3D images seen respectively from the top and from a tilted angle. The image seen from a tilted angle allows one to distinguish the shape of the “droplet” which looks as if its core was solid. On the bottom, the corresponding phase image clearly shows two different zones: the bright zone corresponds to liquid ionic liquid and the dark one in the core of the droplet to the solidified patch.



the precursor is unchanged by the presence of solid patches as long as the area of the precursor patches is much larger than the characteristic lateral size of the solid patches.

### 3.3 Influence of roughness and porosity, evaporated carbon

#### 3.3.1 Evaporated carbon: SiOTSC

Evaporated carbon substrates were developed initially with the hope to obtain smooth substrates of lower surface energy than mica. However, the evaporation process led to rough porous substrates and allowed us to make other observations.

##### 3.3.1.1 Developing evaporated carbon (SiOTSC) substrates

Evaporated carbon substrates are made in several steps. First, a silicon wafer, thoroughly cleaned is coated with Octadecyl-TrichloroSilane (OTS)<sup>20</sup>. The OTS coating results in the modification of the surface energy of the silicon wafer. It can be verified by deposition of water. The concentration of the coating solution (OTS diluted in toluene) and the time of immersion of the silicon wafer in the OTS solution allow for the tuning of the contact angle obtained. In our case, the silicon wafers were coated in order to get a contact angle of 60° for a drop of water. After this step, the surface will provide a good adhesion of the evaporated carbon. Once the OTS coating is performed, a layer of 20 nm of carbon is evaporated on the wafer (This last step was performed with the help of S. Abott). After the evaporation, the substrates should be blown with nitrogen gun to remove exceeding carbon dust. The substrates are then ready for use. They will be referred to as “SiOTSC” because of their preparation process.

##### 3.3.1.2 Characterization of the substrates

The characterization of the SiOTSC substrates was done in two steps. They were first imaged with AFM and then by STM as the carbon coating makes SiOTSC substrates conductive. AFM scans show a rough surface with small pillars: they seldom exceed 20 nm in height (see figure 3.22). The pillars are aligned along the evaporation direction. After AFM imaging, STM imaging revealed a surprising structure of the SiOTSC substrates which could not be imaged with the AFM because of the geometry of the tip. SiOTSC substrates indeed possess small pores which minimum lateral extension is 10 nm<sup>21</sup>. To summarize, SiOTSC substrates are then a new kind of anisotropic substrates with multiscale roughness and porosity. The roughness characteristics of the substrates were measured from the STM images:

---

<sup>20</sup>The cleaning process consists in: Sonication in ethanol ; Rinsing with milliQ water ; sonication in acetone ; rinsing with milliQ water ; drying with nitrogen gun ; piranha cleaning (2/3 pure sulfuric acid for 1/3 hydrogen peroxyde) ; rinsing with milliQ water ; drying with nitrogen gun ; plasma cleaning ; removing eventual remaining dust particles with nitrogen gun.

<sup>21</sup>The succession of pillars and pores with such a small lateral extension did not allow for the AFM tip to penetrate into the pores and then to image them. See the appendix about AFM imaging for further details.

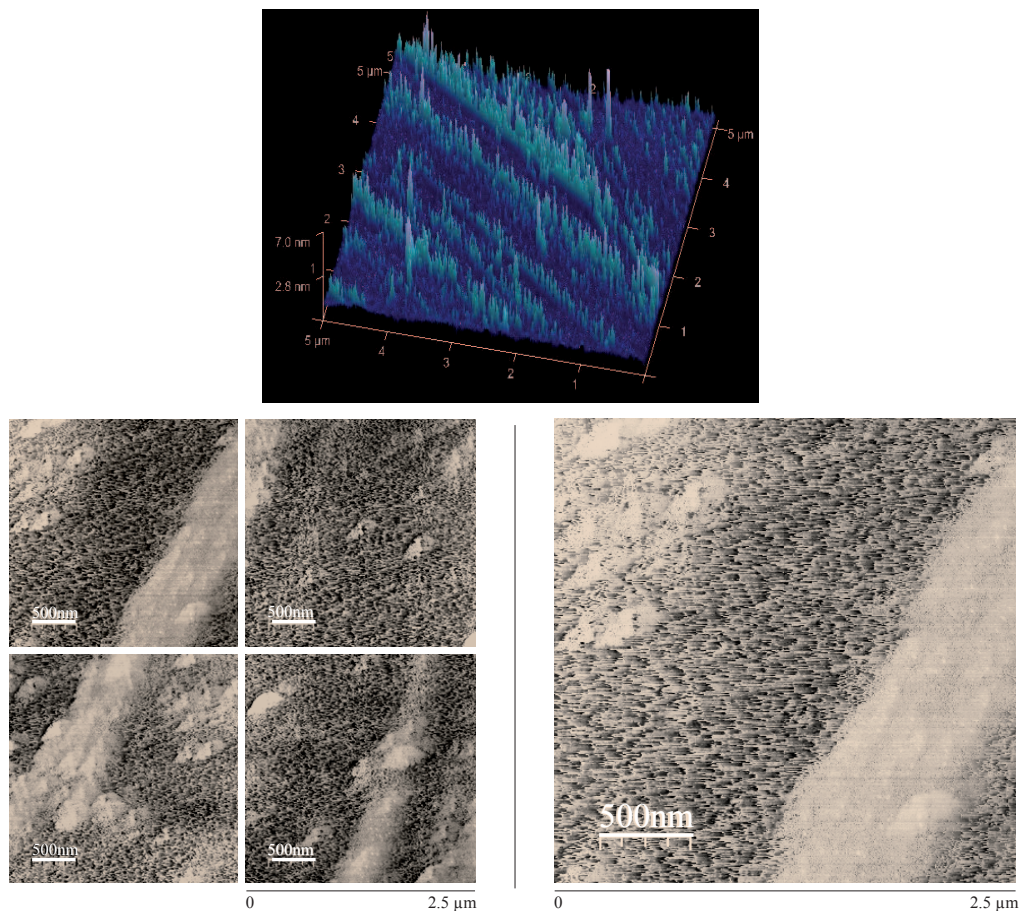


Figure 3.22: On the top,  $5 \times 5 \mu\text{m}$  3D AFM image of SiOTSC substrate. On the bottom, left side, four  $2.5 \times 2.5 \mu\text{m}$  STM scans. On the right side, zoom on one of the four STM scans. The pores appear as black zones.

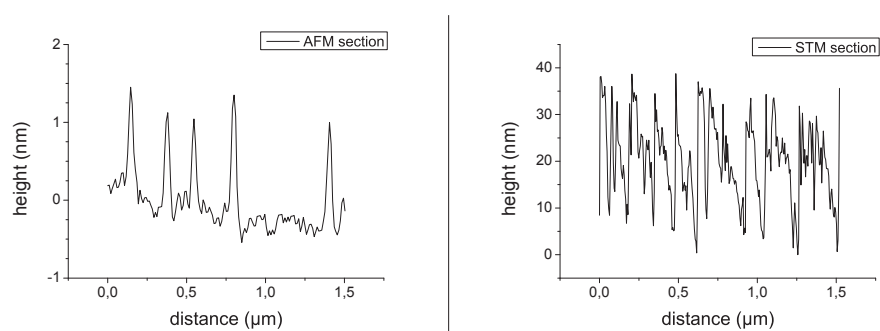


Figure 3.23: Cross-sections of AFM and STM images showing that AFM images do not allow for the observation of porous structures. Scales in distance are the same, but not scales in height.

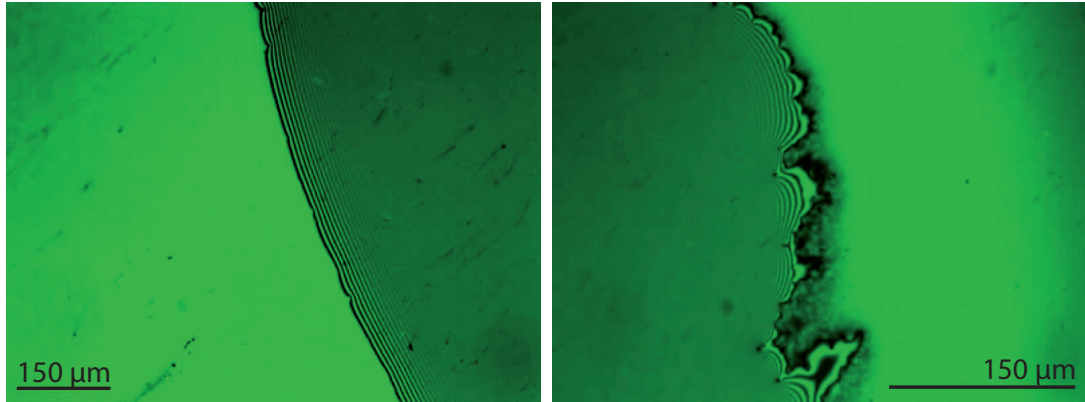


Figure 3.24: On the left side, microscope image of a macroscopic drop of [BMIM][TFSI] on SiOTSC taken 5 min after deposition. On the right side, the same drop, 2h30min after deposition: the contact line is more deformed than at the beginning due to the spreading of the ionic liquid inside the roughness.

RMS roughness	Roughness average	average peak to peak value	max peak to peak value	min peak to peak value
7.2 nm	5.6 nm	64.5 nm	101.4 nm	47.1 nm

From the roughness measurements, it appears that the three-phase contact line of liquid deposited on such a substrate will certainly be pinned on the pillars. It is also likely that for macroscopic contact angles lower than  $90^\circ$ , liquid will penetrate partially into the pores. These hypotheses will be verified by the deposition of macroscopic and microscopic quantities of ionic liquids.

### 3.3.1.3 Macroscopic wetting behaviour

As described in Chapter 1, the effect of roughness is to increase the natural tendency observed on the corresponding smooth substrate: for a smooth substrate which contact angle is above  $90^\circ$ , the contact angle on a corresponding rough substrate will increase and for a smooth substrate which contact angle is below  $90^\circ$ , the contact angle on a corresponding rough substrate will decrease. HOPG substrates (see 3.4) are made of the same material than SiOTSC substrates, but are smoother. One then expects the natural wetting tendency of [BMIM][TFSI] on HOPG to be emphasized on SiOTSC. The macroscopic advancing contact angle of [BMIM][TFSI] deposited on HOPG (i.e. maximum value of the contact angle for the [BMIM][TFSI] / HOPG system) is of  $53.7 \pm 4.0^\circ$ , the contact angle on SiOTSC is then expected to be less than this value. Deposition of a macroscopic quantity of [BMIM][TFSI] indeed leads to drops which contact angle is very low. The contact angle is in fact so low that it could not be measured with the sessile drop method. Instead, measurements were performed by interferometry which is well-adapted to the case of

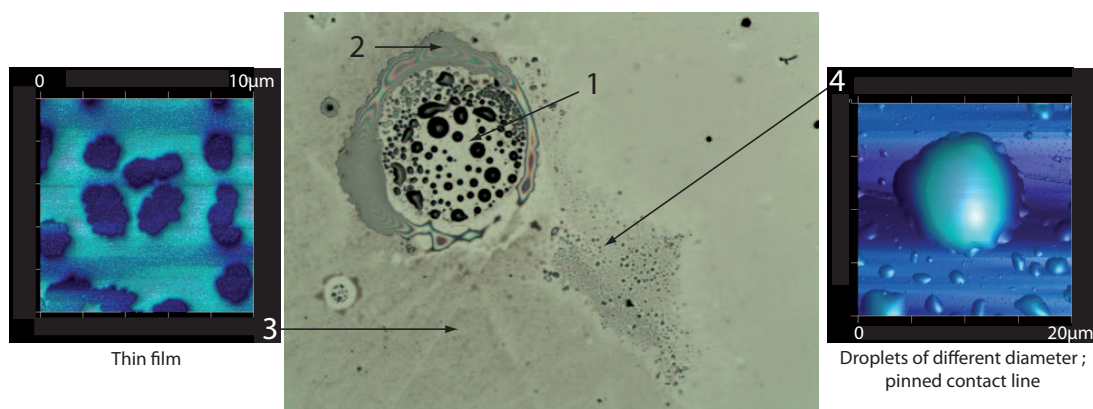


Figure 3.25: Center of the image: image of optical microscope of a sample of SiOTSC with [BMIM][TFSI] deposited by the dispersion method. The different zones are marked by numbers. At the center, in zone 1, drops of ionic liquid are present. They are surrounded by a thick film in zone 2. At the fringe, zones 3 and 4 show respectively thin film and droplets of different size. Corresponding 3D AFM images are presented on both sides of the central picture.

low contact angles (see the appendix about macroscopic contact angle measurements methods). Drops of ionic liquid were then observed under an optical microscope with monochromatic green light (wavelength  $560\text{ nm}$ ). Following the evolution of the shape of the drops with time, it was possible to observe that the contact line of the drops which was at first rather smooth underwent deformations as time elapsed (see figure 3.24). The deformations are due to the fact that some liquid penetrates into the large-scale roughness (that is, between the lines of pillars, which distance is in the micrometer range) ahead of the main drop (see figure 3.24) and then probably inside the pores. This explains the very low contact angle values: basically, the main drop fills the roughness. The contact angle of the drops could be measured on short time scales. On long time scales, only mean values of local contact angles could be measured:

time elapsed	mean contact angle	number of measurements
5 min	$3.1 \pm 1.5^\circ$	80
50 min	$1.8^\circ$ (max value: $3.9^\circ$ )	22
2h30min	$1.5^\circ$ (max value: $5.1^\circ$ )	18

Although on long time scales, the results show large error bars, a clear decrease of the macroscopic contact angle is observed with time. The contact angle finally stabilizes itself at the very low value of  $1.5^\circ$ . Such a small macroscopic contact angle is convenient to image the droplets with the AFM: if the contact angle is low, the droplets will be quite flat and there will thus be no risk of exceeding the vertical resolution of the AFM tip.

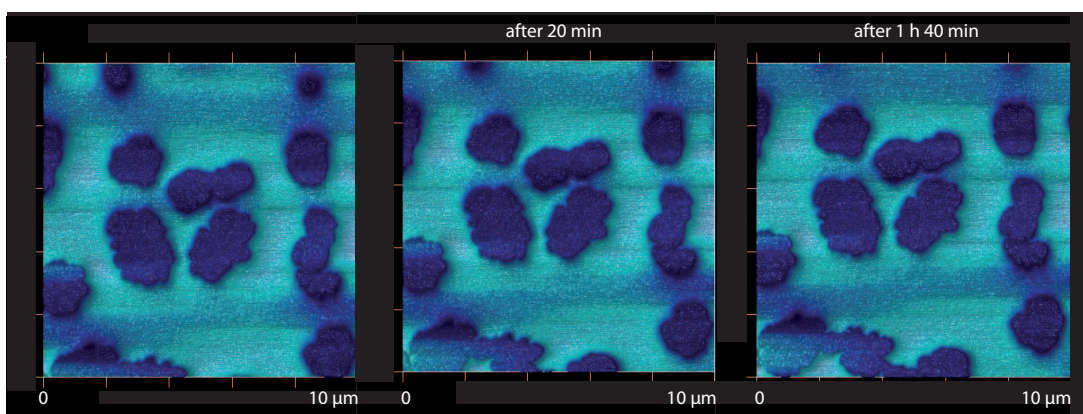


Figure 3.26: 3D AFM scans showing that the thin film of [BMIM][TFSI] does not evolve with time.

### 3.3.1.4 Microscopic wetting behaviour

The ionic liquid was first deposited using the dispersion method. The deposition of [BMIM][TFSI] via the dispersion method follows a specific scenario on a rough substrate such as SiOTSC. The solution first spreads on the sample. Evaporation of ethanol then begins at the edges. The film of ethanol and [BMIM][TFSI] then breaks itself in several locations leaving “cells” of solution. The evaporation of the “cells” then carries on smoothly. The resulting sample is then organized around several cores which correspond to the location of the center of the former “cells”. Observing the cores under optical microscope reveals different zones (see figure 3.25). The general picture looks like an atoll: at the center, drops of ionic liquid (1) are surrounded by a thick film (2) ; on the fringe of the thick film, two structures coexist which are thin film (3) and droplets (4). AFM imaging was performed on the thin film and on the droplets zones.

AFM scans of zone 3 show a thin film of [BMIM][TFSI] which thickness is  $15.8 \pm 3.7 \text{ nm}$ , similar to pillar’s height. This film is thicker than the precursor films observed on mica and does not evolve in time. The same zone of film was indeed followed during 2h without showing any change (see figure 3.26).

Imaging zone 4 reveals droplets of different size which contact line is pinned on the defects (pillars) of the substrate. Contact angle measurements on such droplets then show large error bars. A vibration experiment was then developed with the hope of partially de-pinning the contact line of the droplets. The effect of vibration should indeed consist in observing only mean behaviour on the treated sample ([11]). This is what should happen for rough substrates showing no porosity. In our case, because of the porous structures, the behaviour of vibrated samples was found to be different. The vibration was applied using a loud speaker. An amplified acoustic signal of low frequency and sinusoidal shape was sent to the loud speaker on which the sample was fixed. This experiment was performed on samples where the ionic liquid was deposited by

the dispersion method and by the paintbrush-syringe method ; the results showed the same trend in both cases. After vibration, AFM images did not show a clear de-pinning of the three-phase contact line: the fractal number of the rim of the droplets was of  $1.12 \pm 0.06$  before vibration and of  $1.11 \pm 0.06$  after vibration<sup>22</sup>. Moreover, a qualitative observation of droplets of the same diameter before and after vibration indicated that after the vibration, the height of the droplets decreased. This observation is only qualitative as the AFM that we used does not allow us to find and image the same zone of the sample before and after vibration. Comparisons can only be done on drops of the same diameter and not on the same drop: they can thus only be considered as qualitative results. Another qualitative observation showing the same trend is the measurement of contact angles for drops of the same diameter before and after vibration. Two examples are presented in the table below:

	radius	contact angle
before vibration - first drop -	2.30 $\mu m$	4.1°
after vibration - second drop -	2.28 $\mu m$	3.2°
before vibration - third drop -	2.62 $\mu m$	5.2°
after vibration - fourth drop -	2.66 $\mu m$	4.0°

Finally, because the pinning of the three-phase contact line stays the same after the vibration treatment and because the height and contact angle of droplets seem to decrease, some ionic liquid must penetrate further into the pores of the substrate.

### 3.4 Forward study: STM imaging of droplets of ionic liquids

To our knowledge, STM imaging was never used to image liquid droplets although unlike AFM images, STM images do not show artefacts due to the geometry of the wire (see the appendix about AFM and STM imaging). The reason for this is that STM imaging requires that both substrate and liquid should be conductive. Ionic liquids are conductive liquids and are non volatile, they thus constitute a proper system to develop STM imaging of droplets. For this forward study, a conductive substrate was chosen: Highly Ordered Pyrolytic Graphite (HOPG). HOPG is grade 1 purchased from SPI (SPI-1). This choice was not randomly made as HOPG is easily imaged under STM. Studies of small quantities of ionic liquids deposited on HOPG also have already been performed under AFM and led to a controversy about the presence of droplets: Yokota et al. did not observe any droplets [18], whereas Bovio et al [3] report their existence. In this context, AFM and STM studies of the system present a double interest: developing a new way to image ionic liquid droplets and answering the question about the possible formation of ionic liquid droplets on HOPG.

---

<sup>22</sup>The fractal dimension is measured from the AFM scans. The contour of the droplets is first isolated from phase images. This step is performed on phase images as they show a clearer picture of the contour of the drop as they are free from artefacts due to the geometry of the tip. The fractal dimension of the contour is then measured using the “FracLac” plugin of imageJ which is based on an evolved box-counting method.



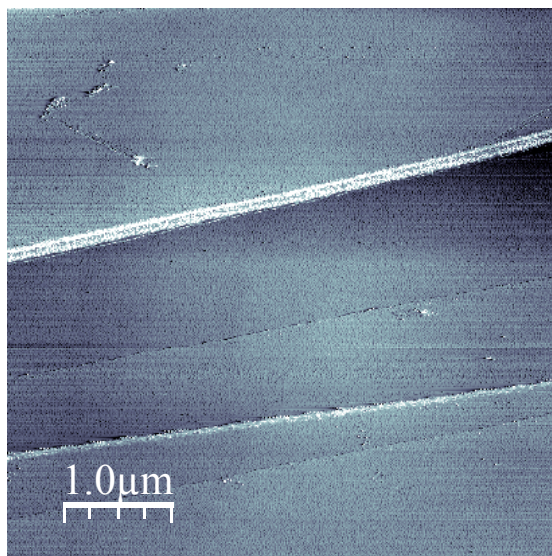


Figure 3.27: STM  $5 \times 5 \mu\text{m}$  scan of a freshly cleaved HOPG substrate.

### 3.4.1 Characterization of HOPG substrates

HOPG is a succession of graphite sheets. The more ordered is the HOPG, the more cleavable it is. The degree of order is then quite important as it will determine the quality of the HOPG substrates which are made with freshly cleaved HOPG. If the cleavage is good, there will indeed be less frontiers between different atomic planes on the surface of the substrate. However, cleaving HOPG is more difficult than cleaving mica and the terraces obtained were never as large as the ones obtained for mica substrates. AFM and STM imaging of the HOPG substrates were done (a characteristic STM scan is presented on figure 3.27). Measurements of the macroscopic contact angle of [BMIM][TFSI] on HOPG were also performed using the sessile drop method. The macroscopic advancing and receding contact angles were found to be respectively of  $53.7 \pm 4.0^\circ$  and  $22.4 \pm 3.2^\circ$ . As in the case of mica, because of the frontiers between different terraces, the contact line showed a stick / slip behaviour during the sessile drop experiment, thus explaining the large hysteresis value. Furthermore, the fact that the macroscopic contact angle is below  $60^\circ$  is again a good configuration for AFM imaging.

### 3.4.2 AFM and STM: Microscopic wetting behaviour

For both AFM and STM studies, HOPG was cleaved just before the deposition of [BMIM][TFSI]. The ionic liquid was deposited using both the paintbrush-syringe method and the dispersion method. First, AFM imaging showed droplets pinned on the frontiers between the terraces of HOPG see figure 3.28. Further investigation would be required in order to measure the

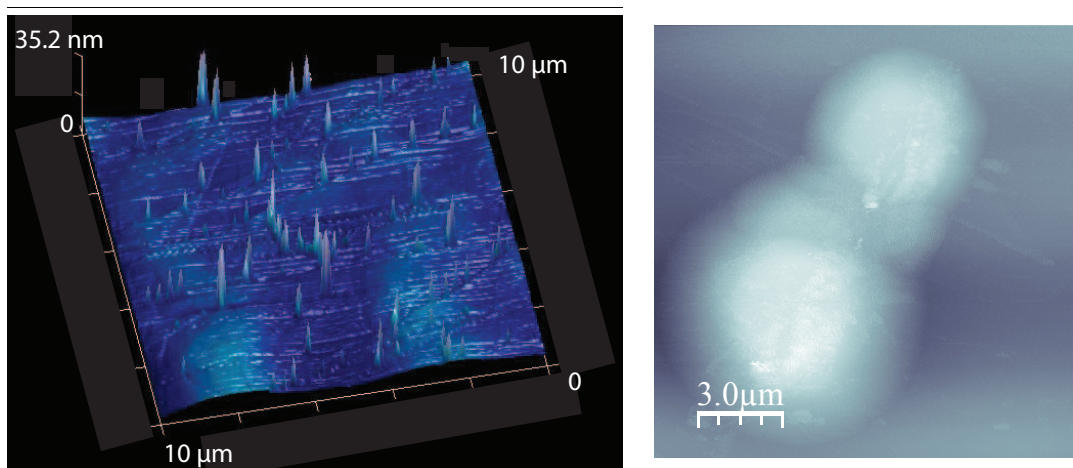


Figure 3.28: On the left side, a  $10 \times 10 \mu\text{m}$ , 3D AFM scan showing droplets of [BMIM][TFSI] pinned on the frontiers of the terraces of freshly cleaved HOPG. On the right side, first attempt of STM imaging for a droplet of [BMIM][TFSI] on HOPG. On the  $15 \times 15 \mu\text{m}$  scan, the droplet also shows pinning.

microscopic contact angle in function of the radius. If droplets could be imaged via STM, data would be even more precise and a non-deformed picture of the foot of the droplets could be provided. A first attempt of STM experiment was performed with M. Krasowska for droplets deposited using the paintbrush-syringe method. A relatively big droplet could be imaged (see figure 3.28). The droplet is not circular due to the deposition method as in the paintbrush-syringe deposition method, the droplets are “thrown” onto the substrate as explained before. The imaging parameters could also be further improved, but the droplet is well-imaged which is a promising result.

### 3.5 Discussion and perspectives

This Chapter presented an exploration of the microscopic wetting properties of ionic liquids on different substrates (mica, SiOTSC, HOPG). None of these substrates proved to be easy to study, but they revealed interesting phenomena.

On mica, the concentration of the dispersions used to deposit the ionic liquid played a major role on the wetting behaviour at small-scales. The films of ionic liquid showed indeed a different structure, liquid for low concentration dispersions and possibly solidified for high concentration dispersions. Focusing on the patches and films, the situation where low-concentration dispersions are used can be compared to the one of the patches left after the aspiration of a macroscopic drop of pure ionic liquid. In that case, it seems possible to propose an explanation although further analysis is required. On the other hand, for the conductive substrates, SiOTSC and



HOPG, analyzing the results is difficult. While it would be quite interesting to use a conductive substrate in order to get rid of geometrical artifacts due to the AFM tip, the comprehension of behaviours controlled by porosity, roughness and pinning is a prerequisite before going any further.

Pinning plays clearly an important role on the microscopic wetting behaviour of ionic liquids even on quite smooth substrates as mica. On mica, the heterogeneities of the surface (mica is a mineral and hence possesses non-identical sites at its surface), and the fact it is charged led to a complex wetting behaviour. However, despite the irregular shape of the observed patches obtained on mica, the existence of the ubiquitous 2 nm film suggests that the substrate induces a structuration of the first IL layers. Knowing the exact structure of this 2 nm film would provide information on mica / ionic liquid interactions. XPS studies or X-ray reflectivity could for example be used. X-ray reflectivity measurements were already performed for ionic liquids on sapphire substrates [8]. The results showed a layering, but could not lead to a clear conclusion on the exact structure of the ionic liquid layers. Numerical simulations done on graphite substrate [7] gave the same trend. Considering this trend and the average size of an ion pair of [BMIM][TFSI], a rough calculation could bring clues about the possible number of layers. As the size of an ion pair of [BMIM][TFSI] is around 0.8 nm and the film is 2 nm thick, one possible scenario would then be a tilted trilayer. It is worth noting though, that the correlated pair anion / cation has an elongated shape [8] therefore the relative orientation of ion pairs allows one to fit the observed thickness. A modelization of the structure using relevant interaction potentials is then a pre-requisite for any analysis of the observed thickness.

At the beginning this study was carried on with the hope of observing a contact angle dependence on the base radius of the droplet at small scales that could have given access to line tension. There is indeed a variation of the contact angle, but it is not clearly related to line tension. What is required now is to write the equilibrium or quasi-equilibrium of a nanometric droplet with its film in terms of surface forces, structuration and pinning.

# Bibliography

- [1] R. Atkin, N. Borisenko, M. Drüschler, S.Z. El Abedin, F. Endres, R. Hayes, B. Huber, and B. Roling. An in situ STM/AFM and impedance spectroscopy study of the extremely pure 1-butyl-1-methylpyrrolidinium tris(pentafluoroethyl)trifluorophosphate/Au(111) interface: potential dependent solvation layers and the herringbone reconstruction. *Phys. Chem. Chem. Phys.*, 13:6849–6857, 2011.
- [2] J.K. Berg, C.M. Weber, and H. Riegler. Impact of negative line tension on the shape of nanometer-size sessile droplets. *Phys. Rev. Lett.*, 105:076103, 2010.
- [3] S. Bovio, A. Podesta, and P. Lenardi, C.and Milani. Evidence of extended solidlike layering in [bmim][ntf2] ionic liquid thin films at room-temperature. *JOURNAL OF PHYSICAL CHEMISTRY B*, 19:6600–6603, 2009.
- [4] A. Checco, P. Guenoun, and J. Dailant. Nonlinear dependence of the contact angle of nanodroplets on contact line curvature. *Phys. Rev. Lett.*, 91:186101–1–4, 2003.
- [5] Fabio Di Francesco, Nicola Calisi, Matteo Creatini, Bernardo Melai, Pietro Salvo, and Cinzia Chiappe. Water sorption by anhydrous ionic liquids. *Green chemistry*, 13:1712–1717, 2011.
- [6] J. Jacquemin, P. Husson, Padua A.A.H., and V. Majer. Density and viscosity of several pure and water-saturated ionic liquids. *Green chemistry*, 8:172–180, 2006.
- [7] Sha Maolin, Zhang Fuchun, Wu Guozhong, Fang Haiping, Wang Chunlei, Chen Shimou, Zhang Yi, , and Hu Jun. Ordering layers of [bmim][pf6] ionic liquid on graphite surfaces: Molecular dynamics simulation. *J. Chem. Phys.*, 128:134504, 2008.
- [8] Markus Mezger, Heiko Schröder, Harald Reichert, Sebastian Schramm, John S. Okasinski, Sebastian Schöder, Veijo Honkimäki, Moshe Deutsch, Benjamin M. Ocko, John Ralston, Michael Rohwerder, Martin Stratmann, and Helmut Dosch. Molecular layering of fluorinated ionic liquids at a charged sapphire (0001) surface. *Science*, 322:424–428, 2008.
- [9] F. Mugele, T. Becker, R. Nikopoulos, M. Kohonen, and S. Herminghaus. Capillarity at the nanoscale: an afm view. *Journal of Adhesion Science and Technology*, 16:951–954, 2002.

- [10] Y. Ohmasa, T. Hoshino, R. Osada, and M. Yao. Surface waves at the liquid-vapor interface of ionic liquid [bmim][tfsi]. *Chemical Physics Letters*, 455:184–188, 2008.
- [11] David Quéré. Non-sticking drops. *Rep. Prog. Phys.*, 68:2495–2532, 2005.
- [12] J.S. Rowlinson and B. Widom. *Molecular Theory of Capillarity*. Dover publications, 2003.
- [13] K.W. Stöckelhuber, B. Radoev, and H.J. Schulze. Some new observations on line tension of microscopic droplets. *Colloids and Surfaces A: Physicochemical and Engineering Aspects*, 156:323–333, 1999.
- [14] F. Tiberg and A.M. Cazabat. Spreading of thin films of ordered nonionic surfactants. origin of the stepped shape of the spreading precursor. *Langmuir*, 10:2301–2306, 1994.
- [15] R.C. Tolman. The effect of droplet size on surface tension. *J. Chem. Phys.*, 17:333, 1949.
- [16] François Vandenbrouck. *Films minces de cristaux liquides*. PhD thesis, Université Paris VI, 2001.
- [17] JY Wang, S Betelu, and BM Law. Line tension effects near first-order wetting transitions. *Phys. Rev. Lett.*, 83:3677–3680, 1999.
- [18] Y. Yokota, T. Harada, and K.I. Fukui. Direct observation of layered structures at ionic liquid/solid interfaces by using frequency-modulation atomic force microscopy. *Chem. Commun.*, 46:8627–8629, 2010.
- [19] F.C. Zhang, M.L. Sha, Ren X.P., Wu G.Z., J. Hu, and Y. Zhang. Morphology and wettability of bmim-pf6 ionic liquid on hopg substrate. *Chin. Phys. Lett.*, 27:086101–1/4, 2010.

# General conclusion

Complex small-scales wetting phenomena were presented: liquid crystals on liquid substrates and ionic liquids on solid substrates. Answers to the common questions “what happens when going towards smaller scales and how does the growing role of interfacial interactions induce structural changes” were specific of the investigated systems. In both cases, the changes when going towards small scales were major and complex ones. Elasticity and anchoring played the main role for liquid crystals, while it was pinning and structuration by the substrate for ionic liquids. It is worth noting that there was also a difference in spatial scales. For liquid crystals, thin nematic films have macroscopic extension whereas their thickness is microscopic. On the contrary, all the dimensions are small for ionic liquids, which made a significant difference in characteristic length scales.

For thin films of liquid crystals, the experiments provided an important set of results aimed to help future theoretical descriptions. The main difficulties encountered were the purity of the liquid crystals (5CB and 7CB) and the thermal stability of the system. It is indeed quite complex to ensure a homogeneous, constant temperature in a liquid surface deposited on another liquid. The required stability increases steeply when coming close to the NI transition, which has been the limiting factor in our experiments.

The case of glycerol substrates raises some questions also. The first one is that the same liquid crystals that formed striped domains, uniform in thickness on water, form striped films, allowing gradients of thickness on glycerol. One possible explanation is that the anchoring constants are different on water and on glycerol (see U. Delabre’s PhD thesis). However, up to date no experiments were able to provide precise values of the constants. Considering films with thickness  $\leq \xi_{UB}$ , a comparison between water and glycerol cannot be made: for these films the diffusion of glycerol molecules in the nematics is critical (see the Appendix about glycerol). In a situation where the experiments did not lead to a firm conclusion, numerical analysis, modeling the way LC molecules organize themselves at the surface of water and glycerol could bring new clues.

Concerning solely the striped phase, its characterization made important steps, both in a theoretical and experimental point of view and the set of results provides a strong constraint to help the development of theories. The case of solid substrates now comes back as the main question: is there stripes on the  $\xi_{UB}$  films on silicon wafers ? As already mentioned, an attempt of AFM experiment was performed with no success. Among remaining questions, one could also

cite the coalescences of domains of different thicknesses on water. In the coalescence zone, one observes larger stripes or digits. The digits are probably caused by the flow of the nematic as they are oriented along its direction. Up to date, no theoretical description is available.

For ionic liquids, the experiments are not at the same stage than the ones for thin films of liquids crystals. Here also, the system possesses on its own quite an amount of complexity: the situation is a non-wetting one, all the dimensions of the system are small, the substrate is charged and the exact chemical composition of its surface is not exactly known. In this perspective, one can hope that the knowledge obtained previously in simpler situations will allow for improving the understanding of the system step by step. There are still many paths that could be explored. As already mentioned in Chapter 3, the most important question to be answered is the exact nature of the 2 nm film on mica. Rough estimations of possible thicknesses for molecularly thick layers of ionic liquids based on the estimated size of the ion pair do not really help to answer. To go further, experiments probing the structure of the film would be required, such as XPS or X-Rays. A theory at intermediate scales as well as a modeling at molecular scales would also help and bring a point of comparison.





# Appendix A

## Macroscopic contact angle measurement methods

### A.1 Sessile drop

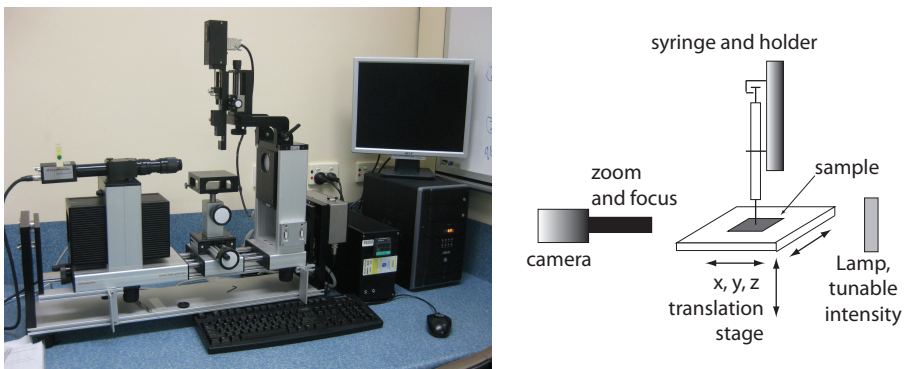


Figure A.1: On the left side, picture of the sessile drop setup. On the right side, schematic representation.

Sessile drop is a method to measure macroscopic contact angles. The sessile drop setup is presented on figure A.1. In this method, a drop, of known volume, is deposited by a syringe on the substrate. The volume of liquid deposited by the syringe is controlled via the computer. The drop is then visualized from the side by a camera. The images taken by the camera are analyzed by the OCA software, which extracts the location of the substrate and the drop's contour. The contour of the drop is fitted by a spherical shape and the contact angle is obtained. Sessile drop allows to perform experiments in different environments. It was used, both in air and in a water cell for advancing, receding and equilibrium contact angle measurements. In air, the precision of



this method, depending on the roughness and defects of the substrate is better than 5 degrees. For experiments done in water cell, the precision is less good.

This method works very well for large contact angles. However, when contact angles are less than  $25^\circ$ , the contour of the drop is not easily localized by the software thus increasing the error bars of the measurements. More accurate methods exist to measure small contact angles as the one based on interferometry which will be presented in the next section.

## A.2 Interferometry

### A.2.1 Fringes of equal thicknesses

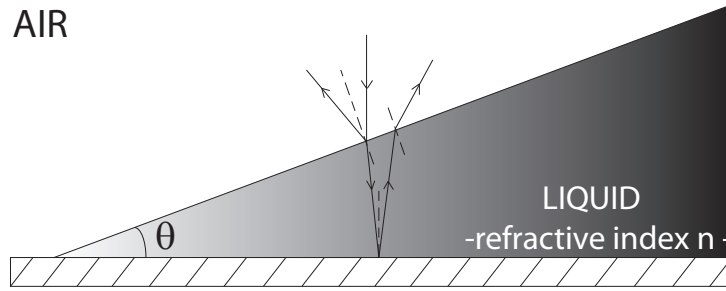


Figure A.2: A thin liquid wedge illuminated by a monochromatic light source, the incidence being normal.

Let us consider a macroscopic drop deposited on a substrate. Close to the three-phase contact line, the drop can be locally considered as a thin wedge (see figure A.2). The contact angle of the drop is small so that the local thickness variation is slow. If the drop is illuminated by a monochromatic light source of wavelength  $\lambda$ , the optical path difference between the two interfering rays in normal incidence is equal to  $2ne$ , where  $n$  is the optical index of the liquid wedge and  $e$  its local thickness. The corresponding phase difference is then:

$$\Delta\phi = \frac{2\pi}{\lambda} 2ne \quad (\text{A.1})$$

Minima in intensity (i.e. dark fringes) are observed when the phase difference is  $\Delta\phi = (2p+1)\pi$  with  $p \in \mathbb{Z}$ . The difference of thickness between two consecutive minima can then be calculated as:

$$\Delta e = \frac{\lambda}{2n} \left( p + 1 + \frac{1}{2} \right) - \frac{\lambda}{2n} \left( p + \frac{1}{2} \right) = \frac{\lambda}{2n} \quad (\text{A.2})$$

The local thickness of the wedge of a drop and then its profile can easily be obtained by plotting the measured thickness versus the distance to the three-phase contact line. The contact angle is deduced from this profile. This method gives precise results only for relatively small contact angles as the fringe spacing is easily measured.

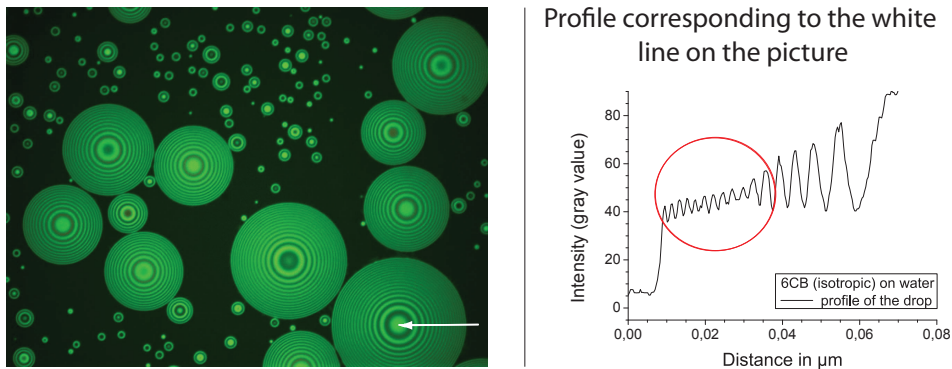


Figure A.3: On the left side, example of macroscopic drops seen under monochromatic green light (6CB (isotropic) on water substrate). On the right, intensity profile corresponding to the white line drawn on the picture. The zone of the intensity profile where measurements were performed is highlighted in red.

## A.2.2 Applications

In practice, the experiment consists in observing a drop under microscope. A filter of known wavelength is placed in the incident beam of light which allows to observe the fringes of equal thickness. The intensity along a radius of the drop is extracted from the microscope images (see figure A.3). On the curve representing the intensity versus the distance, the minima are spotted and the profile of the drop computed.

Interferometry was used in two cases. First, it was used to measure the contact angle of macroscopic drops on solid substrates when the sessile drop could not provide a precise value anymore. This corresponds to low contact angles. Second, it was used to measure the contact angle of macroscopic drops of liquid crystals in liquid isotropic phase deposited on a water substrate. The precision of this method relies mainly on the quality of the microscope images. The profile is indeed obtained through the minima of intensity. The position of those minima is easy to find when the intensity profile is of good quality. However, these positions are not always obvious for a noisy signal. Noise in the signal is sometimes an unavoidable part of the experiment. For example, in the experiments with the liquid crystals, the presence of a liquid substrate implies that the sample is never completely motionless. Even if this motion is reduced as much as possible, there is always a little bit of noise in the microscope images and thus in the intensity signal. In this case, it was not possible to find the minima from the intensity profile automatically (via a custom-made macro) ; the judgement of the user was required to avoid any mistake. As a conclusion, there is no absolute precision for this method, the errors bars must be evaluated depending on the quality of the signal obtained.



# Appendix B

## Langmuir Isotherms

### - Surface pressure versus mean area per molecule isotherms -

#### B.1 Introduction to Langmuir isotherms

Surface pressure versus mean area per molecule isotherms, also called Langmuir isotherms, represent a tool to study the physics of thin films deposited on a liquid phase (an example of Langmuir isotherm is presented on figure B.1). The liquid phase is usually water<sup>1</sup> and the thin films are immiscible with water.

In this appendix, only one category of thin films are considered: Langmuir films. Langmuir films are insoluble films deposited on the liquid subphase as a solution of the substance of interest in a volatile solvent. Once the solution is deposited, it spreads on the subphase. The solvent evaporates and a thin layer of the substance of interest is left. This technique of deposition allows to control the quantity of the substance of interest which is deposited and also to calculate the mean area per molecule after deposition<sup>2</sup>. The mean area per molecule of Langmuir films can easily be changed. A barrier of inert material (e.g. Teflon or Delrin) is placed at the level of the interface between the subphase and the thin film. The barrier is then translated, reducing or increasing the available area for the film and thus the mean area per molecule.

This process corresponds exactly to the one used to obtain a Langmuir isotherm. A Langmuir film is deposited on a trough filled with water. The area per molecule is then varied (compression

---

<sup>1</sup>Some attempts of Langmuir isotherms on glycerol are presented in the next appendix.

<sup>2</sup>Using a solvent ensures an even coverage of the whole surface, therefore a good homogeneity of the final film. This would not necessarily be obtained if a small drop or a crystal was directly deposited.

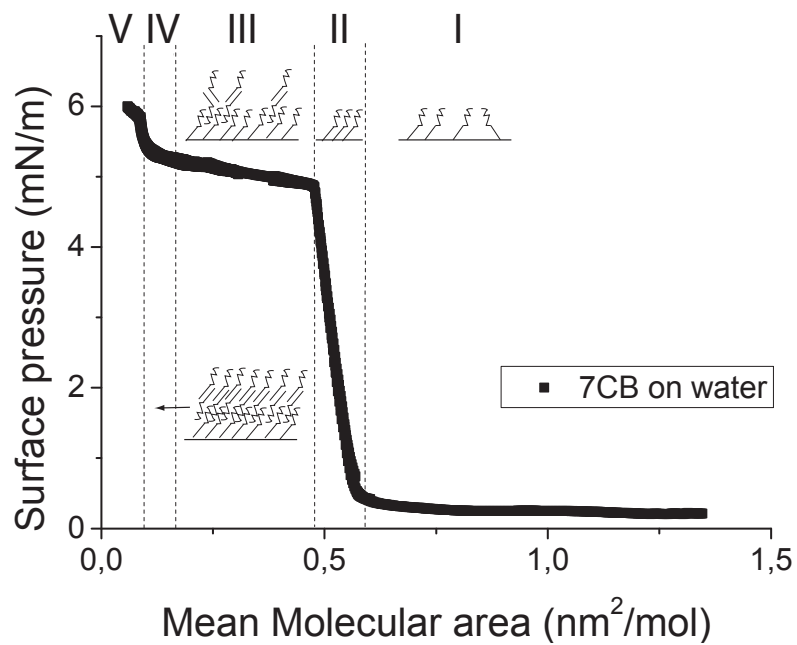


Figure B.1: Example of a surface pressure versus mean area per molecule isotherm for *7CB* on water at room temperature. This isotherm allows one to distinguish several zones. Zone I: diluted monolayer ; zone II: compressed monolayer ; zone III: coexistence of dense monolayer and trilayer ; zone IV: compressed trilayer ; zone V: crystallization in a 3D phase.

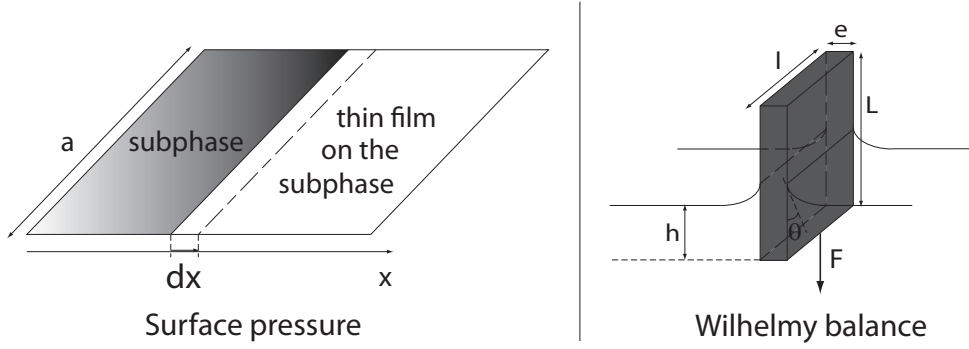


Figure B.2: On the left side: illustration of the thought experiment used to define the surface pressure. On the right side: Measurement of surface tension *via* the Wilhelmy balance method.

or expansion). At the same time, the surface pressure, a  $2D$  equivalent of the  $3D$  pressure is measured. Let us now focus on the surface pressure.

### B.1.1 Surface pressure

Surface pressure,  $\pi$ , is the force per unit length exerted by the thin film on the straight line separating the thin film deposited on a subphase and the bare subphase. The surface tension of the pure subphase is  $\gamma_0$  and the one of the subphase covered by the thin film is  $\gamma_f$ . If the boundary is now moved from a small distance,  $dx$  (see figure B.2), the variation of the surface energy is:

$$\Delta E = \gamma_0 dx a - \gamma_f dx a \quad (\text{B.1})$$

$$\frac{\Delta E}{a} = \pi dx \quad \text{where } \pi = \gamma_0 - \gamma_f \quad (\text{B.2})$$

The surface pressure is then the difference of the two surface tensions. In our experiments, surface pressure was measured through the difference of surface tensions via the Wilhelmy plate method.

### B.1.2 Measurement of the surface tension: the Wilhelmy plate technique

In the Wilhelmy plate technique, a plate is dipped in liquid to a depth  $h$  (see figure B.2). Three forces are exerted on such a plate: its weight, the buoyant force (Archimedes's principle) and the surface tension. The total force, projected on the vertical axis, is then written:

$$F = \rho_p(Lle)g - \rho_w(hle)g + 2(l+e)\cos\theta\gamma \quad (\text{B.3})$$

with  $\rho_p$  and  $\rho_w$ , the respective densities of the plate and of water ;  $L$ ,  $l$  and  $e$ , the dimensions of the plate ;  $g$ , the acceleration of gravity ;  $\theta$ , the angle of the liquid meniscus ;  $\gamma$ , the surface tension of the liquid.  $h$  being kept constant, if this total force is measured in two situations, first for the pure subphase and second for the subphase covered by the film, the difference of the two forces measured gives:

$$\Delta F = 2(l + e)\cos\theta(\gamma_0 - \gamma_f) = 2(l + e)\cos\theta * \Pi \quad (\text{B.4})$$

This result is proportional to the surface pressure and thus allows to measure it. In practice, for a Langmuir isotherm, a calibration measurement is always performed first: the measurement of the force exerted on the plate by the pure subphase. The Langmuir film is then deposited and the variations of the force exerted on the plate by the subphase covered by the thin film are measured. The surface pressure can thus be computed for all the compression levels browsed by the experiment.

In this method, the contact angle  $\theta$  could be the sensitive parameter. To avoid any difficulty, the plates are chosen so that they are completely wetted by the studied liquid. The contact angle is then equal to zero and  $\cos\theta = 1$ . In practice, two different kind of plates were used for our experiments: platinum and paper plates. The platinum plates are treated by sandblast in order to be completely wettable. They are supposed to be inert, which reduces possible risks of contamination during the experiments. However, they are quite difficult to clean after each experiment and residues of liquid crystals left on the plate could lead to a modification of the contact angle. That is why paper plates were preferred for most experiments. The paper plates were purchased from KSV and NIMA. They are made of chromatographic paper and are used only once, thus avoiding any cleaning problem.

## B.2 Description of the Langmuir troughs

Two different Langmuir troughs were used for our experiments [1]: a commercial KSV minimicro 1s [2] and a custom-made trough designed and constructed by J. Meunier and the mechanical workshop of the LPS. The characteristics of both troughs are presented in figure B.3. Both troughs are thermalized by a circulation of water inside the walls of the trough. The KSV trough was the most used. It is a small trough, which implies that less liquid crystal is used and that it is easily cleaned. However, the KSV trough does not allow one to obtain the whole isotherm of one compound at once. It is then necessary to repeat the compression / expansion cycles for several initial quantities of liquid crystals. The small size of the trough also makes it more sensitive to meniscus effects, the meniscus in question being the meniscus on the boundaries of the trough and the meniscus on the barriers<sup>3</sup>. That is why the custom-made trough was used to be sure that the results obtained with the KSV trough were reliable. For both troughs, the

---

<sup>3</sup>The influence of the meniscus present on the boundaries of the trough can be reduced by a fine tuning of the level of water in the trough.

	KSV minimicro 1s	custom-made Langmuir trough
	<p>Wilhemy balance</p> <p>Barriers</p> <p>Wilhelmy plate</p> <p>Trough</p> <p><math>L</math></p> <p><math>l</math></p>	
Dimensions in mm ( $L \times l$ )	$195 \times 51$	$520 \times 155$
Trough	teflon	teflon
Barriers	hydrophilic, Delrin (hydrophilic barriers are supposed to limit the possibility that the thin film comes under the barriers during the compression.)	hydrophobic, teflon

Figure B.3: Technical specifications of the two different Langmuir troughs which were used for our experiments.



same Wilhelmy balance was used to measure the surface pressure.

# Bibliography

- [1] Ulysse Delabre. *Films nématiques minces sur substrats liquides*. PhD thesis, Université Paris VI, 2009.
- [2] KSV NIMA (former KSV). *Operating manual, KSV minimicro 1s*.
- [3] Sylvie Hénon. *Microscopie à l'angle de Brewster : transitions de phases et défauts d'orientation dans des films monomoléculaires*. PhD thesis, Université Paris VI, 1993.



# Appendix C

## About glycerol's tricks

### C.1 Glycerol and Langmuir isotherms experiments

After an extensive study of Langmuir isotherms for liquid crystals deposited on water [2], attempts of measuring Langmuir isotherms on glycerol were made.

Langmuir isotherms on glycerol have previously been studied by Barraud and coworkers ([3] and previous work). Although difficult, due to the very long equilibration time of the surface of this highly viscous liquid, the experiment was well controlled. Here, the situation appears to be more critical. The first difficulty (common to both experiments) is to cope simultaneously with the viscosity, which requires long experiments and slow motions, and the hygroscopic character of glycerol, which requires to control water uptake. Let us be more specific: before beginning a compression / expansion cycle on a Langmuir trough the surface of the subphase must be stable. For water, stability is quickly obtained after it was poured inside the trough and the surface thoroughly cleaned. On the other hand, for glycerol, its viscosity makes this process extremely slow. The time necessary for a glycerol surface to achieve its equilibrium was indeed measured before each attempt of experiment. This measurement was done by pouring the right level of glycerol in the trough and measuring the evolution of the surface pressure measured by the Wilhemy plate. When the surface pressure is stable, the surface of glycerol is at its equilibrium.

The experiments were performed in a closed environment where humidity was monitored and controlled by a desiccant (silicagel). However, the humidity obtained with this method never reached zero. On long time scales such as the one of the relaxation of the glycerol surface, a non zero humidity level can not be neglected. The surface of glycerol absorbs water molecules and at the end of the relaxation the surface which reached the equilibrium is not pure glycerol anymore but glycerol plus a small percentage of water. This explains why our relaxation times are so large, up to 33h. Such a value is not merely the mechanical equilibrium of the glycerol surface, but the progressive uptake of water remaining in the gas phase.

Experiments done under nitrogen atmosphere would suppress the influence of the hygroscopic

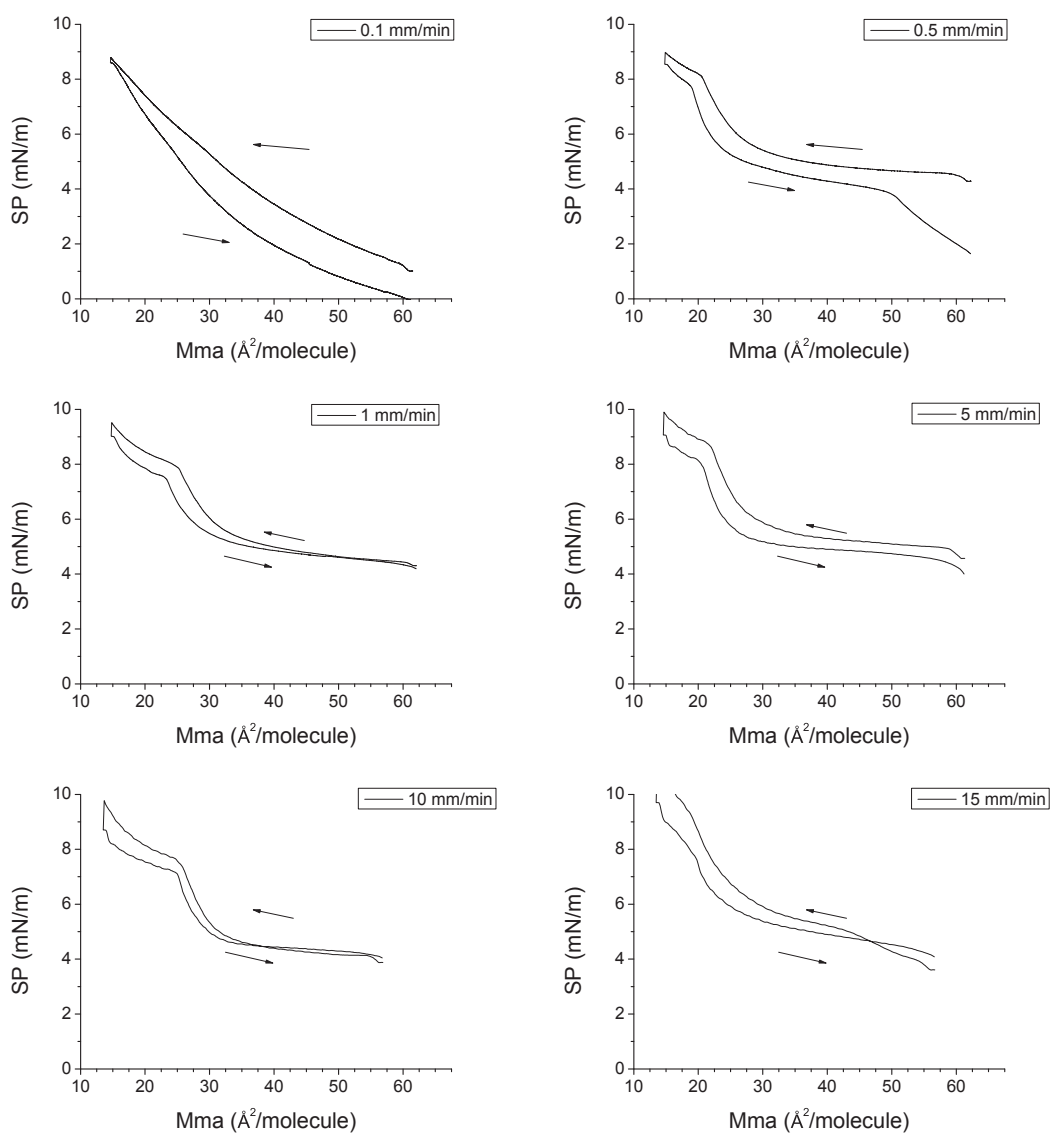


Figure C.1: Study of the influence of the velocity of the barriers on isotherms made on a glycerol substrate. The same quantity of *8CB* was deposited each time. Only the velocity of the barriers was changed. For 15, 10 and 5 mm/min, the isotherms present oscillations (see next figure): the compression / expansion is too fast. For 0,1 mm/min the isotherm shows no step anymore: the compression / expansion is too slow and glycerol seems to penetrate into the molecular film. Intermediate velocities for the barriers providing plausible records in the case of glycerol are then 1 and 0.5 mm/min. However, what is really measured is not clear.

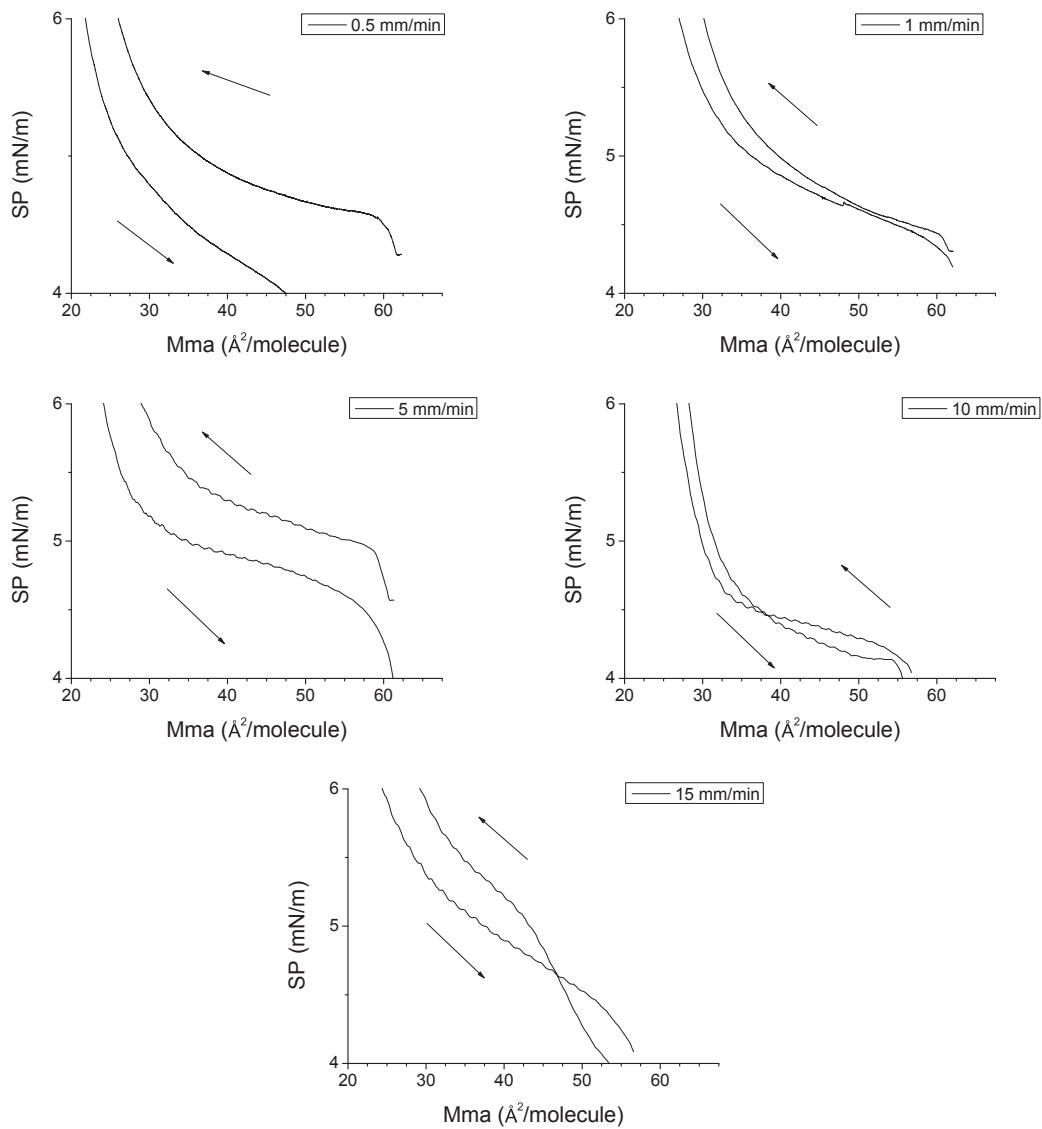


Figure C.2: Zoom on the preceding isotherms. The 15, 10 and 5 mm/min isotherms show oscillations which means that the glycerol's surface is perturbed by the motion of the barriers.

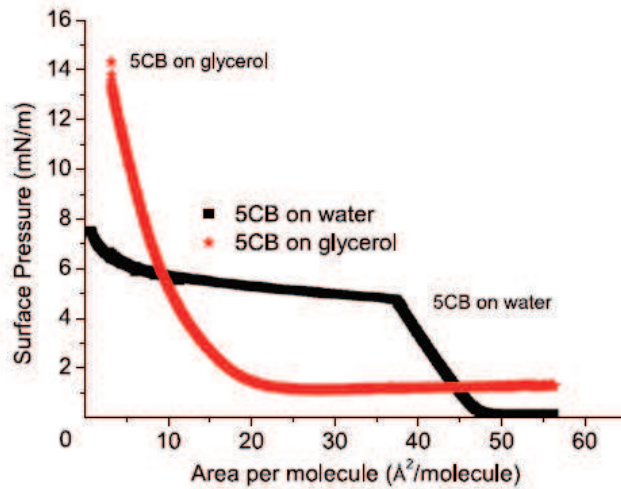


Figure C.3: Image from [2]: Comparison between Langmuir isotherm of 5CB on water and glycerol. For a small molecule such as 5CB, the penetration of glycerol in the liquid crystal layer is fast and the isotherm obtained is interpretable.

behavior of glycerol. However, the large viscosity of glycerol still requires an extremely slow motion of the barriers, and the question now becomes the diffusion of glycerol in the LC film. More precisely, during a compression / expansion cycle, there is a possibility that the motion of the barriers generates a perturbation for the glycerol substrate, which surface would reach the equilibrium. To investigate the consequences of such a phenomenon, the influence of the velocity of the barriers of the trough was studied: compression / expansion cycles in the case of 8CB on glycerol were performed for different velocities of the barriers all else being equal (see figure C.1). 8CB was chosen because its affinity for glycerol is the weakest. The experiment were done at ambient temperature. The viscosity of dry glycerol is then typically 1500 times larger than the one of water.

For high velocities (15 – 5 mm/min), the compression / expansion cycles clearly show oscillations which means that the glycerol has no time to relax (see figure C.2). For a low velocity (0.1 mm/min), the compression / expansion cycle does not show any step. This strongly suggests that glycerol has time to penetrate in the film. Medium velocities (0.5 – 1 mm/min) are then to be chosen. Repeating this velocity test, the isotherms made for a velocity of 0.5 mm/min showed an acceptable reproducibility. This velocity was then the one chosen to perform the experiments. However, we have no guaranty that what is measured is meaningful. Without surprise, the Langmuir isotherms of 5CB, where the penetration of glycerol is faster, are merely non interpretable, regardless of the barrier velocity (see figure C.3). This is even more disappointing that well defined trilayers and "pentalayers" are observed under microscope.

# Bibliography

- [1] R.L. Cook, H.E. King, Chris Jr., A. Herbst, and Herschbach D.R. Pressure and temperature dependent viscosity of two glass forming liquids: Glycerol and dibutyl phthalate. *J. Chem. Phys.*, 100:5178, 1994.
- [2] U. Delabre, C. Richard, and A-M Cazabat. Some specificities of wetting by cyanobiphenyl liquid crystals. *J. Phys : Condensed matter*, 21:464129, 2009.
- [3] J. Richard, A. Barraud, M. Vandevyver, and A. Ruaudel-Teixier. Two-step transfer of conducting langmuir films from a glycerol subphase. *Thin Solid Films*, 159:207–214, 1988.





## Appendix D

# Published articles on thin films of liquid crystals

This Appendix presents the full text of some published articles of the group on thin films of liquid crystals, in bold in the list below:

- Cazabat, A.M. and Delabre, U.; Richard, C. & Cheung Sang, Y. ; Chapter in Nanoscale liquid interfaces, Pan Stanford Publishing, edited by Ondarçuhu, T.
- Cazabat, A.M. and Delabre, U.; Richard, C. & Cheung Sang, Y. ; Experimental study of hybrid nematic wetting films *Advances in Colloid and Interface Science*, 2011, 168, 29-39
- **Delabre, U.; Richard, C. J.; Yip Cheung Sang, Y. & Cazabat, A.-M. ; Thin Liquid Crystal Films on Liquids in the Nematic Range of Temperatures, *Langmuir*, 2010, 26, 13368-13376**
- **Delabre, U.; Richard, C. & A.M., C. ; Thin Nematic Films on Liquid Substrates *J. Phys. Chem. B*, 2009, 113, 3647-3652**
- Delabre, U.; Richard, C. & Cazabat, A.-M. ; Some specificities of wetting by cyanobiphenyl liquid crystals *J. Phys : Condensed matter*, 2009, 21, 464129
- **Delabre, U.; Richard, C.; Meunier, J. & Cazabat, A.-M. ; Line tension of nematic pancakes at the air-water interface: Static and dynamic measurements *Europhysics Letters*, 2008, 83, 66004**
- Delabre, U.; Richard, C. & Guena, G. & Meunier, J. & Cazabat, A.-M. ; Nematic Pancakes Revisited *Langmuir*, 2008, 24, 3998-4006

These articles reflect a collective work and are added to this manuscript to put into perspective the studies presented in Chapter 2. The articles are presented in reverse chronological order.

## Thin Liquid Crystal Films on Liquids in the Nematic Range of Temperatures

Ulysse Delabre, Céline Richard, Yann Yip Cheung Sang, and Anne-Marie Cazabat\*

Université Pierre et Marie Curie et LPS-ENS, UMR 8550 du CNRS, 24 rue Lhomond,  
75231 Paris Cedex 05, France

Received June 14, 2010. Revised Manuscript Received July 7, 2010

Hybrid nematic films deposited on liquid substrates reveal a complex behavior, which is not fully understood. Here, the behavior of the *n*-cyanobiphenyl series on water and glycerol has been studied in a wide temperature range, including the vicinity of the nematic–isotropic (NI) transition. Wettability, allowed film thicknesses, and line tension of nematic domains have been investigated. The study provides a coherent picture of hybrid nematic films, allowing us to account for lower thickness threshold, structure of the film edge, and line tension of domains in the whole nematic range of temperatures.

## I. Introduction

Due to potential applications, the behavior of thin nematic films deposited on solid or liquid substrates is currently a living field of research. “Hybrid films” are a specific case. “Hybrid” means that the anchoring conditions at the free surface and on the substrate are antagonistic and the local orientation of the molecules changes within the film. Many studies deal with cyanobiphenyl liquid crystals, referred to as *n*CB, where *n* corresponds to the length of the aliphatic chain connected to the cyanobiphenyl group.<sup>1–3</sup> The anchoring conditions are antagonist on substrates such as silica, water, or glycerol. The *n*CB molecules tend to lay parallel to these substrates (planar anchoring), while they tend to be normal to the free interface (homeotropic anchoring). The most frequently *n*CBs used are 5-, 6-, 7-, and 8CB, for which the nematic range is around room temperature. They are the ones considered here.

5CB nematic films deposited on glycerol were studied at room temperature by Lavrentovich and Pergamenschik, and Sparavigna and co-workers.<sup>4–8</sup> Under microscope, these films show striking stripe patterns in the thickness range  $20 \text{ nm} \leq d < D \approx 0.5 \text{ }\mu\text{m}$ . No thinner mesoscopic film is visible. The usual defects of nematic phases replace the stripes in films thicker than  $D \approx 0.5 \text{ }\mu\text{m}$ .

On the other hand, nematic 5CB microdroplets deposited on oxidized silicon wafers, or spin coated nematic 5CB films, have been studied using ellipsometry, microscopy, and small angle

X-ray scattering.<sup>9–12</sup> Here, the striking feature is the occurrence of a forbidden range of thickness, visible as a discontinuity in microdroplet profiles, or from the coexistence of films with different thickness. This forbidden range depends only on temperature. A “phase diagram is available for 5CB<sup>12</sup> and is schematized in Figure 1. In the following, LB will be the lower boundary of the forbidden range and UB the upper one. At room temperature, LB is a trilayer of molecules, while  $UB \approx 20 \text{ nm}$ .

More recently, it has become clear that both behaviors are common to all the investigated *n*CBs, and several substrates. The forbidden range of thickness observed on silicon wafers exists also on glycerol and water, and with similar values for LB and UB.<sup>13–15</sup> Noticeably, for 5CB deposited on glycerol at room temperature (15 °C below the nematic–isotropic transition), LB is a trilayer and  $UB \approx 20 \text{ nm}$ . Therefore, the threshold UB coincides with the minimum thickness of the striped films, and this appears to be a general feature for all the systems investigated. While stripe patterns are observable under microscope on glycerol and water but not on silicon wafers, the difference here is merely the wavelength. Patterns with long wavelength (much larger than the film thickness, i.e., observable under microscope) exist only if the planar anchoring is stronger.<sup>4–6</sup> This is the case on water and glycerol but not on silica, where the wavelength is of the order of the film thickness, that is, nonobservable.<sup>16,17</sup> However, the presence of instability patterns in both cases is widely accepted.

Therefore, experimental observations on the various pairs of *n*CB/substrate in the whole nematic range must find a place within a robust, general framework. They will provide a working base for further theoretical analyses. The present paper focuses on striped films,  $D > d \geq UB$ , and is organized as follows:

In a first part, materials and methods are briefly presented. Considering the substrates, previously reported<sup>13–15</sup> similarities and differences are summarized. New results dealing with mutual solubility of the phases answer pending questions and complete that part. The second part presents a complete experimental study of the stripe patterns for 5-, 6-, 7-, and 8CB on water and glycerol

(1) de Gennes, P. G.; Prost, J. *The Physics of liquid crystals*, 2nd ed.; Clarendon Press, Oxford, 1993.

(2) Chandrasekhar, S. *Liquid crystals*, 2nd ed.; Cambridge University Press: New York, 1992.

(3) Oswald, P.; Pieranski, P. *Les cristaux liquides Tome 1*; Gordon and Breach Science Publishers: Paris, 2000.

(4) Lavrentovich, O. D.; Pergamenschik, V. M. *Mol. Cryst. Liq. Cryst.* **1990**, *179*, 125.

(5) Lavrentovich, O. D.; Pergamenschik, V. M. *Phys. Rev. Lett.* **1994**, *73*, 979.

(6) Lavrentovich, O. D.; Pergamenschik, V. M. *Int. J. Mod. Phys.* **1995**, *B9*, 2389.

(7) Sparavigna, A.; Komitov, L.; Strigazzi, A. *Phys. Scr.* **1991**, *43*, 210.

(8) Sparavigna, A.; Lavrentovich, O. D.; Strigazzi, A. *Phys. Rev. E* **1994**, *49*, 1344.

(9) Sparavigna, A.; Lavrentovich, O. D.; Strigazzi, A. *Phys. Rev. E* **1995**, *51*, 792.

(10) Valignat, M. P.; Villette, S.; Li, J.; Barberi, R.; Bartolino, R.; Dubois-Violette, E.; Cazabat, A. M. *Phys. Rev. Lett.* **1996**, *77*, 1994.

(11) Vandenbrouck, F.; Bardou, S.; Valignat, M. P.; Cazabat, A. M. *Phys. Rev. Lett.* **1998**, *81*, 610.

(12) Vandenbrouck, F.; Valignat, M. P.; Cazabat, A. M. *Phys. Rev. Lett.* **1999**, *82*, 2693.

(13) Van Effenterre, D.; Ober, R.; Valignat, M. P.; Cazabat, A. M. *Phys. Rev. Lett.* **2001**, *87*, 125701.

(13) Delabre, U.; Richard, C.; Guéna, G.; Meunier, J.; Cazabat, A. M. *Langmuir* **2008**, *24*, 3998.

(14) Delabre, U.; Richard, C.; Cazabat, A. M. *J. Phys. Chem. B* **2009**, *113*, 3647.

(15) Delabre, U.; Richard, C.; Cazabat, A. M. *J. Phys. Condens. Matter* **2009**, *21*, 464129.

(16) Pergamenschik, V. M. *Phys. Rev. E* **1993**, *47*, 1881.

(17) Pergamenschik, V. M. *Phys. Rev. E* **1993**, *58*, R16.

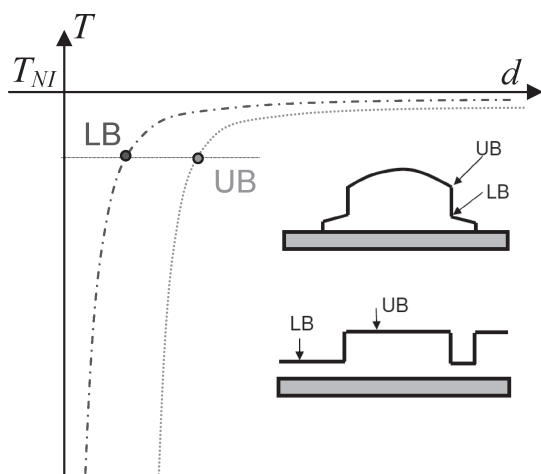


**Figure 1.** Schematic behavior of 5CB on an oxidized silicon wafer.<sup>12</sup> “Phase diagram”: Dependence of the upper and lower boundaries with temperature. The range of thickness between the two boundaries is forbidden. Inset: (top) Schematic microdroplet profile, showing the forbidden range of thickness (LB–UB); (bottom) spin coated film. Orders of magnitude:<sup>12</sup> 15 °C below  $T_{NI}$ , LB = 3.5 nm is a trilayer of molecules, UB  $\approx$  20 nm; 1 °C below  $T_{NI}$ , LB  $\approx$  30 nm, UB  $\approx$  75 nm.

in the whole nematic range of temperatures. Available models are discussed. Noticeably, we reconsider the analyses of the lower thickness threshold for the striped configuration, which is also the upper boundary (UB) of the forbidden range of thickness. We complete the description by taking into account the possibility of thickness gradients, which play a significant role at the film edge. The film edge is further investigated in the third part, which reports line tension measurements in the 6CB/water system close to the nematic–isotropic (NI) transition. A discussion follows.

## II. Materials and Methods

### II.1. Substrates, Liquid Crystals, and Methods. II.1.1.

**Substrates.** The liquid substrates are pure water (18.2 M $\Omega$ .cm) and glycerol from Sigma-Aldrich (purity 99%). Experiments with glycerol are performed in closed boxes with desiccant, in order to avoid uptaking atmospheric water. The solid substrates are oxidized silicon wafers (crystallographic plane (100), p-doped, purchased from Siltronix), cleaned by oxygen plasma. The underlying silicon bears a natural oxide layer typically 2 nm thick, for which the properties are similar to the ones of silica.

**II.1.2. Liquid Crystals.** Two types of liquid crystal samples are used. The “standard” one, purity 98%, was purchased from Sigma Aldrich; the “pure” one, purity >99%, was purchased from Frinton. Transition temperatures available in the literature are the following:

$$T_{\text{solid-nematic}} =$$

$$T_{SN} = 24 \text{ °C for 5CB, } 14.5 \text{ °C for 6CB, } 30 \text{ °C for 7CB}$$

$$T_{\text{solid-smectic}} = T_{SSm} = 21.5 \text{ °C for 8CB,}$$

$$T_{\text{smectic-nematic}} = T_{SmN} = 33.5 \text{ °C for 8CB}$$

$$T_{\text{nematic-isotropic}} =$$

$$T_{NI} = 35.3 \text{ °C for 5CB, } 29 \text{ °C for 6CB, } 42.8 \text{ °C for 7CB, } 40.5 \text{ °C for 8CB}$$

While purity is not critical in most bulk studies, where a mere shift of the nematic–isotropic transition temperature is often the sole consequence of the presence of impurities,<sup>2</sup> the problem is severe as soon as interfaces are concerned. An example is the wide range

of surface tension values of 5CB available in the literature (values have been collected in ref 15), between 0.028<sup>18</sup> and 0.040 N m<sup>-1</sup><sup>19</sup> at room temperature. The prime cause of the difference is the purity of the 5CB, a “standard” one in the first case,<sup>18</sup> and a specifically purified sample in the second one.<sup>19</sup> As at least a part of these impurities is surface-active; they alter the wetting behavior. While all our “pure” nematic compounds wet water, the “standard” 5CB does not wet and the 7CB gives scattered results.<sup>15</sup>

**II.1.3. Methods.** The films are observed under microscope (Polyvar MET-Reichert-Jung) using either a black and white camera (CoolSnap, Photometrics) or a color one (EXI aqua, Q imaging). The Newton scale of colors is used to measure film thicknesses  $d$  larger than 50 nm typically. For thinner films, we use the calibrated gray levels of the black and white camera. Image processing provides high sensitivity, as we are able to image the boundary between a compact monolayer and a trilayer of molecules.<sup>20</sup> Brewster angle microscopy<sup>21</sup> should be required to image the edge of the monolayer.

**II.2. Substrates: Similarities, Differences, and Potential Problems.** If “pure” samples are used, all our  $n$ CB wet water, glycerol, and oxidized silicon wafers, in the nematic range of temperatures.

**II.2.1. Similarities.** On silicon wafers,<sup>12</sup> spin coated films are homogeneous if their average thickness is outside the forbidden range (LB–UB). If this is not the case, two films coexist, for which the thicknesses are LB and UB, respectively, fixed at given temperature; see Figure 1.

**II.2.2. Differences.** Unexpectedly, metastability is the rule on liquid substrates, as already observed with smectic 8CB on water.<sup>22</sup> On both water and glycerol, striped films of different thicknesses  $d \geq UB$  coexist with thinner nonstriped ones,  $d \leq LB$ . These thinner films will be referred to as “molecular” films; see Figure 2. There are also differences in the film behavior depending on the liquid substrate.<sup>13–15</sup> Extended films with or without thickness gradients are observed on glycerol, while smaller domains of constant thickness are observed on water; see Figure 2.

**II.2.3. Potential Problems.** While the differences in film behavior may result from the specific values of anchoring energies,<sup>1–3</sup> an observation requires further study: except for the 8CB, surface pressure isotherms on glycerol at room temperature differ strongly from the (well established<sup>23</sup>) ones on water.<sup>15</sup> While coexistence of monolayers, trilayers, and even “pentalayers” on glycerol is visible under a microscope,<sup>15</sup> no trace of layering is seen with the film balance (KSV mini micro 1S).<sup>15</sup>

After many crosschecks and complementary studies, the reason seems to be simple, although somewhat upsetting. Nothing specific is visible under microscope with  $n$ CB films thinner than typically 1  $\mu$ m, which explains that the question was never raised for striped films. However, for thicker ones, small spheres of glycerol progressively invade the sample (Figure 3). In fact, the solubility of glycerol in the  $n$ CB is not completely negligible, even at room temperature. It increases with decreasing  $n$ , which explains why for the 8CB the surface pressure isotherm is acceptable. It increases also with increasing temperature: actually, this has been used to generate glycerol drops in 5CB.<sup>24</sup> Unfortunately, it becomes questionable to interpret data as a function of temperature, as the possible role of glycerol molecules diffusing in thin films is not yet analyzed. No suspect behavior is observed with water.

For all the  $n$ CBs investigated, approaching the NI transition means heating a liquid substrate. Besides the open question of

(19) Proust, J. E.; Ter-Minassian-Saraga, L. *J. Phys. (Paris)* **1979**, *40*, C3–490.

(20) Delabre, U.; Richard, C.; Meunier, J.; Cazabat, A. M. *Europhys. Lett.* **2008**, *83*, 66004.

(21) Hénon, S.; Meunier, J. *Rev. Sci. Instrum.* **1991**, *62*, 936.

(22) Zou, L.; Wang, J.; Basnet, P.; Mann, E. K. *Phys. Rev. E* **2007**, *76*, 031602.

(23) Inglot, K.; Martynski, T.; Bauman, D. *Liq. Cryst.* **2006**, *33*, 855.

(24) Smalyukh, I. I.; Chernyshuk, S.; Lev, B. I.; Nych, A. B.; Ognysta, Y.; Nazarenko, V. G.; Lavrentovich, O. D. *Phys. Rev. Lett.* **2004**, *93*, 117801.

(18) Gannon, M. G. J.; Faber, T. E. *Philos. Mag.* **1978**, *37*, 117.

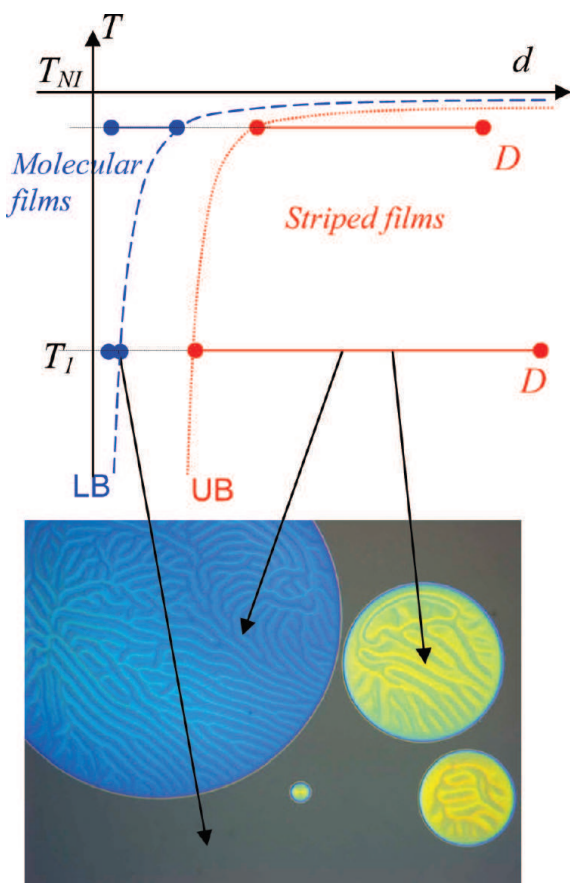


**Figure 2.** “Phase diagram” for *n*CB deposited on liquid substrates. Several film thicknesses coexist, both below LB (“molecular films”, left segment) and above UB. Striped films (right segment) are observed between UB and a maximum thickness *D* above which classical nematic defects replace stripes. At the temperature *T*<sub>1</sub>, well below the NI transition, LB is a trilayer of molecules, which can coexist with a monolayer. Striped films on water are flat domains (picture, 8CB on water) of different thickness in contact with the trilayer. Note that the small domain (bottom, center) is not striped. Size of the picture: 0.18 mm × 0.13 mm.

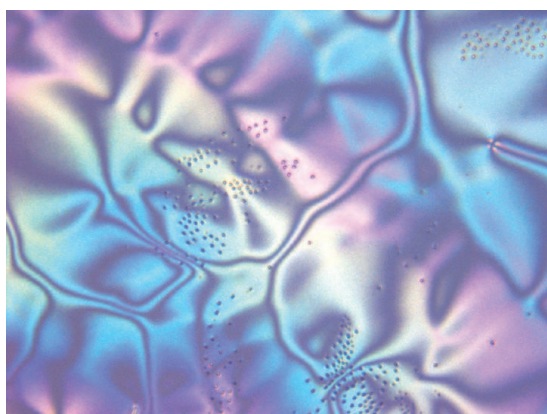


**Figure 3.** Thick film of 5CB deposited on glycerol at 27 °C. After 0.5 h, the characteristic picture of the nematic phase is sprinkled with little glycerol spheres. They are denser for the short *n*CBs (5 and 6CB) and at higher temperature. They do not show up in films thinner than 1 μm typically. Size of the picture: 0.18 mm × 0.13 mm.

enhanced diffusion of glycerol molecules inside the *n*CB film, convection, or any flow in the substrate, must be avoided. Here,

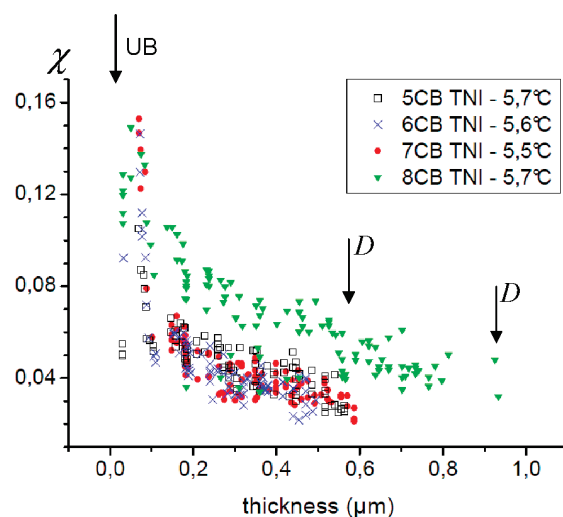


**Figure 4.** Series of *n*CBs on a glycerol substrate.  $\chi = 2\pi(d/\lambda)$  is measured at a given distance from the NI transition. Wavelengths are measured between the lower threshold UB and the upper threshold *D*. Slight differences between 5-, 6-, and 7CB are in the error bars. In contrast,  $\chi$  and the upper threshold *D* are significantly larger for the 8CB. However, what is probably observed here is the vicinity of the (second order) SmN transition. In all cases,  $\chi$  increases at the lower thickness threshold UB but stays significantly smaller than 1.

the situation is worse with water, due to the lower viscosity, and with 7CB and 8CB, where the transition temperature is higher. Even with thin liquid substrates, investigating stripe patterns with these compounds becomes very tricky.

### III. Striped Films on Water and Glycerol

#### III.1. Experimental Investigation of Stripe Patterns.

Here, we are investigating films with thickness  $D > d \geq UB$ ; see Figure 2. Previous studies<sup>13</sup> of stripe patterns on water and glycerol have been repeated with pure compounds and in the whole nematic range of temperatures. As first reported by Lavrentovich and Pergamenschik, the wavelength  $\lambda$  of the stripes increases with the film thickness  $d$ .<sup>5,6</sup> A relevant parameter is the ratio:<sup>6</sup>

$$\chi = 2\pi \frac{d}{\lambda}$$

Small values of  $\chi$  correspond to long (observable) wavelengths; they allow specific approximations in the models. Measured values of  $\chi$  or  $\lambda$  as a function of the thickness  $d$  are reported in Figures 4–6 for various compounds, substrates, and temperatures. The main features are as follows:

- (i) At intermediate thicknesses,  $\chi$  is almost constant and much smaller than 1.

Typical values are around 0.05, both on water and glycerol, which validates the approximation  $\chi \ll 1$ . A proper representation allowing the comparison of the various *n*CBs requires working at a given distance of the NI transition. For 5-, 6-, and 7CB, the curves coincide considering the scattering of the experimental data. We met difficulties with the 8CB, because the nematic range is relatively narrow. (In the smectic range, 8CB films on water<sup>22</sup> or glycerol do not show stripes, because the smectic elasticity differs from the nematic one: twist is not allowed; see below.) In Figures 4 and 5, being far from the NI transition ( $T_{NI} = 40.5$  °C) means for 8CB to be close to the



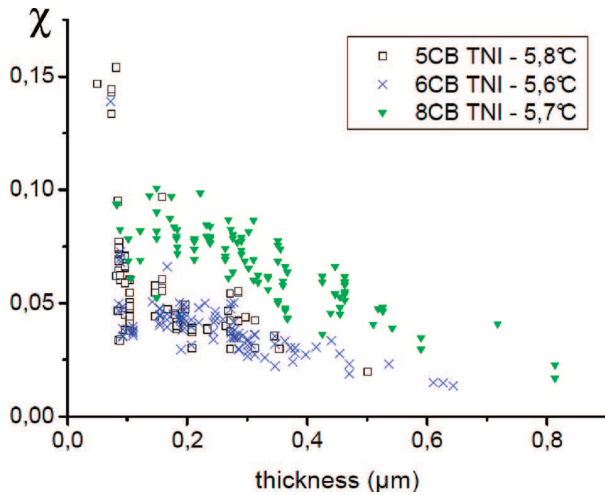


**Figure 5.** Same as before on a water substrate. An experimental difficulty is to avoid convection in the heated water substrate. Measurements are critical for 8CB, and we did not investigate 7CB. The conclusions are the same as those for glycerol.

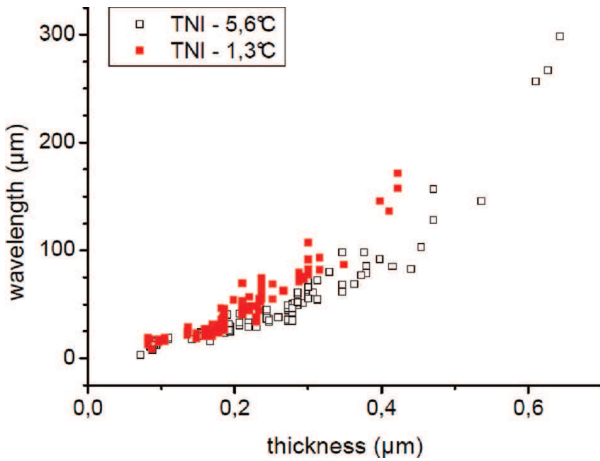


**Figure 6.** 6CB on water. At a given thickness, the wavelength  $\lambda$  increases slightly close to the NI transition. The upper threshold  $D$  for the observation of stripes seems to decrease. This point requires confirmation considering the experimental difficulties when heating water substrates.

smectic–nematic transition ( $T_{\text{SmN}} = 33.5^\circ\text{C}$ ), where  $\chi$  increases. Farther from the SmN transition ( $1.5^\circ\text{C}$  below  $T_{\text{NI}}$ ), usual values  $\chi \approx 0.05$  are recovered on glycerol, but now the temperature is  $39^\circ\text{C}$  and the diffusion of glycerol in 8CB might blur the results. Data on water at  $39^\circ\text{C}$  are compatible with that on glycerol but considerably more scattered, as previously explained.

- (ii) A decrease of  $\chi$ , that is, an increase of  $\lambda$ , is observed at the upper threshold  $D$ . Experiment does not allow to one discriminate between a divergence of the wavelength ( $\chi \rightarrow 0$ ), or a saturation.
- (iii) A scattering of data, but with undoubtedly an increase of  $\chi$ , is observed at the lower threshold UB. Typical UB values are 20–30 nm far from the NI transition. The largest  $\chi$  values are close to 0.15, still significantly smaller than 1.

Complementary experiments with MBBA (4-methoxybenzylidene-4'-butylaniline) on glycerol at room temperature give similar results. UB and  $D$  values are

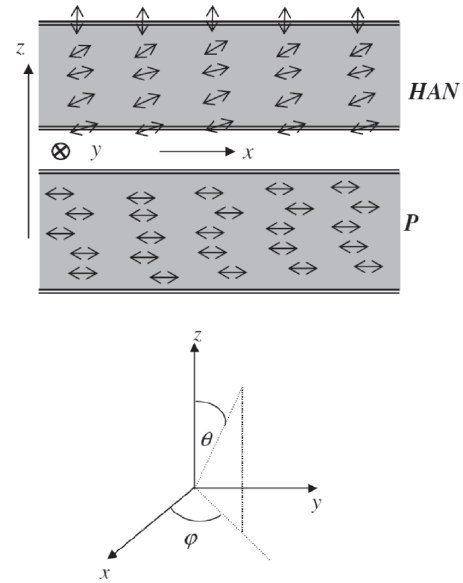


**Figure 7.** Euler angles used for introducing polar  $\theta$  and azimuthal  $\varphi$  orientations. The interfaces are normal to the  $z$  axis. Top: HAN structure. The local orientation rotates inside a  $xz$  plane, and the system is invariant in any  $xy$  plane. Bottom: P structure. The local orientation is everywhere parallel to  $x$ .

similar to the ones in 5CB;  $\chi$  is slightly less in the intermediate range ( $\chi \approx 0.02$ ) but increases faster close to UB ( $\chi_{\text{UB}} \approx 0.18$ ). Note that stripe patterns with MBBA on glycerol were first observed by Lavrentovich and Pergamenschchik.<sup>4</sup>

- (iv) At a given thickness,  $\lambda$  increases ( $\chi$  decreases) with increasing temperature.

As can be seen in Figure 6, where 6CB is deposited on water, the increase is moderate. The upper threshold  $D$  seems to decrease. The same trend is observed for 8CB on glycerol, where  $D$  is around  $0.9 \mu\text{m}$  at  $35^\circ\text{C}$  (figures 4 and 5) and around  $0.6 \mu\text{m}$  at  $39^\circ\text{C}$ , with the still open problem of the enhanced diffusion of glycerol in the 8CB film. Again, data on water are compatible with that of glycerol but are considerably more scattered.

### III.2. Some Generalities about Available Models for Stripe Patterns, and the Usual Terminology.

Striped nematic structures are complex and are not tractable by simple approaches. We first introduce the main points of the available models; equations will be written later.

**III.2.1. The LP Model.** The dependence  $\lambda(d)$  has been investigated by Lavrentovich and Pergamenschchik (LP).<sup>4–6</sup> They use a linear perturbation of a base state referred to as “HAN”, for hybrid aligned nematic.<sup>4–8</sup>

The HAN configuration and the reference frame for the angles  $\theta$  and  $\varphi$  defining the local orientation are presented in Figure 7. In the HAN configuration,  $\varphi = 0$  and  $\theta$  depends only on  $z$ . The local orientation rotates from bottom to top in the plane  $xz$ , and the system is invariant along  $x$  and  $y$ . The HAN structure is usually achieved and studied in experiments where the liquid crystal is put between two solid walls.<sup>1–3</sup> One wall is treated to promote homeotropic anchoring, and the second one is rubbed in the  $x$  direction and promotes planar, nondegenerate anchoring parallel to  $x$  ( $\varphi = 0$ ).

In the present case, the molecules are free to rotate at both interfaces. The perturbation of the HAN state corresponds to

azimuthal periodic oscillations out of the plane  $xz$ , that is, in the  $y$  direction (twist). Now, the angles  $\theta(y,z)$  and  $\varphi(y,z)$  depend on  $z$  and are periodic functions of  $y$ , with the system still being invariant in the  $x$  direction. The periodic structure is referred to as “PHAN” in the literature,<sup>4–8</sup> and P is here for periodic.

The LP model accounts satisfactorily for the intermediate range of thickness, while difficulties are met close to the upper  $D$  and lower UB thickness thresholds of  $\chi(d)$ .

- (i) Considering the lower threshold UB, a HAN configuration exists only above a certain thickness  $d_{\text{HAN-homogeneous}}$  below which it is replaced by a homogeneous one, imposed by the stronger anchoring. As anchoring is stronger on water and glycerol than at the free surface, here the homogeneous configuration is planar. It is referred to as P in the literature; see Figure 7.<sup>4–8</sup> Therefore, the HAN structure cannot be used as a base state below  $d_{\text{HAN-P}}$ , which requires  $\text{UB} \geq d_{\text{HAN-P}}$ . However, values of  $d_{\text{HAN-P}}$  available in the literature<sup>1–3,19</sup> are much larger than the UB values found in our systems.
- (ii) The relevance of a linear analysis is questionable, as the azimuthal deviation  $\varphi$  of the local orientation out of the plane  $xz$  amounts to  $\pm\pi/4$ , which is quite large.
- (iii) The model is not robust at the upper threshold  $D$ , where the predicted  $\chi(d)$  limit jumps from zero to infinity for very small changes of the parameters.

**III.2.2. The AS Model.** Another approach has been developed by Sparavigna and co-workers (AS model).<sup>7,8</sup> Here, the analysis focuses on the values of the thickness boundaries between the possible film structures when the molecules are free to rotate at both interfaces. The important result is that the PHAN structure is found to be intercalated between P and HAN, and therefore the P-HAN transition merely disappears (Figure 8). An obvious consequence is that the thicker PHAN films may possibly be treated as perturbations of the HAN state, but not the thinner ones. Although the wavelengths at the boundaries (i.e., the visibility of the stripes) are not calculated in the AS analysis, one may expect  $d_{\text{PHAN-P}}$  to be close to UB (we only know that  $d_{\text{PHAN-P}} \leq \text{UB}$ ) and  $d_{\text{PHAN-HAN}}$  close to the upper thickness threshold  $D$  for the observation of stripes.

Saying more requires writing explicitly the surface energy of the films. It must be clear that the equations aim at describing films  $d \geq \text{UB}$ , and that a continuous approach with usual approximations is used. The “molecular films”, thinner than LB, are not considered.

**III.3. Continuous Theoretical Description of Hybrid Films.** The free energy of a nematic film contains bulk and surface contributions. Ignoring van der Waals interaction, which plays at lower thicknesses,<sup>13</sup> one may write:<sup>4–8,16,17,25</sup>

$$F = \iiint f_{\text{Frank}} dV + \iint \left[ f_s + K_{13} \vec{k} \cdot \vec{n} \text{div} \vec{n} - (K_{22} + K_{24}) \vec{k} \cdot (\vec{n} \text{div} \vec{n} + \vec{n} \wedge \text{rot} \vec{n}) \right] dS$$

The bulk elastic energy density writes as<sup>26</sup>

$$f_{\text{Frank}} = \frac{1}{2} K_{11} (\text{div} \vec{n})^2 + \frac{1}{2} K_{22} (\vec{n} \cdot \text{rot} \vec{n})^2 + \frac{1}{2} K_{33} (\vec{n} \wedge \text{rot} \vec{n})^2$$

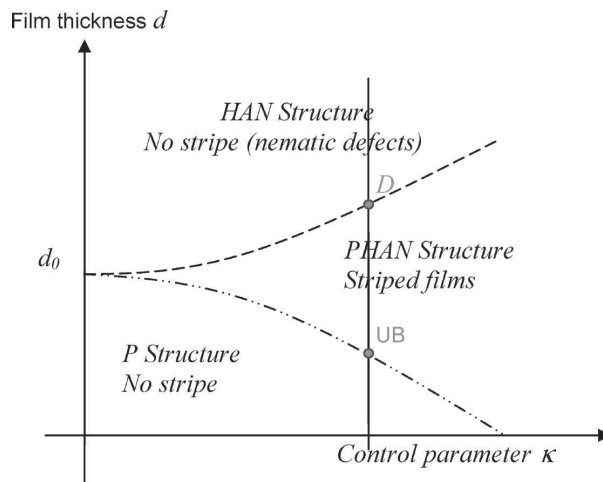


**Figure 8.** Adapted from ref 8. The control parameter  $\kappa$  depends on the elastic constants of the nematic film and will be defined in the main text. For given  $\kappa$ , striped films are observed between the two threshold lines P-PHAN (UB) and PHAN-HAN ( $D$ : stripes are replaced by nematic defects).

Here, the unit vector  $\vec{n}$  gives the local orientation and the three elastic constants  $K_{11}$  (splay),  $K_{22}$  (twist), and  $K_{33}$  (bend) are associated to the three principal deformations. In the surface term,  $f_s$  is the contribution of the two anchorings,  $\vec{k}$  is the unit vector normal to the surface and directed outward,  $K_{13}$  is the splay-bend constant, and  $K_{24}$  the saddle-splay constant. The two last surface terms play only for thin films, and they are relevant parameters for describing the stripe patterns. Anticipating on the forthcoming discussion, the “control parameter”  $\kappa$  in Figure 8 is  $\kappa = K_{24}/K_{11}$ .

The complexity of the elastic response, which contains five elastic constants, has led to various approximations. Considering the bulk elasticity, the “one-constant” approximation  $K_{11} = K_{22} = K_{33} = K$  is frequent.<sup>7,8</sup> However, as surface terms are important here, it is safer to take  $K_{11} = K_{33} = K$ , which is strictly true in the framework of Landau–de Gennes analysis<sup>27</sup> and to refer to experimental data for  $K_{22}$ . For the series of  $n$ CBs,<sup>28</sup>  $K_{33}$  is actually close to  $K_{11}$  (except for 8CB close to the SmN transition, where  $K_{33}$  diverges), while  $K_{22} \approx 0.5K_{11}$ .

There are also approximations for the anchoring term. With reference to the frame presented in Figure 7, polar anchoring can be expressed as<sup>29</sup>

$$f_s = \frac{1}{2} W_H \sin^2 \theta_H + \frac{1}{2} W_P \cos^2 \theta_P$$

At the free interface,  $W_H$  is the homeotropic anchoring energy and  $\theta_H$  the angle between  $\vec{n}$  and the normal to the film (the preferred angle is 0). On the substrate,  $W_P$  is the planar anchoring energy and  $\theta_P$  is the angle between  $\vec{n}$  and the normal (the preferred angle is  $\pi/2$ ). The response of the nematic liquid crystal is characterized by extrapolation lengths  $L_j = K/W_j$ .

Azimuthal anchoring, that is, a preferred value for the azimuthal angles  $\varphi_H$  and  $\varphi_P$  (see Figure 7), can be introduced in a similar way.<sup>7,8</sup>

(27) Sluckin, T. J.; Ponierwierski, A. In *Fluid Interfacial phenomena*; Croxton, C. A., Ed.; Wiley & Sons Ltd.: New York, 1986. Chapter 5, p 215. Sheng, P.; Priestley, E. B. In *Introduction to liquid crystals*; Priestley, E. B., Wojtowicz, P., Sheng, P., Ed.; Plenum Press: New York and London, 1974; Chapter 10, p 143.

(28) Madhusudana, N. V.; Pratibha, R. *Mol. Cryst. Liq. Cryst.* **1990**, *179*, 207.

(29) Rapini, A.; Papoular, M. *J. Phys. (Paris)* **1969**, *30*, C4.

(25) Nehring, J.; Saupe, A. *J. Chem. Phys.* **1971**, *54*, 337.

(26) Frank, F. C. *Discuss. Faraday Soc.* **1958**, *25*, 19.

- (i) The thickness threshold  $d_{\text{HAN-P}}$  has been calculated by Barbero and Barberi<sup>30</sup> for HAN films bounded by two solid walls and  $\varphi_{\text{H}} = \varphi_{\text{P}} = 0$ . The two last surface terms are neglected. The result is

$$d_0 = |L_{\text{H}} - L_{\text{P}}|$$

- (ii) In the LP model,<sup>5,6</sup> all the surface terms are taken into account.  $d_{\text{HAN-P}}$  is calculated by linear perturbation of the HAN state and does not depend on the last surface term, that is, on the “control parameter”  $\kappa$ , in contrast with the AS model. However, it is shifted due to the splay-bend term:<sup>5,6,31</sup>

$$d_{\text{HAN-P}} = |L_{\text{H}} - L_{\text{P}}| \left( 1 - \frac{2K_{13}}{K} \right)$$

The LP model uses five adjustable parameters,  $L_{\text{H}}$ ,  $L_{\text{P}}$ ,  $K_{13}/K$ ,  $K_{24}/K$ , and  $K_{22}/K$ . The best fit with experimental data obtained with 5CB on glycerol leads to a negative value of  $K_{13}/K$ ; therefore,  $d_{\text{HAN-P}} > d_0$ . The upper threshold  $d_{\text{PHAN-HAN}}$  is also calculated.

- (iii) In the AS model,  $K_{11} = K_{22} = K_{33} = K$ , and  $K_{13} = 0$ .<sup>7,8</sup> The thresholds depend on  $k = K_{24}/K$ , with:

$$d_{\text{PHAN-HAN}} \geq d_0 \geq d_{\text{PHAN-P}}$$

The upper threshold is obtained by linear perturbation of the HAN state, and the lower one by linear perturbation of the P state. The corresponding “phase diagram” is represented in Figure 8. In a more recent, numerical work, similar results for the lower threshold  $d_{\text{PHAN-P}}$  have been obtained beyond linear analysis by Krzyzanski and Derfel (KD) with  $K_{13} = 0$ ,  $K_{33} = 1.3K_{11}$ , and  $K_{22} = 0.5K_{11}$ , close to the 5CB case.<sup>32</sup> The remarkable result of these approaches is the possibility to obtain UB values much smaller than  $d_0$ , as illustrated in Figure 8.

In order to explore further this point, we have rewritten the AS approach with the KD values of elastic constants,  $K_{13} = 0$ ,  $K_{33} = 1.3K_{11}$ , and  $K_{22} = 0.5K_{11}$ , including also the possibility of azimuthal anchoring. This is noticeably useful in the presence of thickness gradients, which remove the planar degeneracy.

**III.4. The Lower Stripe Threshold: Extension of the Available Models.** The principle of the calculations is given in the Appendix. A linear perturbation of the P state is introduced. The minimization of the free energy leads to equations in  $\theta$  and  $\varphi$ .<sup>7,8</sup> The condition to obtain a nontrivial solution, that is, a PHAN structure, gives the lower threshold  $d_{\text{PHAN-P}}$ . We solved it numerically for several ratios of polar and azimuthal anchorings at both interfaces. Typical results are reported in Figure 9.

- (i) Without azimuthal anchoring, the KD result is recovered, which is satisfactory.
- (ii) At given  $K_{24}/K_{11}$ , an azimuthal anchoring increases the value of  $d_{\text{PHAN-P}}$  toward the  $d_0$  value. For strong azimuthal anchoring, the Barbero–Barberi value  $d_0$  is recovered. A remarkable, nonintuitive result is that azimuthal anchoring is much more efficient at the homeotropic interface than at the planar one.

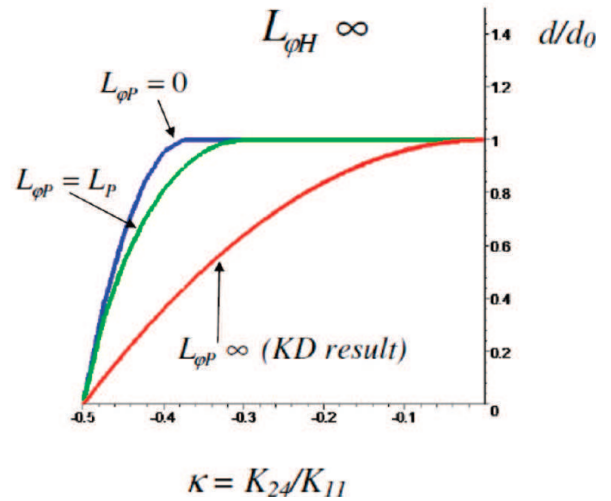
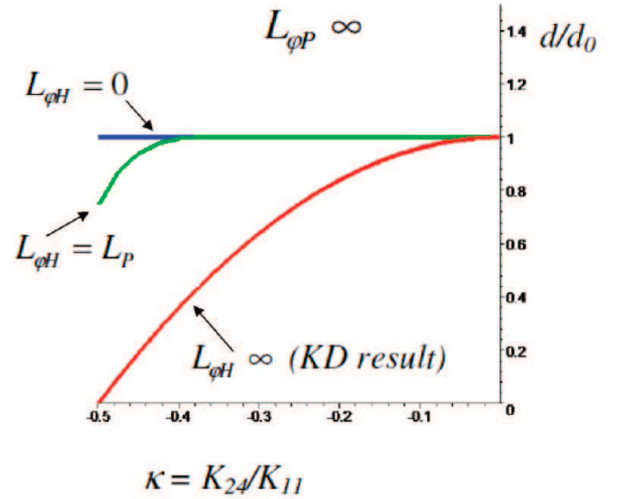


**Figure 9.** P-PHAN threshold UB for several values of the azimuthal extrapolation lengths. The ratio of the polar extrapolation lengths is  $L_{\text{H}}/L_{\text{P}} = W_{\text{P}}/W_{\text{H}} = 2$ . The P-PHAN threshold UB decreases considerably for  $|k = K_{24}/K_{11}| \approx 0.5$ . Top: no azimuthal anchoring on the substrate ( $L_{\varphi\text{H}} = \infty$ ), effect of the azimuthal anchoring at the free (homeotropic) interface.  $L_{\varphi\text{H}} = \infty$ , no azimuthal anchoring at the free interface.  $L_{\varphi\text{H}} = L_{\text{P}}$ : the azimuthal anchoring is equal to the planar anchoring.  $L_{\varphi\text{H}} = 0$ , infinitely strong azimuthal anchoring. Bottom: no azimuthal anchoring at the free surface ( $L_{\varphi\text{P}} = \infty$ ), effect of the azimuthal anchoring at the substrate. Values chosen for the ratios of elastic constants:  $K_{13} = 0$ ,  $K_{33} = 1.3K_{11}$ , and  $K_{22} = 0.5K_{11}$ .

- (iii) A consequence is an increase of the  $d_{\text{PHAN-P}}$  threshold at the edge of films. As stated by several authors,<sup>8,33</sup> a thickness gradient is equivalent to an azimuthal anchoring. Simple geometrical models based on a HAN configuration have been developed for thicknesses larger than  $d_0$ . If  $\Delta\theta$  is the difference of the polar angles at the interfaces and  $\alpha$  the slope of the free surface, then the effective azimuthal extrapolation length writes as<sup>33</sup>

$$L_{\varphi\text{H}} \approx \frac{d}{\alpha\Delta\theta}$$

Here, we are mostly concerned with situations where  $d < d_0$  and where the film structure is far

(30) Barbero, G.; Barberi, R. *J. Phys. (Paris)* **1983**, *44*, 609.

(31) Alexe-Ionescu, A. L. *Int. J. Mod. Phys. B* **1993**, *B7*, 1131.

(32) Krzyzanski, D.; Derfel, G. *Phys. Rev. E* **2001**, *63*, 021702.

(33) Sparavigna, A.; Komitov, L.; Stebler, B.; Strigazzi, A. *Mol. Cryst. Liq. Cryst.* **1991**, *207*, 265. Lavrentovich, O. D. *Phys. Rev. A* **1992**, *46*, R722.



from the HAN configuration. Anyway,  $L_{\phi H}$  does exist, even if it is not easily calculated. Therefore, a structural change from PHAN to P will take place at the edge of the striped films.<sup>8</sup>

**III.5. Comparison with Experiments.** *III.5.1. Available Parameters.* The three bulk elastic constants are relatively well-known for the investigated  $n$ CBs,<sup>28</sup> but this is not the case for the two surface ones. The saddle-splay constant  $K_{24}$  has been investigated by NMR measurements in 5CB<sup>34</sup> and found to be such as  $|K_{24}/K_{11}| \leq 0.6$ . The mere existence of the splay-bend constant  $K_{13}$ , at least in a continuous approach (in the present approach, only the local orientation is allowed to change; the value of the order parameter is constant within the film<sup>27</sup>), is a matter of debate.<sup>35</sup> All these constants decrease with increasing temperature and vanish in the isotropic range. In the framework of the Landau–de Gennes analysis, they scale like the square of the order parameter.

The anchoring energy  $W_H$  at the free interface is of the order of  $10^{-5} \text{ J m}^{-2}$  far from the NI transition.<sup>5,19</sup> For the substrates,  $W_{\text{Pwater}} \approx W_{\text{Pglycerol}} > W_H > W_{\text{Psilica}}$ , although data are scattered. (Besides experimental difficulties, the mere meaning of anchoring depends on the scale, and so do the measured values.) Anchoring energies decrease when approaching the NI transition, and extrapolation lengths increase.<sup>36,37</sup>

Far from the NI transition, accepted values of  $d_0$  are around  $0.3\text{--}0.5 \mu\text{m}$  for 5CB.<sup>8</sup> Similar ones are expected for the other  $n$ CBs. The extrapolation lengths are around the micrometer range.

#### III.5.2. Specific Analysis of the $\chi(D)$ Behavior

- (i) Measured values of the lower stripe threshold UB are in the range  $20\text{--}30 \text{ nm}$ , whatever the substrate and the  $n$ CB. This means that  $UB \ll d_0$ , and therefore, calculations based on AS and KD models are required for the thinner striped films. In the specific cases  $K_{22} = 0.5K_{11}$  and  $K_{33} = 1.3K_{11}$ , experimental values of UB are accounted for if  $|K_{24}| \approx K_{22}$  (Figure 9), compatible with NMR measurements in 5CB.<sup>34</sup> (The relevant parameter is  $|1 - 2(K_{22} + K_{24})/K_{11}|$ ; therefore,  $K_{24}$  and  $-K_{24}$  give identical results.) Unfortunately, calculating wavelengths becomes now quite tricky. Moreover, in such very thin films, both a continuous analysis of elasticity and the simple shape used for the anchoring energy become questionable. The only clear conclusion is that the low value of UB is explained. Noticeably, assuming  $d_0$  to be much smaller than the extrapolation lengths, as in the LP model,<sup>5</sup> it is no longer required.
- (ii) The temperature dependence of  $\chi(d, T)$  at given  $d$  is relatively weak. We expect the wavelength to increase with increasing temperature more or less like the extrapolation lengths, but significant effects, if any, seem to be restricted to the immediate vicinity of the NI transition.

**III.6. Conclusion.** The main features of the  $\chi(d)$  behavior are acceptably understood. Noticeably, the ingredients required to account for the lower thickness threshold for the stripes are

(34) Allender, D. W.; Crawford, G. P.; Doane, J. W. *Phys. Rev. Lett.* **1992**, *67*, 1442.

(35) Oldano, C.; Barbero, G. *Phys. Lett.* **1985**, *110A*, 213. Oldano, C.; Barbero, G. *Nuovo Cimento* **1985**, *D6*, 479. Barbero, G.; Oldano, C. *Mol. Cryst. Liq. Cryst.* **1989**, *168*, 1. Barbero, G.; Oldano, C. *Mol. Cryst. Liq. Cryst.* **1989**, *170*, 99.

(36) Van Sprang, H. A.; Aartsen, R. G. *Mol. Cryst. Liq. Cryst.* **1985**, *123*, 355.

(37) Faetti, S.; Gatti, M.; Paleschi, V.; Sluckin, T. *Phys. Rev. Lett.* **1985**, *55*, 1681.

identified. Experiment shows that this threshold coincides with the boundary UB. This is not strictly demonstrated, as writing the free energy in the complete range of thickness is not yet possible. Very close to  $T_{\text{NI}}$ , as both LB and UB are mesoscopic, a model with a homogeneous order parameter and strong anchorings has been proposed on silicon wafers.<sup>12</sup> At least on water, as we shall see below, such a simple situation is clearly not met. Let us now report line tension measurements, and especially close to the NI transition.

## IV. Line Tension Measurements

Line tensions are measurable on water, as well-defined, flat domains are present. Measurements are easiest with 6CB, which has the lowest range of nematic temperatures. Previous investigations were performed far from the NI transition, both by static and dynamic methods.<sup>20</sup> Here, we investigate the approach to the transition, using only the dynamic method.

**IV.1. Method Used, Previous Measurements, and Further Comment.** The line tension  $\tau$  is deduced from the long-time relaxation dynamics of coalescing domains, selected to have comparable size and thickness.<sup>15,20</sup> The driving parameter for coalescence is the line tension (which is the 2D analogue of surface tension). At late times, the dissipation takes place in the liquid substrate, for which the viscosity is  $\eta_b$ . The relaxation toward the final circular shape of radius  $R_F$  is exponential, with a characteristic time  $T_{\text{rel}}$ .<sup>38</sup>

$$T_{\text{rel}} = \frac{5\pi}{16} \frac{\eta_b R_F^2}{\tau}$$

The line tension increases linearly with the stripe wavelength for thicknesses less than  $0.2 \mu\text{m}$  typically. Moreover, under high magnification, a nonstriped rim, with width  $\delta$  approximately half the wavelength, is seen at the edge of the nematic domains.<sup>20</sup> Using polarized light shows that the rim has a planar (P) configuration. Then a simple model assumes that the main contribution to the line tension is due to the anchoring energy at the free interface, as the planar configuration is unfavorable there.<sup>20</sup>

$$\tau \approx W_H \delta \approx W_H \frac{\lambda}{2}$$

The calculated values of  $\tau$  agree satisfactorily with the measured ones for  $W_H \approx 10^{-5} \text{ J m}^{-2}$ , which is the accepted value for the homeotropic anchoring energy far from the NI transition.

The presence of a planar rim around a hybrid nematic domain is expected if we refer to the discussion of the lower stripe threshold in III.4. Thickness gradients at the domain edge remove the azimuthal degeneracy, which is equivalent to an azimuthal anchoring. The threshold  $d_{\text{PHAN-P}}$  increases toward the value  $h_0 \approx 0.3\text{--}0.5 \mu\text{m}$ , as predicted.

In contrast, the proportionality between  $\tau$  and  $\delta$ , and the success of the very primitive model linking the line tension to the homeotropic anchoring energy  $\tau \approx W_H \delta$ , was not expected.<sup>20</sup>

**IV.2. Vicinity of the NI Transition.** *IV.2.1.* Approaching the transition temperature  $T_{\text{NI}}$  on a water substrate is much more tricky than on silicon wafers. In contrast with the gradual increase of LB observed on the wafers, here there is an abrupt change typically  $1.5 \text{ }^\circ\text{C}$  below  $T_{\text{NI}}$ . The LB value jumps from  $3$  to  $5 \text{ nm}$  to more than  $30 \text{ nm}$ . No intermediate LB values are observed. In the following, the LB film close to  $T_{\text{NI}}$ ,  $30 \text{ nm}$  thick or more, will be referred to as a “thick molecular” film (Figure 10).

(38) Stone, H.; McConnell, H. M. *Proc. R. Soc. London, Ser. A* **1995**, *448*, 97.

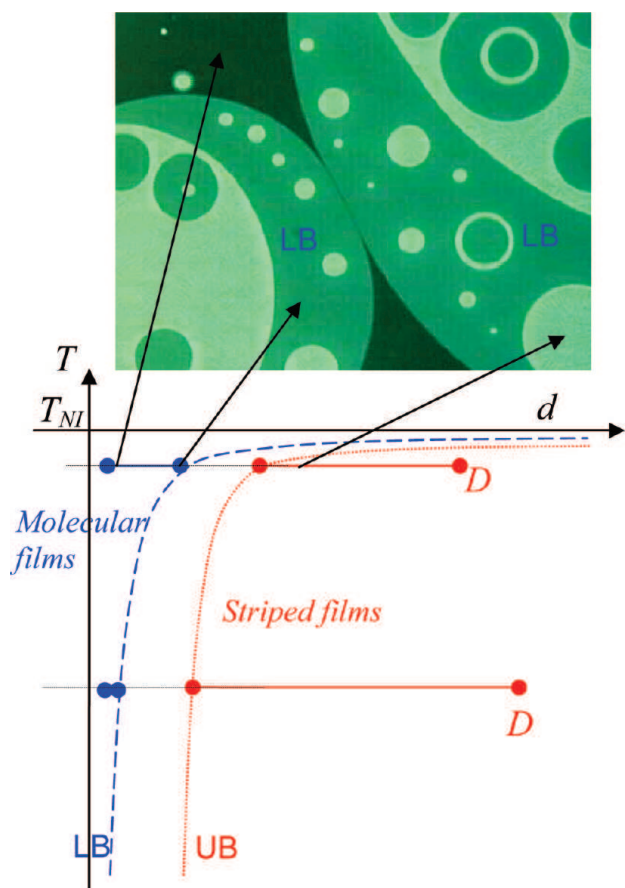


**Figure 10.** Close to the NI transition (6CB on water), some molecular films become significantly thicker, without stripes. Striped domains (the stripes are present, although hardly visible in the picture because of the low magnification) are in contact with the “thick molecular” film of thickness LB. Size of the picture: 0.9 mm × 0.7 mm.

*IV.2.1.* Line tension between the striped domains and this film can be deduced from the dynamics of coalescence between two striped domains of comparable size and thickness surrounded by the thick molecular film. The size of this film must be at least three times the diameter of the domains, which ensures that it does not play in the dynamics.<sup>38</sup>

At late times, the dissipation in the liquid subphase takes over the surface dissipation, like far from the NI transition, and the surface viscosity of the thick molecular film does not play anymore. The relevant parameter is therefore the bulk viscosity  $\eta_b$  of the liquid substrate. The line tension is again deduced from the formula:

$$T_{\text{rel}} = \frac{5\pi}{16} \frac{\eta_b R_F^2}{\tau}$$

The validity of the analysis has been checked by collecting data for coalescence events between domains of different size and comparable thickness (each event corresponds to two domains with the same size and same thickness). This specific check is required in the present situation as the surface viscosity of the thick molecular film is much larger than the one of the trilayer. Figure 11 shows that the squared dependence  $T_{\text{rel}} \propto R_F^2$  is well obeyed.

*IV.2.2.* Rim  $\delta$  at the edge of the striped domains is also measured. When plotted versus the stripe wavelength, no effect of temperature is observed; see Figure 12. In contrast, the line tension  $\tau$  drops down dramatically as soon as the surrounding

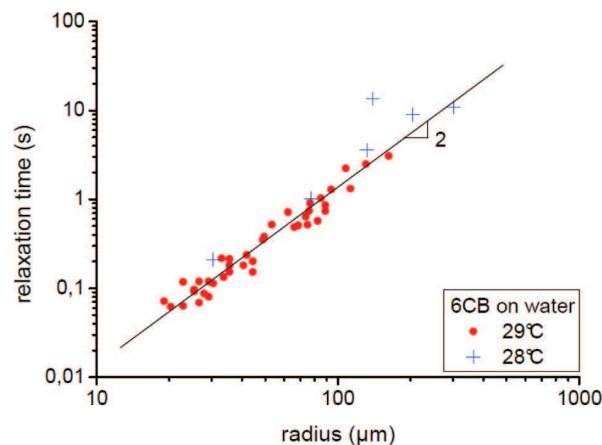


**Figure 11.** Check of the process controlling the dynamics of coalescence. For a collection of coalescing pairs with similar thickness, the relaxation time scales like the square of the radius, which proves that viscous dissipation in the bulk liquid substrate controls the coalescence dynamics. Each point corresponds to one coalescence between two striped domains with same size and thickness on a “thick molecular” surrounding film LB.

film becomes a “thick molecular” film; see Figure 13. If we refer to the model presented above, the difference should therefore be in the value of the anchoring energy  $W_H$ , which decreases close to  $T_{\text{NI}}$ .<sup>37</sup> Assuming  $W_H \approx 1.4 \times 10^{-6} \text{ J m}^{-2}$  accounts for the data close to  $T_{\text{NI}}$ , and such a value is quite plausible. However, even if this specific result is satisfactory, further work is required to understand why on water the LB boundary jumps so suddenly, and which is the structure of the thick molecular film. The behavior of thin hybrid nematic films has been the subject of extensive analyses, both from the theoretical and the experimental point of view.<sup>39–41</sup> It is widely accepted that when the planar anchoring is degenerate, which is the case here, the value of the order parameter is not homogeneous within the film. Then the whole Landau–de Gennes free energy is required for a proper description: both local orientation and local value of the order parameter are needed.<sup>27</sup> While a continuous description works acceptably for the striped films, where the local orientation plays the major role, this is probably not the case for the thick molecular films.

## V. Summary and Conclusion

The present work completes the previous studies of thin nematic films on various substrates. A better control of the purity of the liquid crystal samples, and the investigation of mutual miscibility with the underlying liquid substrate allow us to provide a coherent picture of these systems far from the nematic–isotropic transition.

The available models are discussed, and the relevant results extracted: stripe wavelength in the intermediate range of thickness for the Lavrentovich–Pergamenschchik LP model; thickness thresholds for the stripe pattern for Sparavigna AS and Krzyzanski–Derfel KD models. An extension of the AS model with proper elastic constants and accounting for azimuthal anchoring

(39) Miyano, K. *J. Chem. Phys.* **1979**, *71*, 4108. Miyano, K. *Phys. Rev. E* **1979**, *43*, 51. Tarczon, J.; Miyano, K. *J. Chem. Phys.* **1980**, *73*, 1994.

(40) Yokohama, H. *J. Chem. Soc., Faraday Trans. 2* **1988**, *84*, 1023.

(41) Moses, T.; Shen, Y. R. *Phys. Rev. Lett.* **1991**, *67*, 2033. Feller, M. B.; Chen, W.; Shen, Y. R. *Phys. Rev. A* **1991**, *43*, 6778. Sheng, P.; Li, B.-Z.; Zhou, M.; Moses, T.; Shen, Y. R. *Phys. Rev. A* **1992**, *46*, 946. Zhuang, X.; Marrucci, L.; Shen, Y. R. *Phys. Rev. Lett.* **1994**, *73*, 1513. Qian, T.; Zhuang, X.; Shen, Y. R. *Phys. Rev. E* **1999**, *59*, 1873.

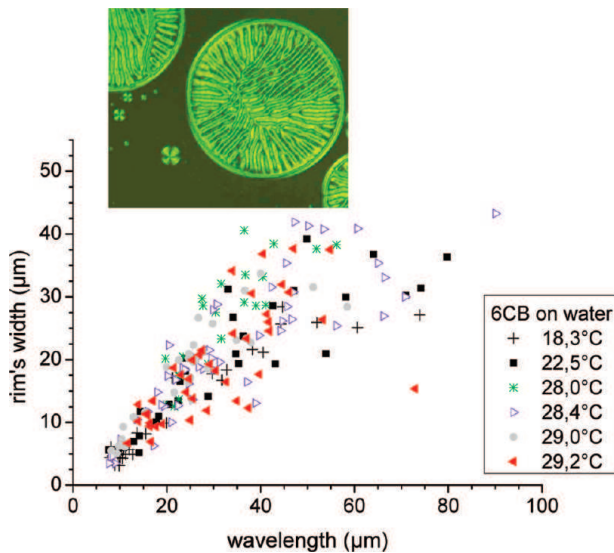


**Figure 12.** Width  $\delta$  of the rim of the striped domains. Even if the data are scattered, one may exclude a significant dependence of  $\delta$  with temperature. Picture taken between crossed polarizers. The smallest domains on the bottom left have a fully planar, radial configuration with a line defect in the center.<sup>20</sup>

has been added. The role of azimuthal anchoring allows one to explain the structure of the edge of nematic domains. A very simple model of line tension using this structure is found satisfactory.

The behavior of the systems when approaching the nematic–isotropic transition has been investigated. A steep decrease of the line tension of nematic domains in coexistence with the “thick molecular films” developing very close to the transition is observed. Results are compatible with the previous model of line tension considering the decrease of the anchoring energies, which is quite satisfactory. However, the structure of the “thick molecular films” is an open problem. Many questions are still unanswered, noticeably considering the difficulty of experiments very close to the transition.

**Acknowledgment.** The present work is supported by the ANR DYNINSTAMOBIL of the French CNRS, and the “Fédération des systèmes complexes”, headed by Pr. M. Ben Amar.

### Appendix: The P-PHAN Threshold

#### 1. Principle of the Calculation: The P-PHAN Threshold.

Let us introduce the calculation in the simple one-constant approximation in the Barbero–Barberi approach:<sup>30</sup> only the polar angles are considered. The free energy per unit area writes as

$$f = \int_0^d \frac{K}{2} \left( \frac{d\theta}{dz} \right)^2 dz + \frac{1}{2} W_H \sin^2 \theta_H + \frac{1}{2} W_P \cos^2 \theta_P$$

The minimization of the free energy at given  $\theta_H$  and  $\theta_P$  gives the Euler–Lagrange equation  $d^2\theta/dz^2 = 0$ . Now the free energy is minimized with respect to the angles  $\theta_H(d)$  and  $\theta_P(d)$ .

$$f = \frac{K}{2d} (\theta_H - \theta_P)^2 + \frac{1}{2} W_H \sin^2 \theta_H + \frac{1}{2} W_P \cos^2 \theta_P$$

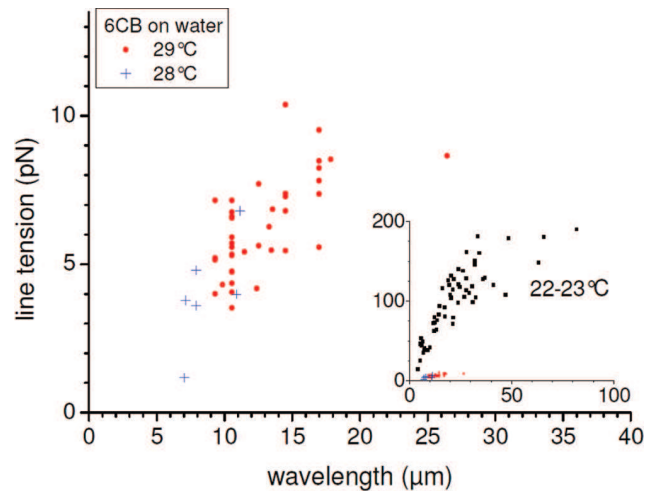


**Figure 13.** Line tension at the edge of striped domains surrounded by a “thick molecular” film of thickness  $LB$  close to the NI transition. Inset: The upper points are the measured line tension far from the transition,<sup>15,20</sup> in which case the surrounding film  $LB$  is a trilayer. The lower ones correspond to the main curve.

The values of the angles are determined by the coupled equations, which are solved numerically:

$$\frac{2K}{d} (\theta_H - \theta_P) + W_P \sin 2\theta_P = 0$$

$$\frac{2K}{d} (\theta_H - \theta_P) + W_H \sin 2\theta_H = 0$$

A nonzero value of  $\theta_H - \theta_P$  requires  $d > d_0$ ,  $d_0 = |L_H - L_P|$ ,  $L_j = K/W_j$ .

**2. The P-PHAN Threshold.** Now all the constants except  $K_{13}$  are considered. The angles  $\theta$  and  $\varphi$  are supposed to be small (we are close to a P configuration), and a linear approximation is used. After the first minimization of the free energy, the equations for the angles are as follows:

For the planar interface

$$K_{11} \left. \frac{d\theta}{dz} \right|_P + (K_{11} - 2(K_{22} + K_{24})) \left. \frac{d\varphi}{dy} \right|_P - W_P \theta_P = 0$$

$$K_{22} \left. \frac{d\varphi}{dz} \right|_P + (K_{22} + 2K_{24}) \left. \frac{d\theta}{dy} \right|_P - W_{\varphi P} \varphi_P = 0$$

For the homeotropic interface

$$K_{11} \left. \frac{d\theta}{dz} \right|_H + (K_{11} - 2(K_{22} + K_{24})) \left. \frac{d\varphi}{dy} \right|_H - W_H \theta_H = 0$$

$$K_{22} \left. \frac{d\varphi}{dz} \right|_H + (K_{22} + 2K_{24}) \left. \frac{d\theta}{dy} \right|_H + W_{\varphi H} \varphi_H = 0$$

Without azimuthal anchoring,  $W_{\varphi H} = W_{\varphi P} = 0$ , the relevant parameters are the ratio  $k = K_{24}/K_{11}$ , and the extrapolation lengths  $L_P = K_{11}/W_P$  and  $L_H = K_{11}/W_H$ . With azimuthal anchoring, two azimuthal extrapolation lengths  $L_{\varphi P} = K_{11}/W_{\varphi P}$  and  $L_{\varphi H} = K_{11}/W_{\varphi H}$  come into play.



Thin Nematic Films on Liquid Substrates<sup>†</sup>U. Delabre,<sup>\*,‡,§</sup> C. Richard,<sup>‡,§</sup> and A. M. Cazabat<sup>‡,§</sup>*Laboratoire de Physique Statistique de l'ENS, 24 rue Lhomond, 75231 Paris Cedex 05, Université Pierre et Marie Curie, 4 place Jussieu, 75252 Paris Cedex 05**Received: July 15, 2008; Revised Manuscript Received: September 11, 2008*

Thin films of cyanobiphenyl liquid crystals (nCB) deposited on water or glycerol have been studied in the nematic temperature range. A common property of the systems is the hybrid anchoring conditions at the film interfaces. The preferred orientation of the nematic director is planar at the liquid interface, and it is homeotropic and somewhat weaker at the air interface. The resulting structure of the film depends on its thickness. Films thicker than  $0.5\ \mu\text{m}$  show the usual defects of nematics. Between  $0.5\ \mu\text{m}$  and  $20\text{--}30\ \text{nm}$ , complex instability patterns such as stripes, “chevrons”, or squares are observed in extended films. Then there is a forbidden range of thickness below in which much thinner structures (usually monolayers and trilayers) are present. The present paper investigates this common behavior in various systems and gives arguments for its analysis.

## Introduction

Thin films of nematic liquid crystals (LC) are confined media, and their physical parameters and structures may significantly differ from the ones of the bulk phases.<sup>1–6</sup> Most studies use cells where the LC is enclosed between two solid walls situated a few tens of micrometers apart.<sup>7–9</sup> The situation is different if the film has a free interface, in which case the thickness is not imposed. Films of different thicknesses may coexist, and a forbidden range of thickness has been observed for films deposited on oxidized silicon wafers.<sup>4–6,10,11</sup>

The anchoring of liquid crystals, that is, the orientation of the nematic director at interfaces, has been widely investigated.<sup>7–9,12</sup> The anchoring of the n-cyanobiphenyls (nCB) is known to be homeotropic at the free interface (nematic director normal to the interface) and planar degenerate on amorphous silica, water, or glycerol (director in the plane of the interface). These hybrid conditions cause a distortion of the nematic order in the LC film, which is usually described as follows:

Let us call  $z$  the normal at the interface which is a  $xy$  plane (Figure 1). For relatively thick films, the two interfaces are independent. Let the director be along  $x$  on the substrate. It will rotate inside a  $xz$  plane to be along  $z$  at the free interface (Figure 1a). Within the one-constant approximation,<sup>13–15</sup> the cost of the elastic distortion per unit area is

$$f_{\text{elastic}} = \frac{K(\pi/2)^2}{2h} \quad (1)$$

where  $h$  is the film thickness and  $K$  the common value of the elastic constants. For thinner films, the angles at interfaces differ from their preferred values. In the present case, if  $\theta_i$  is the effective angle of the director with respect to the normal at interfaces (Figure 1b), the free energy can be written as<sup>16</sup>

$$f = \frac{W_1}{2} \cos^2 \theta_1 + \frac{W_2}{2} \sin^2 \theta_2 + \frac{K(\theta_1 - \theta_2)^2}{2h} \quad (2)$$

$W_1$  and  $W_2$  are the anchoring energies per unit area at the substrate and at the free interface, respectively. Associated characteristic lengths are  $L_1 = K/W_1$  and  $L_2 = K/W_2$ . Such a structure with translational invariance along  $x$  and with the director rotating inside a  $xz$  plane is referred to as a “distorted nematic”.

The cost of elastic distortion is too large for very thin films.<sup>17</sup> Below a threshold thickness  $h_c = |L_1 - L_2|$  a second-order anchoring transition is observed: thinner films show a homogeneous orientation imposed by the stronger anchoring.

Extrapolation lengths are of the order of micrometers at the air, water, and glycerol interfaces with the anchoring being weaker at the free interface ( $L_2 > L_1$ ).<sup>18</sup> The values of anchoring energy on silica are quite scattered in the literature, but it is accepted that it is weaker than the one on air ( $L_2 < L_1$ ).<sup>4,19</sup>

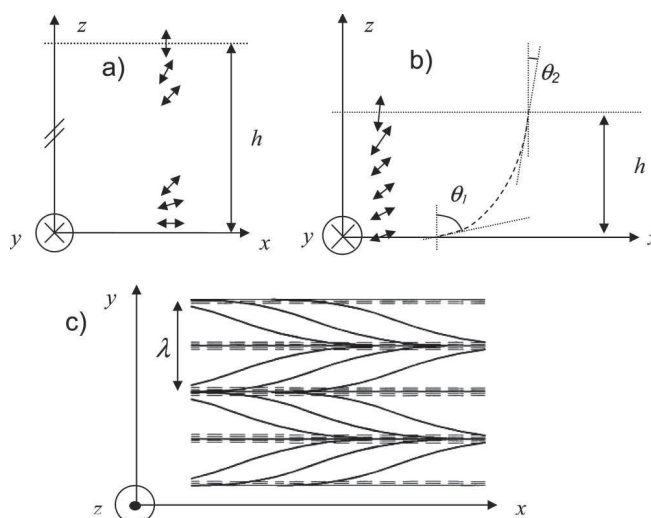


**Figure 1.** (a) Sketch of a thick film structure: the director is along the easy axis at each interface. (b) Sketch of a thin film structure; the director deviates from the easy direction at each interface. (c) Horizontal projection of the director field in stripes (from Sparavigna et al.<sup>27</sup>).

\* To whom correspondence should be addressed.

<sup>†</sup> Part of “PGG (Pierre-Gilles de Gennes) Memorial Issue”.

<sup>‡</sup> Laboratoire de Physique Statistique de l'ENS.

<sup>§</sup> Université Pierre et Marie Curie.

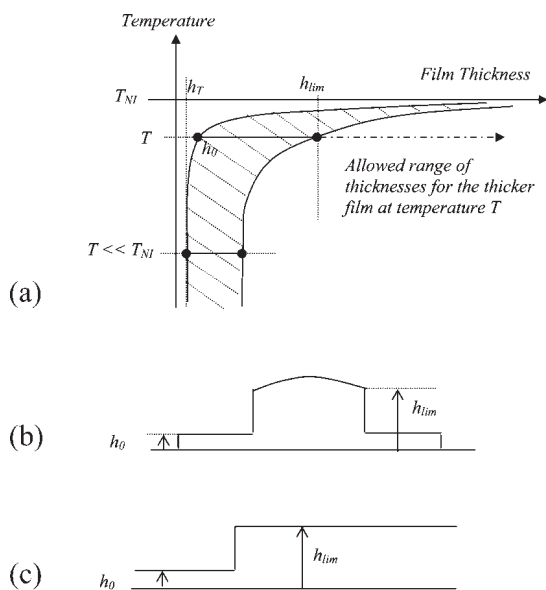


**Figure 2.** Schematic behavior of thin nematic films with antagonist anchoring at interfaces (adapted from Figure 1, ref 20) On silicon wafers, a thickness discontinuity is observed at the edge of a spreading drop (b).<sup>4,10,11</sup> For spin-coated films and average deposited thickness  $h_{\text{average}}$ , a coexistence is observed between films of thickness  $h_0$  and  $h_{\text{lim}}$  respectively if  $h_0 < h_{\text{average}} < h_{\text{lim}}$  (2c), and a homogeneous film of thickness  $h_{\text{average}}$  is observed if  $h_{\text{average}} > h_{\text{lim}}$ .<sup>5,6,10</sup> On a liquid substrate, isolated domains of different thicknesses  $\geq h_{\text{lim}}$  may coexist with the film of thickness  $h_0$ . It is accepted<sup>20–25</sup> that all these domains are in metastable equilibrium, except those of thickness  $h_{\text{lim}}$ , which are in full equilibrium with the film of thickness  $h_0$ .

This leads to the following picture:

- on oxidized silicon wafers, the film is distorted above  $h_c$  and homeotropic below.
- on water and glycerol, the film is distorted above  $h_c$  and planar below.
- except if the two anchoring energies are very close,  $h_c$  is less than micrometer but comparable. The specific case  $L_1 \cong L_2$ , that is,  $h_c \ll \text{micrometer}$ , should be exceptional.
- As the anchoring transition is second-order, nothing specific is expected when the film thickness crosses value  $h_c$ .

Experiments performed in the bulk nematic range of temperatures provide an unexpected landscape, summarized in Figure 2, which analysis is still under debate:

- On oxidized silicon wafers, a thickness discontinuity is observed for both 5CB<sup>4–6,10,11</sup> and 6CB,<sup>20</sup> and on both smooth<sup>5,6,10,11,20</sup> or obliquely evaporated<sup>4</sup> silica. This has been interpreted assuming that the thicker film (thickness  $h_{\text{lim}}$ ) is a distorted nematic ( $h_{\text{lim}} > h_c$ ). It coexists with a thinner film (thickness  $h_0$ ) whose structure is different (see Figure 2a).<sup>4–6,10,11,20</sup> Close to the bulk nematic–isotropic (NI) transition, both films are relatively thick, and the thinner film might be isotropic.<sup>6</sup> Far below the transition,  $h_{\text{lim}} \approx 20–30$  nm, and the thinner film is a well defined trilayer  $h_0 = h_T$ .

- far below the NI transition, the behavior of nCB nematic films on liquids (5CB/glycerol, 6CB/glycerol, 6CB/water,<sup>20</sup> 8CB/glycerol, 8CB/water [present study]) is qualitatively similar to the one on silica. Whatever the system,  $h_{\text{lim}} \approx 20–30$  nm. On water, the thinner film is a trilayer ( $h_0 = h_T$ ) both for 8CB<sup>21–24</sup> and 6CB.<sup>25</sup> On glycerol, the precise structure of the thinner film is not known, but thickness  $h_0$  is still in the molecular range.

- On the same nematic nCB/liquid systems, instability patterns are present for  $h_{\text{lim}} \leq h \leq h_{\text{max}}$ , with  $h_{\text{max}} \approx 0.5–0.6$   $\mu\text{m}$ ,<sup>20</sup> the wavelengths being much larger than the film thickness. Available models consider azimuthal perturbations (twist) of

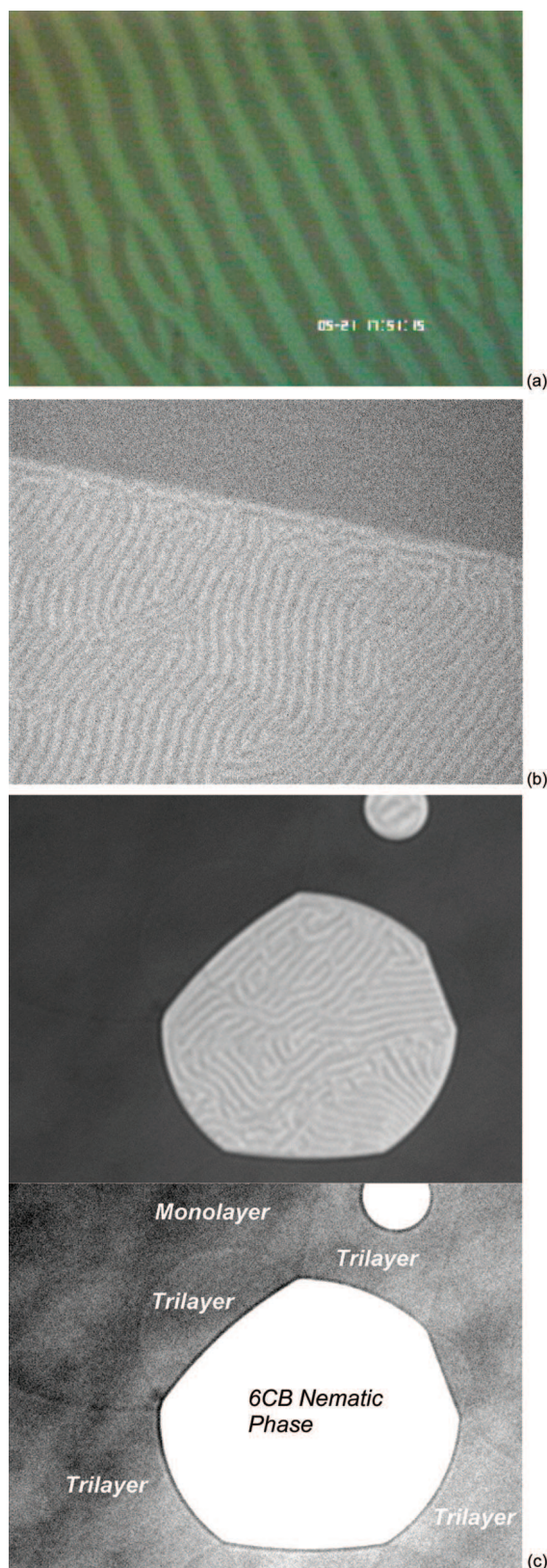


**Figure 3.** Stripe patterns of the nematic 8CB on glycerol at  $T = 35$  °C and 6CB on water at  $T = 22$  °C. (a) Stripes of 8CB on glycerol with  $\lambda \sim 50$   $\mu\text{m}$ . Size of image:  $630$   $\mu\text{m} \times 475$   $\mu\text{m}$ . (b) Stripes of 8CB on glycerol and a film boundary at  $h = h_{\text{lim}} \approx 20$  nm,  $\lambda \sim 2$   $\mu\text{m}$ . Size of image  $52$   $\mu\text{m} \times 70$   $\mu\text{m}$ . The thinner film in the upper part of the figure is probably a trilayer ( $\approx 4$  nm thick), but the structure of these films on glycerol has not yet been precisely investigated. (c) Top: striped domain of 6CB on water at  $T = 22$  °C. Bottom: same picture but enhanced contrast reveals trilayer films which coexist with the nematic phase. Ahead of the trilayers, the continuous phase is a monolayer.<sup>21–25</sup>



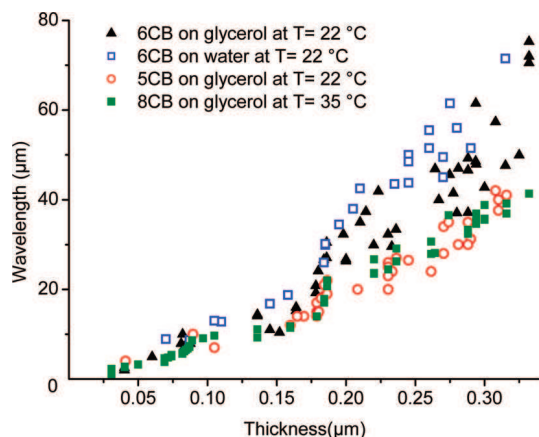


**Figure 4.** Wavelength ( $\mu\text{m}$ ) versus thickness ( $\mu\text{m}$ ) for various compounds. ( $\blacktriangle$ ) 6CB on glycerol, ( $\square$ ) 6CB on water, ( $\circ$ ) 5CB on glycerol, ( $\blacksquare$ ) 8CB on glycerol at  $T = 35^\circ\text{C}$ . While 5CB and 8CB are at the bottom limit of the nematic phase, 6CB is in the middle.

the “distorted nematic” structure, see Figure 1c.<sup>26–28</sup> Perturbations of homogeneous structures (homeotropic or planar) do not lead to long wavelengths.<sup>29</sup>

Therefore, films as thin as 20–30 nm are distorted, while  $h_C = L_2 - L_1$  is at least ten times larger. As previously quoted,<sup>20</sup> eqs 1 and 2, from which the relation  $h_C = |L_1 - L_2|$  results, are written in a continuous approximation and do not include van der Waals interaction. However, the continuous approximation is not expected to be drastically wrong in this range of thickness, and the van der Waals contribution becomes negligible above 40 nm.<sup>20</sup>

The present paper proposes an alternative analysis of the results. The procedure is to accumulate data on various systems in order to exclude explanations based on implausible assumptions, that is, very specific values for anchoring energies and elastic constants.<sup>26</sup> Previous results<sup>20</sup> with 5CB and 6CB films on water and glycerol are implemented by an explorative investigation of the structure of instability patterns. New experiments with 8CB on water and glycerol are also performed.

## Materials and Methods

The nCB liquid crystals are purchased from Sigma-Aldrich and used as received. The bulk transition temperatures are<sup>15</sup>

$$T_{\text{solid-nematic}} = T_{\text{SN}} = 24^\circ\text{C for 5CB, } 14.5^\circ\text{C for 6CB}$$

$$T_{\text{solid-smectic}} = T_{\text{SSm}} = 21.5^\circ\text{C for 8CB}$$

$$T_{\text{smectic-nematic}} = T_{\text{SmN}} = 33.5^\circ\text{C for 8CB}$$

$$T_{\text{nematic-isotropic}} = T_{\text{NI}} =$$

$$35.3^\circ\text{C for 5CB, } 29^\circ\text{C for 6CB, } 40.5^\circ\text{C for 8CB}$$

5CB and 6CB have been studied at room temperature  $22 \pm 1^\circ\text{C}$ , far from the NI transitions. 8CB has been studied both at room temperature (in the smectic range) and between 34 and  $40^\circ\text{C}$  (in the nematic range). Surface induced melting is the rule for the nCB,<sup>30</sup> which means that we do not have to consider the occurrence of a SN or SSm transition.

Pure water ( $18.2\text{ M}\Omega\cdot\text{cm}$ ) and glycerol from Sigma-Aldrich are used as liquid substrates in common Petri dishes. Samples with glycerol must be kept in closed boxes with desiccant in order to avoid uptaking atmospheric water.

Films are obtained by the deposition of drops of solutions of the nCB in hexane. After complete evaporation of the solvent, some local rearrangements including domain coalescence take place during 15–20 mn, and then the films evolve much more

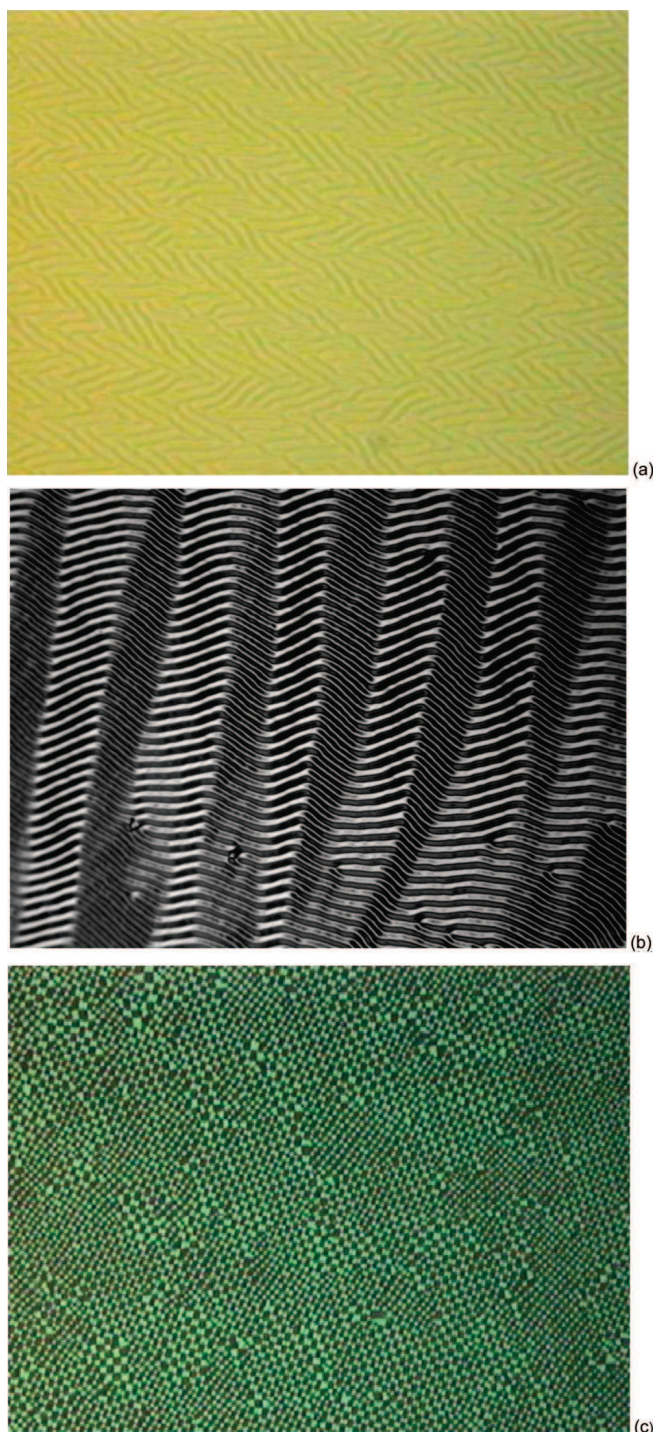


**Figure 5.** (a) “Chevrons” pattern: 8CB on glycerol at  $T = 35^\circ\text{C}$ . Size of image  $630\ \mu\text{m} \times 475\ \mu\text{m}$ . (b) Zig-zag pattern: 5CB on glycerol at  $T = 22^\circ\text{C}$ . Size of image  $320\ \mu\text{m} \times 240\ \mu\text{m}$  (see ref 15, p 203). (c) Square lattice: 6CB on glycerol at  $T = 22^\circ\text{C}$ . Size of image:  $645\ \mu\text{m} \times 480\ \mu\text{m}$ .

slowly over days. While 6CB and 8CB spread both on water and glycerol, 5CB spreads only on glycerol. On water, small droplets with a finite contact angles are obtained. Glycerol is also more convenient than water if heating is needed, because the larger viscosity avoids convection inside the liquid substrate.

The films are observed under microscope (Polyvar MET-Reichert-Jung) and the images recorded for further analysis. The thickness is estimated using the Newton scale of colors. For the thinnest samples, a high sensitivity black and white camera (CoolSnap-Photometrics) is used. The thickness is estimated by

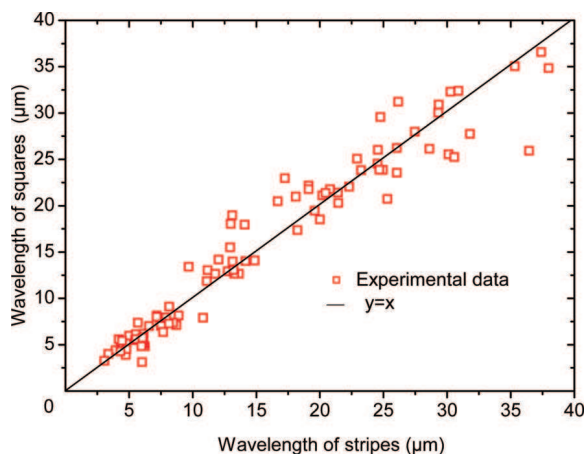


**Figure 6.** Wavelength of squares versus wavelength of stripes. 6CB on glycerol at  $T = 22$  °C.

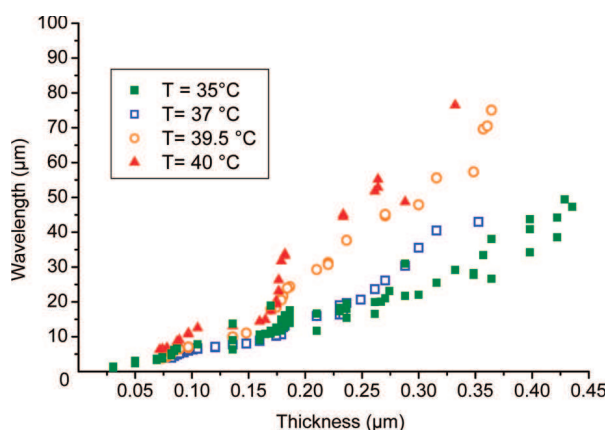


**Figure 7.** Wavelength versus thickness for the 8CB compound on glycerol at various temperatures. (■) Full squares,  $T = 35$  °C; (□) open squares,  $T = 37$  °C; (○) open circles,  $T = 39.5$  °C; (▲) full triangles,  $T = 40$  °C.  $T_{NI}$  (8CB) = 40.5 °C. The seemingly oscillatory behavior of the curves is an artifact due to the spectrum of the microscope lamp.

extrapolation of the data for thicker samples and is cross-checked by the intensity scale of the camera.

## Experimental Results

**Stripe Patterns Far below the NI Transition.** Stripe patterns were observed long ago on 5CB films spread on glycerol.<sup>26,27</sup> More recently, a comparative study has been performed on 5CB/glycerol, 6CB/glycerol, and 6CB/water systems.<sup>20</sup> Similar patterns are obtained in the nematic range for 8CB on both water and glycerol (recording is more critical with water, due to easy convection). Figure 3 gives an example of such patterns on glycerol at 35 °C. Note that instability patterns do not occur in 8CB smectic films, where twist is forbidden.<sup>14,15,22–24</sup>

The wavelength  $\lambda$  of the stripes increases with film thickness  $h$ , more or less linearly between  $h_{lim}$  and typically 0.2–0.3  $\mu\text{m}$ , then steeper, and it diverges at  $h_{max} \approx 0.5–0.6$   $\mu\text{m}$ .<sup>20,26,27</sup> Data including the values obtained with 8CB on glycerol at  $35 \pm 1$  °C for  $h \leq 0.35$   $\mu\text{m}$  are reported on Figure 4. Strictly speaking, the curves cannot be compared quantitatively because 6CB is closer to the NI transition than the two other compounds. However it is clear that the behavior of the three nCB is qualitatively the same.

The only model available has been proposed by Lavrentovich and Pergamenschchik,<sup>26</sup> and it assumes that stripes result from an azimuthal perturbation of the “distorted nematic” structure

(Figure 1c). The complete set of elastic constants which describes splay, bend, and twist deformations. The coupling between them<sup>13–15,26</sup> is required for the analysis. The model agrees on the whole with experimental data for the 5CB/glycerol system, but at the expense of several assumptions:

(1)  $L_1$  and  $L_2$  are very close ( $L_1 = 0.76$   $\mu\text{m}$ ;  $L_2 = 0.86$   $\mu\text{m}$ ,  $L_2 - L_1 = 0.1$   $\mu\text{m}$ ).

(2) Data for  $h < 0.15$   $\mu\text{m}$  are excluded from the fit. The authors state that the thickness might significantly change close to the edge of the film, which might cause azimuthal anchoring contributions not included in the analysis.<sup>26,27</sup> As a matter of fact, the model fails for  $h \leq 1.5$  ( $L_2 - L_1$ ).<sup>26</sup>

(3) Ratios  $K_{13}/K_{11}$ ,  $K_{24}/K_{11}$  of the elastic constants<sup>13–15</sup> are very critical to provide the correct shape of the curve  $\lambda(h)$  at large  $h$  and especially the presence and the position of the wavelength divergence.

These assumptions must be questioned considering the recent<sup>20</sup> and present experiments:

(1) Flat films do exist till  $h = h_{lim} \approx 20–30$  nm, even close to the film edge [ref 20 and Figure 3b].

(2, 3) The shape of the curves  $\lambda(h)$ , and the values of  $h_{lim}$  and  $h_{max}$  are similar for the 5CB/glycerol, 6CB/water and glycerol, 8CB/glycerol systems, and therefore they are very robust.

To summarize, the robustness of the value of  $h_{lim}$  implies that it cannot be always larger than  $L_2 - L_1$ , and the robustness of both the divergence in wavelength and the corresponding value of  $h_{max}$  implies that they cannot depend critically on the ratio of elastic constants. Furthermore, the  $K_{13}$  term should be negligible at large thickness because spatial variations of density and order parameter are of minor importance here.<sup>31</sup>

Alternative numerical methods based on a perturbation analysis of the planar state have been developed<sup>27,32</sup> but failed to describe the spectrum of wavelength for stripe patterns.

In fact, parallel stripes are not the sole instability pattern observable in nematic films on water and glycerol. They have been studied because they can be easily treated as azimuthal perturbations of a base state where the director field belongs to the  $xz$  plane and is invariant along  $x$  (Figure 1). Threshold thickness  $h_c = |L_1 - L_2|$  is calculated for this base state, that is, the “distorted nematic”. However if stripes are not small perturbations, the base state is no longer relevant to predict any threshold thickness. The presence of patterns with different symmetry supports also this assumption.

**Complementary Observations.** Patterns with different symmetries easily coexist with stripes. Examples are given in Figure 5.

Such patterns look very similar to the Williams instabilities observed in planar LC samples when an electric field is applied between the walls.<sup>7–9,14,15</sup> Here, the thickness plays the role of the external field. However the wavelengths are at least a hundred times larger than the thickness, and different structures may be observed and even coexist for the same thickness, while for the electro-hydrodynamical instabilities, they are observed for different field strength or frequency.<sup>14,15</sup>

Squared structures are especially interesting because there is no longer a privileged direction. Note that they are mentioned in the review paper by Lavrentovich and Pergamenschchik<sup>28</sup> but without analysis or comment. In Figure 6, the wavelength of squares is plotted versus the one of stripes for the same film thickness. They are close, and this is the strongest support to our previous assumption: instability patterns are not merely small perturbations of the base state represented in Figure 1a,b.



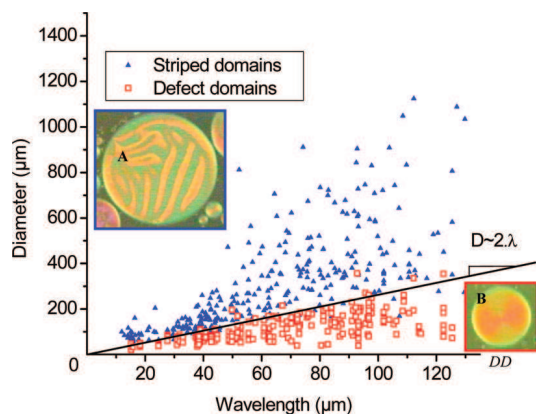


**Figure 8.** Statistical study of radius versus wavelength and the presence of stripes (extended domains) or a nematic defect (vertical disclination line, small domains). ( $\blacktriangle$ ) Full triangles: striped domains. ( $\square$ ) Open squares: defect domains. Domain *DD* (picture B) is the magnified image of one of the little domains visible at the bottom right-hand corner of the main picture A. From the colors, it has the same thickness as the large striped domain but is too small to accommodate stripes.

However, the ingredients of any analysis are still the usual elastic constants, anchoring energies, and characteristic lengths  $L_1$  and  $L_2$ . Noticeably, closer to the nematic–isotropic transition, the wavelength increases at a given thickness (see Figure 7) which is associated to the known divergence of  $K/W$ .<sup>10,14,15</sup>

**Summary and Further Discussion.** For all the systems investigated far below the NI transition, the situation is as follows:

- There is a forbidden range for the thickness of nCB nematic films on silica, water, and glycerol.
- The thinner films are molecular structures, a few nanometers thick.
- The minimum thickness of the thicker films is  $h_{\text{lim}} \approx 20\text{--}30$  nm. These films are distorted nematics and their structure on liquid substrates is modified by instability patterns if thickness  $h$  is less than  $0.6\ \mu\text{m}$  typically. The value of  $h_{\text{lim}}$  is certainly less than  $h_C = |L_1 - L_2|$ .

Let us discuss more specifically the case of these “thicker” films ( $h_{\text{lim}} \leq h \leq h_{\text{max}}$ ).

**Data on Liquid Substrates.** (1) On liquid substrates, instability patterns provide the clue to explain why films thinner than  $h_C$  can be distorted: perturbative analyses<sup>26–28</sup> are not sufficient close to  $h_{\text{lim}}$ , and therefore the threshold thickness calculated using the in-plane base-state is irrelevant. Even if the conclusion is frustrating, a result possibly useful for further theoretical analysis is the similarity in wavelengths for squares and stripes (Figure 6).

While wavelengths and instability patterns are similar on water and glycerol, this is not the case for the film itself. Flat domains of various sizes and thicknesses coexist on water, while extended films are more easily observed on glycerol. Interesting observations can be made on the 6CB/water system:<sup>25</sup> for a given thickness and therefore a given wavelength, domains smaller than the wavelength cannot accommodate stripes (Figure 8). They show a planar orientation of the director with a disclination line in the center. The orientation has a radial symmetry, which means that either the director is radial, or it is orthoradial everywhere.<sup>14,15</sup> This is also the case at the very edge of striped domains, where a planar configuration is clearly present. Until now, the largest thickness for which such domain edges have been observed is  $0.35\ \mu\text{m}$ ,<sup>25</sup> which suggests that this might be a lower threshold for  $h_C$ . However, further studies are needed to support this conjecture.

(2) Close to the wavelength divergence, stripes become the most probable pattern. Squares and “chevrons” are no longer observed (see the scale in figure 6). Therefore, a perturbative treatment with translational symmetry is probably still relevant. The difficulty with the previous model<sup>26–28</sup> is the sensitivity to the ratios of elastic constants. It is worth noting that what happens around  $h_{\text{max}}$  is not a mere divergence of wavelength, but the emergence of nonperiodic patterns of nematic defects which should be included in an energy balance.

**Data on Solid Substrates.** We propose a highly conjectural hypothesis:

Instability patterns are not expected on silica because the homeotropic anchoring (on air) is stronger than the planar one.<sup>4,19,26–29</sup> Moreover, molecules are not free to move on the solid. Therefore, the arguments used on liquid substrates to explain why films thinner than  $h_C$  can be distorted seem irrelevant.

However, the question is not about the presence of developed long-wavelength instability, but it is about the ability of the film to relax the elastic energy due to the hybrid anchoring by azimuthal variations of the director. In a somewhat paradoxical way, a random substrate with many strong anchoring defects<sup>33,34</sup> might be more favorable than a homogeneous one with weaker anchoring.

Data might support such an assumption:

- On evaporated silica,<sup>4</sup> the anchoring is planar, nondegenerate. However, a microscopic droplet spreads with radial symmetry, which shows that the anchoring is weak. The measured values of  $h_{\text{lim}}$  are close to  $30\ \text{nm}$ .<sup>4</sup>
- On smooth hydrophilic silica, one may expect a large heterogeneity. Strong anchoring defects lead to visible structures on macroscopic spreading drops, and they interact with the flow to generate instability patterns.<sup>35</sup> At the microscopic scale, the measured values of  $h_{\text{lim}}$  are slightly less than  $20\ \text{nm}$ .<sup>10</sup>
- On smooth hydrophobic silica, the anchoring is weaker and nothing specific is seen on spreading drops.<sup>11</sup> At the microscopic scale, the measured values of  $h_{\text{lim}}$  at the edge of these drops are close to  $30\ \text{nm}$ .<sup>11</sup>

Quite recently, new configurations of thin nematic films have been proposed both theoretically and numerically which involve order reconstruction or what is called a steplike configuration.<sup>36,37</sup> Such configurations have not been observed yet and more controlled experiments are required to answer the question properly.

## Conclusion

Instability patterns exist in thin nematic films on liquid substrates and relax the elastic energy by twist deformations down to a film thickness about  $20\text{--}30\ \text{nm}$ . Previous studies of stripe patterns in 5CB and 6CB liquid crystals<sup>20,25</sup> are complemented by new ones using the 8CB in the nematic phase. Noticeably, the dependence of stripes wavelength on temperature is investigated. The accumulation of data and the variety of patterns presented here clearly indicate that the analysis of thin nematic films requires more than a simple perturbation theory of a distorted nematic. In addition, the generality of the results we observe on various compounds and in different situations, rules out previous explanations that require precise values or ratios of elastic and anchoring constants.

A simple projection of this analysis to the solid substrate case is tempting but still highly conjectural.

**Acknowledgment.** A study of thin films of liquid crystals on oxidized silicon wafers was initiated in the laboratory of



P.G. de Gennes at the Collège de France more than ten years ago. The ellipsometric study of microdroplets or spin-coated films has been achieved with S. Bardon, M. P. Valignat, F. Vandenbrouck, and D. Van Effenterre. C. Poulard has investigated the spontaneous spreading of larger droplets. A.M.C acknowledges Pierre Gilles de Gennes and the members of the laboratory for the warm and keen surrounding there. We gratefully thank G. Guéna who helped a lot in the rebuilding of the “Collège wetting group” at the ENS and J. Meunier for helpful discussions. The present work is partially supported by the Fédération “Dynamique des Systèmes Complexes”, headed by M. Ben Amar, and the French CNRS (ANR DYNINSTA-MOBI).

## References and Notes

- (1) Evans, R.; Marini Bettelo Marconi, U.; Tarazona, P. *J. Chem. Phys.* **1986**, *84*, 2376.
- (2) Sheng, P. *Phys. Rev. A* **1982**, *26*, 1610.
- (3) Sluckin, T. J.; Ponierwierski, A. *Phys. Rev. Lett.* **1985**, *55*, 2907.
- (4) Valignat, M. P.; Villette, S.; Li, J.; Barberi, R.; Bartolino, R.; Dubois-Violette, E.; Cazabat, A. M. *Phys. Rev. Lett.* **1996**, *77*, 1994.
- (5) Van Effenterre, D.; Ober, R.; Valignat, M. P.; Cazabat, A. M. *Phys. Rev. Lett.* **2001**, *87*, 125701.
- (6) (a) Van Effenterre, D. Ph.D. Thesis, University Pierre et Marie Curie, Paris, France, 2002. (b) Van Effenterre, D.; Valignat, M. P.; Roux, D. *Europhys. Lett.* **2003**, *64*, 526.
- (7) Williams, R. *J. Chem. Phys.* **1963**, *39*, 384.
- (8) Orsay Liquid Crystal group. *Mol. Cryst. Liq. Cryst.* **1971**, *12*, 251.
- (9) Dubois-Violette, E.; de Gennes, P. G.; Parodi, O. *J. Phys. Paris* **1971**, *32*, 305.
- (10) (a) Bardon, S.; Ober, R.; Valignat, M. P.; Cazabat, A. M.; Daillant, J. *Phys. Rev. E* **1999**, *59*–6. (b) Vandenbrouck, F.; Valignat, M. P.; Cazabat, A. M. *Phys. Rev. Lett.* **1999**, *82*, 2693808. (c) Vandenbrouck, F.; Bardon, S.; Valignat, M. P.; Cazabat, A. M. *Phys. Rev. Lett.* **1998**, *81*, 610.
- (11) Poulard, C.; Voué, M.; De Coninck, J.; Cazabat, A. M. *Colloids Surf., A* **2006**, *282*, 240.
- (12) Jérôme, B. *Rep. Prog. Phys.* **1991**, *54*, 391.
- (13) Frank, F. C. *Discuss. Faraday Soc.* **1958**, *25*, 19.
- (14) de Gennes, P. G.; Prost, J. *The Physics of Liquid Crystals*, 2nd ed.; Clarendon Press: Oxford, 1993.
- (15) Oswald, P.; Pieranski, P.; *Les cristaux liquides*: Gordon and Breach Science Publishers, 2000; Vol. 1.
- (16) Rapini, A.; Papoular, M. *J. Phys. (Paris)* **1969**, *30*, C4.
- (17) Barbero, G.; Barberi, R. *J. Phys. (Paris)* **1983**, *44*, 609.
- (18) Perez, E.; Proust, J. E.; Terminassian-Saraga, L.; Mauer, E. *Colloid Polym. Sci.* **1977**, *255*, 1003.
- (19) Zihlerl, P. R.; Podgornik, R.; Žeumer, S. *Phys. Rev. Lett.* **2000**, *84*, 1228.
- (20) Delabre, U.; Richard, C.; Guéna, G.; Meunier, J.; Cazabat, A. M. *Langmuir* **2008**, *24*, 3998.
- (21) de Mul, M. N. G.; Mann, J. A. *Langmuir* **1994**, *10*, 2311.
- (22) de Mul, M. N. G.; Mann, J. A. *Langmuir* **1998**, *14*, 2455.
- (23) Zou, L.; Wang, J.; Basnet, P.; Mann, E. K. *Phys. Rev. E* **2007**, *76*, 031602.
- (24) Läger, J.; Robertson, C. R.; Frank, C. W.; Fuller, G. G. *Langmuir* **1996**, *12*, 5630.
- (25) Delabre, U.; Richard, C.; Meunier, J.; Cazabat, A. M. *Europhys. Lett.*, submitted for publication, 2008.
- (26) Lavrentovich, O. D.; Pergamenschik, V. M. *Phys. Rev. Lett.* **1994**, *73*, 979.
- (27) Sparavigna, A.; Lavrentovich, O. D.; Strigazzi, A. *Phys. Rev. E* **1994**, *49*, 1344.
- (28) Lavrentovich, O. D.; Pergamenschik, V. M. *Int. J. Mod. Phys. B* **1995**, *9*, 2389.
- (29) Pergamenschik, V. M. *Phys. Rev. E* **1993**, *47*, 1881.
- (30) Barberi, R.; Scaramuzza, N.; Formoso, V.; Valignat, M. P.; Bartolino, R.; Cazabat, A. M. *Europhys. Lett.* **1996**, *34*, 349.
- (31) Kiselev, A. D. *Phys. Rev. E* **2004**, *69*, 041701.
- (32) Krzyzanski, D.; Derfel, G. *Phys. Rev. E* **2001**, *63*, 021702.
- (33) Wen, B.; Kim, J.-H.; Yokohama, H.; Rosenblatt, C. *Phys. Rev. E* **2002**, *66*, 041502.
- (34) Chiccoli, C.; Lavrentovich, O. D.; Pasini, P.; Zannoni, C. *Phys. Rev. Lett.* **1997**, *72*, 4401.
- (35) Poulard, C.; Cazabat, A. M. *Langmuir* **2005**, *21*, 6270.
- (36) Sarlah, A.; Zumer, S. *Phys. Rev. E* **1999**, *60*, 1821.
- (37) Chiccoli, C.; Pasini, P.; Sarlah, A.; Zannoni, C.; Zumer, S. *Phys. Rev. E* **2003**, *67*, 050703.

JP8062492

# Line tension of nematic pancakes at the air-water interface: Static and dynamic measurements

U. DELABRE<sup>1,2</sup>, C. RICHARD<sup>2</sup>, J. MEUNIER<sup>1</sup> and A.-M. CAZABAT<sup>1,2(a)</sup>

<sup>1</sup> *Laboratoire de Physique Statistique - 24 Rue Lhomond 75231 Paris Cedex 05, France, EU*

<sup>2</sup> *Université Pierre et Marie Curie - 4 place Jussieu 75252 Paris Cedex 05, France, EU*

received 13 June 2008; accepted in final form 29 July 2008

published online 9 September 2008

PACS 61.30.-v – Liquid crystals

PACS 68.18.-g – Langmuir-Blodgett films on liquids

PACS 47.57.-s – Complex fluids and colloidal systems

**Abstract** – The line tension of nematic Langmuir films on water is investigated using the 6CB member of the cyanobiphenyl liquid-crystals series. Both static and dynamic measurements are performed independently. The line tension increases linearly with film thickness up to  $0.2\ \mu\text{m}$ . The increment of line tension is significantly smaller than for the smectic 8CB compound, due to the difference in the allowed elastic deformations of smectic and nematic films. A simple model of the nematic edge accounts both for the linear dependence and the order of magnitude of the line tension. Moreover, it sheds new light on the structure of thin nematic films on liquid substrates.

Copyright © EPLA, 2008

**Introduction.** – The free energy of Langmuir films at the air-water interface includes bulk and surface terms, but also a contribution associated with the film boundary. The line tension—the two-dimensional analog of surface tension—is the corresponding free energy per unit length. Measurements and theoretical models of the line tension of monolayers on water have been developed over the last twenty years [1–4]. More recently, the line tension of smectic liquid-crystal multilayers has been studied, both theoretically [5] and experimentally [2,6–8]. Experiments at the air-water interface have been performed using 8CB (4'-8-alkyl[1,1'-biphenyl]-4-carbonitrile) at room temperature [6,7]. Increasing the amount of 8CB leads first to simple monolayer domains on water, then to multilayer domains built up by stacked bilayers on top of the monolayer [7,9–11]. While for monolayer and trilayer coexistence means full equilibrium, this is no longer the case for thicker domains. As a matter of fact, domains of different thickness usually coexist in metastable equilibrium with the same trilayer [7,9]. The 8CB molecules bear a large axial dipole moment ( $\sim 5D$  [12,13]) and are parallel in the monolayer, but antiparallel in the bilayers. Line tensions have been measured using Brewster Angle Microscopy (BAM) and analyzing the relaxation of domains previously deformed by hydrodynamic flow [2,7,14]. The line tension  $\tau_w$  of monolayer domains on water is  $1.2 \pm 0.3\ \text{pN}$  [6],

the same order of magnitude as for many monolayer systems [2,3,6]. In contrast, the trilayer-monolayer line tension  $\tau_0$  (a bilayer domain on top of a continuous monolayer) is ten times larger ( $11 \pm 2\ \text{pN}$  [6],  $15 \pm 1\ \text{pN}$  [7]). Accounting for such a large value is not straightforward. It has been assumed [6] that the specific location of the molecules in both the monolayer and the upper bilayer leads to a globally unbalanced dipolar and strong interaction. Such an assumption is supported by the measurements of the surface potential [6,7], indicating that the bilayer in the trilayer structure is significantly distorted. This is also the case for the first bilayer in thicker structures, while the next upper bilayers become rapidly symmetric [7,9].

The line tension between thicker smectic domains and trilayer is found to depend linearly on the domain thickness  $h$  in the range investigated ( $h \leq 60\ \text{nm}$ ) [7]. The increment is  $3.3\ \text{mN/m}$ , or  $11\ \text{pN}$  per added bilayer, which is very similar to the value of  $\tau_0$ . This is too large to be due to the short-range quadrupolar interaction in the symmetric bilayers. According to Oswald's model [5] it is assumed that an edge dislocation—a typical defect of the smectic structure—is present at the boundary of the smectic domain [7]. This corresponds to the folding of smectic layers around a disclination line located at the periphery of the domain [7,15,16]. The associated elastic energy accounts for the high measured line tension.

We are not aware of any line tension measurement of nematic films. Manipulating 8CB domains on water is a

<sup>(a)</sup>E-mail: anne-marie.cazabat@upmc.fr

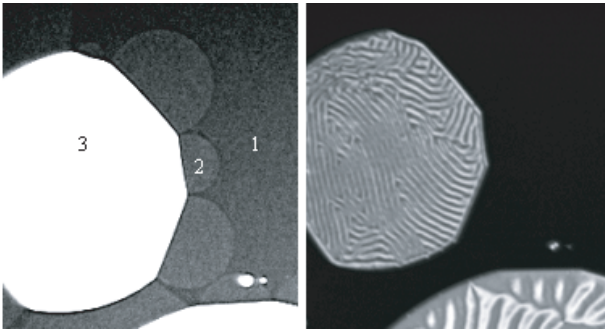


Fig. 1: A nematic domain (3) coexists with trilayer domain (2) which is in equilibrium with the surrounding monolayer (1). The surface pressure of the trilayer can be written in two ways:  $\Pi_2 = \Pi_3 + \tau(h)/R_{23} = \Pi_1 + \tau_0/R_{12}$ . The procedure is repeated for all the trilayer domains contacting (3) and in equilibrium with (1). The picture on the left is over-exposed and the intensity on the nematic domains appears saturated. The wavelength in the domain (3) is about  $5 \mu\text{m}$ . Size of the images:  $210 \mu\text{m} \times 230 \mu\text{m}$ .

difficult task at room temperature [7] and would become a challenge with the added constraint of a temperature control (8CB is nematic between  $33.5$  and  $40.5^\circ\text{C}$ ). The widely used 5CB is nematic at ambient temperature but it does not wet water. The convenient member of the cyanobiphenyl series is the 6CB which has a nematic phase between  $14.5$  and  $29^\circ\text{C}$  and can be spread on water. The same succession and coexistence of monolayer, trilayer and then domains of various thicknesses, is observed by increasing the deposited amount [17]. However, nematic domains show long wavelength stripe patterns which are specific responses of the nematic elasticity to the hybrid anchoring conditions at the two fluid interfaces [17–20]. Such patterns do not exist in smectic films, where the corresponding twist deformation is forbidden [15,16].

**Materials and methods.** – Solutions of 6CB (Sigma-Aldrich, purity 98%, used as received) in hexane are deposited on pure water ( $18.2 \text{M}\Omega \cdot \text{cm}$ ) at room temperature ( $22 \pm 1^\circ\text{C}$ ). The films are observed under microscope (Polyvar MET-Reichert-Jung) and the images recorded. After complete evaporation of the solvent, some local rearrangements including domain coalescence take place during about 20 mn. Then the films evolve much more slowly over days. While the structures of monolayer and trilayer seem very similar in the nematic and smectic case, respectively, this is no longer the case for thicker films: the next film after the trilayer ( $h = 3.5 \text{nm}$ ) is significantly thicker in the nematic case ( $h = 30 \text{nm}$ ) and shows the stripe patterns characteristic of nematic elasticity. Stripes are observed for thickness  $30 \text{nm} \leq h \leq 0.6 \mu\text{m}$ , and provide also an easy way to measure  $h$  if the curve  $\lambda(h)$  has been previously drawn [17,18]. The wavelength  $\lambda$  is much larger than the thickness  $h$ . For 6CB on water, it is close to  $250h$  for  $h \leq 0.35 \mu\text{m}$  (see fig. 5a) and increases steeper at larger thickness [17]. Two independent procedures have

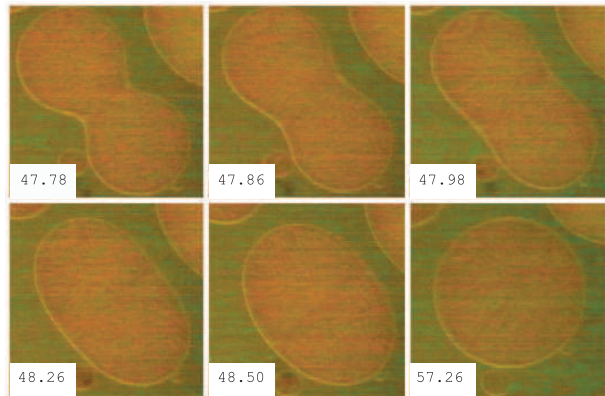


Fig. 2: (Colour on-line) Dynamic of relaxation just after coalescence of two pancakes with same thickness (*i.e.* same colour). The numbers at the bottom left of the pictures indicate time in seconds. Focussing is done on the edge of the domains, and the contrast of the stripes is poor. Size of the images:  $715 \mu\text{m} \times 700 \mu\text{m}$ .

been used for line tension measurements, taking advantage of the preserved specific structures due to the metastability of the thicker domains —like in the smectic case [7]— induced during deposition and solvent evaporation.

- 1) Static measurements are run several hours after the deposition. At very low concentration, relatively thick domains ( $h \leq 0.35 \mu\text{m}$ ) can be found, coexisting in metastable equilibrium with trilayer domains, which themselves coexist with a continuous monolayer (fig. 1). In that case, the wide dynamics of the camera (CoolSnap-Photometrics) allows us to visualize not only the nematic domain, but also the boundary between the trilayer and the monolayer (fig. 1).
- 2) Moreover, during the initial transient, at a somewhat larger concentration, a rare but interesting situation occurs when coalescence takes place between two nematic domains surrounded by a continuous trilayer with both the same thickness and a similar size (fig. 2). These dynamic processes are recorded and analyzed afterwards.

#### Line tension measurements. –

*Static measurements of domain shapes* (fig. 1). The two-dimensional film pressures  $\Pi_i$  on both sides of the boundary between coexisting films are linked by the analogous Laplace law at 2 dimensions, even in metastable equilibrium (which is a local minimum of the free energy). Figure 1 illustrates the procedure which is used to link the line tension  $\tau(h)$  between a domain of thickness  $h$  and the trilayer to the line tension  $\tau_0$  between the trilayer and the continuous monolayer.  $R_{ij}$  is the curvature radius of the 2-dimensional boundary between  $i$  and  $j$ :

$$\Pi_2 = \Pi_3 + \frac{\tau(h)}{R_{32}} = \Pi_1 + \frac{\tau_0}{R_{12}}. \quad (1)$$

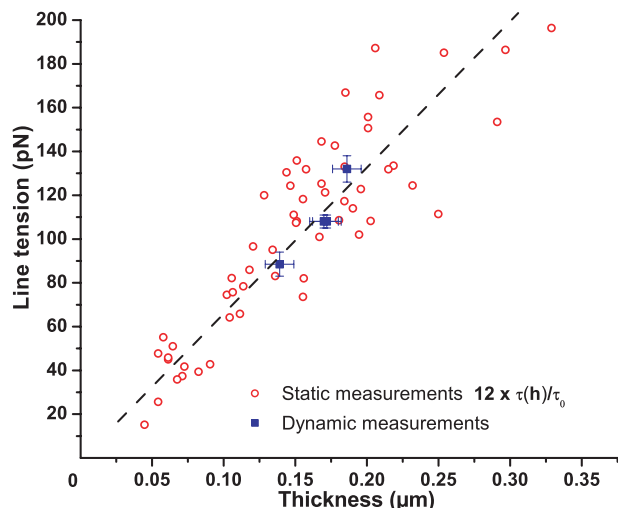


Fig. 3: (Colour on-line) Line tension of nematic pancake *vs.* thickness. Full squares: dynamic measurements. Circles: static measurements reported as  $12 \times \tau(h)/\tau_0$ .

Repeated and systematic measurements show that the ratio  $\tau(h)/\tau_0$ : i) is the same everywhere on the boundary of a given domain and ii) depends only on the thickness for different domains. This validates the procedure and allows us to define unambiguously a line tension. In addition, boundaries between phases in fig. 1 show a very regular shape with a constant radius of curvature, indicating that long-range electrostatic effects can be neglected in line tension measurements [2,4]. The results are reported in fig. 3 (open circles). The trend is a linear variation of  $\tau(h)$  with  $h$ , at least up to  $0.20 \mu\text{m}$ . For larger thickness, line tension and curvature radii are large, and the procedure becomes inaccurate.

*Dynamic measurement of the relaxation dynamics* (fig. 2). Absolute values of the line tension can be deduced from the coalescence dynamics of two domains with equal thickness and similar size, surrounded by the trilayer. Here, we follow the analysis used in BAM studies [2,6,7]. If the bulk dissipation is dominant, then at the end of the coalescence process, the relaxation dynamics towards a circular shape of radius  $R_0$  becomes exponential with a characteristic time  $\Theta$  [2,7,14]:

$$\Theta \approx \frac{5\pi}{16} \frac{\eta_{B,water} R_0^2}{\tau(h)}, \quad (2)$$

where  $\eta_{B,water}$  is the viscosity of water. A typical semi-logarithmic plot of the domain anisotropy *vs.* time is given in fig. 4. Three thicknesses have been investigated. The results are  $\tau(h) = 88.5 \text{ pN}$  for  $h = 0.14 \mu\text{m}$ ,  $\tau(h) = 108 \text{ pN}$  for  $h = 0.17 \mu\text{m}$ , and  $\tau = 132 \text{ pN}$  for  $h = 0.18\text{--}0.19 \mu\text{m}$  (fig. 3, full squares). They agree with a linear variation of  $\tau(h)$  and coincide with the static results for  $\tau_0 = 12 \pm 1.5 \text{ pN}$ , a value very close to the one found for the smectic 8CB.

Note that the bulk dissipation dominates provided  $R_0 \geq \eta_{B,6CB} \cdot h / \eta_{B,water}$  [7]. Indeed a rough estimate of the

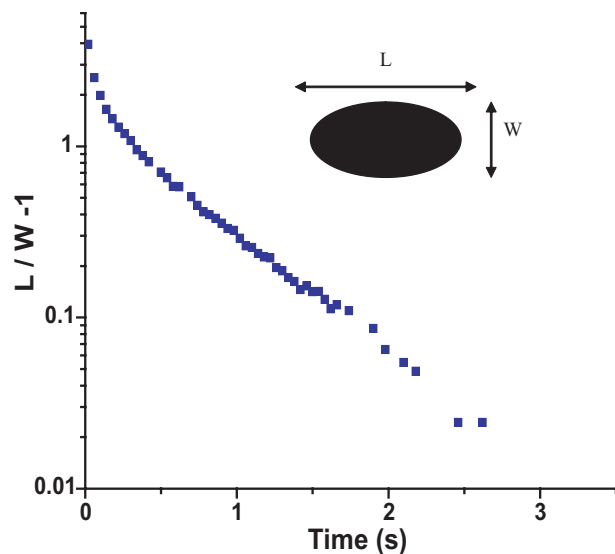


Fig. 4: (Colour on-line) Typical graph of the relaxation dynamics (semi-log plot). At short time (a few milliseconds) the coalescence between two individual domains is observed. At longer time, the relaxation of the resulting domain towards a circular shape is exponential. The anisotropy  $L/W - 1$  has been shown to be the relevant parameter [2,7].

surface viscosity  $\eta_s$  is given by  $\eta_s \sim \eta_{B,6CB} \cdot h$ , where  $\eta_{B,6CB}$  is the bulk viscosity of the nematic 6CB [7,21]. The largest value of  $h$  is  $0.35 \mu\text{m}$ . With  $\eta_{B,6CB} = 30 \text{ mPa} \cdot \text{s}$ , the condition becomes  $R_0 \geq 10 \mu\text{m}$ , which is always largely fulfilled. This supports the use of eq. (2) in the calculation of  $\tau(h)$ .

**Comments and discussion.** – Considering the line tension between monolayer and trilayer, it is quite satisfactory to find that the values are close for the smectic 8CB and the nematic 6CB. Actually, the two compounds are similar, and the nature of the order in the bulk is not expected to play at that scale. The combination of static and dynamic procedures in the present measurement supports the assumption by Lauger [6] that the structure of the trilayer is very specific. In contrast, the line tension between a nematic domain and the trilayer is, for a given thickness, significantly smaller than the one between a smectic domain and the trilayer. Typically, the slope  $\tau(h)/h$  is  $0.7 \text{ mN/m}$  for the nematic domain, instead of  $3.3 \text{ mN/m}$  for the smectic one [7]. Our assumption is that the difference between the elastic response of smectic and nematic phases, respectively, accounts for the change in the line tension values for the corresponding films.

How the edge of a nematic domain looks like is not obvious. In fact, the mere structure of the nematic domains on water is still controversial [17]. Hybrid anchoring conditions occur at the interfaces: planar on the substrate, homeotropic on air (normal to the interface). The structure of thick nematic films in that case is well known. Let  $x, y$  be the plane of interface, then the director is along  $z$  at the free interface. Let us assume that the director is along



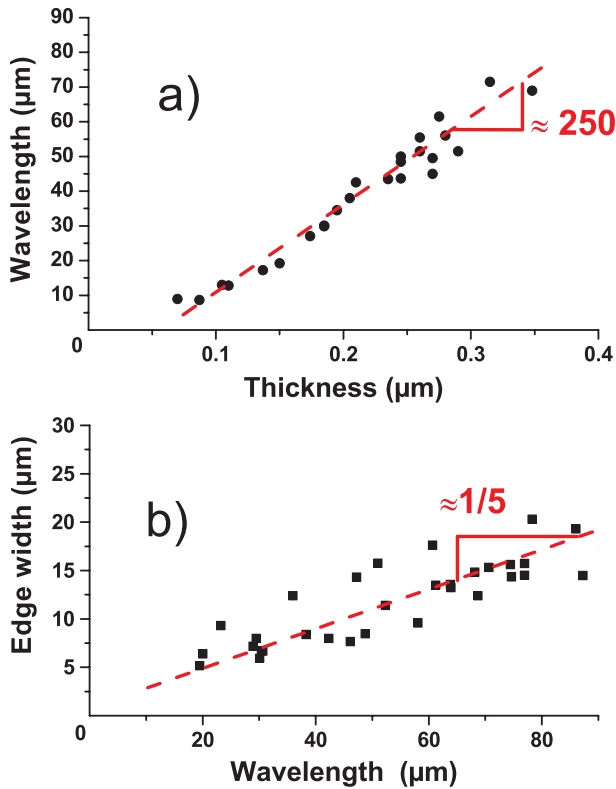


Fig. 5: (Colour on-line) a) Wavelength *vs.* thickness. Wavelength of stripes increases almost linearly with thickness up to  $0.3 \mu\text{m}$  with a factor of  $\sim 250$ . b) Edge width *vs.* wavelength. The edge width is about  $\lambda/5$  for this thickness range:  $0.1 \mu\text{m} \leq h \leq 0.35 \mu\text{m}$ . The edge is not sharp and is about  $50h$ .

$x$  at the substrate. It rotates from bottom to top of the film inside the  $(x, z)$ -plane, the structure being invariant by any translation parallel to the  $(x, y)$ -plane. This configuration is referred to as a “distorted nematic”. However, on a liquid substrate like water, the planar anchoring is stronger than the homeotropic one and is degenerate so the molecules are free to move. Stripe patterns are one characteristic response of a “distorted nematic” in that case: the director oscillates out of the  $(x, z)$ -plane. The corresponding twist term is usually treated as a first-order perturbation of the “distorted nematic” configuration [18–20,22]. The “distorted nematic” configuration is not allowed for very thin films [23], the cost in elastic energy becoming larger than the anchoring energy below a threshold thickness  $h_c$  which is about a micron or less typically. The orientation of the director for  $h \leq h_c$  is normally imposed by the stronger anchoring. In contrast, experiments provide evidence of striped films in the thickness range  $30 \text{ nm} \leq h \leq 0.6 \mu\text{m}$ . The stripe phase has been observed before in distorted or homogenous (fully homeotropic or planar) thick samples in the presence of an electric or a magnetic field [24,25]. Even if formally the thickness can play the role of the external field, the situation of thin films is specific because surface-like terms must be included in the theory. This is an old problem which has not been clearly answered yet [17–20,22].

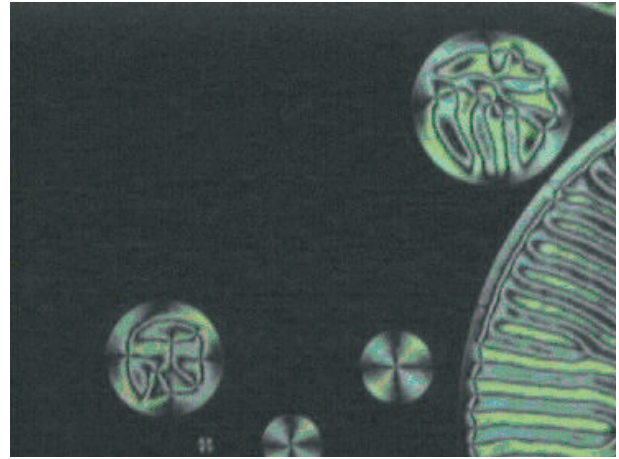


Fig. 6: (Colour on-line) Nematic domains between crossed polarizers. The surrounding trilayer appears black. The three largest domains are striped, even if the pattern becomes irregular in the two smaller ones. Three smaller domains are also present, where only the black cross characteristic of a radial nematic order with a defect in the center is visible. At the edge of the striped domains, the black cross is again present. All the domains have approximately the same thickness (*i.e.* the same colour).

Further investigations provide a plausible answer to the problem, and also a model for the line tension. First, stripes exist only if the radius of the domain is larger than the stripe wavelength. Smaller domains show the characteristic nematic defects, (see fig. 6). Second, the edge of the striped domains is not sharp. A systematic study shows that the apparent width of the edge in the range  $0.1 \mu\text{m} \leq h \leq 0.35 \mu\text{m}$  is approximately  $\lambda/5$  (see fig. 5(b)). A counter-intuitive result is that the nematic edge has a weak slope ( $\sim 1/50$ ).

A plausible answer to the presence of stripes in films much thinner than the micrometer is that these stripes are not merely small perturbations of a “distorted nematic” configuration taken as the base state in the model [18–20,22]. The corresponding twist relaxes the elastic energy in an efficient way. Therefore, when stripes are present, the threshold thickness calculated assuming a “distorted nematic” configuration [23] is no longer relevant. An immediate consequence is that inside the edge, which is too narrow to accommodate stripes and relax elastic energy, the “distorted nematic” configuration is not allowed. As the planar anchoring is stronger, the film must be planar everywhere in the edge (with a radial orientation of the director as the local slope removes the planar degeneracy [19,22]). The possibility of an anchoring transition close to the edge of a striped domain (5CB on glycerol) was already mentioned by Sparavigna *et al.* [19]. Figure 6, where the domains are observed between crossed polarizers, supports the present model, showing crossed extinctions in the domain edge, with a good optical contrast. In the edge, which has a small slope ( $1/50$ ), the director is approximately orthogonal to the preferred

(homeotropic) orientation at the upper interface. The energy cost is due to the anchoring energy at the free interface, which is the dominant contribution (the van der Waals contribution is negligible for  $h \geq 40$  nm [17]). The corresponding area per unit length is approximately the width of the edge. The anchoring energy per unit area is typically  $10^{-5}$  J/m<sup>2</sup> [18,19,26], the width is  $50h$ , therefore the line tension becomes  $\tau(h) \approx 5 \cdot 10^{-4}h$  (N), very close to the experimental value  $7 \cdot 10^{-4}h$  (N).

**Conclusion.** – The line tension of 6CB nematic domains on water substrates has been measured by a combination of static and dynamic measurements. The results coincide if, as far as monolayer and trilayer are concerned, the 6CB behaves like the 8CB, the next even member of the cyanobiphenyl series, which is highly probable. The measured values of the line tension for thicker films are significantly less in nematics than in smectics. A simple model accounts quantitatively for the measured values, and removes the inconsistencies of the present descriptions of nematic films on liquid substrates [17–19]. The stripe patterns observed on water or glycerol and due to twist deformations relax efficiently the elastic distortion energy. As they cannot be treated as first-order perturbations of the “distorted nematic” structure, the corresponding thickness threshold [23] is irrelevant for striped films. In contrast, the anchoring transition takes place at the edge of the films, which is too narrow to accommodate stripes. The next step is to check the present model on glycerol substrates, where the stripe patterns are similar to the ones on water, but where the trilayer structure is still unknown.

\*\*\*

We gratefully acknowledge financial support from the Fédération “Dynamique des Systèmes Complexes”, headed by Professor M. BEN AMAR, and from the Centre National de la Recherche Scientifique, ANR DYNINSTA-MOBI. We thank Professor L. LÉGER for enlightening discussions on liquid-crystal elasticity.

## REFERENCES

- [1] ANDELMAN D., BROCHARD F. and JOANNY J.-F., *J. Chem. Phys.*, **86** (1987) 3673.
- [2] MANN E. K., HENON S., LANGEVIN D., MEUNIER J. and LEGER L., *Phys. Rev. E*, **51** (1995) 5708.
- [3] BENVENU D. J. and MCCONNELL H. M., *J. Phys. Chem.*, **96** (1992) 6820; **97** (1992) 6686.
- [4] RIVIERE S., HENON S. and MEUNIER J., *Phys. Rev. Lett.*, **95** (1995) 2506.
- [5] HOLYST R. and OSWALD P., *Int. J. Mod. Phys. B*, **9** (1995) 1515.
- [6] LAUGER J., ROBERTSON C. R., FRANK C. W. and FULLER G. G., *Langmuir*, **12** (1996) 5630.
- [7] ZOU L., WANG J., BASNET P. and MANN E. K., *Phys. Rev. E*, **76** (2007) 031602.
- [8] GEMINARD J. C., LAROCHE C. and OSWALD P., *Phys. Rev. E*, **58** (1998) 5923.
- [9] DE MUL M. N. G. and MANN J. A. jr., *Langmuir*, **10** (1994) 2311.
- [10] XUE J., JUNG C. S. and KIM M. W., *Phys. Rev. Lett.*, **69** (1992) 474.
- [11] FRIEDENBERG M. C., FULLER G. G., FRANK C. W. and ROBERTSON C. R., *Langmuir*, **10** (1994) 1251.
- [12] LACAZE E., ALBA M., GOLDMANN M., MICHEL J.-P. and RIEUTORD F., *Eur. Phys. J. B*, **39** (2004) 261.
- [13] DRUON C. and WACRENIER J. M., *J. Phys. (Paris)*, **38** (1977) 47.
- [14] STONE H. A. and MCCONNELL H. M., *Proc. R. Soc. London, Ser. A*, **448** (1995) 97.
- [15] DE GENNES P.-G. and PROST J., *The Physics of Liquid Crystals* (Clarendon Press, Oxford) 1993.
- [16] OSWALD P. and PIERANSKI P., *Les cristaux liquides* (Gordon and Breach Science Publishers) 2000.
- [17] DELABRE U., RICHARD C., GUENA G., MEUNIER J. and CAZABAT A.-M., *Langmuir*, **24** (2008) 3998.
- [18] LAVRETOVICH O. D. and PERGAMENSHCHIK V. M., *Phys. Rev. Lett.*, **73** (1994) 979.
- [19] SPARAVIGNA A., LAVRETOVICH O. D. and STRIGAZZI A., *Phys. Rev. E*, **49** (1994) 1344.
- [20] PERGAMENSHCHIK V. M., *Phys. Rev. E*, **47** (1993) 1881.
- [21] WINTERSMITH J. R., ZOU L., BERNOFF A. J., ALEXANDER J. C., MANN J. A., KOIJMAN E. E. and MANN E. K., *Phys. Rev. E*, **75** (2007) 061605.
- [22] LAVRETOVICH O. D. and PERGAMENSHCHIK V. M., *Int. J. Mod. Phys. B*, **9** (1995) 2389.
- [23] BARBERO G. and BARBERI R., *J. Phys. (Paris)*, **44** (1983) 609.
- [24] LONGBERG F. and MEYER R. B., *Phys. Rev. Lett.*, **55** (1985) 718.
- [25] ALLENDER D. W., HORNEICH R. M. and JOHNSON D. L., *Phys. Rev. Lett.*, **59** (1987) 2654.
- [26] PEREZ E., PROUST J. E., TERMINASSIAN-SARAGA L. and MAUER E., *Colloid Polym. Sci.*, **255** (1977) 1003.



## Appendix E

# AFM and STM imaging of ionic liquids

The resolution limit of an optical microscope depends on the light wavelength and of the magnification. For the shortest wavelength and the biggest magnification, optical microscopes can hardly resolve points distant from more than  $0.2 \mu\text{m}$  and diffraction rings (Airy discs) appear on the image which is obtained. To scan smaller scales other microscopy techniques are used. Two of them, of the Scanning Probe Microscopy (SPM) “family” are presented in this appendix: Atomic Force Microscopy (AFM) and Scanning Tunneling Microscopy (STM). Unlike the optical microscope, they do not rely on the use of light to image the samples and therefore overcome the resolution limits of traditional (optical) microscopes.

### E.1 Atomic Force Microscopy (AFM)

The experiments were performed with Nanoscope IIIa fitted with a Multimode III module (Bruker, former Veeco) and later with a Multimode VIII module (Bruker). The figure E.1 shows the Multimode module.

In the AFM imaging technique<sup>1</sup>, a tip placed at the end of a flexible cantilever comes close to the scanned surface. The characteristics of the sample (e.g. topography and mechanical properties) are determined via the tip -sample interactions. Several AFM modes have been developed in order to cover the wide range of experimental systems. For each mode, the strength of the sample-tip interaction is different. These modes are:

- Contact mode, where the cantilever directly and continuously touches the surface of the sample. This mode has an atomic resolution. However, it is used only to image hard solids

---

<sup>1</sup>AFM can also be used to measure forces. The tip - sample interaction is then measured as a function of their relative distance. One then obtains force curves. The analysis of force curves allows to deduce the exact nature of the interaction between the tip and the sample.



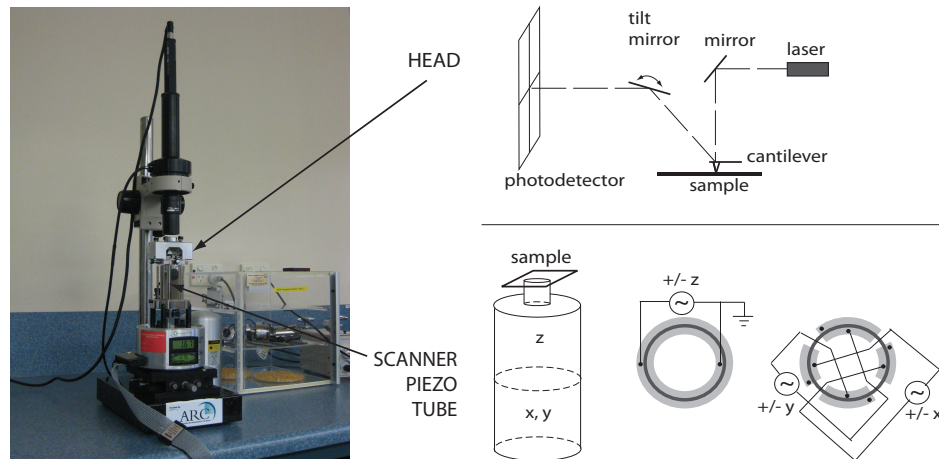


Figure E.1: On the left, picture of the Multimode III module is shown. On the right, the way the head and the scanner work is described for both Multimode III and VIII. In the head, the laser beam detects the changes in the deflection of the cantilever. The scanner piezo tube is responsible for the motion in  $x$ ,  $y$  and  $z$  of the sample.

as the risk of damaging the sample with the tip is very high;

- Tapping mode, where the tip touches alternately the surface with a well defined frequency. Using a feedback loop, the tip-sample interaction is maintained at a constant level via the variation of the amplitude of the cantilever's oscillation. This mode has a nanometer resolution. It is well-adaptated to solid and soft surfaces both in air and in liquid environment;
- Non-Contact mode, a variant of the tapping mode where the tip never touches the sample's surface. To image liquids without deforming them, the non-contact mode is the only one that can be used.

### E.1.1 Non-contact and intermittent-contact AFM

In non-contact mode, the cantilever oscillates at a given frequency [5]. To ensure a maximum sensitivity, this frequency is close to the mechanical resonance (usually 5 – 10% below). The tip experiences surface forces when close to the surface of the sample. These forces are kept constant by a feedback loop which acts on the amplitude of the oscillation of the cantilever. The non-contact mode is a particular case of the tapping mode. The difference between these two modes relies in the choice of the parameters of the AFM.

In the non-contact mode, the tip never touches the surface of the sample. This can be achieved if the tip experiences only long-range forces (Van der Waals interaction in air). If the tip happens to touch periodically the surface of the sample, the imaging is said to be intermittent-contact (IC) mode [10]. The tip experiences then repulsive and adhesion forces. When imaging a

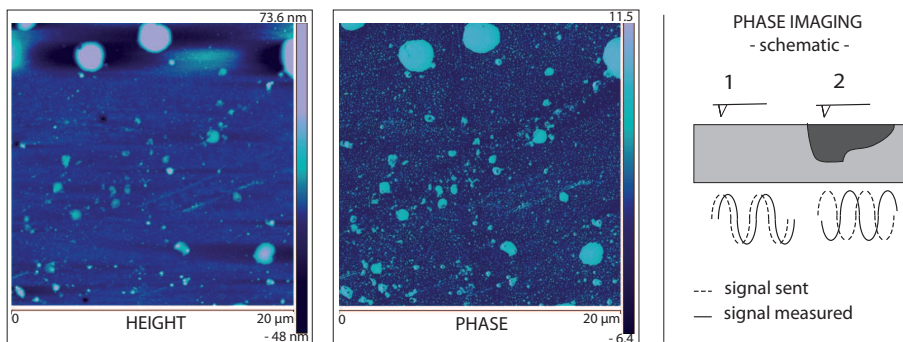


Figure E.2: On the left, example of height and phase image for [BMIM][TFSI] on SiOTSC. The images are not flattened. On the right, the principle of phase imaging is described: the phase image is constructed from the phase lag between the signal sent to the cantilever and its actual oscillation. This phase lag is different for different kind of material.

sample, it is possible to switch between these two modes. Changing from a non-contact mode to an intermittent contact mode can be a problem when liquids are imaged. The contact between the tip and the liquid creates a meniscus. This deforms more or less the sample's image and contaminates the tip<sup>2</sup>. Non-contact mode is then the most appropriate AFM mode to image liquids<sup>3</sup>.

### E.1.2 Height and phase images

The height image gives the topography of the sample. It is directly obtained through the measurement of the tip-cantilever oscillation. Height image is sensitive to the geometry of the tip. It can also show noise due to the scanning process. Noise can be due for example to a tilt angle between the surface and the tip. The AFM image then appears as tilted. To summarize, an height image can typically show artifacts which are a tilt, a bow or random darker lines (low frequency noise). These artifacts can be removed using the flattening function of the analysis software (Nanoscope Analysis in our case). However, flattening can also modify the shape of the features that are present on the image. In particular contact angle measurements should then be performed on unflattened height images.

The phase image scans the difference in composition of the different zones of the sample by detecting variations in adhesion, friction, viscoelasticity and other mechanical properties. This detection is done via the phase lag of the cantilever's oscillation relative to the signal sent to the cantilever by the piezo driver (see figure E.2). Unlike the height image, the phase image is then free from deformations due to the tip geometry.

<sup>2</sup>Tip contamination is easily seen on phase image. The meaning of the phase image is detailed in the following paragraph.

<sup>3</sup>Two examples of non-contact mode imaging applied to liquids can be found in references [3] for the case of water and [2] for the case of alkanes.

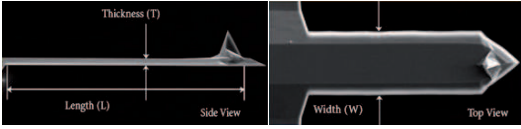

	<i>NSG10</i>	<i>NSG01</i>	<i>FESP</i>
Picture			
Material	Single crystal silicon, N type, 0.01 – 0.025 Ohm-cm, antimony doped	Single crystal silicon, N type, 0.01 – 0.025 Ohm-cm, antimony doped	0.01 – 0.025 Ohm-cm Antimony (n) doped Si
Reflective side	Au	Au	
Tip curvature radius	typical 6 nm, guaranteed 10 nm	typical 6 nm, guaranteed 10 nm	nominal 8 nm, maximal 12 nm
Cantilever length ( $\mu\text{m}$ )	$95 \pm 5$	$125 \pm 5$	$225 \pm 25$
Cantilever width ( $\mu\text{m}$ )	$30 \pm 3$	$30 \pm 3$	23, range $28 \pm 5$
Cantilever thickness ( $\mu\text{m}$ )	$2.0 \pm 0.5$	$2.0 \pm 0.5$	2.75, range 2.0 – 3.5
Resonant frequency (kHz) (min / typical / max)	140 / 240 / 390	87 / 150 / 230	50 / 75 / 100
Spring constant (N/m) (min / typical / max)	3.1 / 11.8 / 37.6	1.45 / 5.1 / 15.1	1 / 2.8 / 5

Figure E.3: Characteristics of the cantilevers of the *NSG10*, *NSG01* and *FESP* series (cf [7], [6])

### E.1.3 Imaging ionic liquid droplets

#### E.1.3.1 Cantilevers characteristics

Two different type of NT-MDT non-contact cantilevers were used with the Multimode III module: *NSG10* and *NSG01* series. With the Multimode VIII module, soft-tapping cantilevers were used: Bruker, *FESP* cantilevers. The figure E.3 summarizes their respective properties. The *NSG10* cantilevers were the most used with Multimode III. Their lateral resolution is better than for the cantilevers of the *NSG01* series. However, their vertical resolution is worse. The limited vertical resolution can lead to difficulties while imaging higher droplets. For example, it was not possible to image properly droplets higher than 50 – 60 nm. The combination Multimode VIII and *FESP* cantilever was able to overcome this problem: much higher droplets (more than 1  $\mu\text{m}$ ) could be imaged. The lateral resolution was also improved.

#### E.1.3.2 Setting AFM parameters

An AFM experiment on Multimode III or Multimode VIII begins with the set-up assembling, i.e. placing the scanner, head, sample and cantilever holder ; approaching the cantilever to the surface of the sample ; focusing the laser beam on the cantilever. Once these “mechanical steps”

are done, the AFM parameters need to be set. Setting properly the AFM parameters is what will determine the quality of the image. Sensitive steps are detailed:

- First, the cantilever must be tuned. Tuning the cantilever consists in finding its precise resonant frequency. The range of frequencies browsed by the AFM must be set according to the characteristic range of frequencies provided by the supplier for each type of cantilevers. The expected result of the tuning is a resonant frequency close to the typical resonant frequency given by the supplier. For example the expected result for a cantilever of the *NSG10* series is around  $240\text{ kHz}$ . Any value belonging to the range  $140 - 390\text{ kHz}$  is considered to be acceptable (see figure E.3). Cantilevers with damaged tips or misaligned lasers give usually no result or a wrong result for the tuning step.
- When imaging liquids, it is possible that the system is still spreading when the imaging process begins. The scan rate must then be fixed to its fastest possible value, however the value cannot be too fast to avoid tip contamination and damage. For our setup, the scan rate was chosen to be  $0.5\text{ Hz}$ .
- The amplitude set point is the parameter which constrains the amplitude of the oscillation of the cantilever. Therefore, it controls the maximal possible distance between the cantilever and the surface of the sample. When imaging a droplet, two contrary necessities impose the choice of the amplitude set point: First, the tip needs to be close enough of the surface of the sample in order to sense its presence. Second, the tip should not be too close to the surface of the sample in order to avoid any contact. The choice of the amplitude set point has then to be done in a narrow window. The typical value, depending on the cantilever-liquid systems imaged was in between  $0.5$  and  $2\text{ V}$ .
- To avoid noise in the image, the integral and proportional gains must be set as low as possible respecting the relation: proportional gain 20% higher than integral gain for Multimode III in tapping mode and for Multimode VIII in soft tapping mode.
- Finally, the number of lines of the image is chosen. The greater is the number of lines, the better is the resolution of the image. Increasing the number of lines decreases the velocity of the tip (that should be not too high to avoid tip damage) and, for the constant scan rate, increases the time needed to take a full AFM image. For example, taking a picture containing  $512 \times 512$  lines is then longer than taking a picture containing  $256 \times 256$  lines. The maximal resolutions used were  $512 \times 512$  with Mutimode III and  $1024 \times 1024$  for Multimode VIII.

### E.1.3.3 An optimal contact angle range

In order to get images of droplets of reliable contact angles, the droplets need to be small (to ensure high Laplace pressure and negligible deformations). They also need to be quite flat in order to minimize deformations of the image due to tip geometry: the more sharp is the feature

to be imaged, the more important will be the distortion due to the tip (cf figure E.4). This geometrical constraint obviously excludes the possibility of imaging droplets which contact angle is more than  $90^\circ$ .

In fact, a contact angle close to  $90^\circ$  is already too much to obtain a proper image. Let us take as an example butyl - methyl - imidazolium bis (trifluoromethylsulfonyl) - imide ([BMIM][TFSI]) on Teflon®AF1600 surface. In that case, the macroscopic contact angles are:

$$80 \pm 2^\circ \quad \textit{advancing} \quad (\text{E.1})$$

$$75 \pm 2^\circ \quad \textit{receding} \quad (\text{E.2})$$

Tapping mode AFM imaging of such droplets was impossible. To understand why, the system was observed with optical microscope upon AFM imaging<sup>4</sup>. This approach allowed us to focus on droplets bigger than others, i.e. visible under the optical microscope. After the tip engagement with the surface, the scanning of the Teflon®AF1600 begun with no problems. However, when the tip reached the droplet, the AFM image showed almost no difference in a height image. The image was looking like the one of the bare substrate, with streaks of ionic liquid. These streaks seemed to be left by the tip which was proved by the phase change in the phase image. Observing the phenomenon under optical microscope, it was possible to see that the droplet was dragged by the AFM tip. After some time, the tip released the droplet. The final droplet's location on the substrate was clearly different than its original one. The mechanism is detailed on figure E.5. This leads to a question: Is the tip - droplet interaction so strong that the droplet gets attached to the tip or is the affinity between the ionic liquid and the substrate not strong enough to prevent the droplet dislocation during the AFM imaging ? The first possibility can be excluded as it was possible to image the same ionic liquid on different substrates, i.e. HOPG, SiOTSC<sup>5</sup> and mica. The surface energy of these three substrates is significantly higher than the surface energy of Teflon®AF1600, thus their affinity for [BMIM][TFSI] is bigger. This results in liquid spreading and lower contact angles (less than  $60^\circ$ ).

<sup>4</sup>In this experiment, droplets were created using two different techniques: the emulsion of ethanol and the syringe paintbrush.

<sup>5</sup>For further details on SiOTSC substrates, see chapter 3.

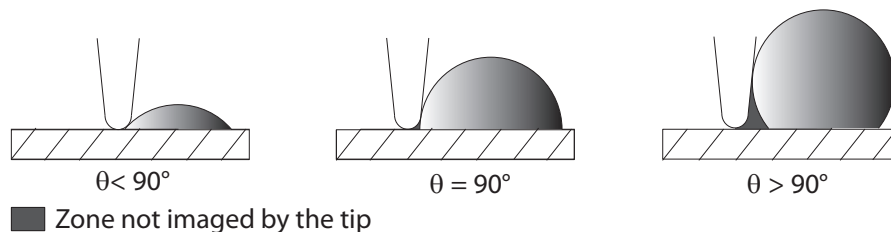


Figure E.4: Influence of the geometry of the tip in the process of imaging droplets. The same problem occurs in the case of the edge of ultra-thin films.

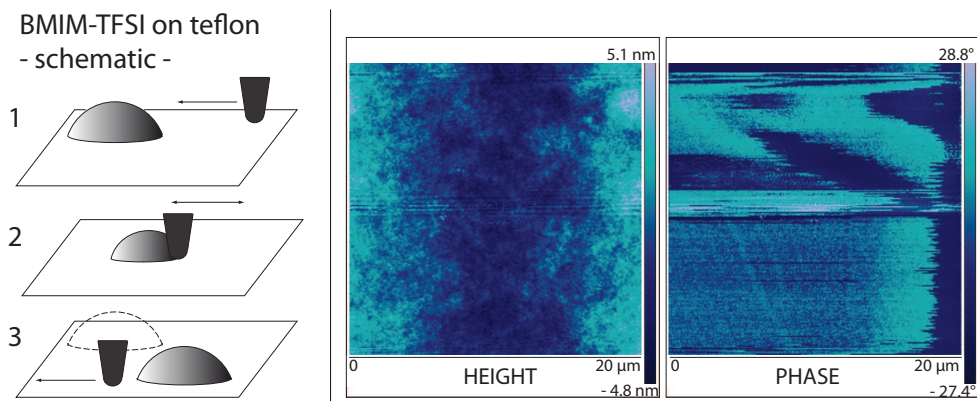


Figure E.5: AFM imaging of [BMIM][TFSI] (butyl - methyl - imidazolium bis (trifluoromethyl-sulfonyl) - imide) on Teflon®AF1600. On the left side: schematic view of the tip coming towards the droplet, dragging it for some time and finally releasing it. On the right side: AFM image corresponding to such a situation. The height image does not show any special feature, whereas the phase image clearly corresponds to a contaminated tip. This phenomenon can be seen by the streaks of different phase on the phase image.

The exact limit in macroscopic contact angle for our system was not measured, however, good and reproducible results were obtained for macroscopic contact angles below  $60^\circ$ .

## E.1.4 Sensitivity and limits of the technique

### E.1.4.1 Piezo scanner

The oscillations of the cantilever are controlled by piezoelectric crystal (see figure E.1). The piezoelectric allows to control the cantilever in x, y, and z direction independently. Despite this extremely precise arrangement, the sensitivity of the piezo presents some drawbacks. Piezo electric material is sensitive not only to electric current variations, but also to temperature and humidity changes. For example, a variation of one or two degrees of the temperature in the AFM room can create problems when imaging thick features<sup>6</sup> [8] (see figure E.6). Thus, the temperature needs to be carefully controlled.

Open-loop scanners present also another feature: the piezo drift. The piezo drift's effect is a translation in x and y of the zone scanned by the AFM. This phenomenon implies that after a first AFM image has been taken, the following one will not be centered on the exact same zone (see figure E.7). The drift must then be compensated. For our AFM, the compensation is done by the user by changing manually the x and y coordinates in the Nanoscope software ; it

<sup>6</sup>It is worth noting that with Multimode 8 it is possible to image extremely high droplets,  $> 200$  nm in height. In that case it is possible to obtain a slight wobble on the top part of the profile of the droplet. This wobble is however way less important than the one obtained when the temperature is too high, if the parameters of the AFM are properly set by the user.

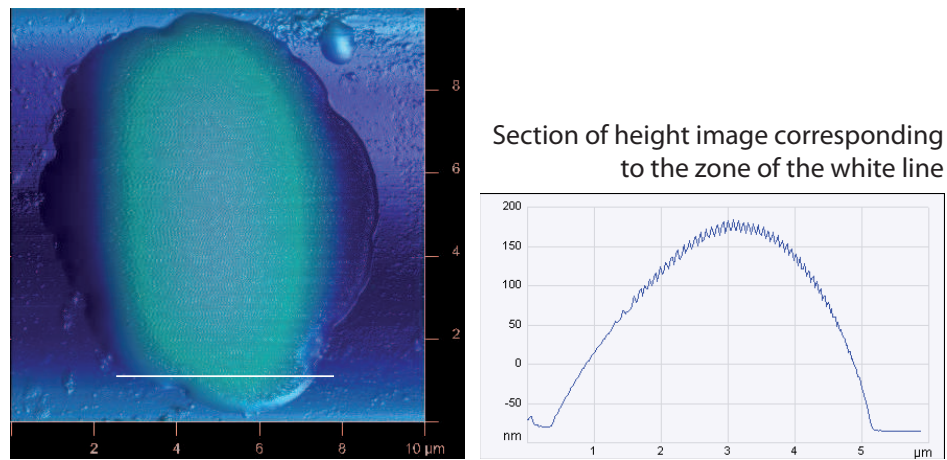


Figure E.6: On the left, 3D mixed height and phase image of [BMIM][TFSI] on SiOTSC. On the right, the section of the height image corresponding to the zone drawn by a white line. On this section, the surface of the droplet does not appear regular. It shows oscillations. These oscillations are typical of a situation where thick features are imaged while the temperature has increased even if we do not really know what process comes into play.

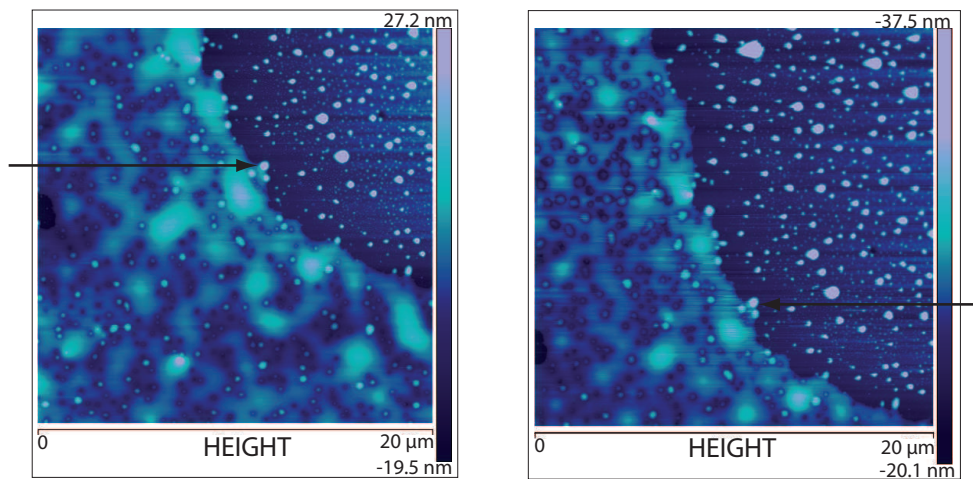


Figure E.7: Example of the piezo drift for [BMIM][TFSI] on SiOTSC with Multimode III. The image on the left was taken just before the one on the right. There is a clear drift which can be seen by the zone underlined by an arrow. Less drift is observed with Multimode VIII.

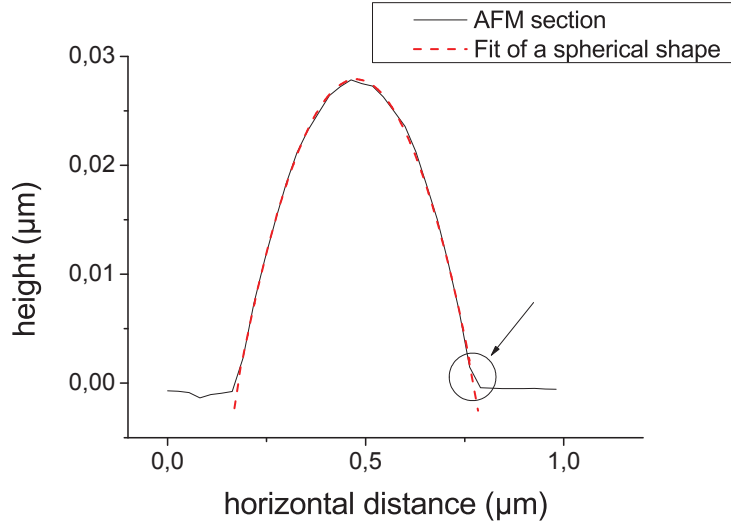


Figure E.8: AFM section of a droplet of [BMIM][TFSI] on mica substrate (plain line) and fit of a spherical shape (dashed line). The fit of the spherical shape corresponds well with the core of the droplet but clearly differs from the AFM profile on the foot of the droplet. In this case, the lateral extension of the circled zone is not large enough to be significant compared to the lateral resolution of the AFM tip. It is worth noting that the presence of a significant foot for IL droplets was only observed in the case of a contaminated sample.

implies that the user estimates roughly the expected piezodrift. This estimation is not always of the highest precision. For example, on Multimode III, it was not easy to image the same desired zone during long periods of time or to zoom on a zone of the sample<sup>7</sup>. This problem is emphasized for small AFM scans. For example, a given x, y translation appears not as dramatic on a  $30 \times 30 \mu m$  scan as on a  $2.5 \times 2.5 \mu m$  scan.

#### E.1.4.2 Tip-induced distortions

The distortions induced by the geometry of the tip were already introduced in paragraphs E.1.2 and E.1.3.3. The main consequences for our systems are that:

- The zone where the droplet comes into contact with either the substrate or the ultra-thin film can not be fully resolved. In the case of our data, contact angle measurements should not rely on this zone. The same conclusion can be drawn for the joint part between ultra-thin films and the substrate. The thickness of ultra-thin films can be measured, but not the precise shape of their vertical boundaries.

<sup>7</sup>Some AFM and STM possess systems which allow an automatic compensation of the piezo drift. Closed-loop scanners and Bruker Scan Assist Module for MultiMode overcome this problem. This was the case for the STM that we used. Note that the Scan Assist Module was present on Multimode VIII. However, droplets could not be imaged with the Scan Assist mode. They had to be imaged with Soft Tapping.



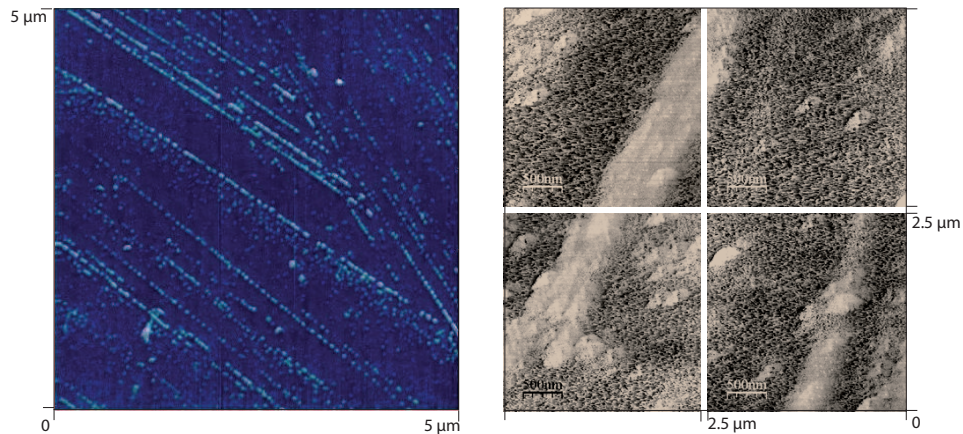


Figure E.9: Comparison of AFM and STM images of SiOTSC surface. On the left side: an AFM scan of SiOTSC. On the right side: an STM scan of SiOTSC. The AFM scan shows no porous structure whereas the STM scan clearly does. The lack of porous structure on the AFM image is due to the geometry of the tip of the AFM whereas this problem is overcome in STM image as tunneling current is used to get the image of the surface.

- Because of its lateral dimensions, the AFM tip cannot penetrate into small porous structures and therefore cannot image them. For example, small porous structures were present on our SiOTSC substrates. However, they were not imaged by the AFM. Only STM images revealed their presence (see figure E.9).

The main limitation of the AFM is then due to the geometry of the tip. That is why AFM studies find a good complement in techniques like STM, where the geometry of the wire does not play any role in the imaging process.

## E.2 Scanning Tunneling Microscopy (STM)

### E.2.1 STM imaging

The experiments were performed with Ntegra Prima (NT-MDT)(cf [9]). The figure E.10 shows the Ntegra Prima setup.

In the STM technique [1], a sharp metallic wire is placed above a conductive sample. Between the wire and the sample, a bias voltage is applied. When the wire comes close to the surface of the sample (i.e. below one nanometer), a tunneling current flows from the sample to the wire. The tunneling current changes exponentially with the wire / sample separation. The relationship between the tunneling current and the wire /sample separation is then an excellent parameter to scan this separation. In practice, during an STM scan, the tunneling current is kept constant via a feedback loop which acts on the distance separating the wire and the sample. By scanning

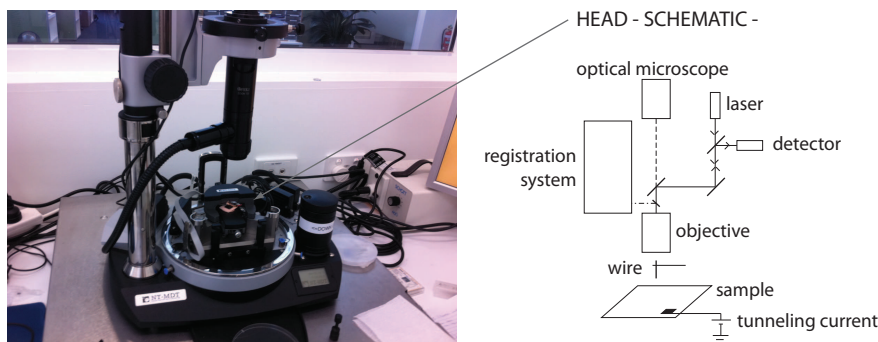


Figure E.10: On the left, picture of the Ntegra Prima setup. On the right, the way the head works is described.

the entire surface of the samples, STM can then give very precise images. For model samples, such as HOPG, the image can get the true atomic resolution. However, the resolution is strongly affected by the quality of the sample and the quality of the wires.

## E.2.2 STM wires

The wires used for the experiments were 0.25 mm Platinum / Iridium wires (Pt/Ir) purchased from Nanoscience instruments. Pt Ir wires are the most commonly used as well as chemically etched tungsten wires. Pt/Ir wires are supposed to give better atomic resolution because of the very low reactivity of Platinum. However, the Pt / Ir wires do not have a shape as uniform as the etched tungsten ones.

## E.2.3 Imaging ionic liquid droplets

To our best knowledge, STM imaging of ionic liquids droplets has been never done before. Encouraging preliminary experiments were done at the end of this PhD thesis, which allowed us to image droplets of *BMIM* – *TFSI* on HOPG substrate (see Chapter 3). These first results were possible because both ionic liquids and HOPG are conductive. The motivation of these experiments lies in the fact that, unlike AFM images, STM images do not suffer from deformations due to the geometry of the wire. This lack of deformation constitutes a great opportunity in the perspective of imaging ultra-thin films and of measuring the true profile of droplets. The comparison of AFM and STM images for the same system could indeed allow to clearly evaluate the influence of the geometry of the AFM tip on the image. This is mostly important for critical zones such as the foot of the droplet or the vertical boundary linking ultra-thin films to the substrate. Another motivation to use STM is that it is a faster imaging

technique than AFM<sup>8</sup>. It thus has more potential to follow the spreading process of conductive liquids.

---

<sup>8</sup>Furthermore, STM's temporal resolution could be further improved in the future: see reference [4].

# Bibliography

- [1] G. Binnig, H. Rohrer, Ch. Gerber, and E. Weibel. Surface studies by scanning tunneling microscopy. *Phys. Rev. Lett.*, 49:57–61, 1982.
- [2] A. Checco, H. Schollmeyer, J. Daillant, P. Guenoun, and R. Boukherroub. Nanoscale wettability of self-assembled monolayers investigated by noncontact atomic force microscopy. *Langmuir*, 22:116–126, 2006.
- [3] A. Gil, J. Colchero, M. Luna, J. Gómez-Herrero, and A.M. Baró. Adsorption of water on solid surfaces studied by scanning force microscopy. *Langmuir*, 16:5086–5092, 2000.
- [4] A.A. Khajetoorians and A. Kubetzka. STM hits the fast lane. *Nature Nanotechnology*, 5:830–831, 2010.
- [5] T. Martin, C.C. Williams, and H.K. Wickramasinghe. Atomic force microscope - force mapping and profiling on a sub one hundred angstroms scale. *J. Appl. Phys.*, 61:4723, 1987.
- [6] FESP AFM probes webpage. <http://www.bruckerfmprobes.com/Product.aspx?ProductID=3259>.
- [7] NT-MDT AFM probes webpage. <http://www.ntmdt.com/product/spm-accessories>.
- [8] Veeco metrology group. *MultiMode SPM instruction manual*, 1997.
- [9] NT-MDT Ntegra webpage. <http://www.ntmdt.com/device/ntegra-prima>.
- [10] Q. Zhong, D. Innissa, K. Kjollerb, and V.B. Elingsb. Fractured polymer/silica fiber surface studied by tapping mode atomic force microscopy. *10.1016/0039-6028(93)90582-5*, 290:L688–L692, 1993.



## Appendix F

# Films around droplets with a base radius exceeding $1.8 \mu\text{m}$

## - [BMIM][TFSI] on mica substrates deposited via low-concentration dispersions -

When [BMIM][TFSI] is deposited on mica substrates via low concentration dispersions, one can observe patches of ionic liquid as well as droplets surrounded by a film. The patches and films are pinned on the mica. The scanning process of the AFM (tip scanning the sample in non-contact mode) allows for unpinning the ionic liquid. The patches/film are then enabled to flow. The case of “small droplets”, base radius less than around  $1 \mu\text{m}$ , was described in Chapter 3: a film with uniform in thickness surrounds them. When scanned by the AFM, this film tends to evolve towards 2 nm in thickness, a thickness corresponding to the one of patches of ionic liquid deposited on mica without using any ethanol. This situation could be understood if one supposes that the film coexisting with droplets is structurally close to the one corresponding to a zero disjoining pressure. It would then explain that it is well defined and that it governs the evolution of the system: the droplet then simply adapts to let the film go towards its preferred structure.

It accounts for all the observations except for the case of ‘big droplets’. When the base radius of the droplets exceeds around  $1.8 \mu\text{m}$  the film surrounding droplets is no longer uniform in thickness. Two thicknesses coexist: the first one is a film, thinner than the patches and the second the 2 nm one, corresponds to patches scattered on the film (see figure F.1). This coexistence has been observed only on a scale of several hours after deposition. Nothing allows to suppose that the coexistence will not relax on longer times scales towards a uniform thickness. Even if it is probably not an equilibrium configuration, the fact that patches and film thinner than patches can coexist is not understood yet. The formation around “big droplets” of a film

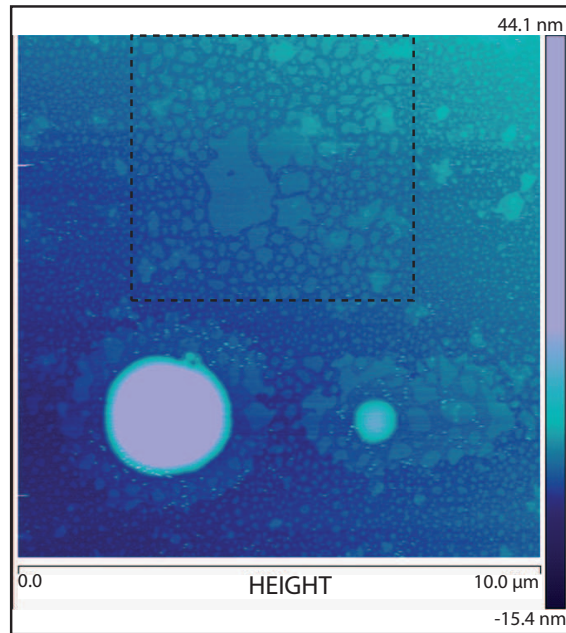


Figure F.1: Example of “big droplets” and their surroundings: a film coexists with patches. The thickness of the patches is around 2 nm, whereas the film is thinner, around 1,4 nm. The picture is a height image of high purity [BMIM][TFSI] on a freshly cleaved mica disk. The square zone on the top part of the image, where the patches spread, corresponds to the zone scanned just before.

thinner than the patches is indeed quite puzzling. As long as they are deposited on the mica with low-concentration dispersions, droplets show a fairly constant contact angle, around  $4^\circ$ , not depending on the base radius. No arguments in terms of Laplace pressure or line tension help to explain the observations. The question is open.

# Contents

<b>1</b>	<b>An introduction to wetting phenomena</b>	<b>3</b>
1.1	Phenomenological description	3
1.1.1	Common observations, some questions and comments	3
1.1.2	Total wetting, partial wetting, Contact angle	4
1.1.3	Interfacial tension	5
1.1.4	Young's law	6
1.1.5	Initial spreading parameter, thermodynamic equilibrium	7
1.1.6	Contact angle hysteresis	8
1.1.7	Wetting on an heterogeneous substrate, Wenzel and Cassie-Baxter models	10
1.2	Towards thin films and microscopic scales	12
1.2.1	Macroscopic, mesoscopic and microscopic scale	12
1.2.2	Thin flat films	12
1.2.3	Surface tension: long range and short range interactions	13
1.2.4	Static non-flat films, transition zone	14
1.2.5	Dynamic case: Adiabatic precursor films, diffusive films	16
1.2.6	Line tension and modified Young equation	19
1.2.7	Preliminary comment: Line tension versus boundary tension	20
1.2.8	Measurement of boundary tension	20
1.2.9	Measurement of line tension	23
1.3	Conclusion	25
<b>2</b>	<b>Thin films of liquid crystals</b>	<b>31</b>
2.1	Introduction to hybrid nematic films	31
2.1.1	Liquid crystals, general introduction	31
2.1.2	Nematic elasticity	34
2.1.3	Liquid crystals at an interface: about anchoring	39
2.1.4	Uniaxial nematic / Isotropic phase transition in bulk: phenomenological model of Landau - de Gennes	42
2.1.5	Hybrid Aligned Nematic (HAN) films	43



2.2	Review of wetting properties and questions to be answered . . . . .	45
2.2.1	From classical HAN films towards hybrid nematic thin films . . . . .	45
2.2.2	Solid substrates: Forbidden thickness range . . . . .	46
2.2.3	Liquid substrates: One system, two problems . . . . .	48
2.2.4	Characterization of the striped phase . . . . .	53
2.2.5	From nematic phase to liquid phase, a phase transition and a wetting transition - 6CB on water substrate - . . . . .	61
2.2.6	Existing models of striped patterns far from the NI transition . . . . .	76
2.2.7	General conclusion . . . . .	80
<b>3</b>	<b>Small volume of ionic liquid in contact with selected substrates</b>	<b>93</b>
3.1	Going towards nano-scales . . . . .	93
3.1.1	About ionic liquids . . . . .	93
3.1.2	Methods for the deposition of small droplets of ionic liquids . . . . .	94
3.1.3	How to visualize wetting processes on nano-scales ? . . . . .	96
3.2	Wetting on a model of smooth hydrophilic substrate . . . . .	96
3.2.1	About mica substrate . . . . .	96
3.2.2	Macroscopic wetting behaviour . . . . .	98
3.2.3	Discussion about reproducibility of the experiments . . . . .	103
3.2.4	Microscopic wetting behaviour: precursor and droplets . . . . .	107
3.3	Influence of roughness and porosity, evaporated carbon . . . . .	120
3.3.1	Evaporated carbon: SiOTSC . . . . .	120
3.4	Forward study: STM imaging of droplets of ionic liquids . . . . .	125
3.4.1	Characterization of HOPG substrates . . . . .	126
3.4.2	AFM and STM: Microscopic wetting behaviour . . . . .	126
3.5	Discussion and perspectives . . . . .	127
<b>A</b>	<b>Macroscopic contact angle measurement methods</b>	<b>135</b>
A.1	Sessile drop . . . . .	135
A.2	Interferometry . . . . .	136
A.2.1	Fringes of equal thicknesses . . . . .	136
A.2.2	Applications . . . . .	137
<b>B</b>	<b>Langmuir Isotherms</b>	<b>139</b>
B.1	Introduction to Langmuir isotherms . . . . .	139
B.1.1	Surface pressure . . . . .	141
B.1.2	Measurement of the surface tension: the Wilhelmy plate technique . . . . .	141
B.2	Description of the Langmuir troughs . . . . .	142
<b>C</b>	<b>About glycerol's tricks</b>	<b>147</b>
C.1	Glycerol and Langmuir isotherms experiments . . . . .	147

<b>D</b>	<b>Published articles on thin films of liquid crystals</b>	<b>153</b>
<b>E</b>	<b>AFM and STM imaging of ionic liquids</b>	<b>175</b>
E.1	Atomic Force Microscopy (AFM) . . . . .	175
E.1.1	Non-contact and intermittent-contact AFM . . . . .	176
E.1.2	Height and phase images . . . . .	177
E.1.3	Imaging ionic liquid droplets . . . . .	178
E.1.4	Sensitivity and limits of the technique . . . . .	181
E.2	Scanning Tunneling Microscopy (STM) . . . . .	184
E.2.1	STM imaging . . . . .	184
E.2.2	STM wires . . . . .	185
E.2.3	Imaging ionic liquid droplets . . . . .	185
<b>F</b>	<b>Films around droplets with a base radius exceeding <math>1.8 \mu\text{ m}</math></b>	<b>189</b>

# Summary

At a time where miniaturization is one of the main challenges in science, the physics of wetting at small-scales is far from being completely understood. The structuring role of the interface(s), the heterogeneities of the substrate or the occurrence of line effects over surface effects begin to matter. The aim of the present experimental PhD thesis is then to bring new clues to help the development of theoretical analysis. Two complex small-scale systems are studied: thin films of nematic liquid crystals on liquid substrates as well as droplets and precursors of ionic liquids on solid substrates.

Compared to an usual liquid, two ingredients must be added to describe the wetting properties of nematic liquid crystals: elasticity which is the source of long range interactions and anchoring which describes the specific role played by the boundary conditions. On a liquid substrate, thin films with antagonist anchorings exhibit complex structures and thickness coexistence. Different systems were studied under optical microscope both in the nematic range and around the nematic / isotropic transition. The results were compared to available models based on continuum theory of nematic elasticity.

Ionic liquids are molten salts at ambient temperature. They are now ubiquitous in industry, which explains that their wetting behaviour on small-scales is a hot topic. Small quantities of ionic liquid were deposited on several substrates, smooth or rough. The landscape obtained, droplets and thin films, was then imaged using Atomic Force Microscopy (AFM). The results were compared to available models for thin films and nanoscopic drops.

A une époque où la miniaturisation est l'un des principaux défis de la science, la physique du mouillage aux petites échelles est loin d'être complètement comprise. Le rôle structurant des interfaces, les hétérogénéités du substrat ou l'occurrence d'effets dits de "ligne" commencent à se faire sentir. Le but de la présente thèse, expérimentale, est d'apporter de nouveaux indices permettant le développement des analyses théoriques. Deux systèmes à petite échelle et complexes ont été étudiés: les films minces de cristaux liquides sur substrat liquide et les précurseurs de liquides ioniques sur substrats solides.

La description des propriétés de mouillage des cristaux liquides nématiques nécessite deux ingrédients s'ajoutant à ceux des liquides usuels: l'élasticité, qui est source d'interactions à longue portée et l'ancrage qui décrit le rôle spécifique joué par les conditions aux limites. Sur un substrat liquide, les films minces nématiques avec des conditions d'ancrage antagonistes montrent des structures complexes ainsi qu'une coexistence d'épaisseurs. Différents systèmes ont été étudiés au microscope optique dans la gamme de température nématique et aux alentours de la transition nématique / isotrope. Les résultats ont été comparés aux modèles disponibles qui sont basés sur une théorie continue de l'élasticité nématique.

Les liquides ioniques sont des sels surfondus à température ambiante. Ils sont devenus omniprésents dans l'industrie, ce qui explique que la compréhension de leur mouillage soit un sujet brûlant. De faibles quantités de liquides ioniques ont été déposées sur différents substrats, lisses ou rugueux. Le paysage que l'on obtient, gouttelettes et films minces, a été imagé par AFM (Atomic Force Microscopy). Les résultats ont été comparés aux modèles disponibles pour les films minces et les gouttes nanoscopiques.